Manganese-based cathode materials for zinc-ion and lithium-sulfur batteries

UNIVERSITY OF THE
WITWATERSRAND,
JOHANNESBURG

Mercy Njeri Nduni

A dissertation submitted to the Faculty of Science at the University of Witwatersrand in the fulfillment of the requirements for the degree of

Masters of Science (Chemistry)

Supervisor: Prof. Kenneth I. Ozoemena

Co-supervisors: Dr. Thapelo P. Mofokeng and Dr. Aderemi B. Haruna

March, 2024

DECLARATION

I declare that this thesis is my own, unaided work. It is being submitted for the degree of Masters of Science at the University of the Witwatersrand, Johannesburg. It has not been submitted before for any degree or examination in any other university.

Signature……..  ……**Date**……30th August 2024……

DEDICATION

This is for you, dad (Moses Nduni Ndungu) and mum (Alice Muthoni Nduni). My only goal in life, is to make you proud.

ACKNOWLEDGMENTS

I acknowledge God for the gift of life, health, peace, and favor throughout my academic life. My academic journey is a testimony of His mercies.

Special recognition to my supervisor Prof. Kenneth I. Ozoemena for accepting my call for supervision and for believing that I am a capable student which granted me the confidence and motivation in my research. He has been a very strong pillar in my academic and social life as an advisor and mentor. He also inspires me and this helps me in achieving my academic goals. I thank my co-supervisors: Dr. Aderemi B. Haruna and Dr. Thapelo P. Mofokeng who have been part of the long journey and are always ready to help even after hours with no complaints. They have taught, advised, and trained me and I will forever remain grateful. I believe I had the best supervisors anyone could wish for.

Many thanks to Prof. Girum and the ESIMSAD project for nominating me as one of their students. Without the scholarship, none of this would have been possible. Prof. Girum not only plays the role of coordinating supervisor of the project but also holds sessions with all the EU students and advises us.

I acknowledge Prof. Wuping Wu for inviting me to visit his laboratory at South East University, China. Dr. Zaichun Liu, and Dr. Tao Wang for their assistance, and Weijia Fan and Tan Xu.

Many thanks to the MEET group for the continuous sessions throughout the year and the CATMAT group for always listening to our presentations and answering our questions.

My sincere thanks to Tebogo who has assisted me throughout my project. His patience and dedication have been of great help and I appreciate his contribution. I acknowledge all my friends for being part of my journey.

Finally, I thank my parents, brothers, and sister for always checking up on me and going out of their way to support my dreams and life decisions. My heartfelt gratitude to my grandmother Karen Wambui.

RESEARCH OUTPUTS

Manuscripts being prepared for publication

1. **Mercy N. Nduni,** Thapelo P. Mofokeng, Aderemi B. Haruna, and Kenneth I. Ozoemena, “Investigating and comparing the properties of α-MnO_2 and β-MnO_2 in aqueous zinc-ion batteries” (under review for publication).
2. **Mercy N. Nduni,** Thapelo P. Mofokeng, Aderemi B. Haruna, and Kenneth I. Ozoemena, “Pechini-assisted Synthesis of High-Entropy Spinel Nanoparticles for Rechargeable Aqueous Zinc-ion batteries” (under review for publication).

CONFERENCES

1. Pechini-assisted Synthesis of High-entropy Spinel Nanoparticles for Aqueous Zinc-ion Batteries, Poster presentation at 33rd CATSA Conference from 5th to 8th November 2023, held in Mossel Bay (Western Cape).
2. High-Entropy Spinel Oxide $(CoCuFeMnNi)_3O_4$ /OLC as an Electrocatalyst for High-Performance Lithium-Sulfur Batteries. Poster presentation at the 6th International Symposium on Electrochemistry Conference from 3rd to 4th April, held at the University of Johannesburg (UJ), and 32nd annual Catalysis Society of South Africa International Conference from 13 to 16 November 2022, held in Cathkin Park in Central Drakensberg.

PROFESSIONAL ORGANIZATIONS

1. Member, South African Chemical Institute

AWARDS/ SCHOLARSHIP

1. The Intra-Africa Academic Mobility Scholarship under the project Electrochemical Science and Innovative Materials for Sustainable Africa Development (ESIMSAD) under a master's program at the University of the Witwatersrand, in January 2022.

2. The Pan African University Scholarship to study master's in Energy Engineering Track at the University of Tlemcen, Algeria (February 2022).

3. I was awarded an award for the ‘Most Interactive Student’ award at ARUA CoE-MEN Capacity Building Workshop 2023 from 31st July to 3rd August held at the University of the Witwatersrand.

ABSTRACT

Scientists face a challenge in developing new materials that are highly innovative to set a technological precedent while maintaining the application relevance for a substantial timeline. One significant strategy in new material exploration is the advancement of high-entropy alloys whereby this field has gained new properties with a high potential for technological implementation. This master's thesis extends the entropy idea to oxide materials, particularly manganese oxide materials. It also uses microwave irradiation to enhance the properties of these oxides.

Firstly, microwave irradiation and hydrothermal synthesis routes were used to synthesize β-MnO_2 and α-MnO_2 respectively. Physical characterization was done using XRD, SEM, and TGA to investigate the crystallinity, morphology, and thermal stability. According to the TGA results, β-MnO_2 showed a higher thermal resistance of 87% compared to α-MnO_2 whose thermal resistance was 83%. SEM images showed nanorods of β-MnO_2 that were bigger and much shorter than the nanowires of α-MnO_2. Electrochemical characterizations that included CV, GCD, and EIS were then conducted on aqueous zinc-ion batteries. α-MnO_2 showed higher diffusion kinetics which was evident in the CV and EIS analysis while β-MnO_2 had better energy storage properties which was portrayed in the GCD analysis.

Secondly, we synthesized the novel high-entropy oxide $(CoCuMnFeNi)_3O_4$ by Pechini-assisted synthesis. We employed this synthesis technique because it uses low temperatures in the production of pure and homogenous oxides. We performed physical characterization and electrochemical measurements for aqueous zinc-ion batteries. We then incorporated two types of carbon (Ketjen black and Super C45 (carbon black) and determined the electrochemical performance. According to our results, Ketjen black showed an improved performance which we postulated it to its large surface area.

Lastly, we employed the $HESO_x$ as an electrocatalyst in lithium-sulfur batteries. We synthesized $HESO_X$/OLC/S and OLC/S by melt-diffusion process. OLC/S was employed as a control in the electrochemical characterizations. The results showed that $HESO_x$ had higher diffusion kinetics which was achieved from the lower ΔE_p and R_{CT} values. $HESO_x$

also had a high capacity retention of 74%. On the other hand, OLC/S had better energy storage capacity shown by its high specific capacity of 523.10 $mAhg^{-1}$ at 0.1 C.

Table of Contents

LIST OF FIGURES

LIST OF TABLES

LIST OF SCHEMES

LIST OF SYMBOLS

α	Alpha
Å	Angstrom
β	Beta
°	Degree
ε_d	D-band center
ω	Frequency
γ	Gamma
λ	Lambda
/	Or
θ	Theta
i.e.	That is
σ	Warburg coefficient
Φ_{spec}	Spectrometer work function
%	Percentage

LIST OF ABBREVIATIONS

AC:	Alternating current
A:	Ampere
AZIBs:	Aqueous zinc-ion batteries
AIBs:	Aluminium-ion batteries
Ag^{-1}:	Ampere per gram
a.u:	Arbitrary units
I_{pa}:	Anodic peak current
BoL:	Beginning of life
BT:	Bioassay technology
BE:	Binding energy
BET:	Brunauer Emmet Teller
CB:	Carbon black
S_{conf}:	Configurational entropy
CE:	Coulombic efficiency
CPE:	Constant phase element
R_{CT}:	Charge transfer resistance
R_{CPE}:	Constant phase element resistance
R_{CEI}:	Cathode electrolyte resistance
I_{pc}:	Cathodic peak current
CV:	Cyclic voltammetry
i:	Current
Cif:	Crystallographic information file

cm:	Centimeter
DFT:	Density functional theory
DME:	Dimethoxyethane
DOL:	Dioxolane
C_{DL}:	Double layer capacitance
DTA:	Differential thermal analysis
EC:	Electrical conductivity
EIS:	Electrochemical impedance spectroscopy
EoL:	End of life
EES:	Electrochemical energy storage devices
EDL:	Electrochemical double layer
EEI:	Electrode electrolyte interface
E/S:	Electrolyte to sulfur ratio
ESCA:	Electron spectroscopy for chemical analysis
eV	Electron volts
R_{ele}:	Electronic resistance
F:	Faraday
FTIR:	Fourier transform infrared spectroscopy
FWHM:	Full-width half maximum
GITT:	Galvanostatic intermittent titration technique
Hz:	Hertz
HEMs:	High-entropy materials

HER:	Hydrogen evolution reaction
HEA:	High-entropy alloys
HEPi:	High-entropy phosphates
$HESO_x$:	High-entropy spinel oxides
HOMO:	Highest occupied molecular orbital
ICE:	Initial coulombic efficiency
R_{ion}:	Ionic resistance
Z_{im}:	Imaginary impedance
JCPDS:	Joint committee on powder diffraction standards
KE:	Kinetic energy
kg:	Kilogram
KB:	Ketjen black
L:	Litre
Log:	Logarithm
LSBs:	Lithium-sulfur batteries
LIBs:	Lithium-ion batteries
LiPSs:	Lithium polysulfides
LiTFSi:	Lithium bis (trifluoromethane sulfonyl) imide
LUMO:	Lowest occupied molecular orbital
M:	Molarity
mm:	Millimeter
µm:	Micrometer

mA:	Milliampere
$mAhg^{-1}$:	Milliampere-hours per gram
mF:	Millifarad
Mins:	Minutes
MIBs:	Magnesium-ion batteries
-ve:	Negative
NMC:	Nickel, manganese, cobalt
NMP:	N-methyl pyrrolidone
No:	Number
nm:	Nanometer
OLC:	Onion-like carbon
1D:	One dimension
OER:	Oxygen evolution reactions
R_s:	Ohmic resistance
OSM:	Oxygen storage materials
O_x:	Oxidation
+ve:	Positive
PA:	Polyamide
pH :	Potential of hydrogen
I_p:	Peak current
E_p:	Peak voltage
ΔE_P:	Peak charge separation
PVDF:	Polyvinylidene fluoride

KIBs:	Potassium-ion batteries
PBSs:	Prussian-blue analogs
PXRD:	Powder X-ray diffraction
Z_{RE}:	Real impedance
R_{ed}:	Reduction
rGO:	Reduced graphene oxide
RE:	Rare earth
SHE:	Standard hydrogen electrode
SA:	Surface area
SIBs:	Sodium-ion batteries
SEM:	Scanning electron microscopy
SEI:	Solid electrolyte interface
TEM:	Transition electron microscopy
TM:	Transition metal
TMO:	Transition metal oxide
TOPO:	Tri-n-octylphosphinine oxide
2D:	Two-dimension
3D:	Three-dimension
TGA:	Thermogravimetric analysis
V:	Volt
wt:	Weight
W:	Watts
XRD:	X-ray diffraction

XPS:	X-ray photoemission spectroscopy
ZIBs:	Zinc-ion batteries

Chapter 1

Introduction

1.0. Background of study

1.0.1. Electrochemical energy storage devices (EES)

Developing ideal large-scale EES systems depends on certain criteria i.e. affordability, reliability and safety, long cycle life and high gravimetric energy, energy efficiency, and power densities [1, 2].

These EES systems are divided into:

i. Those that work *via* charge accumulation at the electrode/electrolyte interface (EEI).
ii. Those that depend on redox reactions which are accompanied by the transportation of ions.

These energy storage systems include capacitors, batteries, and fuel cells.

Definitions

- ✓ Batteries- One or multiple electrically connected electrochemical cells that have terminals to supply electrical energy[3].
- ✓ Anode - Negative electrode where oxidative chemical reactions occur. It is usually an electron donor[4]
- ✓ Cathode - Positive electrode where reductive chemical reactions occur [5]-[6]. It is usually an electron acceptor.
- ✓ Separator- The physical barrier between the cathode and anode that prevents electrical shorting [7-10].
- ✓ Electrochemical capacitor- There are two types. The first one is the electric double-layer capacitors that store electrical energy in the electrochemical double layer (EDL) [11-14] while the second is pseudocapacitors which store electrical energy through a mixture of non-faradaic and faradaic reactions [15].

The energy-providing processes that are common features usually occur at EEI phase boundary. Batteries and fuel cells generate electrical energy by the conversion of chemical energy at the electrodes by redox reactions [3]. Reactions that occur at the anode are given a negative term because they usually occur at lower electrode potentials. There exists a major contrast between fuel cells and batteries. This is because batteries are usually closed systems whose main charge transfer mediums are anodes and cathodes whereby they usually take the active role in the redox reactions and hence are mostly termed as 'active masses' and the storage /conversion of energy happens in the same compartment. Fuel cells on the other hand are open systems whereby the redox reactions that happen are usually from external factors from the environment such as atmospheric oxygen or fuels that include hydrogen from tanks [16, 17].

Electrochemical capacitors (also known as supercapacitors) are quite different since energy is not usually delivered *via* redox reactions. Hence, some terms such as anode and cathode are not commonly used. There is a formation of EEI and EDL/Helmholtz layer [18] that usually results in electron movement through an external wire [19]. Supercapacitors have been commercialized in some markets such as memory protection in multiple electronic devices [20] [21], batteries have attained vast applications [22-25], while fuel cells have found usefulness in space applications [26, 27]. In a capacitor, the electrodes' surface area, pore size distribution, and conductivity are determinants of the amount of adsorption of charge.

Ragone plots demonstrate fuel cells have high-energy characteristics, supercapacitors have high-power properties [28], and batteries have intermediate energy and power attributes. The ultrahigh gravimetric power densities are caused by the rapid surface adsorption/desorption processes. With the advances in technology, there exists metal/air batteries (metal/air fuel cells) which are hybrids of batteries and fuel cells. The internal combustion engine characteristics supersede those of all other energy systems. However, it is subject to Carnot cycle limitations (which is an idealized system in which the work done is isentropic and the heat transfer to and from the system is isothermal and reversible [29] and therefore it operates under lower frequencies. The efficiency of combustion engines is determined by the Carnot cycle.

There is a major difference between the practical and theoretical energy storage capabilities that are delivered. These include:

- ✓ There are some inert parts of the system that include current collectors and diluents that are very useful for the operation.
- ✓ There occurs some internal resistance which results in internal losses.
- ✓ There is minimal utilization of the active masses.

Batteries are further categorized into primary, and secondary batteries. By definition, the primary battery is a cell/combination of cells used to generate electrical energy until exhausted and then discarded [30, 31]. In contrast, secondary batteries/rechargeable batteries can be restored to the original condition by passing an electric current in the reverse direction to the current flow when the cell is discharged [32].

The merits of batteries are that their mode of operation occurs over a wide temperature range and in any orientation, there are different options of chemical systems and voltages, they deliver high current pulses, and occur in different sizes. Their high working voltages and capacities enable them to achieve high energy densities. They have lower gravimetric densities due to the kinetics limited mass diffusion.

1.0.2. Pechini method of synthesis

This synthesis method is employed in this research work in Chapter 5 and 6. It uses low temperatures to obtain pure and homogenous oxides such as high-entropy oxides (HEOs) [33], $BiFeO_3$ [34] ,ZrO_2 [35] , $GaAlO_3$ [36], NbO_2 [37] and ZnO [38]. This research work employs Pechini method in the synthesis of spinel HEOs.

Figure 1.1 shows the reaction mechanism that occurs, which is based on two chemical processes i.e. chelation and polyesterification. Chelates are formed by the reactions between metal cations and hydroxycarboxylic acids. These cations are obtained by mixing salts of either chlorides, hydroxides, carbonates, nitrates and isopropoxides in water. However, carbonates are associated with the formation of CO_2 [39, 40], while chlorides generate Cl_2 which is poisonous [41] [42]. This research work mainly focuses on the nitrate salts due to their affordable prices. After chelation, a gel is formed using polyalcohols such as ethylene glycol through a polyesterification method. This is followed

by calcination in air with the purpose of breaking down the polymer which usually 'chars' at ~ 400°C. Lastly, the cations are oxidized by calcining at 500°C-900°C to form crystallites of mixed cation oxides. The significance of this last calcination is the removal of all organic products and the formation of oxides.

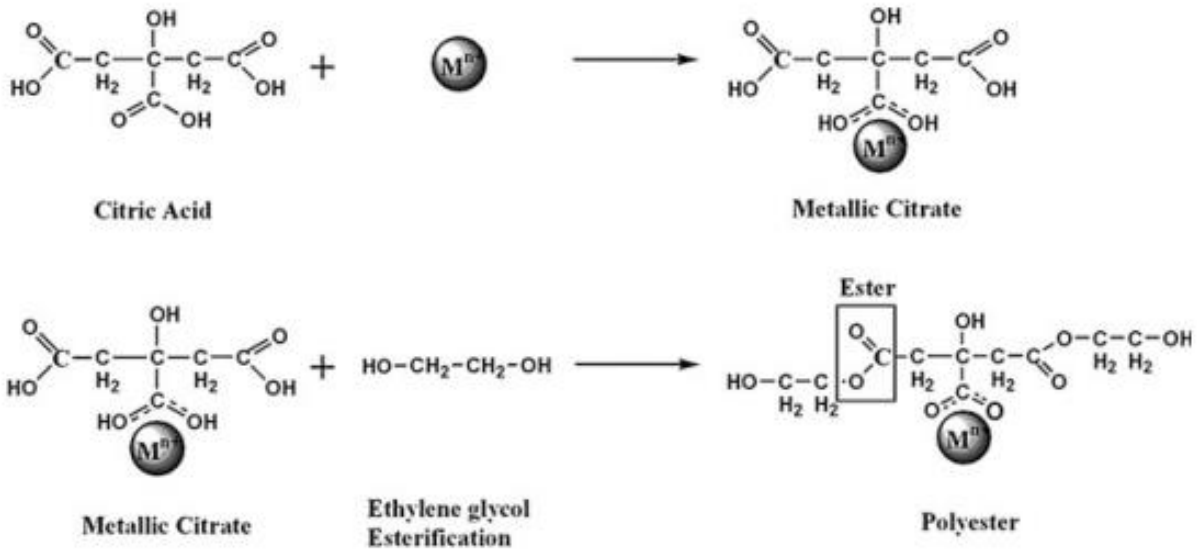

Figure 1.1: Pechini method of synthesis [43]

1.1. Aim and objectives

1.1.1. Aim

The main aim of this research work was to synthesize and characterize manganese-based cathode materials for 'beyond lithium' batteries (zinc-ion and lithium-sulfur batteries).

1.1.2. Objectives

1. To synthesize $(CoCuMnFeNi)_3O_4$ using low-temperature Pechini-assisted synthesis.
2. To synthesize α-MnO_2 using the hydrothermal method.
3. To synthesize β-MnO_2 using the microwave synthesis method.
4. To study the structure, morphology and composition of $(CoCuMnFeNi)_3O_4$, α-MnO_2 and β-MnO_2.

5. To determine the electrochemical properties of $(CoCuMnFeNi)_3O_4$ in zinc-ion and lithium-sulfur batteries.
6. To investigate the electrochemical properties of α-MnO_2 and β-MnO_2 in zinc-ion batteries.
7. To determine the effect of (Mn^{2+}) additive in the electrochemical properties of α-MnO_2.

1.2. Thesis outline

Chapter 1: It introduces the energy storage systems and Pechini-method of synthesis.

Chapter 2: This chapter gives a detailed introduction to zinc-ion batteries, manganese oxide cathodes for zinc-ion batteries, and high-entropy oxides for both zinc-ion batteries and lithium-sulfur batteries.

Chapter 3: It provides details of the experimental procedures and explains the characterization techniques.

Chapter 4: It provides the results and discussion of α-MnO_2 and β-MnO_2 for zinc-ion batteries.

Chapter 5: It provides the results and discussion of $(CoCuMnFeNi)_3O_4$ for zinc-ion batteries.

Chapter 6: It provides the results and discussion of $(CoCuMnFeNi)_3O_4$ for lithium-sulfur batteries.

Chapter 7: It concludes and gives recommendations for future methods.

1.3. References

1. Beaudin, M., et al., Energy storage for mitigating the variability of renewable electricity sources. Energy Storage Smart Grids Plan. Oper. Renew. Var. Energy Resour, 2014. **14**(4): p. 1-33.
2. Dehghani-Sanij, A.R., et al., Study of energy storage systems and environmental challenges of batteries. Renewable and Sustainable Energy Reviews, 2019. **104**: p. 192-208.
3. Winter, M. and R.J. Brodd, What Are Batteries, Fuel Cells, and Supercapacitors? Chemical Reviews, 2004. **104**(10): p. 4245-4270.
4. Kim, J., J. Lee, and Y. Tak, Relationship between carbon corrosion and positive electrode potential in a proton-exchange membrane fuel cell during start/stop operation. Journal of Power Sources, 2009. **192**(2): p. 674-678.
5. Manthiram, A., A reflection on lithium-ion battery cathode chemistry. Nature Communications, 2020. **11**(1): p. 1550.
6. Mohamed, N. and N.K. Allam, Recent advances in the design of cathode materials for Li-ion batteries. 2020. **10**(37): p. 21662-21685.
7. Li, A. and A.C.Y. Yuen, A Review on Lithium-Ion Battery Separators towards Enhanced Safety Performances and Modelling Approaches. 2021. **26**(2).
8. Zhang, L., et al., High-safety separators for lithium-ion batteries and sodium-ion batteries: advances and perspective. Energy Storage Materials, 2021. **41**: p. 522-545.
9. Pan, Y., et al., Functional membrane separators for next-generation high-energy rechargeable batteries. National Science Review, 2017. **4**(6): p. 917-933.
10. Liu, F. and X. Chuan, Recent developments in natural mineral-based separators for lithium-ion batteries. RSC Advances, 2021. **11**(27): p. 16633-16644.
11. Burke, A., CAPACITORS | Application, in Encyclopedia of Electrochemical Power Sources, J. Garche, Editor. 2009, Elsevier: Amsterdam. p. 685-694.
12. Kurzweil, P., CAPACITORS | Electrochemical Double-Layer Capacitors, in Encyclopedia of Electrochemical Power Sources, J. Garche, Editor. 2009, Elsevier: Amsterdam. p. 607-633.

13. Sagadevan, S., et al., Chapter two - Fundamental electrochemical energy storage systems, in Advances in Supercapacitor and Supercapattery, N. Arshid, M. Khalid, and A.N. Grace, Editors. 2021, Elsevier. p. 27-43.
14. Pollet, B.G., et al., 22 - Fuel-cell (hydrogen) electric hybrid vehicles, in Alternative Fuels and Advanced Vehicle Technologies for Improved Environmental Performance, R. Folkson, Editor. 2014, Woodhead Publishing. p. 685-735.
15. Mofokeng, T.P., et al., Scalable synthesis of K+/Na+ pre-intercalated α-MnO2 via Taylor fluid flow-assisted hydrothermal reaction for high-performance asymmetric supercapacitors. Journal of Electroanalytical Chemistry, 2023. **948**: p. 117809.
16. Sedighizadeh, M. and A. Rezazadeh, Comparison between Batteries and Fuel Cells for Photovoltaic System Backup. Proc World Acad Sci e, 2007. **26**.
17. O'Hayre, R.P. Fuel cells for electrochemical energy conversion. in EPJ Web of Conferences. 2017. EDP Sciences.
18. Lakshmi, K.C.S. and B. Vedhanarayanan, High-Performance Supercapacitors: A Comprehensive Review on Paradigm Shift of Conventional Energy Storage Devices. Batteries, 2023. **9**(4): p. 202.
19. Naseri, F., et al., Supercapacitor management system: A comprehensive review of modeling, estimation, balancing, and protection techniques. Renewable and Sustainable Energy Reviews, 2022. **155**: p. 111913.
20. Conte, M., Supercapacitors technical requirements for new applications. Fuel cells, 2010. **10**(5): p. 806-818.
21. Wang, R., M. Yao, and Z. Niu, Smart supercapacitors from materials to devices. InfoMat, 2020. **2**(1): p. 113-125.
22. Broussely, M. and G. Pistoia, Industrial applications of batteries: from cars to aerospace and energy storage. 2007: Elsevier.
23. Pistoia, G., Lithium-ion batteries: advances and applications. 2013.
24. Wang, Y., et al., Lithium and lithium ion batteries for applications in microelectronic devices: A review. Journal of Power Sources, 2015. **286**: p. 330-345.
25. Srinivasan, V. Batteries for vehicular applications. in AIP conference proceedings. 2008. American Institute of Physics.

26. Burke, K. Fuel cells for space science applications. in 1st International Energy Conversion Engineering Conference (IECEC). 2003.
27. Brey Sánchez, J.J., et al. Use of fuel cells and electrolyzers in space applications: From energy storage to propulsion/deorbitation. in E3S web of conferences. 2017.
28. Zhang, J., M. Gu, and X. Chen, Supercapacitors for renewable energy applications: A review. Micro and Nano Engineering, 2023. **21**: p. 100229.
29. Lutz, A.E., R.S. Larson, and J.O. Keller, Thermodynamic comparison of fuel cells to the Carnot cycle. International Journal of Hydrogen Energy, 2002. **27**(10): p. 1103-1111.
30. Owens, B.B., P. Reale, and B. Scrosati, PRIMARY BATTERIES | Overview, in Encyclopedia of Electrochemical Power Sources, J. Garche, Editor. 2009, Elsevier: Amsterdam. p. 22-27.
31. Lu, S., et al. Non-rechargeable battery remaining useful life prediction with interactive attention sequence to sequence network. in 2022 IEEE 20th International Conference on Industrial Informatics (INDIN). 2022.
32. Lankey, R.L. and F.C. McMichael, Life-Cycle Methods for Comparing Primary and Rechargeable Batteries. Environmental Science & Technology, 2000. **34**(11): p. 2299-2304.
33. Schweidler, S., et al., Synthesis of perovskite-type high-entropy oxides as potential candidates for oxygen evolution. Frontiers in Energy Research, 2022. **10**: p. 983979.
34. García-Zaleta, D.S., et al., Solid solutions of La-doped BiFeO3 obtained by the Pechini method with improvement in their properties. Ceramics International, 2014. **40**(7, Part A): p. 9225-9233.
35. Neris, A.M., et al., Undoped tetragonal ZrO 2 obtained by the Pechini method: thermal evaluation of tetragonal–monoclinic phase transition and application as catalyst for biodiesel synthesis. Journal of Thermal Analysis and Calorimetry, 2021. **143**: p. 3307-3316.
36. Oliveira, H., et al., Structural and optical properties of GdAlO3: RE3+ (RE= Eu or Tb) prepared by the Pechini method for application as X-ray phosphors. Journal of alloys and compounds, 2009. **488**(2): p. 619-623.

37. Tractz, G.T., et al., Nb2O5 synthesis and characterization by Pechini method to the application as electron transport material in a solar device. Solar Energy, 2021. **216**: p. 1-6.
38. Rodrigues, E., et al., ZnO nanoparticles with tunable bandgap obtained by modified Pechini method. Applied Physics A, 2019. **125**(8): p. 504.
39. Agrinier, P., et al., Fast back-reactions of shock-released CO2 from carbonates: an experimental approach. Geochimica et Cosmochimica Acta, 2001. **65**(15): p. 2615-2632.
40. Frezzotti, M.-L. and J.L.R. Touret, CO2, carbonate-rich melts, and brines in the mantle. Geoscience Frontiers, 2014. **5**(5): p. 697-710.
41. Wang, Y., et al., Recent advances in electrocatalytic chloride oxidation for chlorine gas production. Journal of Materials Chemistry A, 2021. **9**(35): p. 18974-18993.
42. Molina, M.J., et al., Antarctic stratospheric chemistry of chlorine nitrate, hydrogen chloride, and ice: Release of active chlorine. Science, 1987. **238**(4831): p. 1253-1257.
43. Dimesso, L., Pechini processes: an alternate approach of the sol–gel method, preparation, properties, and applications. Handbook of Sol-Gel Science and Technology, 2016. **2**: p. 1-22.

Chapter 2

Literature review

2.0. Zinc-ion batteries (ZIBs)

Fossil fuel consumption leads to an abundant elevation in toxic gases such as NO_X and SOx concentration in the atmosphere which leads to global warming. This results in the focus on renewable energy sources and EES systems. Lead acid batteries are still dominating the market for large-scale applications. This is mainly because they are affordable and durable. However, lead compounds are quite harmful to health even when used in smaller amounts and concentrations.

ZIBs were developed in 1899 [1, 2]. However, lithium-ion batteries (LIBs) superseded this technology because they have high gravimetric energy densities [3], great cycle life, and are lightweight. However, the power densities and energy efficiencies are not satisfactory. This is because they have low ionic conductivities which is a result of organic electrolytes and solid electrolyte interface formation. There are attempts to replace the LIBs due to the increasing price of the Li components and the safety concerns associated with this battery. Selection of the LIBs is according to the principle that: The chemical potential of the reaction is such that the anode reaction is less than (LUMO) and the cathode reaction is greater than (HOMO) of electrolyte [4]. SIBs have also been developed due to the availability and affordability of sodium and their comparable electrochemical mechanisms to the LIBs. $Na_3V_2(PO_4)_3$ and $NaTi_2(PO_4)_3$ are employed as sodium-ion cathode materials because of their thermal stabilities and open but rigid frameworks [5] [6] . Some scientists have also employed red phosphorous and tin that have been used commercially although they experience vast volume variation and less electrical conductivity during the electrochemical processes [7]-[8]. These batteries experience certain types of challenges. First and foremost, their operation voltage is low. There are also slow reaction kinetics and inferior electrode stability. This is as a result of the differences in ionic size. Na^+ ionic size (1.02Å) [9] is larger than of Li^+ (0.76Å). The desired electrodes that have

long-term cyclability and satisfactory storage capacity of Na^+ have not yet been developed.

KIBs have also been studied because of their low redox potential (2.92 V) which provides them with a high operation voltage. However, they experience a demerit due to a large ionic radius of K^+ (1.38 A) [4]. Hence, they have different issues in cycling stability and transport kinetics.

Multivalent ion batteries are also gaining a lot of interest because they allow the transfer of multiple electrons. MIBs are divalent and have a high volumetric energy density of about 3833 $mAhcm^{-3}$ and their reduction potential (2.4 V vs SHE) is low [10]. However, they suffer from some challenges such as finding cathode materials to insert Mg^{2+} ions reversibly [11], due to the formation of MgO film on the cathode surface and divalent nature of magnesium These challenges arise from the high electrostatic interactions between the host lattice of cathode materials and divalent Mg^{2+} [12]. These strong electrostatic interactions lead to slow Mg^{2+} diffusion kinetics and prevent the cathode from achieving its best potential. There is also a lack of compatible electrolytes since the narrow voltage windows of electrolytes are not able to meet the high energy densities required [13].

This has led to the exploration of zinc-ion batteries whereby some aspects are considered in designing these electrodes. These include;

1. The cathode materials' redox potential should be lower than the upper voltage of the decomposition of water.
2. The electrolyte’s pH should be chosen with respect to the reactions of the cathode materials.
3. A chemically stable current collector considering pH variation during discharge and charge processes.

The anode materials for ZIBs are categorized into:

1. Those materials that demonstrate Zn^{2+} stripping/plating behavior. An example of these materials is zinc plate.
2. Those materials with Zn^{2+} intercalation behavior.

2.0.1. Non- Zn based anodes

This type of anode lacks metallic zinc, instead, it contains a reversible ion channel that enables Zn^{2+} ions insertion and extraction. These types of anodes include Mo_6S_8 and $Na_{0.14}TiS_2$. Zn^{2+} is usually in the cathode or present in the electrolyte. Insertion or extraction of Zn^{2+} ions in these anode materials is useful in the realization of energy storage. The anode material undergoes a phase change during the process of charging or at the end of the discharge process.

A multistep intercalation of Zn^{2+} ions occurs in the Mo_6S_8 anode. This can be written as:

Equation1: $Zn^{2+}+Mo_6S_8+2e^- \rightarrow ZnMo_6S_8$……2.1

Equation 2: $Zn^{2+}+Mo_6S_8+2e^- \rightarrow Zn_2Mo_6S_8$……..2.2

The intercalation materials that are selected should have good electronic and ionic conductivities. Crucial parameters in the selection of high-performance intercalated anodes include satisfactory potential and capacity, high ICE, good rate performance, and stable cyclability. The sluggish extraction/insertion kinetics of Zn^{2+} in these anode materials leads to a decline in overall battery performance. Zn^{2+} intercalated anode that contains large spaces provides an ideal host for Zn^{2+} and leads to an improvement in the dynamics of insertion and extraction of Zn^{2+}, however, this highly space internal structure lowers the material's mechanical strength. This leads to a high occurrence of structural collapse after repeated battery operation.

2.0.2. Zinc anode

Zinc is a reactive electrode material based on its location in the electrochemical series. The zinc anode demonstrates a variety of different behaviors depending on two factors which are the electrode's potential and electrolyte's pH. At a pH greater than 4, there exists high over potential that limits hydrogen evolution.

The reaction occurring in mildly acidic solutions is different from that in alkaline solutions i.e.

(Mildly acidic) $Zn \rightarrow Zn^{2+} + 2e^-$ [14]……(2.3)

(Alkaline) $Zn + 4OH^- \rightarrow \{Zn(OH)_4\}^{2-} + 2e^-$ [15]……(2.4)

which is further reduced to

$\{Zn(OH)_4\}^{2-} \rightarrow ZnO + 2OH^- + H_2O$.....(2.5)

To explain the electrodes' mass transfer processes, the Nernst-Planck equation is used [16] i.e.

$$j = \frac{qCD}{kT}\frac{dV}{dx} - D\frac{dC}{dx} + Cv_x \quad \text{.....(2.6)}$$

where q is the unit charge, C is the concentration, x is the distance, T is the temperature, V_x is the convection velocity, D is the diffusion coefficient, V is the electric potential and k is the Boltzmann constant.

Zn^{2+} dissolution and deposition process is affected by three factors that are convection intensity, concentration, and potential gradient.

Zinc solubility escalates in the alkaline electrolytes since they are conducive to the formation of Zn^{2+} for example $[Zn(OH)_4^{2-}]$ [17] [18]. The transition that occurs in zinc anode in alkaline electrolytes is ($ZnO\text{-}Zn(OH)_4^{2-}\text{-}Zn$) i.e. (solid-solute-solid transition). ZnO (which is among the products of discharge) passivates the zinc surface and decreases the utilization of zinc active materials. Unequal deposition and dissolution of zinc occurs at any location of the anode's surface therefore leading to major changes in the morphology of the electrodes and growth of dendrites in the continuous cycles [19].

During electrochemical reactions zinc undergoes corrosion. During the discharge process, zinc loses electrons to form Zn^{2+} which usually dissolves in the electrolyte. The HER then augment the concentration of OH^- ions and insoluble substances are formed during the charging process. Zinc undergoes corrosion in both alkaline and acidic environments. In alkaline environments, the main corrosion product (ZnO), which is formed on the surface when the pH is greater than 5.8. In near aqueous or acidic environments when there is no presence of a complexation agent, Zn^{2+} is the main dissociation product. The major compounds of corrosion products are $Zn(OH)_2$, ($ZnCO_3$), and ($ZnSO_4$) [20]. The corrosion potential usually increases with an increase in Zn^{2+} ions

concentration because Zn^{2+} acts as a cathodic inhibitor [1]. In addition, corrosion reactions increase surface area, which then increases the zinc anode consumption and overall performance deterioration of the battery.

There is dendrites formation in the zinc anode which majorly depends on the electrolyte's pH and the local current density. Dendrites, which are mostly needle-shaped, grow on zinc's surface during battery operation. They eventually penetrate the membrane and reach the positive electrode of the battery. This results in short-circuiting and a major decline in the capacity [21]. There occurs higher working potential and solubility of zinc salts when the electrolyte is alkaline, however, the growth of dendrites and changes in shapes are more serious compared to a mild electrolyte [22]. Three forms of dendrites mainly occur i.e.

- ✓ Primary dendrite
- ✓ Multi-dendrites
- ✓ Secondary dendrites

Primary dendrites mostly form on the zinc hexagonal crystals' edge facets [23] while the secondary dendrites are formed by branched growth that occurs at the edges of the primary dendrites [24]. Zinc corrosion and zinc dendrites formation are mainly attributed to the unequal distribution of zinc on the 2D zinc foil and the planar region [25].

Major attempts have been made to reduce the zinc dendrites [26]-[27]. These include backside plating configuration, use of electrode additives such as activated carbon, and use of protective layers such as buffer coatings. The electrode additives are beneficial because the zinc ions preferentially deposit on the pore structures of the additives instead of depositing on the metal zinc surface. These pore structures can also accommodate the zinc dendrite's deposition and the insoluble anodic products. This ensures the highly active zinc surface that leads to a major performance enhancement. The buffer coatings prevent the formation of macroscale dendrites.

3D architecture has also been employed since it amplifies the electrified surface leading to a uniform distribution throughout the anode structure, it leads to interconnected pathways creation inside the porous structure leading to the enhancement of the long-

range electronic conductivity and it is useful in maintaining the shape of the electrode during the dissolution of zinc hence avoiding the zinc dendrites formation [1]. For instance, Tian *et al*. [28] used 3D architecture in the synthesis of high-loading cathodes with excellent cycling stability of over 650 cycles and a remarkably high specific capacity of 344.8 $mAhg^{-1}$. Zheng *et al.* [29] synthesized a 3D integrated anode that had a dendrite-free morphology and an excellent lifespan of more than 380 hours. Zhang *et al.* [30] synthesized a 3D rigid electrode that had connecting pores that ensured ion deposition was uniform. This electrode also performed well under harsh conditions such as compression and soaking. Idrees *et al.* [31] designed a 3D composite anode whose main purpose was to control dendrite formation and regulate the deposition of Zn^{2+} ions.

Zinc evolution and HER are among the very competitive reactions. The effect of HER is a decrease in the CE [32, 33] of anode plating/stripping and continuous consumption of the zinc metal. Often, excess zinc has to be provided to ensure normal battery cycles. Hydrogen evolution leads to the generation of gas that has a negative effect of batteries such as sealed battery systems that include button batteries. This is due to an increase internal air pressure of the battery [34] that results in swelling [35] and leads to breakage. It also leads to an augmentation in the electrolyte's local pH which is a significant source of hydroxide ions. However, the undesirable side reactions usually lessen the life and the capacity of the zinc. HER reactions should be inhibited so as to improve the charge ability of the zinc. The byproducts that are usually formed by the harmful reactions of the Zn^{2+} lead to passivation of the surface of zinc which affects the zinc dissolution and transport of Zn^{2+}. Passivation leads to an insulating film formation on the electrode's surface which restricts the movement of hydroxide ions or discharge products hence averting further discharge.

When $[Zn(OH)_4]^{2-}$ reaches its solubility limit during the discharge of the zinc electrode, there is precipitation of zinc oxide on the electrode's surface. This reduces the pore size of porous zinc electrodes. When its solubility limit is exceeded, it immediately precipitates and there is a complete blockage of the remaining pore volume and there is the occurrence of passivation. ZnO which is nonconductive, increases the impedance of the

electrode and decreases the plating/stripping CE. In conclusion, alleviation of the side reactions is crucial in the development of long-lived aqueous anode materials.

2.0.2.1. Surface modification of the zinc anode

This strategy main purpose is to ensure uniform deposition of zinc by the construction of an artificial layer whose purpose is to attain a flat deposition of layers and uniform zinc nucleation instead of using co-protective layers for zinc anode.

The types of protective layers that have been used include;

- ✓ **Organic and inorganic coatings**

Their main role is to prevent and inhibit dendrite growth occurrence and other side reactions. Functional materials that have been employed include materials that are:

- ❖ Carbon-based compounds
- ❖ Metallic materials
- ❖ Inorganic nonmetallic materials
- ❖ Composite materials

The conductivity of carbon materials is good which is crucial for stabilizing the plating/stripping behavior of Zn^{2+} by the modification of the zinc anode interface.

Other materials that have been used include TiO_2, $CaCO_3$, and ZrO_2 [36]-[37]. Surface coating is done to gain a denser and more uniform zinc deposition layer that leads to the inhibition of the formation of dendrites that leads to the enhancement of CE and cycling stability of ZIBs. This reduces the direct anode-electrolyte contact and prevents zinc corrosion and the formation of zinc oxide. For instance Song *et al.* [38] designed a hybrid TiO_2 coating that immobilized water molecules hence preventing parasitic reactions that occur in ZIBs. This protective layer regulated zinc deposition and stabilized the anode. Naresh *et al*. [39] synthesized mesoporous TiO_2 nanoparticles that enabled dendrite free anodes and the fabricated battery showed a specific capacity of 102 $mAhg^{-1}$ after 5000 cycles at high current density. Kang *et al.* [40] used $CaCO_3$ coatings to achieve uniform zinc plating/stripping of zinc anodes. The battery delivered high specific capacities of around 124 $mAhg^{-1}$ at high current densities (1 Ag^{-1}) after 1000 cycles. Sun *et al.* [41] used atomic layer deposition to coat ZrO_2 on the zinc's surface which showed excellent

cycle stability with low corrosion rates. ZrO_2 coating functions as an insulating layer since it is electrochemically and chemically inert.

- ✓ **Polymer materials**

They have a strong coordination with zinc and a hydrogen bond network that leads to the protection of the zinc anode. Polymers that have been used include polyamide (PA) coating. Polyamide increases the zinc nucleation sites that results to formation of a uniform and dense zinc deposition layer. This can be shown by the work done by Xi et al [42] which showed an inhibition of hydrogen evolution, corrosion, and dendrites. They assembled a pouch cell that delivered a cycle life of over 1500 hours at 0.5 $mAcm^{-2}$ and a specific capacity of 150 $mAhg^{-1}$ after 120 cycles.

2.0.3. Zinc cathodes

The properties that are required for cathodes for zinc-ion batteries are:

1. Cathodes with special layered and tunnel structures, since the larger the pores, the ease in hosting insertion and extraction of zinc ions.
2. Cathodes that are stable between OER and HER potential ranges.
3. Cathodes that possess high energy, working voltage, and capacity.
4. Cathodes with long cycle life during continuous charge and discharge process.
5. Cathodes that are affordable and eco-friendly.

Figure 2. shows the classification of ZIBs cathode materials. From this figure, vanadium and manganese materials represent a higher percentage than Prussian-blue analogues and organic materials. This is due to their multiple merits.

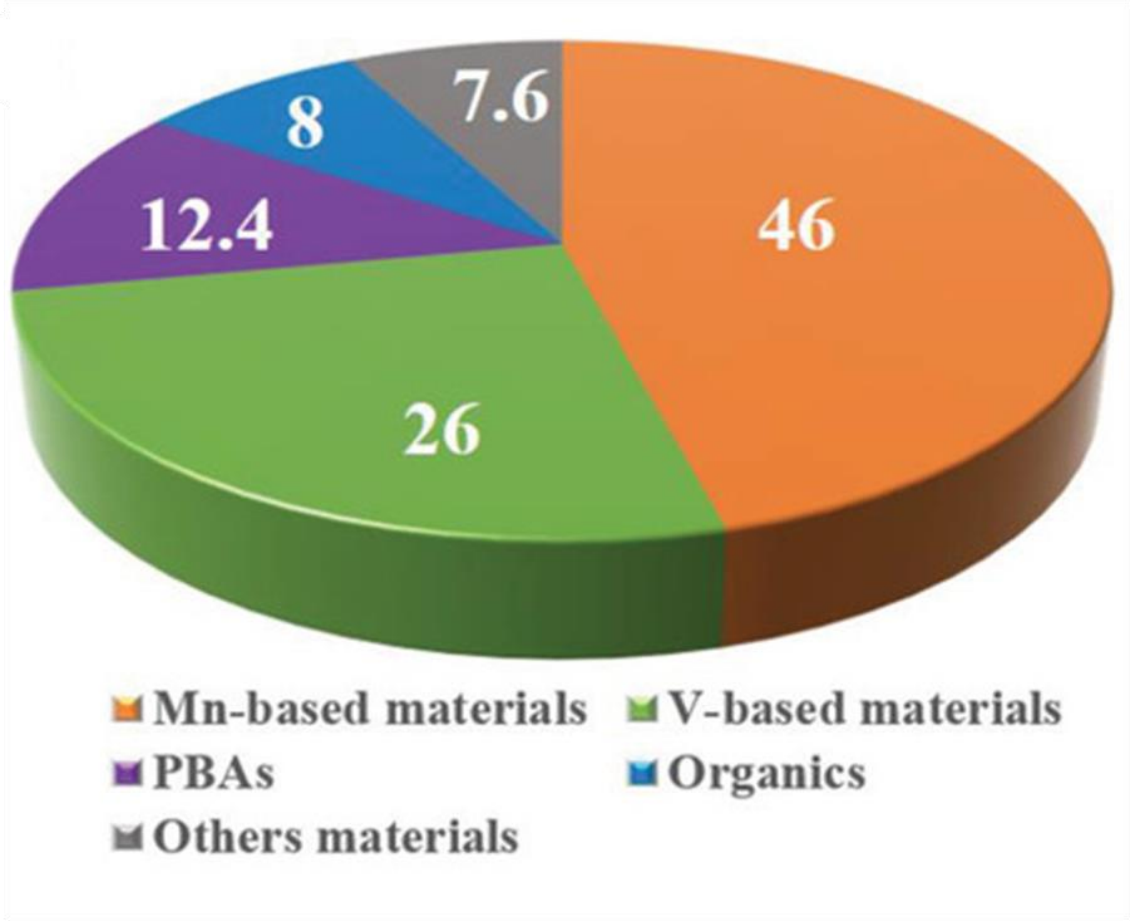

Figure 2.1: Classification of cathodes in ZIBs [43]

2.0.3.1. Vanadium-based materials

Firstly, vanadium is able to realize multi-electron transfer and high capacities due to its rich valence states that varies from +2 to +5. Vanadium materials are classified to vanadates, vanadium oxides, oxygen free vanadium compounds, and vanadium phosphates [43]. Various vanadium oxides can be obtained due to the multiple valence states, such as VO_2, V_2O_5 and $V_3O_7.H_2O$. VO_2 has multiple crystal frameworks that include VO_2 (B,M,D), VO_2 (R), VO_2 (A) which have monoclinic, rutile, and tetragonal structures [44]. V_2O_5 possesses hydrogen bonds and weak van der waals interactions between the layers and strong covalent bonds in the lattice, that enable Zn^{2+} to be embedded and detached easily, hence the excellence performance of this structure [45]. $V_3O_7.H_2O$ is an oxide with a mixed valence state with $V^{4+/}V^{5+}$ ratio of 1:2 [46].

Vanadates are derivatives of clusters or ions with vanadium oxides. These clusters or ions comprise of alkali metal ions transition metal ions, and alkaline earth metal ions. Vanadium phosphates that include $Na_3V_2(PO_4)_3$ and $Li_3V_2(PO_4)_3$ have shown to have stable frameworks and high output voltages [47]. The oxygen-free vanadium compounds include VS_2 whereby the structure is comparable to that of graphite where six sulfur atoms surround the vanadium atom [48] and VS_4 with a 1D chain structure has been reported to function as a great intercalation material with a capacity retention of 85% of more than 500 cycles [49]. VS_2 has a wide interlayer spacing that promotes insertion of Zn^{2+} as shown by Chen *et al.* [50].

Vanadium-based compounds experience demerits such as high costs, low operational voltages, and toxicity which limits their applications.

2.0.3.2. Manganese-based materials

MnO_2 is mostly due to its major merits which include:

- ✓ High theoretical capacity (308 $mAhg^{-1}$) [51, 52].
- ✓ It is less toxic and costly [53, 54].
- ✓ It has a high redox potential [55].
- ✓ It is abundant in nature and offers green environmental protection.
- ✓ It has a stable output voltage platform (1.5 V vs Zn^{2+}/Zn) [56].
- ✓ It consists of nano-sized particles that have a high SA-to-volume ratio.

It however faces limitations that result in capacity fading and weak C.E. These include:

1. It is prone to quick charge-discharge property.
2. Irreversible formation of unwanted products on cathodes such as $Mn(OH)_2$ or Mn_2O_3 and ZnO or $Zn(OH)_2$ on anodes.
3. Active materials dissolution.
4. The structure undergoes an irreversible phase transition, changes in volume, and structural collapse during repeated insertion and extraction of Zn^{2+} ions [57].
5. MnO_2 materials have poor electrical conductivity that leads to slow kinetics.

MnO_6 (basic structural unit of MnO_2) can be assembled by sharing the edges/corners into tunnel/spinel/layered type of structures. This leads to formation of multiple crystal structures of MnO_2 [58] i.e. (1x1 cross-section) tunnel structure is β-MnO_2 (pyrolusite) [59,

60] formed from single chains, (1x2 cross-section) tunnel structure is R-MnO_2 (ramsdellite) built from single and double chains, (1x1 & 1x2 cross-section) tunnel structure **i**s *γ*-MnO_2 (Nsutite) which has a co-existence of (1x1 and 1x2) cross-sections [61, 62], (2x2 cross-section) tunnel structure is *α*-MnO_2 (hollandite) [63] whereby all tunnels are built from corner double chains [64], (2x3 cross-section) tunnel structure is also referred to romanechite MnO_2 whereby tunnels are developed by double and triple chains, and (3x3 cross-section) tunnel structure is known as todorokite type MnO_2 [65] that has large tunnels since it is built from triple chains of MnO_6 octahedral. These large tunnels can accommodate various cations and water and are responsible for their better rate performances and higher capacities. *α*-MnO_2 has been the most studied because its preparation is cost-effective, it has a steady tunnel structure hence it can accommodate H^+ and Zn^{2+}, and possesses high energy densities [58]. The studies on *α*-MnO_2 include [66]-[67].

2.0.3.2.1. α-MnO_2

There are various mechanisms observed in the Zn/MnO_2 battery.

2.0.3.2.1.1. Zn^{2+} insertion/extraction

Zn^{2+} insert/extract in the *α*-MnO_2 cathode in a reversible reaction in the presence of $ZnSO_4$ or $Zn(NO_3)_2$ electrolyte. There is a conversion of *α*-MnO_2 to $ZnMn_2O_4$ after the insertion of Zn^{2+} [68] according to the reaction shown below:

$Zn^{2+} + 2e^- + 2MnO_2 \rightarrow ZnMn_2O_4$ [57, 58]……...(2.7)

This reaction is termed to be like a ‘respiration pattern due to the expansion of the cell volume.

2.0.3.2.1.2. H^+/Zn^{2+} co-insertion & extraction

H^+ insertion brings about the formation of MnOOH and [$Zn(OH)_2$] $ZnSO_4.H_2O$ which is a byproduct [69]. After insertion of H^+ the electrodes’ surface environment becomes saturated with OH^- which reacts with the Zn^{2+} to form the zinc-hydroxide sulfate(ZHS) byproduct due to its strong Lewis acid nature. Formation of ZHS is significant because it balances the proton (H^+) of the electrolyte, and reduces the desolvation of Zn^{2+} which

promotes the intercalation of Zn^{2+} ions. It however leads to the consumption of sulphate ions and water in the electrolyte.

2.0.3.2.1.3. Dissolution/deposition of MnO_2

Mn^{4+} is not directly reduced to Mn^{2+} during the discharge process. It is partly converted to Mn^{3+} which is responsible for Jahn-Teller distortion in manganese oxide which leads to capacity degradation [70]. The valence state changes from Mn^{4+} (t_{2g}^3) to Mn^{3+} ($t_{2g}^3e_g^1$) during discharging. This high spin electronic configuration of Mn^{3+} leads to a disproportionation reaction to produce soluble manganese ions [71].

Other structures include:

- **Layered structure**

The MnO_6 octahedral are assembled into sheets by sharing their edges. After the discharge process, the spinel type $ZnMn_2O_4$ emerges and phases such as MnOOH, Mn_2O_3, and ZnO are not detected [68] [72] [73].

- **3D structure**

It is the Mn_3O_4 (Hausmannite). Its structure is spinel whereby Mn^{2+} is in the tetrahedral sites and Mn^{3+} in the octahedral sites. $ZnMn_2O_4$ has been developed [74, 75]. However, it is not fit for the insertion of Zn^{2+} because it has a large electrostatic repulsion between Zn^{2+} ions and the lattice [76].

- **(ε-MnO_2)**

It is a metastable phase that has been discovered through the deposition of electrocatalytic MnO_2 in high current densities. It mainly consists of face shared YO_6 and MnO_6 whereby Y symbolizes vacancy [77].

There is mutual transformation of MnO_2 structures. For instance, drying and loss of partial water layers transform buserite (10 Å) to birnessite (7 Å) [78] [79]. The transformation of birnessite to buserite can be obtained by the exchange of sodium ions with magnesium ions due to the strong hydration effect of magnesium ions. Moreover, the exchange of sodium ions in birnessite with Li^+, Mg^{2+}, K^+, and Ba^{2+} leads to the formation of ramsdellite, spinel, hollandite, todorokite, pyrolusite, and romanechite phases. These various

transformations are followed by the exit or entrance of various cations or molecules of water which is significant in the mechanism of ZIBs [77].

Zn^{2+} ion intercalation in MnO_2 is accompanied by deformation of the host structure. There is a strong interaction between the Zn^{2+} and the (MnO_6) octahedral which is because of the large charge density of Zn^{2+}.

2.0.4. Prussian blue analogs-based cathodes

They have a chemical formula of $A_xM_1[M_2(CN)_6]_y \cdot nH_2O$ ($0 \leq x \leq 2$; $y \leq 1$) whereby M symbolizes transition metals and A represents alkaline cation [80]. It is also given by the formula $A_xFe[Fe(CN)_6]$ where A represents alkali metal [81]. They have an open framework structure [82] which enables them to tune the electrochemical properties, have enough redox active sites, and have strong structural stability. However, they possess a high operating voltage (1.5-1.8 V), hence they exhibit low specific energy densities (around 100-120 Wh/kg) which are calculated based on the electrode materials' active mass [83]. They have low capacities that make them uncompetitive in most battery applications.

2.0.5. Organic Compounds

They have been utilized due to their multi-electron reactions, wide electrochemical window, biodegradability, and low toxicity. They have malleable lattices and soft crystal structures that permit molecular orientations which frees up the active sites. This promotes facile and reversible interactions with Zn^{2+}. These compounds include quinones and polyaniline compounds, whereby quinones are mostly used due to their low polarization.

2.0.6. Electrolytes

Their main role is to provide an ionic conduction path. Electrolytes are divided into aqueous, non-aqueous, and gel/solid electrolytes. The stability of the electrolytes is within certain voltage ranges and exceeding these voltage ranges leads to decomposition. The two factors that affect stability of electrolyte are its purity and composition. An appropriate electrolyte for ZIBs ought to have a high ion transference number [84], have high ionic conductivity, adapt to a wide range of temperatures, and have an enlarged electrochemical stability window to suppress OER and HER reactions [84].

Aqueous electrolytes are solutions of completely dissociated negative and positive ions of salts of strong bases and acids. Their merits include high tolerance against environmental moisture, excellent ionic conductivity, high flexibility in the manufacturing environment, low cost, non-flammability properties, and environmentally benign [69, 85]. Their drawbacks are that they have a narrow electrochemical stability window and have poor compatibility with the electrode materials.

The aqueous solvent-based electrolytes have a high conductivity that is caused by their dielectric constants which cause stable ionic species and large solvating power that is responsible for the hydrogen bridge bonds formation and enables protons to have the unique Grotthus conductivity mechanism. They show an electrochemical stability window of 1.23 V [86]. This is attributed to the decomposition of free water molecules into hydrogen and oxygen gas [87]. However, this stability window can be extended to approximately 2 V due to kinetic effects.

Aqueous electrolytes have gained dominance in ZIBs because they are cheap, safe, and provide better stability for the electrodes. However, neutral aqueous electrolytes are preferred. This is because zinc dendrites and zinc oxide which is a byproduct are easily formed in alkaline aqueous electrolytes [64]. $ZnSO_4$ and $Zn(CF_3SO_3)_2$ are the most widely used electrolytes due to their compatibility with electrodes and stability [88]. $Zn(CF_3SO_3)_2$ has a disadvantage whereby it is expensive which limits its applications [64] however, it exhibits good reversibility of zinc deposition and rapid kinetics since there is quicker Zn^{2+} transportation due to the reduction of water molecules surrounding Zn^{2+} due to the bulky $CF_3SO_3^-$ [89]. Zinc nitrate has also been used. However, there is the degradation of the zinc anodes which is mostly due to the high oxidant property of NO^{3-} [90] [91].

Non-aqueous electrolytes have lower conductivities because the ions are bound to each other. This is because they have a lower dielectric constant and solvating power that leads to ion formation even at low salt concentrations. They also show much higher viscosities. These electrolytes are limited to approximately 4.6 V whereby exceeding the voltage limit leads to polymerization of the solvent system [92]. Their merits include:

- ✓ They have a wide electrochemical window.
- ✓ They have a wide library of cathode candidates.

Whereas their drawbacks include;

- ✓ They have low ionic conductivity.
- ✓ They are flammable.
- ✓ They are toxic.
- ✓ They are highly sensitive to the ambient atmosphere.
- ✓ There is a high cost of electrolytes solvents and salts.

Gel electrolytes have also been used. They feature a solid-like dimensional stability which is promising for ZIBs. They include zinc salts such as $ZnCl_2$, $ZnSO_4$, $Zn(CF_3SO_3)_2$, additives such as LICl, $MnSO_4$, and Na_2SO_4, polymeric frameworks such as (gelatin and gum) and a specific amount of water [93] [94]. Polymeric frameworks function in providing mechanical integrity and they enable good contact for the electrodes/electrolytes interface. These electrolytes have the major merit of decreasing system side effects such as the electrode material's dissolution, zinc dendrites growth, and decomposition of water because they have a limited amount of free water. They however have poor mechanical strength and low ionic conductivity which limits their applications.

Certain additives such as $MnSO_4$ have been added to the Zn/MnO_2 battery. Without the additives, the battery displays capacity fading during the initial fifteen cycles that are mainly due to the dissolution of Mn^{2+} resulting from Mn^{3+} disproportionation [1]. $MnSO_4$ addition balances the equilibrium of Mn^{2+} between the dissolution of MnO_2 electrode and electrolyte thereby stability.

2.0.7. HEOs application in ZIBs

LIBs have been in commercialization since the 1990s because of their high energy density, lightweight design, and long lifespan [95]. They however experience numerous challenges such as their high prices, minimum lithium resources, and use of poisonous electrolytes [96]. Metal-ion charge carriers such as Na^+ and K^+ ion batteries have been studied. However, their safety remains to be a major concern. ZIBs have gained numerous recognition which is attributed to their merits which include their high volumetric energy density (5851 $mAhcm^{-3}$), high gravimetric capacities (820 $mAhg^{-1}$) [97], decreased

cost, non-toxicity, low equilibrium, advanced safety, low flammability, and environmental benignity since they use aqueous electrolytes [53, 54, 98, 99].

The characteristics of zinc metal include its high ideal theoretical capacity (820 $mAhg^{-1}$), its low redox potential (-0.76 V vs SHE), small bare ion radius (approximately 0.74 Å), and small hydrated ionic radius (approximately 4.6 Å) [100].

Their use however is restricted to the availability of suitable cathode materials because of the great electrostatic reaction between Zn^{2+} and the crystal structure of the cathode materials [56]. Several cathode materials have been developed using oxides of cobalt, manganese, and vanadium, and recently, Prussian blue analogues (PBA) have attracted the attention of most scientists [80] [101]. However, PBAs are disadvantaged due to their low capacity while vanadium oxides are expensive. This has led to a great focus on the manganese oxides due to their abundance and the high safety of materials. ZIBs are based on aqueous electrolytes which are advantageous because they have higher ionic conductivities than non-aqueous electrolytes.

The tunnel structures of MnO_2 have the merit of providing open pathways and multiple active sites for the storage and diffusion of Zn^{2+} ions. However, they face a demerit of severe structure collapse during the discharging. The layered structures possess larger spacing channels which favor fast and reversible zinc intercalation and extraction. However, there exists a phase transition during cycling that leads to large volume changes and structural collapse. Manganese oxide spinels have been developed and have shown outstanding properties and performance. Wu *et al.* [102] have synthesized $ZnMn_3O_4$ spinel through solvothermal synthesis route that showed excellent rate and cycle performance due to inhibition of manganese dissolution while Tao *et al.* [103] synthesized cobalt and nickel substituted spinel $ZnMn_2O_4$ that showed excellent performance since it was able to suppress Jan Teller distortion.

Cobalt oxide spinels have also been explored as a cathode and they revealed a suitable channel for Zn^{2+} ion diffusion. For instance Yang *et al.* synthesized oxygen deficient nanowires that showed a specific capacity of 119 $mAhg^{-1}$ and 111% capacity retention after 5000 cycles [104]. Zhang *et al.* [105] have doped Zn to Co_3O_4 which showed a high

specific capacity and outstanding rate performance. A combination of cobalt and manganese oxide aimed at providing synergistic effects of multiple states of the valence electron has also been studied and has a consequence of facilitating the redox reactions hereby increasing the electrochemical performance. Yadav *et al.* [97] $MnCO_2O_4$ spinel showed a high capacity of 595 $mAhg^{-1}$ and an 85% capacity retention after 250 cycles. MnO_2 usage is mostly due to its low interfacial impedance and superior electrochemical properties however it suffers from John Teller distortion hence limiting its performance. Cobalt oxides have superior performance however the price of metal cobalt continues to escalate and the demand for low-cobalt electrodes continues to grow [106].

Inspired by the aforementioned considerations, high-entropy oxides consisting of cobalt, nickel, iron, copper, and manganese have been explored in this study. The main reason for employing these five metals is due to the core effects that include lattice distortion, sluggish diffusion, high entropy, and cocktail effect. Currently, only two papers have been published on HEOs for ZIBs. Liu *et al.* [107] synthesized $Co_{0.6}Ni_{0.6}Fe_{0.6}Mn_{0.6}Cu_{0.6}O_4$ that had excellent stability of 115.3 $mAhg^{-1}$ after 1500 cycles at a high current density. They attributed this excellent performance to the broadened d-band centers ($\varepsilon_{d)}$ and the cocktail effect of the metal constituents. Jia *et al.* [108] synthesized a Manganese-rich $Mn_{0.85}Co_{0.03}Fe_{0.03}Ni_{0.03}Cu_{0.03}Cr_{0.03}O/C$ that showed excellent capacity retention of 93.2% at a higher current density of 10 Ag^{-1} after 10,000 cycles. They attributed this performance to the limited manganese dissolution caused by a higher Mn-O bonding that resulted from the synergistic contribution of the metals.

2.0.8. Strategies used in overcoming the challenges in ZIBs

2.0.7.1. Use of oxygen storage materials (OSM)

They can be defined as materials that store/release oxygen at elevated temperature and oxygen partial pressure. Materials such as ceria (CeO_2) have been utilized as oxygen carriers because of these aspects: their redox properties (low redox potential between Ce^{3+} and Ce^{4+}), large oxygen transfer properties, high reactivity and hardness, high ionic conductivity, stability at high temperatures, and strong ultraviolet radiation absorption ability, interaction with metal oxides to create active interfaces, and they possess multiple oxygen vacancies in their surface which function to stabilize metal particles. CeO_2

functions as an effective catalyst due to Ce^{4+} to Ce^{3+} redox shift which leads to the creation of anion deficiency [109].

2.0.7.2. Defect engineering

The main aim of defect engineering has been to facilitate the diffusion of ions and increase the number of active sites for MnO_2 materials [110]. Among the multiple defects, oxygen vacancies have shown to improve the cathode's performance. It is a surface modification technique used to modify the materials' surface to improve the transport of charged particles. It leads to an increase in adsorption sites and promotes proton and Zn^{2+} diffusion [111]. Defects ameliorate the deficiencies occurring during Zn^{2+} storage such as poor conductivity, sluggish kinetics, and insufficient active sites. Several researchers have studied defect engineering on MnO_2 for ZIBs. For instance, Ni-doped alpha MnO_2 nanowires have been synthesized with both anion and cation deficiencies [111] which had a maximum specific capacity of 346 $mAhg^{-1}$ and a significant improvement in the rate performance. Xiong *et al.* [112] have employed defect engineering for the synthesis of oxygen-deficient σ-MnO_2 which had excellent performance with a specific capacity of 345 $mAhg^{-1}$. Han *et al.* [113] introduced oxygen defects to beta MnO_2 which had an excellent capacity retention of 94% after cycling for 300 cycles, and a specific capacity of 302 $mAhg^{-1}$. Wang *et al.* [114] synthesized superfine defect-engineered MnO_2 that showed a high energy density of 406 $Whkg^{-1}$ and excellent durability of more than 1000 cycles without any capacity degradation. Ang *et al.* [115] have synthesized birnessite MnO_2 that is oxygen deficient which showed a high specific capacity of 378 $mAhg^{-1}$ and a high energy density of 520 $Whkg^{-1}$.

2.1. Moving towards Lithium-Sulfur Batteries using High Entropy Materials

2.1.1. Introduction

Energy is a crucial sector affecting the world today. The major issue arising from energy is that energy production is less than its consumption. The demand for energy is greater and keeps on increasing as the population increases. This has led to countries that cannot sustain the energy demands of their population. For instance, many countries have a

load-shedding schedule that involves some daily power cutoffs in specific towns within specific hours. This leads to many economic-related problems in the country, and this trend is spreading to other parts of Africa and the world at large. There is a need to come up with EES to store the renewable energy obtained from both sun and wind.

The first prototype developed for LSBs was in the year1960s while LIBs were successfully commercialized in the 1990s [116]. This first prototype demonstrated enormous promise as one of the high-energy-density materials. The fall of LIBs has been mostly due to the fire explosions involved with it and their low energy density which makes them unable to fulfill the rising demands [117]. This has attributed to the rise of LSBs. The theoretical energy density associated with these batteries is beyond impeccable since it is approximately 6-7 times more than that of LIBs [118], its usage is friendly to the environment, it is cheaper compared to its predecessor LIBs due to a fairly low cost of the raw materials, and earth abundance of the sulfur cathode [119]. The high energy density is brought about by the high theoretical capacities of sulfur (1675 $mAhg^{-1}$) [118, 120, 121] and lithium (3860 $mAhg^{-1}$) [122, 123]. The major difference between LIBs and LSBs lies in their means of mechanical energy storage whereby LIBs operate due to the intercalation of the Li^{+} into layered electrode materials [124] while the LSBs' mode of operation is based on two mechanisms [125]. The first mechanism is metal plating/stripping on the lithium anode while the second mechanism is sulfur conversion reaction.

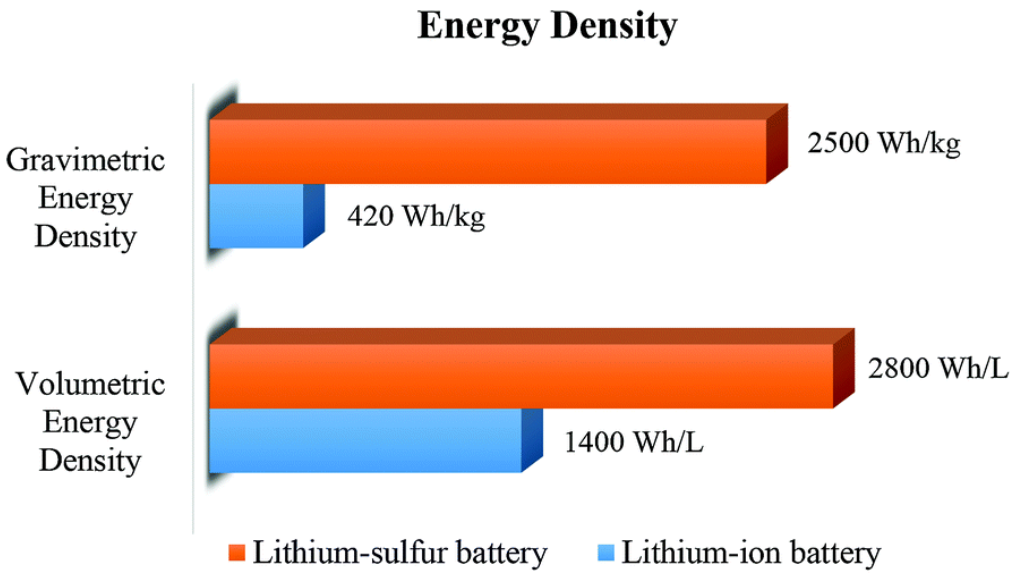

Figure 2.2: Energy density comparison plots of LIBs and LSBs [126]

LSBs experience some shortcomings which include kinetic difficulty rendered by insulating properties of charging and discharging end products, the rapid loss of active materials due to the changes in the volume that occur during cycling, reduced CE and cycling stability caused by shuttle effect, electrolyte consumption caused by limited diffusion, uneven side reactions of the LiPSs and sulfur and parasitic reactions for the lithium metal anodes and dendrite growth [127].

2.1.2. Overview of lithium-sulfur batteries

These batteries are composed of four components. These are anode (lithium), separator, electrolyte, and cathode (sulfur). The sulfur cathode mainly consists of sulfur, a conductive agent such as carbon, and a binder which is mostly (polyvinylidene fluoride) that is mixed in certain ratios using NMP and coated on a current collector which is mostly aluminium foil. The most commonly used electrolyte is an organic ether electrolyte (LiTFSI), combined with 1,2 (DME) and 1,3 (DOL). LiTFSI is used mostly because of its strong thermal stability, good compatibility with ether solvent, good dissociation ability, and high ionic conductivity [128]. The electrochemical reactions that occur during charge-discharge are:

Reactions at the **cathode**:

$S_8 + Li^+ + 16e^- \rightarrow 8\ Li_2S$ ……(2.8)

Reactions at the **anode**

$Li \rightarrow Li^+ + e^-$……..(2.9)

Overall reaction: $S_8 + 16Li \rightarrow 8Li_2S$ ……(2.10)

Elemental sulfur usually exists as a S_8 ring. This ring is normally formed by a combination of 8 sulfur atoms. S_8 is normally in its charged state hence discharge is the first reaction step in charge-discharge analysis. Lithium is oxidized to Li^+ and e^- which pass through the electrolyte and external circuit in that order to the cathode (sulfur) during discharge. At the cathode side, the reduction of S_8 and Li^+ by electrons occurs to form Li_2S [129]. The reverse occurs during charging. The potential window between the (–ve) and (+ve) reactions in the LSBs is (1.7 V-2.8 V).

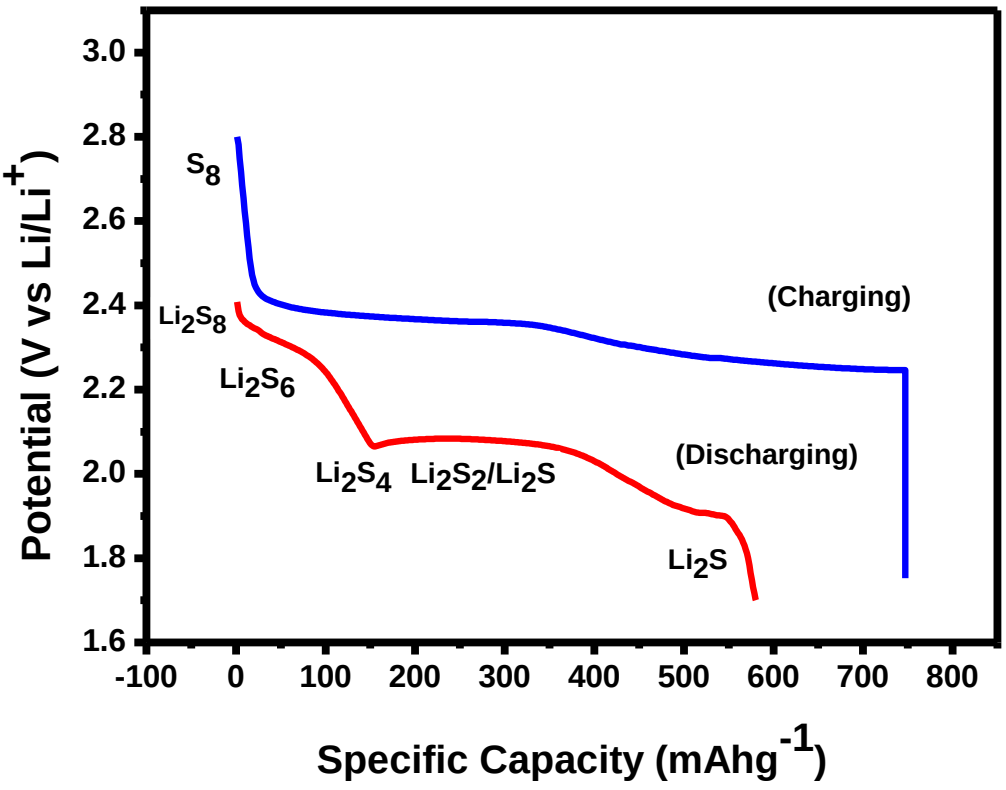

Figure 2.3: Profile showing the LSBs reduction processes

2.1.3. Discharge stages in LSBs

2.1.3.1. Solid-liquid phase

This is the ring opening of S_8 after it gains electrons. S_8^{2-} is formed. It accounts for a quarter of the theoretical specific capacity of the LSBs [129].

2.1.3.2. Liquid-liquid phase

A series of complex reduction reactions occur to the S_8^{2-} whereby it is further reduced to S_6^{2-} and S_4^{2-}. This 2nd stage corresponds to the 1st discharge plateau of LSBs. It is faster because the polysulfides are soluble [129].

2.1.3.3. Liquid-solid phase

This leads to the polysulfides' conversion to Li_2S_2 and Li_2S. These products have poor electrical conductivity and contribute to the main theoretical capacity of these batteries.

2.1.3.4. Solid-solid phase

Li_2S_2 is reduced to insoluble Li_2S. Li_2S_2 and Li_2S have poor solubility and electrical conductivity hence it is a slow reaction and Li_2S formed is highly polarized.

The charging process (oxidation process) facilitates the removal of lithium [129].

2.1.4. Diffusion of polysulfides

LiPSs are negatively(-ve) charged polar substances. They are Lewis bases, they provide excess electron pairs to Lewis acids and this leads to the formation of coordination bonds. Metal atoms with multiple polar sites can strongly bond to the LiPSs through interactions such as polar-polar interactions, lewis acid-base interactions, and even sulfur chain catenation. This is important in anchoring and trapping the polysulfides to the host surface [130].

Polysulfides are soluble in ether electrolyte which is mostly used in LSBs whereby they are dissolved in the form of molecules. They also have a big tendency to form clusters. The structures of the formed polysulfides such as Li_2S_4, Li_2S_6, Li_2S_8 are polar which makes them interact with other polar molecules.

The dissolution of polysulfides has one major advantage, whereby it improves the speed of mass migration which promotes electrochemical reactions kinetics [131]. Polysulfides that are formed at the sulfur cathode undergo two major processes before they reach the lithium anode. This include diffusion and dissolution. In order for diffusion to occur, the polysulfides have to pass through the separator, and hence diffusion can be easily controlled through the modifications of the separator and S_8 electrode. To solve the shuttle effect, there are some strategies done on the sulfur cathode. These include:

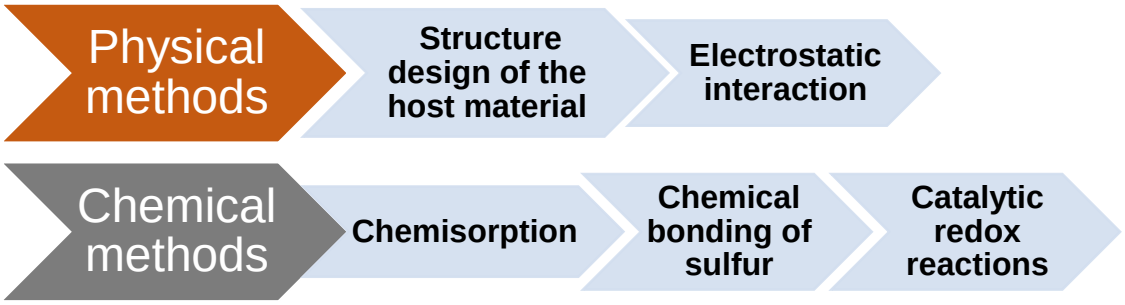

Figure 2.4: Physical and chemical methods used to adsorb polysulfides

2.1.5. Physical methods

2.1.5.1. Structure design of the host material

Two mechanisms have been proposed. These are cladding and layered mechanisms. The cladding is divided into single-layer and multi-layer cladding whereby the preparation of the single layer is easier and more simple while the sulfur content is much more in the multi-layer cladding. The cladding structure is very related to a cage-like structure while a layered structure behaves like a sieve which has the function of suppressing polysulfide diffusion. The conductivity and thickness of the cladding coating must be taken into consideration.

The single-layer coating is usually done using 2 methods:

- ✓ Preparation of cladding material is done prior to the introduction to host material by heat treatment. It leads to formation of a structure that is more stable which is

helpful in reducing the volume expansion of sulfur. The shortcoming of this method is that there is a relatively low sulfur loading.

- ✓ The cladding is coated directly on the sulfur surface. The merit of this method is that it has good contact with sulfur. This provides a better electron channel for the sulfur which increases its utilization. The shortcoming of this method is sulfur's volume expansion owing to the close contact of the S_8 and the cladding.

Coating materials which have been used include materials made of carbon, metal oxides and polymers whose main functions is to inhibit diffusion of polysulfides and function as a support for the volume expansion of sulfur.

The layered structure is made up of:

- ✓ Macroscopic layered structure - contains an electrode layer that contains sulfur and additional layers for polysulfide diffusion suppression.
- ✓ Microscopic layered structure - it functions by encapsulating sulfur right in the middle of the layered material.

Layered structures have the benefit of increasing the diffusion paths of the polysulfides.

2.1.5.2. Adsorption of polysulfides by electrostatic interaction

Polysulfides have a structure which is asymmetrical hence their positive and negative charge centers have the ability to separate. They are also susceptical to electric fields which can be eliminated by the fabrication of a micro-electric field inside the sulfur cathode.

Scientists have added $BaTiO_3$ additive to the sulfur cathode which is a ferromagnetic material and it has the ability to polarize thereby creating an internal electric field. It has the ability to adsorb the polysulfides by electrostatic action. These electrostatic adsorption takes into account that there is no overlapping between the positive and negative centers at any point.

2.1.6. Chemical effect

2.1.6.1. Chemisorption

It is the polysulfide immobilization by formation of chemical bonds and is applicable because of the existence of concentration gradient of the polysulfides. The host material

that is used is either bonded to the sulfur in the polysulfides, the lithium in LiPSs or to both of them. Characterization of chemical interactions has been done through multiple ways. These include, the bond energy, the charge transfer and distribution, the bond length, and the density of the states.

The LiPSs adsorption has been done by metallic and non-metallic elements. The non-metallic elements are divided into those based on carbon and those not based on carbon while the metallic elements include metal oxides, metal carbides, and metal nitrides. These metallic elements have 2 capabilities whereby they are able to adsorb the polysulfides and also promote polysulfide conversion. This adsorption by the metallic compounds is brought about by the dipole-dipole interactions and also the Lewis acid base theory.

2.1.6.2. Fixing polysulfides by redox reactions

Thiosulfate and polythionate complexes have indicated occurrence of redox reactions.

2.1.6.3. Promotion of polysulfide conversion by catalysis

Catalysis plays a major role, whereby there should be faster rate increase in the conversion of soluble LiPSs to insoluble Li_2S since the amount of polysulfides that tend to diffuse will decrease by a major extent.

2.1.7. Shuttle effect

The effect of this shuttle effect is that it leads to a reduction of the active material's utilization rate which reduces the cycling stability of LSBs. It also leads to self-discharge and reduces the CE of the LSBs.

During discharge, the evolution of sulfur is divided to 4 stages:

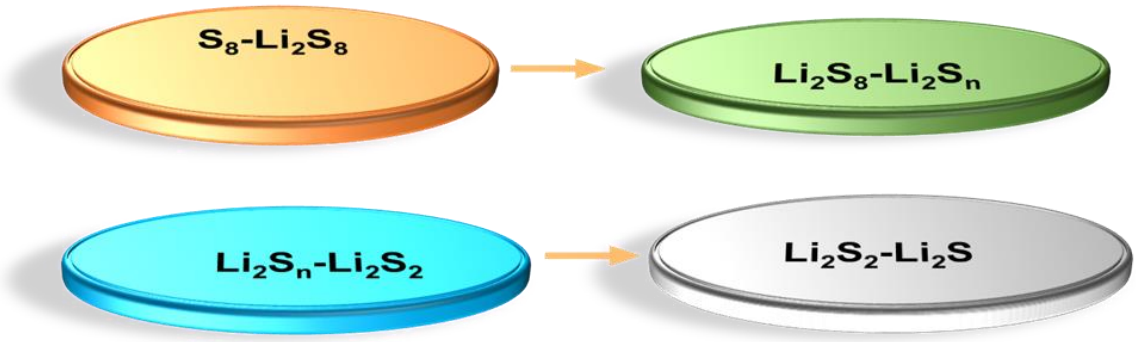

Figure 2.5: Reduction processes in LSBs

The shuttle effect is mainly brought about by polysulfide dissolution in the organic liquid electrolyte. Different techniques have been used to alleviate these problems to modify the LSB since it is the future energy storage battery.

Multiple scholars have come up with different ways to fix the problems associated with LSBs. For instance, in 2009, Nazar *et al.* incorporated sulfur within a conductive carbon matrix using a thermal melt treatment procedure to alleviate the insulating nature of sulfur. This is because carbon has a high conductivity compared to sulfur which is an insulator and its loose clusters form a porous framework that contains the redox products [116]. The consequence of this method is that it is difficult to utilize and stabilize the active sulfur material. There are agglomerates from insulating sulfur that form inactive cores within the sulfur carbon mixture and this limits the cathode redox reactions. Carbon also causes high tortuosity which limits the electrolyte diffusion and this leads to heterogeneous reactions occurring in the sulfur cathode.

Aurbach *et al.* also tried to solve the shuttle effect whereby they studied the ($LiNO_3$) additive [132]. This additive has also been studied by other scholars and its major benefit involves the stable SEI formation which acts as a protective layer on the lithium anode. Their results showed CE was increased to 98%. This process also helped reduce the shuttle effect which is among the challenges facing LSBs. This additive should be added in a way that does not reduce the sulfur content.

The kinetic issue can be solved by developing heterogeneous polysulfide electrocatalysts and homogenous polysulfide redox mediations. The polysulfide electrocatalysts reduce the activation energy barriers by accelerating the redox kinetics at the cathode while the polysulfide redox mediation introduces an extrinsic kinetically favorable redox couple that participates in sulfur redox reactions.

Since sulfur is an electronic insulator, major physical and chemical modifications of its morphology have been done whereby sulfur porous carbon-based nanocomposites and sulfur conductive polymer nanocomposites have been used to increase sulfur conductivity. It also has the major benefit of suppressing the polysulfide reactions.

2.1.8. Redefining the challenges experienced in LSBs

2.1.8.1. Use of catalysts

The catalysts employed in LSBs perform the functions stated as follows:

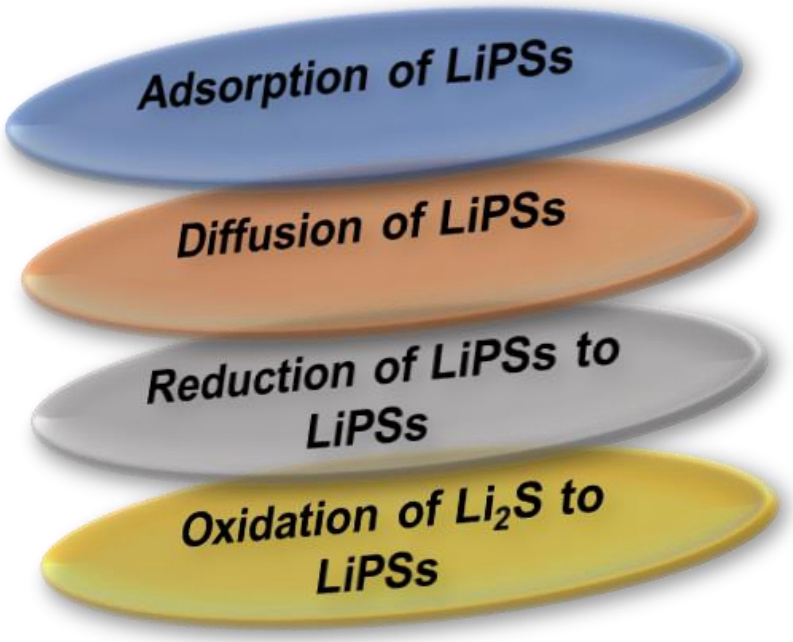

Figure 2.6: Functions of catalyts

- ✓ Adsorption towards LiPSs

The high adsorption ability of LiPSs is one of the major qualities of the catalyst. Carbonaceous materials such as 1D carbon nanotubes and 2D carbon nanosheets have been widely studied. However, they anchor sulfur by the physisorption method which leads to weak confinement. Scholars have incorporated heteroatoms to regulate the surface chemistry of these carbon materials but recently, approaches have been made towards transition metal compounds that include nitrides, oxides, and borides.

- ✓ Diffusion of the adsorbed LiPSs

Consideration of the anchoring ability and the diffusion barrier needs to be done fully.

- ✓ Reduction of LiPSs to Li_2S

Li_2S_4 conversion contributes to approximately 75% of the theoretical capacity which is not only significant in controlling the reduction reaction rate but also in improving the sulfur utilization. There however exists some challenges in the interconversion when carbonaceous materials are used. These include a high nuclear barrier caused by poor lithium ions and electron transportation. Catalysts that facilitate the conversion from high to low-order LiPSs with regard to kinetics and thermodynamics should be considered.

- ✓ Oxidation of Li_2S to LiPSs

Oxidation of Li_2S to LiPSs and then to S_8 is a significant reaction since it is responsible for reducing the energy barrier and it contributes to high sulfur utilization and CE.

The catalysts that have been studied for LSBs are categorized into two:

- ✓ Conventional catalysts- They have been used to immobilize and catalyze LIPSs under ideal conditions. They include metal oxides, sulfides, and phosphates [133].

- ✓ Emerging catalysts- They are used under lean electrolyte and high S_8 loading conditions. They include catalysts with defects, heterostructures catalysts, and single-atom catalysts.

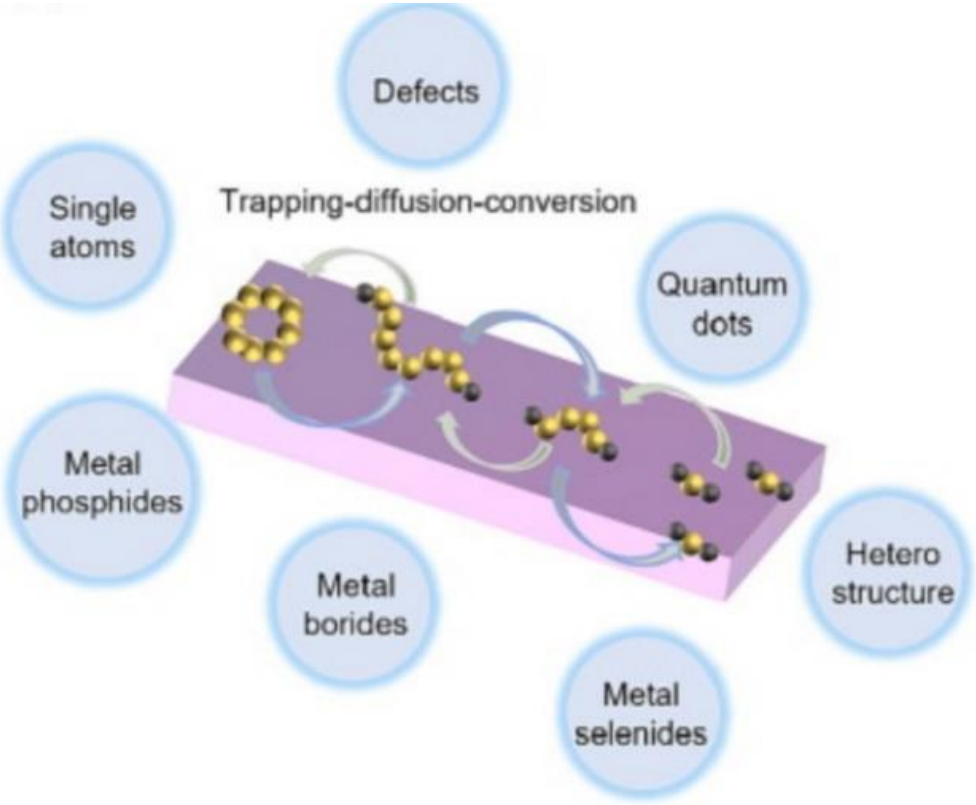

Figure 2.7: Illustrations of emerging catalysts [133]

Reduction of Li_2S_4 to Li_2S_2/Li_2S is a rate-limiting step, there is a high increase in the concentration of LIPSs and this leads to a rise in the shuttle effect. The catalysts are very crucial because they serve as electrolyte additives, separator modifiers and even serve as cathode matrixes.

2.1.8.1.1. Requirements for a catalyst

- ✓ Abundant catalytic active sites

These abundant catalytic active sites function to immobilize the soluble LIPSs and provide the nucleation sites for the deposition of Li_2S_2 and Li_2S. The bulk catalysts can be downsized into nanodots or single atoms which enlarges the exposed surface areas for abundant catalytic sites. The activity of these active sites can be increased by improving

their density and boosting the activity whereby atomic engineering is one of the methods of improving the active site density while defect engineering has been proposed to improve the active site activity since it adjusts the local electronic structures [134].

- ✓ Excellent electronic and ionic conductivities.
- ✓ Strong lithium polysulfide adsorption ability.
- ✓ Multifunctional capabilities.

The solid-liquid-solid phase in LSBs makes it difficult for a single catalyst to regulate this redox reaction simultaneously hence the need for a multifunctional catalyst. The major functions of the catalyst are to stabilize the lithium anode, bidirectional catalysis during the charging and discharging process, and smooth immobilization and conversion of LiPSs which helps reduce the shuttle effect. Catalysis of Li_2S to LiPSs intermediates and eventually to sulfur has the advantage of increasing the rate of utilization of sulfur and CE. The stabilization of the lithium is very necessary for the durability of LSBs and it is done using modified separators [133].

- ✓ Synergy of functional components

The combination of two or more catalysts improves the overall catalytic performance. For instance, the combination of both metal oxide catalysts and metal nitride leads to adverse merits because metal oxides have high polarities to absorb the LIPSs while metal nitrides have great conductivities.

In many cases, the catalysts do not function by themselves. They are usually embedded in carbon whose function is to uniformly disperse the catalyst particles with rapid electron transfer pathways [135].

2.1.8.1.2. Screening and identification of electrocatalysts

The purpose of the electrocatalysts is to decrease Li_2S_2 or Li_2S deposition on the sulfur surface. They perform this function by not only enhancing the transport of charge but also accelerating the migration of ions. They also act as intermediates of the redox reaction that occurs in LSBs and electron transportation pathways to reduce the charge transfer resistance.

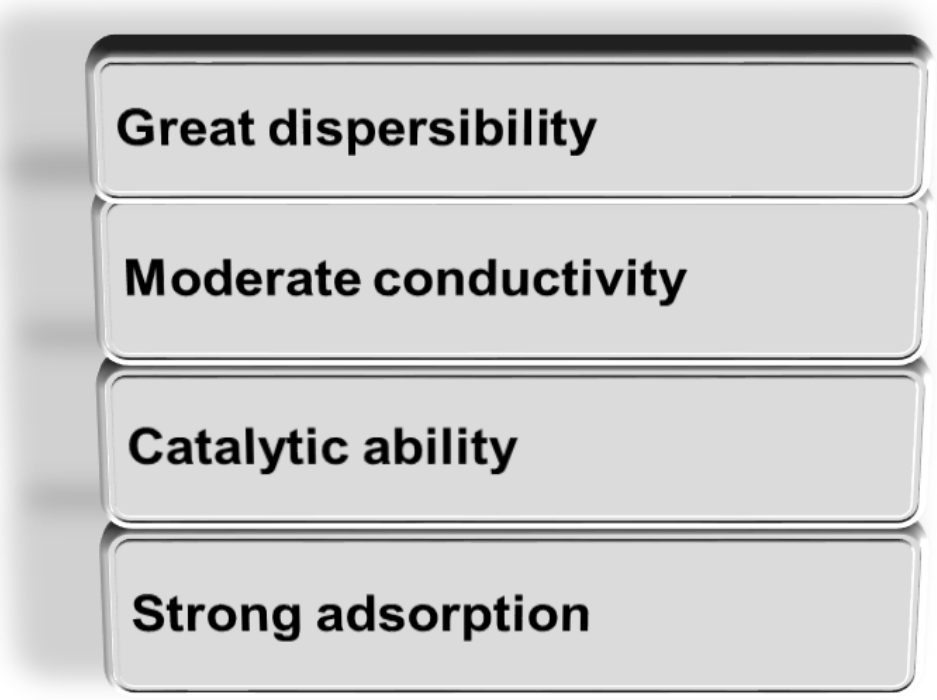

Figure 2.8: Characteristics of electrocatalysts

2.1.8.1.3. The types of catalysts used in LSBs

2.1.8.1.3.1. Single-atom catalysts

They function roles on the sulfur cathode which include promoting the reaction kinetics anchoring the LiPSs, and regulating the rate-limiting steps by lowering the phase transition energy barriers. Uniformly distributed single-atom catalysts are obtained by coordinating them with non-metal groups on carbon substrates. They portray a disadvantage whereby it is difficult to synthesize a high-loading single-atom catalyst using a high-yielding and low-cost procedure [136].

2.1.8.1.3.2. Defective side catalysts

Defect engineering is very useful in electronic conductivity and ionic diffusion of catalysts because it narrows the band gaps, it allows the introduction of polarity and catalytic activity to nonpolar materials. The classification of defective catalysts is: synergy, heteroatom doping, and vacancy engineering (anion and cation vacancies) [137].

2.1.8.1.3.3. Quantum dot

The quantum dots that have been synthesized by other scholars include carbon quantum dots[138], carbon nitride quantum dots [139], water-soluble quantum dots [140], and functional nanodots [141].

2.1.8.1.3.4. Heterogeneous catalysts

There is a need for heterogeneous catalysts to achieve strong adsorption of the LiPSs and high electronic conductivity. The main advantage of a heteroatom structure is that it combines the merits of different materials and also introduces interfaces with high catalytic activity [142].

2.1.8.1.3.5. Other catalysts

These include metal borides that have an empty 2p orbital and a unique electronic structure which is attributed to the strong trapping ability of the lithium polysulfides while their metallic character brings about high electrical conductivity. Mesoporous carbon and carbon nanotubes have also been used as hosts to encapsulate the sulfur through a physisorption technique. They however face a disadvantage whereby they partially confine the polysulfides by physisorption and the volume expansion that occurs during the discharge process.

2.1.8.2. Introduction of a kinetic promoter

The kinetic promoters that have been used include oxides, sulfides[143], nitrides, and polymers [144]. These promoters have various advantages from the rate performances to the lifespan of LSBs.

2.1.8.3. Development of electrolyte

The electrolyte is so important since each electrolyte formula defines a particular lithium-sulfur reaction pathway. Most scholars have been using ether-based electrolytes that support the dissolution-precipitation pathways [145]. Many attempts addressing the electrolyte include:

- ✓ High ionic conductivity with LiPSs.
- ✓ Sparingly LiPSs dissolution – which refers to a low LiPSs concentration.

2.1.8.4. Lithium protection

Lithium metal has a -3.04 V reducing potential versus the SHE which brings a huge contribution to the energy density and working voltage of the LSBs. This low potential is responsible for the lithium-reducing properties and its ability to react with electrolyte's components. Lithium metal and electrolyte reaction generates reduction products which are deposited on the surface to form the SEI which is inhomogeneous in its structure and composition which leads to inhomogeneous lithium plating/stripping [146]. This non-even SEI also leads to the growth of lithium dendrites which promotes parasitic reactions. During the lithium plating/stripping process, the dendritic lithium undergoes oxidation but in the process 'dead lithium' which is a partially electrically insulating layer that does not undergo oxidation is formed. This 'dead lithium has the demerit of hindering electrolyte diffusion and lithium ion transportation which is among the things that contribute to the failure of the LSBs.

The LiPSs intermediates worsen the scenario because once they diffuse to the anode side, they react rapidly with the lithium anode causing the formation of insoluble lithium sulfide in the SEI which leads to formation of lithium dendrites [147]. The SEI layer has a limitation whereby it is not strong and stable to withstand the plating/stripping process during the operation of the cell which causes poor battery cyclability, and even low CE. The lithium metal anode protection is usually done by modifying the SEI formed by making sure it is stable. The strategies that have been proposed are:

2.1.8.4.1. High concentration of salts in the electrolyte

Increase in the salt concentration leads to the vanishing of the free solvent molecules and this leads to an electrolyte with a 3D structure. The disappearance of the free solvent molecules is important because it avoids the reaction with the lithium metal anode which in general increases the long term stability of the battery. Furthermore, this lack of free solvent molecules leads to a reduction in the polysulfide shuttle effect which avoids the lithium metal anode poisoning. Also, the SEI that is formed by the salt reduction products (which is mostly rich in inorganic compounds) leads to an SEI which has a superior quality. Likewise, the solvent activity reduction result into a change in the sulfur conversion pathway, whereby in the other electrolytes the conversion follows a

dissolution-precipitation pathway. In this case, the pathway is simply a quasi-solid pathway which is quite significant since it reduces the volume of the electrolyte for good functioning of the LSB.

This process however portrays some limitations in terms of cost, viscosity, and density. In terms of viscosity, it is 10 times more than in the conventional electrolytes. This leads to longer times of wetting in order to impregnate the separator and the electrodes. Also, the high density compromises the energy density of these batteries and the higher salt concentration usage increases the cost of the battery.

This method has not been fully successful and scholars have been focusing on dilution of the high concentration of salts which has an advantage of solving the electrolyte depletion that is a major cause of failure of these lithium-sulfur batteries.

2.1.8.4.2. Use of additives

The additives have been fully modified for LSBs because they are very useful in stable SEI formation which is useful in avoiding the reactivity of the lithium anode and reducing the LIPS shuttle effect. $LiNO_3$ additive has commonly been used in LSBs because of its major merit which is its ability to form a strong nitrogen-based SEI. It however faces a limitation whereby it is not capable of reducing the loss of sulfur during the SEI formation and there are some concerns of safety due to the oxidation of the nitrate ion.

LiF has also been used as an additive that has been used which is the main component in the salt (LiTFSI). There is a less stable sulfur-fluorine bond, and the FSI^- is favorable to be reduced on the lithium metal anode which leads to enhancement of the mechanical strength in the SEI. Furthermore, halogenated anions metal cations promote an improvement to the SEI because they are able to form an electrostatic shield, they avoid the dendrites formation and they form a stable structure that remains even during long term cycling. This electrostatic shield is formed due to adsorption of cations on the surface of lithium and this generates an electrostatic repulsion that causes lithium to be deposited in the valleys. This leads to a uniform morphology that is free of dendrites.

2.1.9. Cathode materials that have been employed in LSBs

2.1.9.1. Transition metal oxides

They have catalytic behaviors similar to those of noble metals, however they have ionic bonds that equip them with strong polarities which enable them to effectively capture the LiPSs. They are also affordable compared to noble metals and hence they have been used in broad applications. Polar metal oxides have been widely investigated since their intrinsic conductivity impacts the redox kinetics of lithium-sulfur batteries.

They however face a disadvantage whereby they have poor electrical conductivity. This is a great concern for their application in LSBs since it increases the resistance of the battery and lowers the rate capability. Some strategies have been developed to lead to an increase in the electrical conductivity. These include creation of inherent defects or vacancies on the transition metal oxide hosts and also hybridization of the TMO with conductive porous carbon. These hybrid composites are advantageous since they inhibit the polysulfides by physisorption and chemisorption.

2.1.9.2. Transition metal chalcogenides

By definition they are materials comprised of transition metals and chalcogenides elements such as sulfur, selenium, and tellurium. The transition metal sulfides possess a unique surface composition whereby the metal-sulfur bonds are weak which makes them very competitive in the electrocatalysis of the lithium-sulfur battery. There also exists interaction of sulfur-sulfur bond with the lithium polysulfides which gives them their high electrochemical activity. The transition metal selenides possess high defect densities, are polar and possess higher electrical conductivity.

2.1.9.3. Transition metal nitrides and metal carbides

They possess better electrical conductivity, which is used to convert the long-chain LiPSs. LiPSs have strong affinity for the transition metal nitride which helps to alleviate the deposition of the lithium sulfides on the sulfur cathode. They assist in the reactivation process back into the lithium polysulfides. The metal carbides have been studied for LSBs because of their metallic conductivities which are useful in rapid reactions. They however

have a lower binding energy with the lithium polysulfides since their anion occupy interstitial sites in their metal lattices.

2.1.9.4. Metal borides and phosphides

Transition metal oxides such as metal borides, metal phosphides possess good qualities such as good chemical adsorption, strong polarity, and high electrocatalytic properties which qualifies them as electrocatalysts for LSBs [148]. These metal borides and phosphides have numerous compositions and crystal structures, strong electronegativity, easy to assess electronic states and good electric conductivity which is attributed to their metal-metalloid bonds (metal-phosphide, metal boride) and covalent bonds made up of metalloid-metalloid bonds (phosphide-phosphide, boride-boride) [149]. The good conductivity is beneficial because it provides a faster transport path of electrons while their strong polarities helps them to anchor the lithium polysulfides hence reducing the shuttle effect which is useful in the improvement of the cycling performance.

Some of these metal borides and phosphides have a very unique feature whereby they possess noble-like catalytic properties. This is quite advantageous because they can find applications in oxygen reduction reactions and even photocatalytic water splitting reactions. The high catalytic activities are useful in the conversion reactions of elemental sulfur to lithium polysulfides intermediates and eventually to solid lithium sulfide products in the electrochemical reactions.

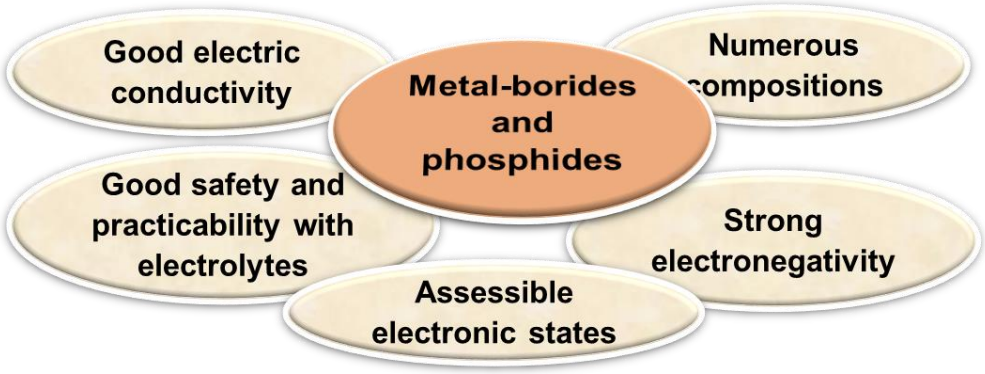

Figure 2.9: Properties of Metal-borides and phosphides

Boron has unique properties whereby its electronic structure is unique, has an empty orbital and is highly electronegative hence when mixed with metal cations, it forms rich metal borides [150]. The metal borides effectively anchor the LiPSs intermediates due to the synergistic metal-sulfur and boron-sulfur bonds. In-order to achieve these merits, the metal borides and phosphides have been prepared in the nano-size dimensions with the intention of providing additional active sites for electrochemical reactions.

2.1.9.5. MXenes (transition metal carbides, carbonitrides, nitrides)

The MXenes have significant properties which include: high electrical conductivity, they are rich in defects and vacancies, their specific surface area is large and they portray good mechanical strength [151]. Upon the use in LSBs, they solve quite a number of challenges. For instance, their metallic conductivity is useful in providing rapid electron transfer to fully maximize the utilization of sulfur. Their large specific surface area equips them with a surface for the electrochemical reactions and also aids in the construction of 3D composite materials for the lithium anode and sulfur cathode. They also have a highly hydrophilic property that is caused by their abundant surface terminations which induce nucleation and suppression of the growth of lithium dendrites [152]. In addition, the presence of metal centers and polar functional groups allow them to bond with the lithium polysulfides which equally makes them suitable adhesives for lithium polysulfide chemisorption.

They also experience some disadvantages whereby they have a tendency to stack and this limits the transportation of electrons and ions along the vertical direction, which sacrifices the lithium-sulfur batteries performance. Furthermore, it is complicated for a MXenes to balance the functions required in lithium-sulfur batteries which include the physical capture, chemisorption properties, and the catalytic conversion of the lithium polysulfides. This clearly indicates that the MXenes can only improve the performance of the lithium-sulfur battery to only a limited extent.

Efforts have been made to alleviate these challenges. This include the usage of heterostructures which by definition are different types of semiconductors with the same crystal structures, atom spacing and thermal expansion coefficient. The heterostructures

in the MXenes combine the merits of different components with an aim of making up for the shortcomings of MXenes [153]. This leads to a provision of more active sites and it promotes the charge transfer. In addition, they have introduced an internal electric field at the heterogeneous structure interface that is responsible of accelerating the ion diffusion kinetics.

MXenes also portray merits when used as a lithium host. Its high conductivity and fast ionic diffusion coefficient property enables it to achieve fast electrochemical reactions during charge and discharge. Its feasible structure designs with other materials into 3D porous hybrid materials are very useful in alleviating the volume expansion in the lithium anode. Furthermore, the functional groups on the MXenes surface have a certain degree of lithiophilicity which induces a uniform distribution of the lithium-ion flux and is useful in achieving a high lithium loading.

2.1.9.6. High-Entropy Materials (HEMs)

Alloying involves the addition of small portions of secondary elements to primary elements. Alloys are grouped into 3 major categories depending on their mixing entropies. The first category is the low-entropy alloys which are generally composed of few (1 or 2) principal elements. The second category is the medium-entropy alloys that are composed of 2 to 4 principal elements while the last category is the high-entropy alloys, which typically involves the combination of 5 or more dominant principal elements with a concentration between 5% and 35% [154]. They are entropy stabilized single phase crystalline solutions which present very distinct electrochemical properties.

The four core effects of HEMs are lattice distortion, cocktail effect, sluggish diffusion, and high-entropy which correspond to the materials structure, performance, kinetics and thermodynamics [155]. The high-entropy effect is responsible for lowering the free energy of solid solution phases hence facilitating their formation especially under high temperatures. The sluggish diffusion in HEAs occurs because of the difference between the neighboring atoms of each lattice and also the local atomic configuration which leads to different bonding and local energies [156]. The slow diffusion process allows good stability and high temperature strength that exists in HEAs. Lattice distortion is mostly

brought about by the differences in size of the different atoms in the lattice and is mostly important in strengthening of the solid solution. The cocktail effect simply brings about synergy which leads to interesting properties since each element has its own individual characteristics and benefits.

HEA confine the sulfur molecules in the LSBs by chemical interaction/chemisorption. This leads to strong confinement of the sulfur species which brings about high rate of utilization of sulfur and cycle stability.

High-entropy alloys can be traced back to 2004, by two independent studies. One study by Brian Cantor [166] and the other by Yeh. Cantor *et al.* [157] where they investigated 5% each of 20 elements (Mn, Cr, Fe, Co, Ni, Cu, Ag, W, Mo, Nb, Al, Cd, Sn, Pb, Bi, Zn, Ge, Si, Sb, Mg). Yeh *et al.* [158] focused on an alloy design with multiple principal elements in equimolar or near equimolar ratios. According to their studies, solid solutions are more stable because of their large configurational entropy while the intermetallic structures resulted in brittleness and difficulty in processing. They calculated the configurational entropy change per mole during the formation of a solid solution from n(number) of elements using the equation:

$$\Delta S_{conf} = - k \ln W = - R \left(\frac{1}{n} \ln \frac{1}{n} + \frac{1}{n} \ln \frac{1}{n} + \ldots \frac{1}{n} \ln \frac{1}{n}\right) = - R \ln \frac{1}{n} = R \ln n \quad \ldots\ldots\ldots\ldots\ldots\ldots 2.9$$

whereby k is the Boltzmann's constant, W is the number of ways of mixing and R is the gas constant.

This concept of HEAs has been further expanded to high-entropy ceramics which are further divided to high-entropy (carbides, borides, oxides, silicides, sulfides).

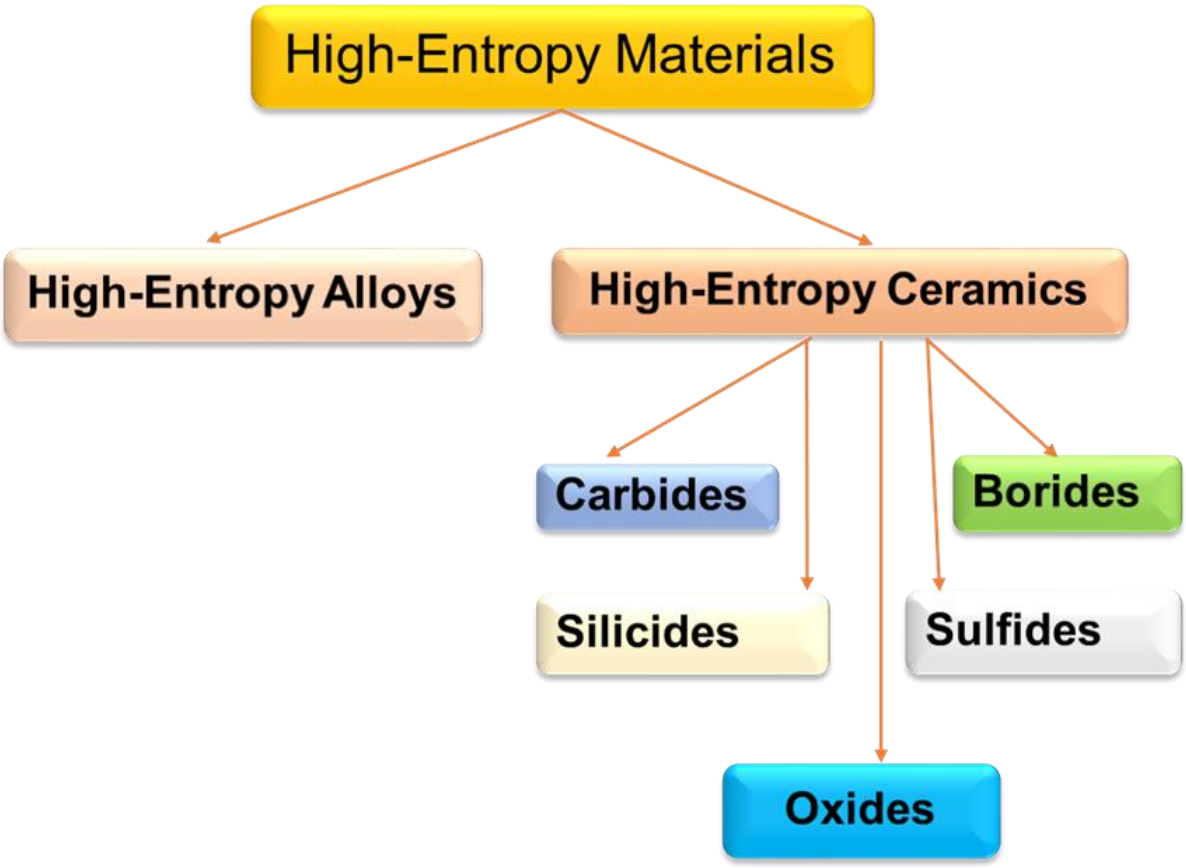

Figure 2.10: Classification of high-entropy materials

The combination of different metals allows the formation of different crystalline structures such as rock salt, spinel, and fluorite phases. The high-entropy materials have a unique characteristic whereby they reduce the free energy to make the system phase stable. They do this by increasing the configurational entropy S_{config} whereby according to Yeh *et al.* [159] S_{config}=1.50 R helps to resist the strong bonding forces of the atoms at high temperature hence it is a necessary condition.

High-entropy ceramics are solid solutions of inorganic compounds with one or many Wyckoff sites shared by equal or near-equal atomic ratios of multi-principle elements [160]. They portray outstanding qualities such as superionic conductivity, colossal dielectric constant, super hardness, and strength, and enhanced electromagnetic wave absorption ability. They have found many applications in the field of thermal protection

and insulation, rechargeable batteries, hard and wear resistance coatings, and electromagnetic wave absorption.

2.1.9.6.1. Preparation methods for HEMs

Table 2.1: Preparation methods of HEMs

Formula	Preparation method	Application	Ref/Year
$FeCoNiMgCr(OH)(OH_3)$	Solvothermal synthesis	Oxygen evolution reaction	[161] 2023
Pt-Ir-Pd-Ru-Rh	Low-temperature Solvothermal synthesis	Determination of performance of the High-entropy alloy nanocatalysts	[162] 2019
$(Mg_{0.2}Co_{0.2}Ni_{0.2}Cu_{0.2}Zn_{0.2})O$	Hydrothermal synthesis	Lithium-ion battery	[163] 2022
PtPdRuRhCe	Carbothermal	Ammonia oxidation	[164] 2018
$(Y_{0.2}Yb_{0.2}Sm_{0.2}Eu_{0.2}Er_{0.2})_2O_3$	Electrospinning method	Synthesis of high-entropy ceramics	[165] 2022
$(La_{0.2}Nd_{0.2}Sm_{0.2}Dy_{0.2}Yb_{0.2})_2Zr_2O_7$	Electrospinning method	Thermal insulation materials	[166] 2022

(CoFeNiMnMoPi)	Spray pyrolysis	Oxygen evolution reactions	[167] 2021
(MgCoNiCuZn)O	Green microwave assisted	Lithium-ion batteries	[168] 2021
(PtPdFeCoNi) in rGO	Microwave heating process	Scalable synthesis of high entropy alloy nanoparticles	[169] 2021
CoMnNiFeCr	Combinational Co-sputtering	Oxygen reduction catalyst	[170] 2018
$(FeCoNiCrMnXLi)_3O_4$ where X= Copper, Magnesium, Zinc	Ball milling	Lithium-ion batteries	[171] 2021
$(Co_{0.2}Mn_{0.2}Fe_{0.2}Zn_{0.2}Ti_{0.2})_3O_4$	Ball milling Conventional solid-state reaction	Provide ideas for application of high entropy ceramics in energy, electrolysis, and catalysis	[172] 2022
$MnCoNiCuZnO_5$	Ball milling	Negative temp.	[173]

	coefficient thermistors	2022

2.1.9.6.1.1. Wet chemistry synthesis

It is made up of hydrothermal and solvothermal methods whose major differences are that for hydrothermal, there is the usage of water to dissolve the reactants while for solvothermal the reactants are dissolved in an organic solvent. Temperature, pH, and concentration of reactant influence both the particle size and morphology of the product formed. The major merits of this method are that it is cost-effective, the nanoparticles formed are of high purity and quality, and it occurs under low temperatures. However, this method has a disadvantage whereby it leads to phase separation of the elements because most metallic elements are not miscible at thermodynamic equilibrium conditions [174].

Qi Jiang *et al.* [161] synthesized FeCoNiMgCr(OH)(OCH_3) by solvothermal method for applications in the oxygen evolution reactions.

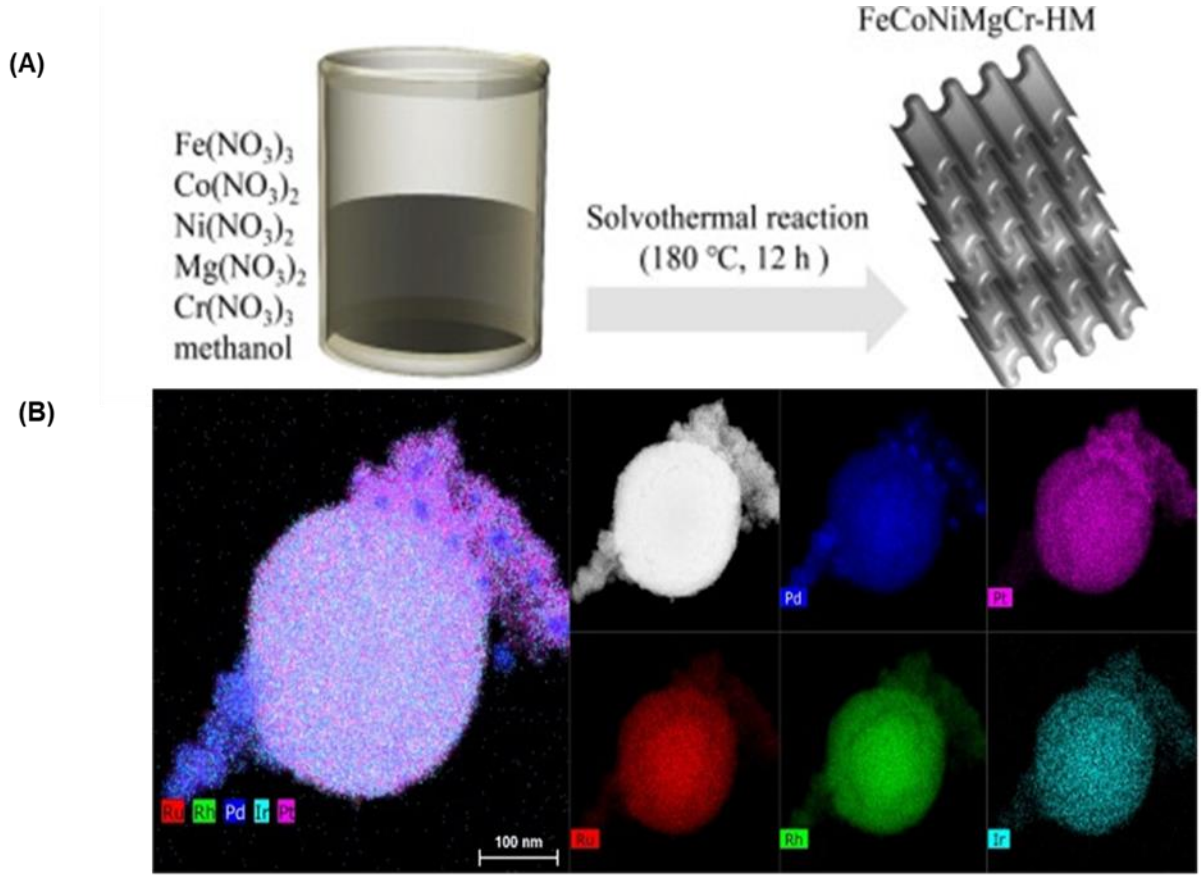

Figure 2.11 :**(A)** Solvothermal method [175], **(B)** STEM-EDS for $Pt_{0.2}Ir_{0.2}Pd_{0.2}Ru_{0.2}Rh_{0.2}$ [176]

After electrochemical activation, the synthesized FeCoNiMgCr-HM exhibited outstanding performance which is attributed to the five cation's synergistic effects and complete surface reconstruction which is brought about by the methoxyl group. The methoxyl group does this due to its high ability to attract electrons and because it is a strong Bronsted base.

Broge *et al.* [162, 176] also synthesized Pt-Ir-Pd-Ru-Rh nanoparticles using the solvothermal method. They then investigated the formation mechanism by employing in-situ XRD analysis, and STEM-EDS.

Guo *et al.* [163] prepared $(Mg_{0.2}Co_{0.2}Ni_{0.2}Cu_{0.2}Zn_{0.2})O$ from (NiO, MgO, CuO, CoO, ZnO) for applications in the LIBs.

2.1.9.6.1.2. Carbothermal shock method

The merits of this method are that the high-entropy nanoparticles synthesized have a narrow particle size distribution and uniform dispersion. It makes use of high temperature (>2000K) for the production [177] which causes quick thermal decomposition of the metal salts precursors. The high temperature is then followed by rapid cooling to ambient temperatures. They use high temperature in order to drive the rapid “fusion” and “fission” whereas the cooling rates facilitate kinetic control over thermodynamic mixing regimes. The merit of this method is that the structural and chemical stability is higher compared with the conventional methods of synthesis.

Yuan Wu *et al.* [164] synthesized (PtPdRuRhCe) nanoparticles by carbothermal shock method as catalysts for ammonia oxidation. This novel nanoscale HEA showed outstanding catalytic performance whereby they portrayed great catalytic stability brought about by the high-entropy of the nanoparticles.

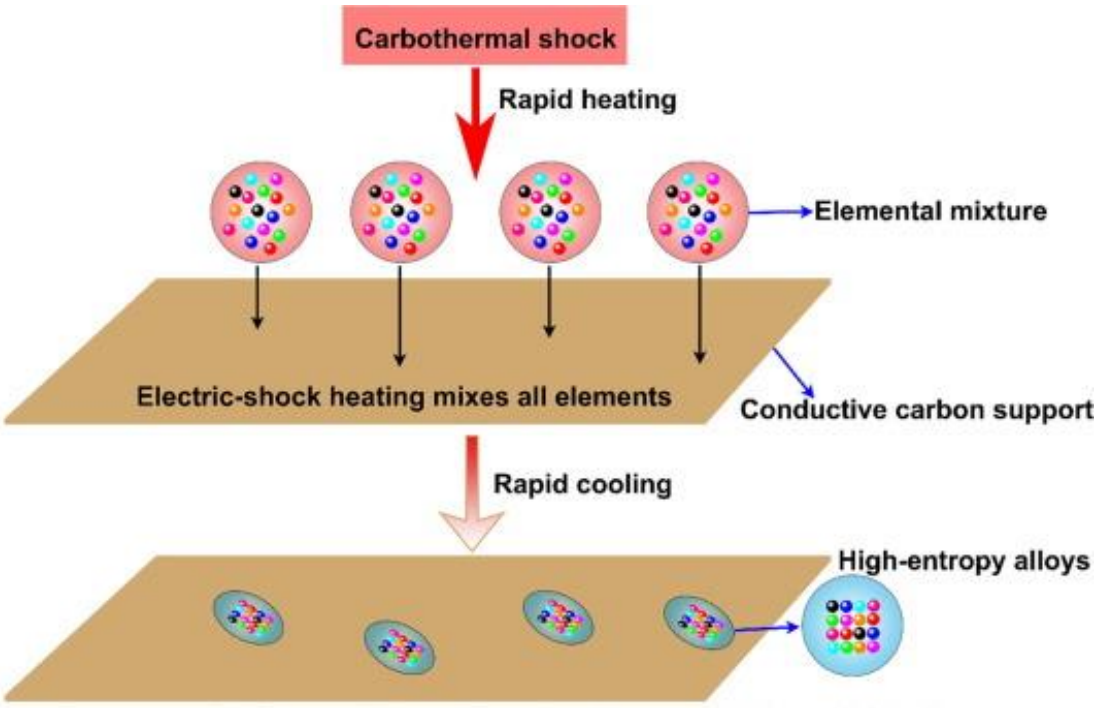

Figure 2.12: Carbothermal shock method synthesis for nanoscale HEA [178].

2.1.9.6.1.3. Electrospinning technology

It is used to prepare nanofibers with a controlled morphology and composition. It is an electrostatically driven process whose function is in the fabrication of continuous nanofibers whose diameters range from 10nm to several micrometers. The procedure involves adding a precursor solution that contains 5 metal salts to the needle of the electrospinning machine. The merits of this method are there is a homogenous distribution of elements and the synthesis temperature used is lower. Yan Xing *et al.* [165] synthesized $(Y_{0.2}Yb_{0.2}Sm_{0.2}Eu_{0.2}Er_{0.2})_2O_3$ using this method. According to this method of synthesis, the synthesis temperature used was 1000°C lower than that applied in solid-state synthesis.

Zeshuai Li *et al.* [166] also fabricated $(La_{0.2}Nd_{0.2}Sm_{0.2}Dy_{0.2}Yb_{0.2})_2Zr_2O_7$ using this method. They prepared the rare-earth zirconates materials due to their amazing properties that include good thermal stability and thermal shock resistance. They used FTIR to illustrate the formation of nanofibers and TEM, SEM, and XRD to confirm the uniform composition of the nanofibers.

2.1.9.6.1.4. Spray pyrolysis

This method has a demerit whereby it requires the usage of high temperature and vacuum conditions, and the equipment and cost of operation it needs is very high. However, the production of powders with small particle sizes and good dispersion is very easy which serves as an advantage. Qiao *et al.* [167] synthesized (CoFeNiMnMoPi) for oxygen evolution reaction in the form of highly uniform spherical particles. They controlled the particle size by tuning the parameters in the synthesis such as precursor concentration, flow rate, and the temperature of synthesis.

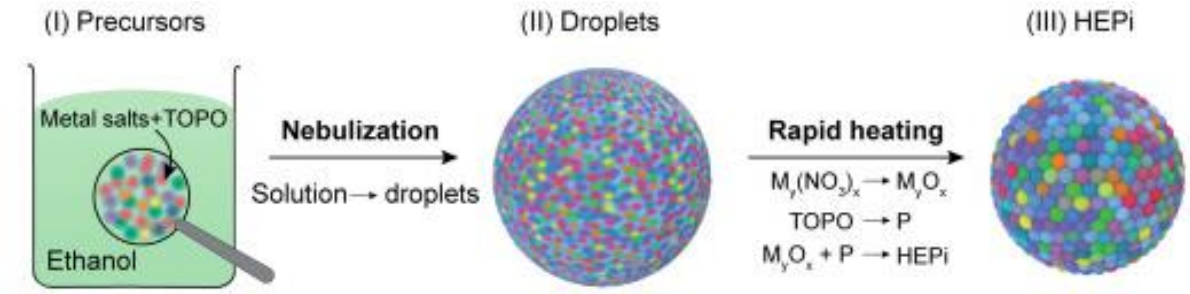

Figure 2.13: Synthesis using Spray Pyrolysis [167]

2.1.9.6.1.5. Microwave-assisted synthesis

It has several merits that include fast cooling and heating rates, applicability to carbon materials of various sizes, and high achievable temperatures [179]. This allows this method to have great potential in the production application of nanomaterials.

Kheradmandfard *et al.* [168] synthesized (MgCoNiCuZn)O via ultrafast green microwave-assisted synthesis for lithium-ion battery application.

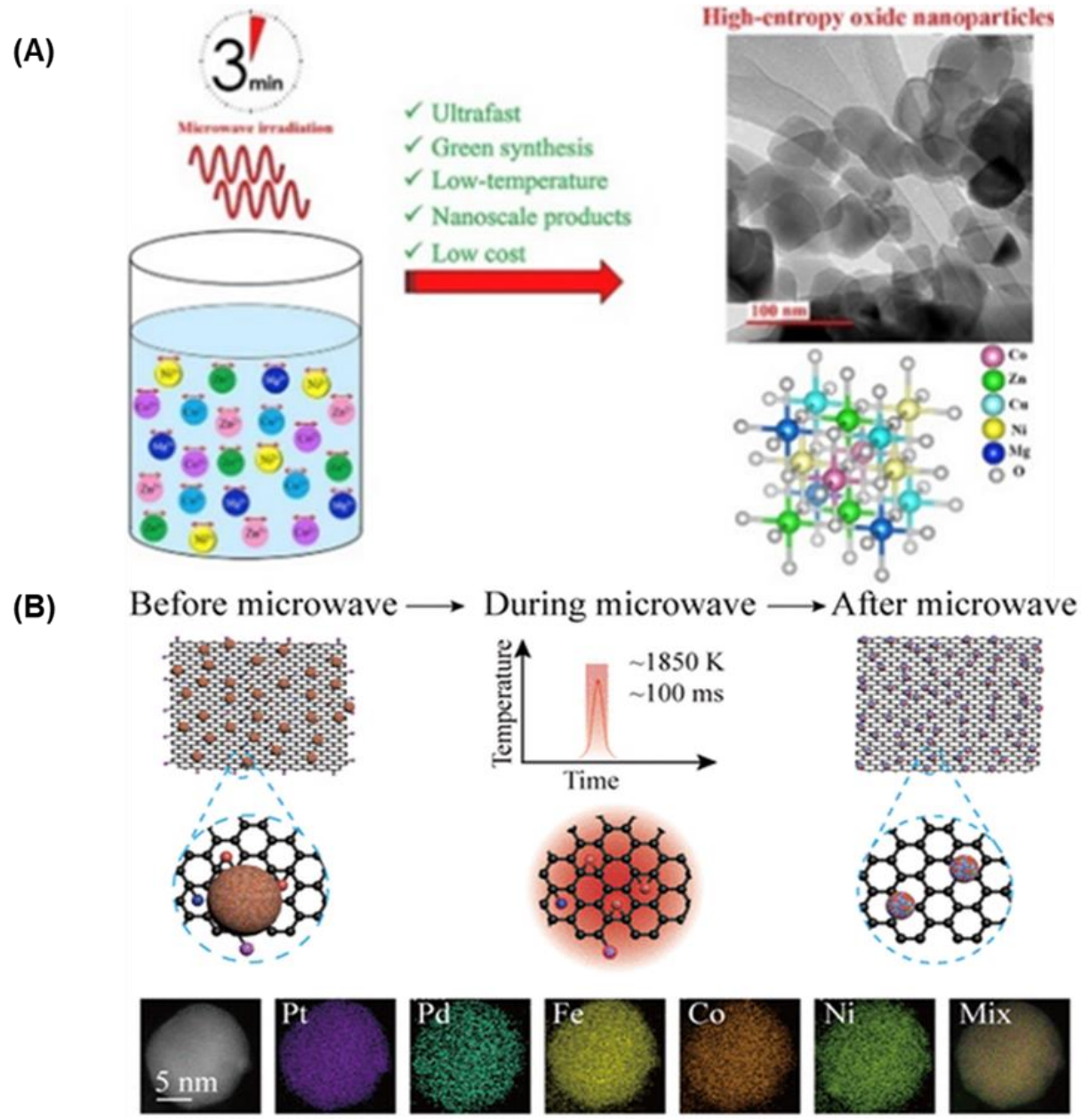

Figure 2.14: (A) Microwave assisted synthesis[168], **(B)** Formation of nanoparticles on (rGO) by microwave heating [174].

Qiao *et al.* [169] synthesized (PtPdFeCoNi) nanoparticles on reduced graphene oxide film (rGO) using this method. The method was successful whereby they obtained (PtPdFeCoNi) with a uniform size distribution without any elemental and phase separation

2.1.9.6.1.6. Sputtering deposition

The different forms of sputtering include direct current sputtering, co-sputtering, and radio frequency magnetron sputtering [177]. It operates under the principle of changing the metallic surface state of target using interaction of different ions in the gas under the action of magnetic and electric fields.

Tobias *et al.* [170] synthesized the cantor alloy (Co-Mn-Ni-Fe-Cr) by combinational co-sputtering. The major merit of this method is that it leads to exact tailoring of the composition of elements.

2.1.9.6.1.7. Ball milling method

Using this method, metal powders are deformed, cold welded, and broken in a ball mill which is useful for elements to achieve atomic-level alloying. The mechanism involves violently rotating or vibrating a sample which is placed in a bowl. The collision that occurs leads to a solid-state reaction. Duan *et al.* [171] synthesized $(FeCoNiCrMnXLi)_3O_4$ where X= represents copper, magnesium, and zinc for LIBs using this technique. Wang *et al.* [172] synthesized $(Co_{0.2}Mn_{0.2}Fe_{0.2}Zn_{0.2}Ti_{0.2})_3O_4$ by the conventional solid-state process while Fan *et al.* [173] synthesized a novel $MnCoNiCuZnO_5$ complex phase ceramic by traditional solid-state reaction technology for application in thermistors.

Other than entropy different parameters affect the electrochemical performance of high-entropy materials. These include:

Element content: HEMS that have been studied and reported, are made up of elements in equimolar configurations which makes them have a high configurational entropy which has an advantage of maintaining better phase-stable structures but has a demerit whereby this configuration limits the redox reactions during cycling. Hence adjusting the elemental content is crucial in achieving both a crystal structure that is stable and has a high cationic redox capacity [180].

Synthesis process: Different properties are exhibited by the HEMs when there are different reaction conditions such time and temperature, even though the synthesis process is the same. The different reaction conditions lead to different particle sizes and

crystallinities of the high-entropy oxide (HEO) which strongly affect electrochemical performance [180].

The composition of elements: The different compositions of HEMs bring about different crystal structures. The roles of different elements have also been investigated whereby cobalt provides high electrical conductivity with good chemical compatibility [181], magnesium assists in the stabilization of the phases, while copper assists with charge compensation at electrodes.

Stabilization of the crystal structure (addition of active sites): HEMs normally increase the material's electrochemical properties by increasing the number of reactive sites and defects such as lattice disorder and oxygen vacancies. Oxygen vacancies function in regulating the electronic structure which includes energy band structure, electron cloud density, density of states, and modulating the coordination environment for the activation of active centers and intermediates' stabilization [180].

2.1.9.7. High-Entropy Oxides (HEO)

Rost *et al* [182] synthesized the first HEO in 2015. The crystal structures for HEOs include rock-salt, spinel, fluorite, and perovskite structures [183]. The formula for a spinel structure is AB_2O_4 where A and B are divalent and trivalent cations respectively. A cations occupy the tetrahedral of the crystal while B cations occupy the octahedral of the crystal. This situation is not always applicable as there may be the occurrence of reverse as seen in $(CrMnFeNiCu)_3O_4$ where Ni^{2+} ions occupy the octahedral sites instead of the tetrahedral crystal sites. The reaction temperature is quite significant since improper temperature induces the phase conversion from spinel to rock salt.

The perovskite structure has a general formula of $(RE)(TM)O_3$ where TM and RE represent transition and rare earth metals respectively. The RE's main function is to stabilize the perovskite structure while the transition metal determines the main properties. In the fluorite structure, the cations occupy the corner tops and face centers of the cubic cells location while the anions occupy the center of the cubes location [180].

HEOs are important in achieving high electrochemical performance, especially under high sulfur loading and low E/S ratio conditions. The catalytic properties of HEOs are based

on different factors. First and foremost, the metal cations. These play a major role because of the synergy brought about by the different metal cations. Secondly, the polar surfaces that are used to bond with the sulfur species lead to an increase in the electrochemical kinetics [184]. As proved by theoretical calculations, the polar transition metal oxides interact with the LiPSs via a metal-sulfur bond due to the interaction of the M atoms in the HEO and the sulfur atoms in the lithium sulfide.

The synthetic routes for the synthesis of HEOs include high-temperature methods such as flame and nebulized spray pyrolysis, reverse co-precipitation, and solid phase sintering. These methods have major limitations whereby they require high annealing temperatures, they require long preparation time, they require high energy consumption, and expensive equipment for the reactions. There is a great need for new studies regarding synthesis procedures that entail low annealing temperature techniques. The different methods of synthesis do not change the high-entropy oxides' crystal structure and this shows the excellent phase stability of these oxides in the synthesis process.

High-entropy oxides are mainly produced as nanoparticles and nanoporous structures for catalysis. The traditional methods that require high temperature for crystallization limit the size of the powder particles hence preventing them from forming nanoparticles. The formation of nanoparticles is important to optimize the active sites and SA.

Harsh synthesis conditions and materials susceptibility to phase separation are two main challenges observed during the synthesis of HEMs. Also, the phase transition competition of different structures at high temperature is a major challenge in single-phase solid solution formation [180].

The preparation methods of HEOs depend on whether the material formed is bulk, nanostructures or thin films. The preparation methods for HEOs include:

Sol-gel method/solution combustion method – This method is advantageous because it is easy to handle. It involves dissolving metal nitrates in deionized water with metal chelators. The synthesis of the sol is by addition of an organic matter to the solution of metal nitrate. The organic matter play a role as fuels for reactions and reducing agents while the metal nitrates function as oxidizing agents [180]. Stirring of these nitrates occurs

before they are subjected to heat evaporation to form a viscous gel, which is then subjected to calcination at high temperatures before presintering. Grinding, prilling, sifting, and dry pressing are then performed [185].

Other methods involve mechanically mixing metal oxides with ball milling to obtain a homogenous powder. Solid-state reaction is also very common in synthesizing HEOs. The other methods include coprecipitation, solvothermal methods, hydrothermal, spray pyrolysis, and chemical reduction whereby coprecipitation is usually used for large-scale production. The challenges that have been experienced in the solid phase reaction method include a wide range of oxidation potentials of metallic elements at high temperatures which leads to the formation of impurities and phase separation.

All discussed synthesis methods employ high temperatures in the formation of HEMs. This research focuses on the Pechini synthesis method to synthesis HEO $(CrMnFeNiCu)_3O_4$. This method stands out among several chemical synthesis methods due to the use of different temperatures and proportions of metallic cations and citric acid, which enables controlled agglomerate morphology and stoichiometry, low toxicity and compositional homogeneity in the production of the oxide.

2.2. References

1. He, P., et al., Building better zinc-ion batteries: A materials perspective. EnergyChem, 2019. **1**(3): p. 100022.
2. Mackereth, M., R. Kou, and S. Anwar, Zinc-Ion Battery Research and Development: A Brief Overview. European Journal of Engineering and Technology Research, 2023. **8**(5): p. 70-73.
3. Horiba, T., Lithium-ion battery systems. Proceedings of the IEEE, 2014. **102**(6): p. 939-950.
4. Jia, X., et al., Active Materials for Aqueous Zinc Ion Batteries: Synthesis, Crystal Structure, Morphology, and Electrochemistry. Chemical Reviews, 2020. **120**(15): p. 7795-7866.
5. Zhang, H., Polyanionic cathode materials for sodium-ion batteries. 2019, Dissertation, Karlsruhe, Karlsruher Institut für Technologie (KIT), 2018.
6. Ren, J., et al., Typical cathode materials for lithium-ion and sodium-ion batteries: From structural design to performance optimization. Carbon Neutralization, 2023. **2**(3): p. 339-377.
7. Liu, S., et al., Nanoporous Red Phosphorus on Reduced Graphene Oxide as Superior Anode for Sodium-Ion Batteries. ACS Nano, 2018. **12**(7): p. 7380-7387.
8. Li, Z., J. Ding, and D. Mitlin, Tin and tin compounds for sodium ion battery anodes: phase transformations and performance. Accounts of chemical research, 2015. **48**(6): p. 1657-1665.
9. Zhai, X.-Z., et al., Layered Birnessite Cathode with a Displacement/Intercalation Mechanism for High-Performance Aqueous Zinc-Ion Batteries. Nano-Micro Letters, 2020. **12**(1): p. 56.
10. Asif, M., S. Kilian, and M. Rashad, Uncovering electrochemistries of rechargeable magnesium-ion batteries at low and high temperatures. Energy Storage Materials, 2021. **42**: p. 129-144.
11. Shterenberg, I., et al., The challenge of developing rechargeable magnesium batteries. Mrs Bulletin, 2014. **39**(5): p. 453-460.

12. Rashad, M., et al., Recent advances in electrolytes and cathode materials for magnesium and hybrid-ion batteries. Energy Storage Materials, 2020. **25**: p. 342-375.
13. Zhang, Y., et al., Challenges and recent progress in the design of advanced electrode materials for rechargeable Mg batteries. Energy Storage Materials, 2019. **20**: p. 118-138.
14. Mageto, T., et al., Development of high-performance zinc-ion batteries: Issues, mitigation strategies, and perspectives. Journal of Energy Storage, 2023. **70**: p. 108081.
15. Zeng, X., et al., Recent progress and perspectives on aqueous Zn-based rechargeable batteries with mild aqueous electrolytes. Energy Storage Materials, 2019. **20**: p. 410-437.
16. Wang, T., et al., Anode Materials for Aqueous Zinc Ion Batteries: Mechanisms, Properties, and Perspectives. ACS Nano, 2020. **14**(12): p. 16321-16347.
17. Wang, C., et al., Rechargeable zinc-air batteries with neutral electrolytes: Recent advances, challenges, and prospects. EnergyChem, 2021. **3**(4): p. 100055.
18. Liu, Y., et al., Rechargeable aqueous Zn-based energy storage devices. Joule, 2021. **5**(11): p. 2845-2903.
19. Zuo, Y., et al., Zinc dendrite growth and inhibition strategies. Materials Today Energy, 2021. **20**: p. 100692.
20. Bayaguud, A., Y. Fu, and C. Zhu, Interfacial parasitic reactions of zinc anodes in zinc ion batteries: Underestimated corrosion and hydrogen evolution reactions and their suppression strategies. Journal of Energy Chemistry, 2022. **64**: p. 246-262.
21. Wang, J., et al., Strategies towards the challenges of zinc metal anode in rechargeable aqueous zinc ion batteries. Energy Storage Materials, 2021. **35**: p. 19-46.
22. Fu, X., et al., The etching strategy of zinc anode to enable high performance zinc-ion batteries. Journal of Energy Chemistry, 2024. **88**: p. 125-143.
23. Jabbari, V., T. Foroozan, and R. Shahbazian-Yassar, Dendritic Zn Deposition in Zinc-Metal Batteries and Mitigation Strategies. Advanced Energy and Sustainability Research, 2021. **2**(4): p. 2000082.

24. Yufit, V., et al., Operando visualization and multi-scale tomography studies of dendrite formation and dissolution in zinc batteries. Joule, 2019. **3**(2): p. 485-502.
25. Wan, F., et al., Energy Storage Chemistry in Aqueous Zinc Metal Batteries. ACS Energy Letters, 2020. **5**(11): p. 3569-3590.
26. Higashi, S., et al., Avoiding short circuits from zinc metal dendrites in anode by backside-plating configuration. Nature communications, 2016. **7**(1): p. 11801.
27. Garcia, G., E. Ventosa, and W. Schuhmann, Complete prevention of dendrite formation in Zn metal anodes by means of pulsed charging protocols. ACS applied materials & interfaces, 2017. **9**(22): p. 18691-18698.
28. Ma, H., et al., Tailoring Pore Structures of 3D Printed Cellular High-Loading Cathodes for Advanced Rechargeable Zinc-Ion Batteries. Small, 2021. **17**(29): p. 2100746.
29. Zeng, L., et al., 3D Printing Architecting Reservoir-Integrated Anode for Dendrite-Free, Safe, and Durable Zn Batteries. Advanced Energy Materials, 2022. **12**(12): p. 2103708.
30. Zhang, M., et al., Boosting uniform charge distribution using 3D rigid electrodes with interconnected gyroid channels to achieve stable and reliable zinc-ion batteries. Journal of Materials Chemistry A, 2022. **10**(13): p. 7195-7206.
31. Idrees, M., et al., 3D printed PC/SiOC@Zn hybrid composite as dendrite-free anode for Zn-Ion battery. Nano Energy, 2022. **100**: p. 107505.
32. Wang, H., et al., Controlled deposition via a bifunctional layer enables dendrite-free zinc metal batteries. Chemical Engineering Journal, 2023. **470**: p. 144147.
33. Xue, M., et al., Carbon-assisted anodes and cathodes for zinc ion batteries: From basic science to specific applications, opportunities and challenges. Energy Storage Materials, 2023. **62**: p. 102940.
34. Liu, M., et al., Strategies for pH regulation in aqueous zinc ion batteries. Energy Storage Materials, 2024: p. 103248.
35. Zhou, W., et al., Cotton-derived cellulose film as a dendrite-inhibiting separator to stabilize the zinc metal anode of aqueous zinc ion batteries. Energy Storage Materials, 2022. **44**: p. 57-65.

36. Li, B., et al., A facile coating strategy for high stability aqueous zinc ion batteries: Porous rutile nano-TiO2 coating on zinc anode. Surface and Coatings Technology, 2021. **421**: p. 127367.
37. Liu, Y., et al., Ultrathin ZrO2 coating layer regulates Zn deposition and raises long-life performance of aqueous Zn batteries. Materials Today Energy, 2022. **28**: p. 101056.
38. Song, T.-B., et al., Zn anode surface engineering for stable zinc-ion batteries: Carbon dots incorporated mesoporous TiO2 as a coating layer. Chemical Engineering Journal, 2023. **471**: p. 144735.
39. Naresh, N., et al., Dendrite-free Zn anodes enabled by a hierarchical zincophilic TiO2 layer for rechargeable aqueous zinc-ion batteries. Applied Surface Science, 2022. **606**: p. 154932.
40. Kang, L., et al., Nanoporous CaCO3 Coatings Enabled Uniform Zn Stripping/Plating for Long-Life Zinc Rechargeable Aqueous Batteries. Advanced Energy Materials, 2018. **8**(25): p. 1801090.
41. Sun, S., et al., Protecting Zn anodes by atomic layer deposition of ZrO 2 to extend the lifetime of aqueous Zn-ion batteries. Energy Advances, 2024. **3**(1): p. 299-306.
42. Xi, M., et al., A novel solvent system of polyamides achieves new application in ZIBs by aggregation induced Lewis acid-base centers. Chemical Engineering Journal, 2023. **461**: p. 141987.
43. Chen, L., Q. An, and L. Mai, Recent advances and prospects of cathode materials for rechargeable aqueous zinc-ion batteries. Advanced Materials Interfaces, 2019. **6**(17): p. 1900387.
44. Zhou, T., et al., Cathode materials for aqueous zinc-ion batteries: A mini review. Journal of Colloid and Interface Science, 2022. **605**: p. 828-850.
45. Wang, L. and J. Zheng, Recent advances in cathode materials of rechargeable aqueous zinc-ion batteries. Materials Today Advances, 2020. **7**: p. 100078.
46. He, P., et al., High-Performance Aqueous Zinc–Ion Battery Based on Layered H2V3O8 Nanowire Cathode. Small, 2017. **13**(47): p. 1702551.
47. HUANG, Q.-f., et al., Application of vanadium phosphate in aqueous zinc-ion batteries. Chinese Journal of Engineering, 2023. **45**(7): p. 1175-1186.

48. Shuai, H., et al., Recent Advances of Transition Metal Sulfides/Selenides Cathodes for Aqueous Zinc-Ion Batteries. Advanced Energy Materials, 2023. **13**(4): p. 2202992.
49. Zhu, Q., et al., VS 4 with a chain crystal structure used as an intercalation cathode for aqueous Zn-ion batteries. Journal of materials chemistry A, 2020. **8**(21): p. 10761-10766.
50. Chen, T., et al., VS2 nanosheets vertically grown on graphene as high-performance cathodes for aqueous zinc-ion batteries. Journal of Power Sources, 2020. **477**: p. 228652.
51. Jing, F., et al., Dual ions intercalation drives high-performance aqueous Zn-ion storage on birnessite-type manganese oxides cathode. Energy Storage Materials, 2022. **49**: p. 164-171.
52. Zhang, Y., et al., Electrodeposited ε-MnO2 on carbon fibers as an ideal cathode material for aqueous zinc-ion batteries. Materials Letters, 2024. **361**: p. 135993.
53. Liu, Y., et al., Spontaneously dissolved MnO: A better cathode material for rechargeable aqueous zinc-manganese batteries. Chemical Engineering Journal, 2023. **473**: p. 145490.
54. Zhao, B., et al., Cathode materials for aqueous zinc-ion batteries and prospect of self-supporting electrodes: A review. Journal of Energy Storage, 2023. **73**: p. 109174.
55. Wu, J., et al., Boosting the Capacity and Life-span of Zn-Supplied Cathode in “Rocking-Chair” Aqueous Zn-Ion Batteries by Vanadium-Manganese Coupling Strategy. Materials Today Energy, 2024: p. 101505.
56. Gao, X., et al., Three-Dimensional Manganese Oxide@Carbon Networks as Free-Standing, High-Loading Cathodes for High-Performance Zinc-Ion Batteries. Small Structures, 2023. **4**(5): p. 2200316.
57. Xu, Y., et al., Recent Advances on Challenges and Strategies of Manganese Dioxide Cathodes for Aqueous Zinc-Ion Batteries. ENERGY & ENVIRONMENTAL MATERIALS, 2023. **6**(6): p. e12575.

58. Zhang, N., et al., Understanding of the charge storage mechanism of MnO2-based aqueous zinc-ion batteries: Reaction processes and regulation strategies. Journal of Energy Chemistry, 2023. **82**: p. 423-463.
59. Liu, M., et al., Tuning phase evolution of β-MnO2 during microwave hydrothermal synthesis for high-performance aqueous Zn ion battery. Nano Energy, 2019. **64**: p. 103942.
60. Han, R., et al., Eu doping β-MnO2 as cathode materials for high specific capacity aqueous zinc ion batteries. Journal of Energy Storage, 2024. **80**: p. 110250.
61. Wang, J., et al., Recent progress in interfacial engineering strategies for Mn-based oxide cathodes in aqueous zinc-ion batteries: Mechanisms, modifications, and performance enhancement. Energy Storage Materials, 2023. **63**: p. 103015.
62. Dai, H., et al., Design of manganese dioxide for supercapacitors and zinc-ion batteries: similarities and differences. Energy Mater., 2022. **2**(6): p. 200040.
63. Griščenko, Ņ., et al., Improvement of manganese dioxide cathode by molybdenum doping in highly acidic electrolyte. Journal of Energy Storage, 2024. **76**: p. 109847.
64. Ming, J., et al., Zinc-ion batteries: Materials, mechanisms, and applications. Materials Science and Engineering: R: Reports, 2019. **135**: p. 58-84.
65. Liu, N., et al., Recent advances and perspectives on vanadium- and manganese-based cathode materials for aqueous zinc ion batteries. Journal of Energy Chemistry, 2021. **59**: p. 134-159.
66. Kim, S.J., et al., Unraveling the dissolution-mediated reaction mechanism of α-MnO2 cathodes for aqueous Zn-ion batteries. Small, 2020. **16**(48): p. 2005406.
67. Fenta, F.W., et al., Structural engineering of α-MnO2 cathode by Ag+ incorporation for high capacity aqueous zinc-ion batteries. Journal of Power Sources, 2022. **548**: p. 232010.
68. Guo, Y., Y. Zhang, and H. Lu, Manganese-based materials as cathode for rechargeable aqueous zinc-ion batteries. Battery Energy, 2022. **1**(2): p. 20210014.
69. Chodankar, N.R., et al., Zn-ion Batteries: Charge Storing Mechanism and Development Challenges. ChemSusChem, 2023. **16**(21): p. e202300730.

70. Liao, Y., et al., Unveiling performance evolution mechanisms of MnO2 polymorphs for durable aqueous zinc-ion batteries. Energy Storage Materials, 2022. **44**: p. 508-516.
71. Geng, Y., et al., Electrolyte additive engineering for aqueous Zn ion batteries. Energy Storage Materials, 2022. **51**: p. 733-755.
72. Alfaruqi, M.H., et al., Structural transformation and electrochemical study of layered MnO2 in rechargeable aqueous zinc-ion battery. Electrochimica Acta, 2018. **276**: p. 1-11.
73. Guo, C., et al., Ultrathin δ-MnO2 nanosheets as cathode for aqueous rechargeable zinc ion battery. Electrochimica Acta, 2019. **304**: p. 370-377.
74. Zhang, H., et al., Extracting oxygen anions from ZnMn2O4: Robust cathode for flexible all-solid-state Zn-ion batteries. Energy Storage Materials, 2019. **21**: p. 154-161.
75. Yan, L., et al., An innovation: Dendrite free quinone paired with ZnMn2O4 for zinc ion storage. Materials Today Energy, 2019. **13**: p. 323-330.
76. Soundharrajan, V., et al., The dominant role of Mn2+ additive on the electrochemical reaction in ZnMn2O4 cathode for aqueous zinc-ion batteries. Energy Storage Materials, 2020. **28**: p. 407-417.
77. Song, M., et al., Recent Advances in Zn-Ion Batteries. Advanced Functional Materials, 2018. **28**(41): p. 1802564.
78. Tian, Z.-R., et al., Effects of Water, Cations, and Structure on Energetics of Layer and Framework Phases, Na x Mg y MnO2⊙ n H2O. The Journal of Physical Chemistry B, 2000. **104**(20): p. 5035-5039.
79. Scheitenberger, P., H. Euchner, and M. Lindén, The hidden impact of structural water–how interlayer water largely controls the Raman spectroscopic response of birnessite-type manganese oxide. Journal of Materials Chemistry A, 2021. **9**(34): p. 18466-18476.
80. Zampardi, G. and F. La Mantia, Prussian blue analogues as aqueous Zn-ion batteries electrodes: Current challenges and future perspectives. Current Opinion in Electrochemistry, 2020. **21**: p. 84-92.

81. Li, M., et al., A Structural Perspective on Prussian Blue Analogues for Aqueous Zinc-Ion Batteries. Batteries & Supercaps, 2023. **6**(11): p. e202300340.
82. Li, Y., et al., Prussian blue analogs cathodes for aqueous zinc ion batteries. Materials Today Energy, 2022. **29**: p. 101095.
83. Li, G., et al., Developing Cathode Materials for Aqueous Zinc Ion Batteries: Challenges and Practical Prospects. Advanced Functional Materials, 2024. **34**(5): p. 2301291.
84. Zheng, Z., et al., Electrolyte additives toward practical aqueous zinc-ion batteries: recent advances and future challenges. Next Energy, 2023. **1**(4): p. 100073.
85. Huang, S., et al., Recent Progress in the Electrolytes of Aqueous Zinc-Ion Batteries. Chemistry – A European Journal, 2019. **25**(64): p. 14480-14494.
86. Lv, Y., et al., Recent Advances in Electrolytes for “Beyond Aqueous” Zinc-Ion Batteries. Advanced Materials, 2022. **34**(4): p. 2106409.
87. Xiang, Y., et al., Shackling the aqueous electrolyte via metal-organic frameworks to realize high energy density zinc-ion batteries. Nano Energy, 2023. **117**: p. 108873.
88. Yan, H., et al., Insight into the electrolyte strategies for aqueous zinc ion batteries. Coordination Chemistry Reviews, 2022. **452**: p. 214297.
89. Du, Y., et al., Electrolyte Salts and Additives Regulation Enables High Performance Aqueous Zinc Ion Batteries: A Mini Review. Small, 2022. **18**(43): p. 2104640.
90. Li, Z. and A.W. Robertson, Electrolyte engineering strategies for regulation of the Zn metal anode in aqueous Zn-ion batteries. Battery Energy, 2023. **2**(1): p. 20220029.
91. Bhuvaneswari, B., et al., Structural, thermal and electrochemical characterization of cellulose acetate–based solid biopolymer electrolyte for zinc ion batteries. Ionics, 2022. **28**(8): p. 3865-3875.
92. Winter, M. and R.J. Brodd, What Are Batteries, Fuel Cells, and Supercapacitors? Chemical Reviews, 2004. **104**(10): p. 4245-4270.
93. Huang, S., et al., Recent progress in the electrolytes of aqueous zinc-ion batteries. Chemistry–A European Journal, 2019. **25**(64): p. 14480-14494.

94. Hu, F., et al., The gel-state electrolytes in zinc-ion batteries. Batteries, 2022. **8**(11): p. 214.
95. Dai, H., et al., Design of manganese dioxide for supercapacitors and zinc-ion batteries: similarities and differences. Energy Materials, 2022. **2**: p. 200040.
96. Tang, B., et al., Issues and opportunities facing aqueous zinc-ion batteries. Energy & Environmental Science, 2019. **12**(11): p. 3288-3304.
97. Yadav, N., et al., Mnco2o4 spinel microsphere assembled with flake structure as a cathode for high-performance zinc ion battery. Journal of Energy Storage, 2023. **64**: p. 107148.
98. Tay, I.R., J. Xue, and W.S.V. Lee, Methods for Characterizing Intercalation in Aqueous Zinc Ion Battery Cathodes: A Review. Advanced Science, 2023. **10**(26): p. 2303211.
99. Cui, X., et al., Unraveling the electrochemical charge storage dynamics of defective Oxides-Based cathodes toward High-Performance aqueous Zinc-Ion batteries. Chemical Engineering Journal, 2023. **478**: p. 147197.
100. Yin, J., et al., Electrochemical Zinc Ion Capacitors: Fundamentals, Materials, and Systems. Advanced Energy Materials, 2021. **11**(21): p. 2100201.
101. Xiong, T., et al., Defect engineering in manganese-based oxides for aqueous rechargeable zinc-ion batteries: a review. Advanced Energy Materials, 2020. **10**(34): p. 2001769.
102. Wu, X., et al., Green-low-cost rechargeable aqueous zinc-ion batteries using hollow porous spinel ZnMn 2 O 4 as the cathode material. Journal of Materials Chemistry A, 2017. **5**(34): p. 17990-17997.
103. Tao, Y., et al., Nickel and cobalt Co-substituted spinel ZnMn2O4@N-rGO for increased capacity and stability as a cathode material for rechargeable aqueous zinc-ion battery. Electrochimica Acta, 2020. **331**: p. 135296.
104. Yang, F., et al., Rational construction of multidimensional oxygen-deficient Co3O4 nanosheet/nanowire arrays as high-performance electrodes for aqueous Zn-ion batteries and asymmetric supercapacitors. Journal of Alloys and Compounds, 2021. **879**: p. 160439.

105. Zhang, Y., et al., Fabrication of Zn-doped Co3O4 as cathode material for aqueous rechargeable Zn-ion batteries. International Journal of Electrochemical Science, 2023. **18**(9): p. 100268.
106. Yu, B., et al., Recent advances on low-co and co-free high entropy layered oxide cathodes for lithium-ion batteries. Nanotechnology, 2023.
107. Du, K., et al., High Entropy Oxides Modulate Atomic-Level Interactions for High-Performance Aqueous Zinc-Ion Batteries. Advanced Materials, 2023. **35**(51): p. 2301538.
108. Jia, H., et al., High-entropy doping strategy towards reinforced Mn-O bond for durable aqueous zinc ion batteries. Nano Energy, 2024. **122**: p. 109348.
109. Zhang, X.-m., et al., Dynamic active sites over binary oxide catalysts: In situ/operando spectroscopic study of low-temperature CO oxidation over MnOx-CeO2 catalysts. Applied Catalysis B: Environmental, 2016. **191**: p. 179-191.
110. Xiong, T., et al., Defect engineering of oxygen-deficient manganese oxide to achieve high-performing aqueous zinc ion battery. Advanced Energy Materials, 2019. **9**(14): p. 1803815.
111. Huang, J., et al., Improving the capacity of zinc-ion batteries through composite defect engineering. RSC advances, 2021. **11**(54): p. 34079-34085.
112. Xiong, T., et al., Defect Engineering of Oxygen-Deficient Manganese Oxide to Achieve High-Performing Aqueous Zinc Ion Battery. Advanced Energy Materials, 2019. **9**(14): p. 1803815.
113. Han, M., et al., Oxygen defects in β-MnO2 enabling high-performance rechargeable aqueous zinc/manganese dioxide battery. Iscience, 2020. **23**(1).
114. Wang, J., et al., Superfine MnO2 Nanowires with Rich Defects Toward Boosted Zinc Ion Storage Performance. ACS Applied Materials & Interfaces, 2020. **12**(31): p. 34949-34958.
115. Ang, Z.W.J., et al., Oxygen-Deficient Birnessite-MnO2 for High-Performing Rechargeable Aqueous Zinc-Ion Batteries. ChemNanoMat, 2020. **6**(9): p. 1357-1364.
116. Zhao, M., et al., A Perspective toward Practical Lithium–Sulfur Batteries. ACS Central Science, 2020. **6**(7): p. 1095-1104.

117. Zhang, L., et al., Effective electrostatic confinement of polysulfides in lithium/sulfur batteries by a functional binder. Nano Energy, 2017. **40**: p. 559-565.
118. Mori, R., Cathode materials for lithium-sulfur battery: a review. Journal of Solid State Electrochemistry, 2023. **27**(4): p. 813-839.
119. Li, G., Z. Chen, and J. Lu, Lithium-Sulfur Batteries for Commercial Applications. Chem, 2018. **4**(1): p. 3-7.
120. Zhang, Y., et al., Lithium–Sulfur Batteries Meet Electrospinning: Recent Advances and the Key Parameters for High Gravimetric and Volume Energy Density. Advanced Science, 2022. **9**(4): p. 2103879.
121. Park, J.-W., et al., Flexible high-energy-density lithium-sulfur batteries using nanocarbon-embedded fibrous sulfur cathodes and membrane separators. NPG Asia Materials, 2021. **13**(1): p. 30.
122. Liu, Y., et al., LiXGe containing ion-conductive hybrid skin for high rate lithium metal anode. Chemical Engineering Journal, 2019. **371**: p. 294-300.
123. Xu, W., et al., Lithium metal anodes for rechargeable batteries. Energy & Environmental Science, 2014. **7**(2): p. 513-537.
124. Nitta, N., et al., Li-ion battery materials: present and future. Materials Today, 2015. **18**(5): p. 252-264.
125. Chen, J., et al., Post lithium-sulfur battery era: challenges and opportunities towards practical application. Science China Chemistry, 2022.
126. Seh, Z.W., et al., Designing high-energy lithium-sulfur batteries. Chemical Society reviews, 2016. **45 20**: p. 5605-5634.
127. Zheng, Y., et al., Metal–organic frameworks for lithium–sulfur batteries. Journal of Materials Chemistry A, 2019. **7**(8): p. 3469-3491.
128. Liu, G., et al., Electrolyte Issues in Lithium–Sulfur Batteries: Development, Prospect, and Challenges. Energy & Fuels, 2021. **35**(13): p. 10405-10427.
129. Li, Z., et al., Wide application of metal-organic frameworks in lithium–sulfur battery. Materials Today Sustainability, 2023. **22**: p. 100392.
130. Yao, Y., et al., High-Entropy Materials: Features for Lithium–Sulfur Battery Applications. Metals, 2023. **13**(5): p. 833.

131. Deng, C., et al., Inhibition of polysulfide diffusion in lithium–sulfur batteries: mechanism and improvement strategies. Journal of Materials Chemistry A, 2019. **7**(20): p. 12381-12413.
132. Aurbach, D., et al., On the Surface Chemical Aspects of Very High Energy Density, Rechargeable Li–Sulfur Batteries. Journal of The Electrochemical Society, 2009. **156**(8): p. A694.
133. Shi, F., et al., Emerging catalytic materials for practical lithium-sulfur batteries. Journal of Energy Chemistry, 2023. **76**: p. 127-145.
134. Yang, J.-L., et al., Rich Heterointerfaces Enabling Rapid Polysulfides Conversion and Regulated Li2S Deposition for High-Performance Lithium–Sulfur Batteries. ACS Nano, 2021. **15**(7): p. 11491-11500.
135. Xu, Z.-L., et al., Visualization of regulated nucleation and growth of lithium sulfides for high energy lithium sulfur batteries. Energy & Environmental Science, 2019. **12**(10): p. 3144-3155.
136. Zhao, C., et al., A high-energy and long-cycling lithium–sulfur pouch cell via a macroporous catalytic cathode with double-end binding sites. Nature Nanotechnology, 2021. **16**(2): p. 166-173.
137. Wang, P., et al., Emerging Catalysts to Promote Kinetics of Lithium–Sulfur Batteries. Advanced Energy Materials, 2021. **11**(7): p. 2002893.
138. Hu, Y., et al., Carbon Quantum Dots–Modified Interfacial Interactions and Ion Conductivity for Enhanced High Current Density Performance in Lithium–Sulfur Batteries. Advanced Energy Materials, 2019. **9**(7): p. 1802955.
139. Hu, X., et al., Versatile, Aqueous Soluble C2N Quantum Dots with Enriched Active Edges and Oxygenated Groups. Journal of the American Chemical Society, 2020. **142**(10): p. 4621-4630.
140. Xu, Z.L., et al., Exceptional catalytic effects of black phosphorus quantum dots in shuttling-free lithium sulfur batteries. Nature Communications, 2018. **9**(1).
141. Xiao, Z., et al., Ultrafine Ti3C2 MXene Nanodots-Interspersed Nanosheet for High-Energy-Density Lithium–Sulfur Batteries. ACS Nano, 2019. **13**(3): p. 3608-3617.

142. Zhou, T., et al., Twinborn TiO2–TiN heterostructures enabling smooth trapping–diffusion–conversion of polysulfides towards ultralong life lithium–sulfur batteries. Energy & Environmental Science, 2017. **10**(7): p. 1694-1703.
143. Yuan, Z., et al., Powering Lithium–Sulfur Battery Performance by Propelling Polysulfide Redox at Sulfiphilic Hosts. Nano Letters, 2016. **16**(1): p. 519-527.
144. Frischmann, P.D., et al., Redox-active supramolecular polymer binders for lithium–sulfur batteries that adapt their transport properties in operando. Chemistry of Materials, 2016. **28**(20): p. 7414-7421.
145. Park, J.-W., et al., Ionic liquid electrolytes for lithium–sulfur batteries. The Journal of physical chemistry C, 2013. **117**(40): p. 20531-20541.
146. Bi, C.-X., et al., Protecting lithium metal anodes in lithium–sulfur batteries: A review. Energy Material Advances, 2023. **4**: p. 0010.
147. Nanda, S. and A. Manthiram, Lithium degradation in lithium–sulfur batteries: insights into inventory depletion and interphasial evolution with cycling. Energy & Environmental Science, 2020. **13**(8): p. 2501-2514.
148. Gao, R., et al., Metal phosphides and borides as the catalytic host of sulfur cathode for lithium–sulfur batteries. International Journal of Minerals, Metallurgy and Materials, 2022. **29**(5): p. 990-1002.
149. Carenco, S., et al., Nanoscaled Metal Borides and Phosphides: Recent Developments and Perspectives. Chemical Reviews, 2013. **113**(10): p. 7981-8065.
150. Qin, Research progress on metal borides as cathode carrier materials for Li–S batteries, Nonferrous Met. Eng, 2021. **11**.
151. Wu, S., et al., Interface engineering of MXene-based heterostructures for lithium-sulfur batteries. Nano Research, 2023.
152. Zhang, D., et al., Horizontal Growth of Lithium on Parallelly Aligned MXene Layers towards Dendrite-Free Metallic Lithium Anodes. Advanced Materials, 2019. **31**(33): p. 1901820.
153. Pang, J., et al., Potential of MXene-Based Heterostructures for Energy Conversion and Storage. ACS Energy Letters, 2022. **7**(1): p. 78-96.

154. Tsai, M.-H. and J.-W. Yeh, High-Entropy Alloys: A Critical Review. Materials Research Letters, 2014. **2**(3): p. 107-123.
155. Hsu, W.-L., et al., Clarifying the four core effects of high-entropy materials. Nature Reviews Chemistry, 2024. **8**(6): p. 471-485.
156. Dąbrowa, J. and M. Danielewski, State-of-the-Art Diffusion Studies in the High Entropy Alloys. Metals, 2020. **10**(3): p. 347.
157. Cantor, B., et al., Microstructural development in equiatomic multicomponent alloys. Materials Science and Engineering: A, 2004. **375-377**: p. 213-218.
158. Yeh, J.-W., et al., Nanostructured High-Entropy Alloys with Multiple Principal Elements: Novel Alloy Design Concepts and Outcomes. Advanced Engineering Materials, 2004. **6**(5): p. 299-303.
159. Yeh, J.-W., Alloy design strategies and future trends in high-entropy alloys. Jom, 2013. **65**: p. 1759-1771.
160. Xing, Y., et al., Low temperature synthesis of high-entropy (Y0.2Yb0.2Sm0.2Eu0.2Er0.2)2O3 nanofibers by a novel electrospinning method. Journal of Materials Science & Technology, 2022. **103**: p. 215-220.
161. Jiang, Q., et al., A highly efficient high-entropy metal hydroxymethylate electrocatalyst for oxygen evolution reaction. Chemical Engineering Journal, 2023. **453**: p. 139510.
162. Bondesgaard, M., et al., General solvothermal synthesis method for complete solubility range bimetallic and high-entropy alloy nanocatalysts. Advanced Functional Materials, 2019. **29**(50): p. 1905933.
163. Guo, H., et al., Design and fabrication of high-entropy oxide anchored on graphene for boosting kinetic performance and energy storage. Ceramics International, 2022. **48**(3): p. 3344-3350.
164. Yao, Y., et al., Carbothermal shock synthesis of high-entropy-alloy nanoparticles. Science, 2018. **359**(6383): p. 1489-1494.
165. Xing, Y., et al., Low temperature synthesis of high-entropy (Y0. 2Yb0. 2Sm0. 2Eu0. 2Er0. 2) 2O3 nanofibers by a novel electrospinning method. Journal of Materials Science & Technology, 2022. **103**: p. 215-220.

166. Li, Z., et al., Characterization of novel high-entropy (La0. 2Nd0. 2Sm0. 2Dy0. 2Yb0. 2) 2Zr2O7 electrospun ceramic nanofibers. Ceramics International, 2022. **48**(9): p. 12074-12078.
167. Qiao, H., et al., A high-entropy phosphate catalyst for oxygen evolution reaction. Nano Energy, 2021. **86**: p. 106029.
168. Kheradmandfard, M., et al., Ultrafast green microwave-assisted synthesis of high-entropy oxide nanoparticles for Li-ion battery applications. Materials Chemistry and Physics, 2021. **262**: p. 124265.
169. Qiao, H., et al., Scalable synthesis of high entropy alloy nanoparticles by microwave heating. ACS nano, 2021. **15**(9): p. 14928-14937.
170. Löffler, T., et al., Discovery of a multinary noble metal–free oxygen reduction catalyst. Advanced Energy Materials, 2018. **8**(34): p. 1802269.
171. Duan, C., et al., New spinel high-entropy oxides (FeCoNiCrMnXLi) 3O4 (X= Cu, Mg, Zn) as the anode material for lithium-ion batteries. Ceramics International, 2021. **47**(22): p. 32025-32032.
172. Wang, B., et al., Spinel-type high-entropy (Co0. 2Mn0. 2Fe0. 2Zn0. 2Ti0. 2) 3O4 oxides constructed from disordered cations and oxygen vacancies. Journal of Alloys and Compounds, 2022. **897**: p. 163188.
173. Fan, L., et al., A novel MnCoNiCuZnO5 complex-phase ceramic for negative temperature coefficient thermistors. Materials Science in Semiconductor Processing, 2022. **142**: p. 106489.
174. Qiao, H., et al., Scalable Synthesis of High Entropy Alloy Nanoparticles by Microwave Heating. ACS Nano, 2021. **15**(9): p. 14928-14937.
175. Jiang, Q., et al., A highly efficient high-entropy metal hydroxymethylate electrocatalyst for oxygen evolution reaction. Chemical Engineering Journal, 2023. **453**: p. 139510.
176. Broge, N.L., et al., Autocatalytic formation of high-entropy alloy nanoparticles. Angewandte Chemie, 2020. **132**(49): p. 22104-22108.
177. Yao, Y., et al., High-Entropy Materials: Features for Lithium–Sulfur Battery Applications. Metals, 2023. **13**(5): p. 833.

178. Wu, Y., et al., Eight in one: high-entropy-alloy nanoparticles synthesized by carbothermal shock. Science Bulletin, 2018. **63**(12): p. 737-738.
179. Wang, Y. and Y. Wang, High-entropy alloys in catalyses and supercapacitors: Progress, prospects. Nano Energy, 2022. **104**: p. 107958.
180. Ma, J. and C. Huang, High entropy energy storage materials: Synthesis and application. Journal of Energy Storage, 2023. **66**: p. 107419.
181. Li, M. and J. Lu, Cobalt in lithium-ion batteries. Science, 2020. **367**(6481): p. 979-980.
182. Rost, C.M., et al., Entropy-stabilized oxides. Nature communications, 2015. **6**(1): p. 8485.
183. Fu, M., et al., High-entropy materials for energy-related applications. iScience, 2021. **24**(3).
184. Tian, L., et al., High-Entropy Spinel Oxide Nanofibers as Catalytic Sulfur Hosts Promise the High Gravimetric and Volumetric Capacities for Lithium–Sulfur Batteries. ENERGY & ENVIRONMENTAL MATERIALS, 2022. **5**(2): p. 645-654.
185. Liu, Z.-Y., et al., Novel high-entropy oxides for energy storage and conversion: From fundamentals to practical applications. Green Energy & Environment, 2023. **8**(5): p. 1341-1357.

CHAPTER THREE

Experimental methods and characterization techniques

3.0 Introduction

Materials used in the synthesis, synthesis routes, characterization, and electrochemical procedures of electrode materials are summarized in this chapter.

3.1. Chemicals and Materials

Manganese (II) Sulphate Monohydrate ($MnSO_4.H_2O$), Ammonium Persulphate ($(NH4)_2S_2O_8$), Copper (II) Nitrate Trihydrate ($Cu(NO_3)_2.3H_2O$), Cobalt (II) Nitrate Hexahydrate ($CoNO_3.6H_2O$), Manganese (II) Nitrate Tetrahydrate ($MnNO_3)_2.4H_2O$), Iron (III) Nitrate Nonahydrate ($FeN_3O_9.9H_2O$), Nickel (II) Nitrate Hexahydrate ($NiNO_3.6H_2O$), citric acid, Cerium Nitrate Hexahydrate ($Ce(NO_3)_3.6H_2O$), ethylene glycol, sulfur, Ketjen black, carbon black, OLC, PVDF, NMP, Ceria (CeO_2), and Potassium hydroxide (KOH).

3.2. Synthesis methods

3.2.1. Hydrothermal synthesis method of α-MnO_2

Scheme 3.1. shows the synthesis method. Typically, 3.3804g $MnSO_4.H_2O$ (0.02mol) and 4.464g $(NH_4)_2S_2O_8$ (0.02mol) were both dissolved separately in deionized water and allowed to stir for 30 minutes for the purpose of obtaining homogenous solutions. This was followed by mixing the two solutions and stirring for another period of 30 minutes, then it was transferred to an autoclave at 180°C for 45 minutes. The mixture was allowed cool to room temperature. The resultant product was collected, centrifuged using deionized water and vacuum dried at 85°C to obtain α-MnO_2.

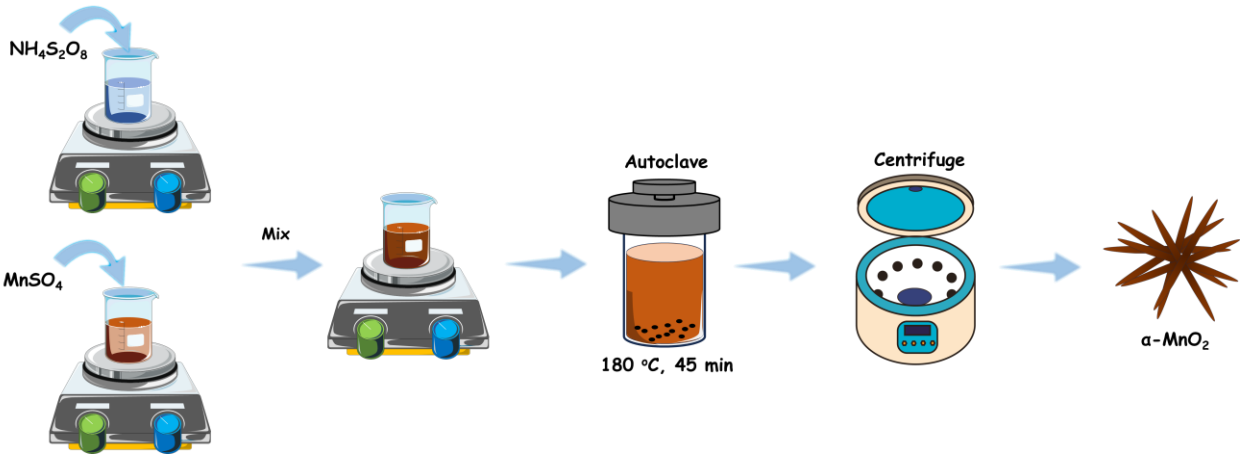

Scheme 3.1: Hydrothermal synthesis scheme of α-MnO_2

3.2.2. Microwave irradiation synthesis method of β-MnO_2

Scheme 3.2 shows the synthesis method. It follows the same procedure as hydrothermal method. The only difference was that instead of heating in an autoclave, the mixture was subjected to microwave irradiation at 300W and 180°C for 45 minutes.

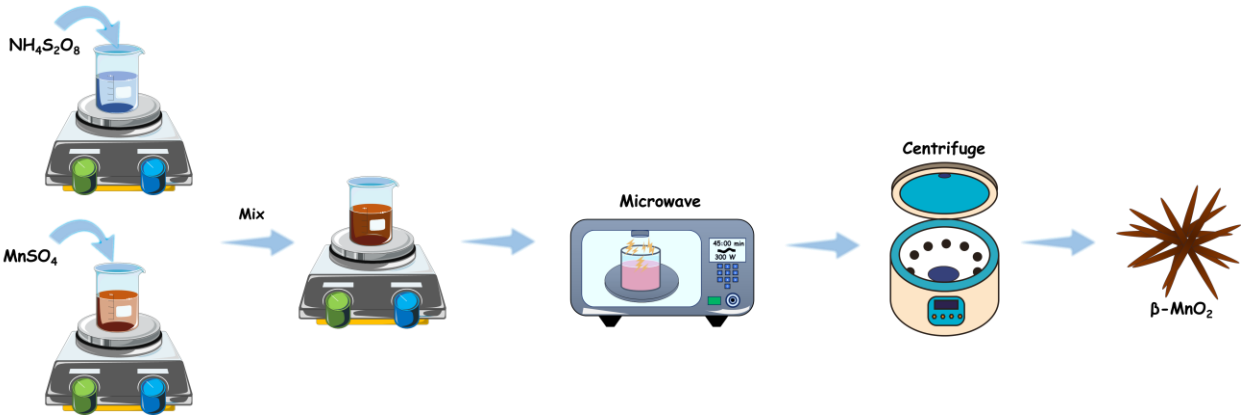

Scheme 3.2: Microwave irradiation synthesis scheme of β-MnO_2

3.2.3. Pechini synthesis method of $(CoCuMnFeNi)_3O_4$

The synthesis was done by Pechini-assisted synthesis. The stoichiometry amounts of nitrate salts of $Cu(NO_3)_2.3H_2O$, $CoNO_3.6H_2O$, $MnNO_3.4H_2O$, $FeN_3O_9.9H_2O$, $NiNO_3.6H_2O$ were weighed and then dissolved in distilled water. They were added dropwise to the mixture of ethylene glycol and citric acid prepared in the ratio (4:1). The resultant solution

was then heated to 90°C**.** This temperature was maintained under constant stirring until the gel formed was combusted to form a powder product. This product was calcined at 500°C and this temperature was maintained for 6 hours in air with the purpose of eliminating any carbonaceous materials.

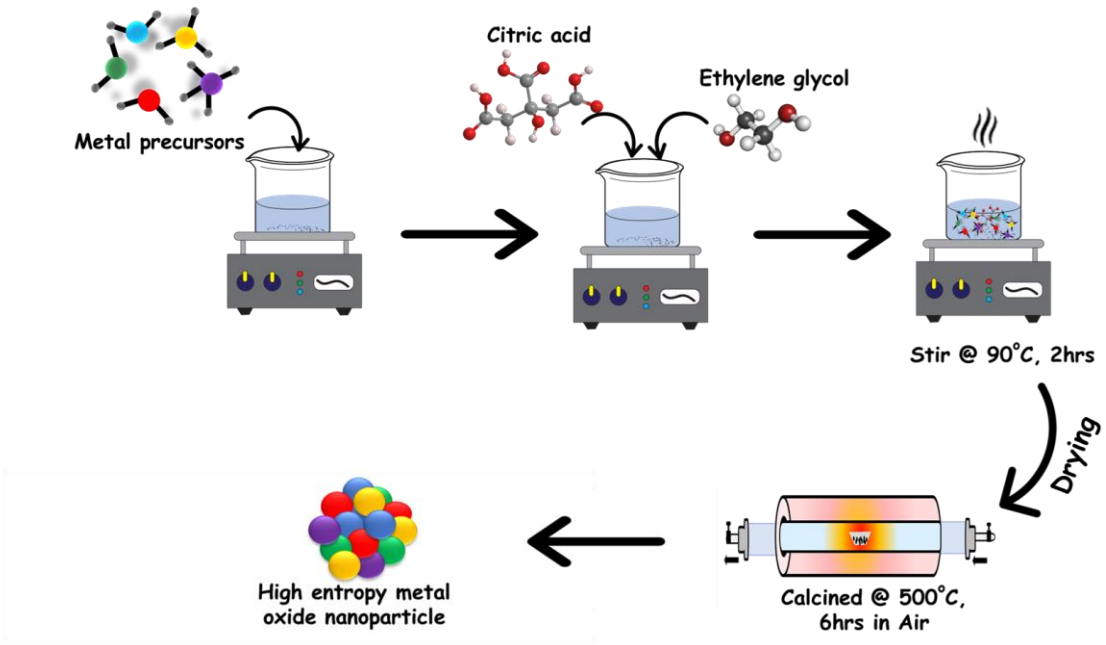

Scheme 3.3: Pechini method synthesis scheme of $(CoCuMnFeNi)_3O_4$

3.2.4. Melt diffusion synthesis of $(CoCuMnNiFe)_3O_4$/S

Scheme 3.4 shows the encapsulation of sulfur that was done by melt diffusion. This was achieved by mixing 0.05g of $(CoCuMnNiFe)_3O_4$, 0.1g of (OLC) and (0.15g) of sulfur and hand milling them for 30 minutes. The product was oven dried at 155°C for a period of 12 hours. A black powder was obtained upon cooling and abbreviated $(CoCuMnNiFe)_3O_4$/OLC/S.

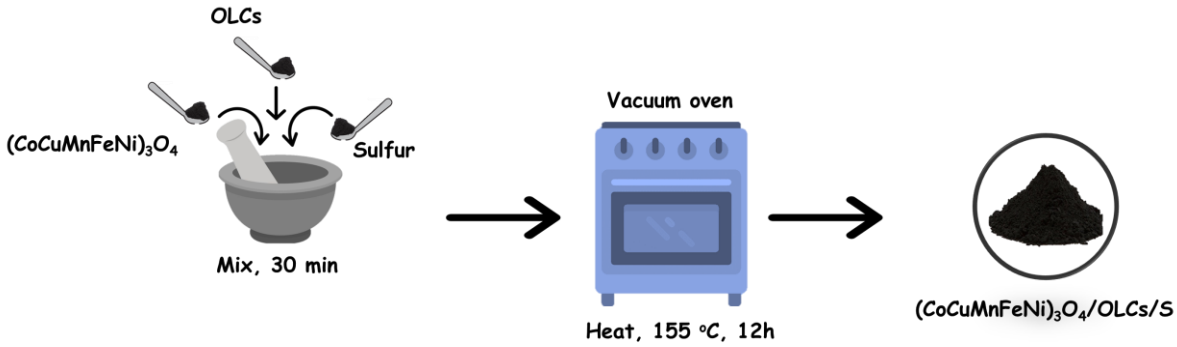

Scheme 3.4: Melt diffusion synthesis scheme of $(CoCuMnFeNi)_3O_4$/OLC/S

3.2.5. Melt diffusion synthesis of OLC/S

Scheme 3.5 shows sulfur encapsulation in OLC by melt diffusion method. Typically, 0.1g of OLC carbon and 0.1g of sulfur were weighed, mixed, and hand-milled for 30 minutes. This was followed by heating in an electric oven at 155°C for 12 hours. The mixture was cooled, collected, and labeled OLC/S.

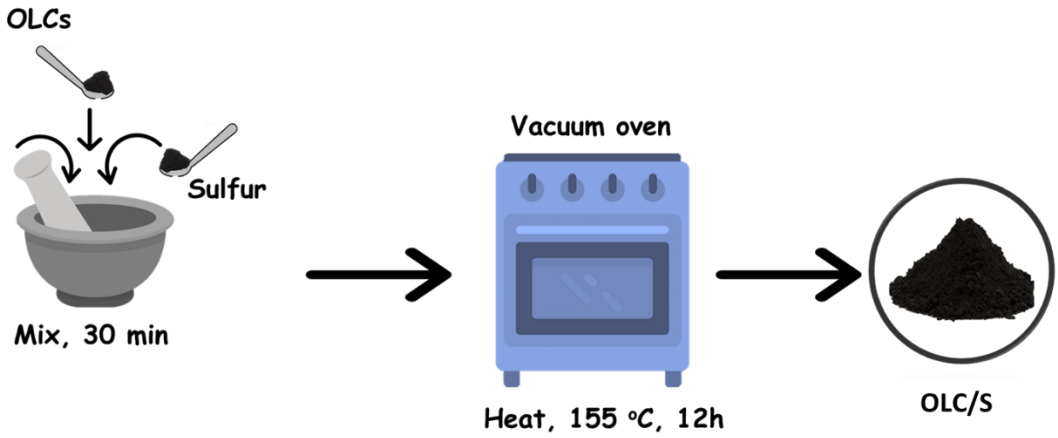

Scheme 3.5: Melt diffusion synthesis scheme of OLC/S

3.3. Material characterization techniques

3.3.1. X-ray Diffraction

This technique determines the materials' crystal structures. It usually detects crystalline materials that have crystal domains greater than 3-5nm. Materials are mostly classified into 2 categories:

- ✓ Crystalline materials
- ✓ Amorphous materials

The arrangement of atoms in a regular ordered 3D pattern is referred to as crystal structure in crystalline materials. This crystal structure extends through a distance that is much larger than the interatomic separations. The crystalline materials can be either single crystals or polycrystalline, whereby the single crystal order extends through the whole material's volume. Seven crystal systems exist i.e.: cubic, rhombohedral, tetragonal, orthorhombic, monoclinic, triclinic, and hexagonal. For this research work, we focused more on the cubic and tetragonal systems. The interplanar spacing ('d' spacing) is usually defined as the distance between adjacent planes. The orientation and the 'd' spacing are usually defined by 3 integers (h, k, l) which are referred to as the miller indices. Polycrystalline materials mainly consist of many small single crystals referred to as grains that are usually separated by grain boundaries. Atoms that are arranged in an irregular manner pattern create the amorphous materials.

3.3.1.1. XRD working principle

It operates by constructive interference principle between the sample and X-rays. Interaction between a beam of X-rays and the target atom leads to scattering of X-ray photons in different directions. This may result in elastic and inelastic scattering, whereby in inelastic scattering there is change in energy between scattered and incident photon while elastic scattering is the reverse process. The scattered waves then superimpose, and when the waves are in phase it is referred to as constructive interference while if they are out of phase it is known as destructive interference. A diffraction pattern is produced that informs more on the atom's arrangement in the crystal structures. This diffraction pattern is analyzed in different ways with the most common being Bragg's law:

$$n\lambda = 2d \sin\theta \quad \text{.....3.1}$$

where λ is the wavelength, n is an integer and 'd' is the interplanar spacing between the planes.

The XRD instrument is usually composed of the following working apparatus: A source of x-rays, a sample holder and a detector. The source produces x-rays that illuminate the

sample. These X-rays are diffracted and enter the detector. The diffraction angle is usually changed by moving the detector and the sample and the intensity is measured and diffraction data is obtained.

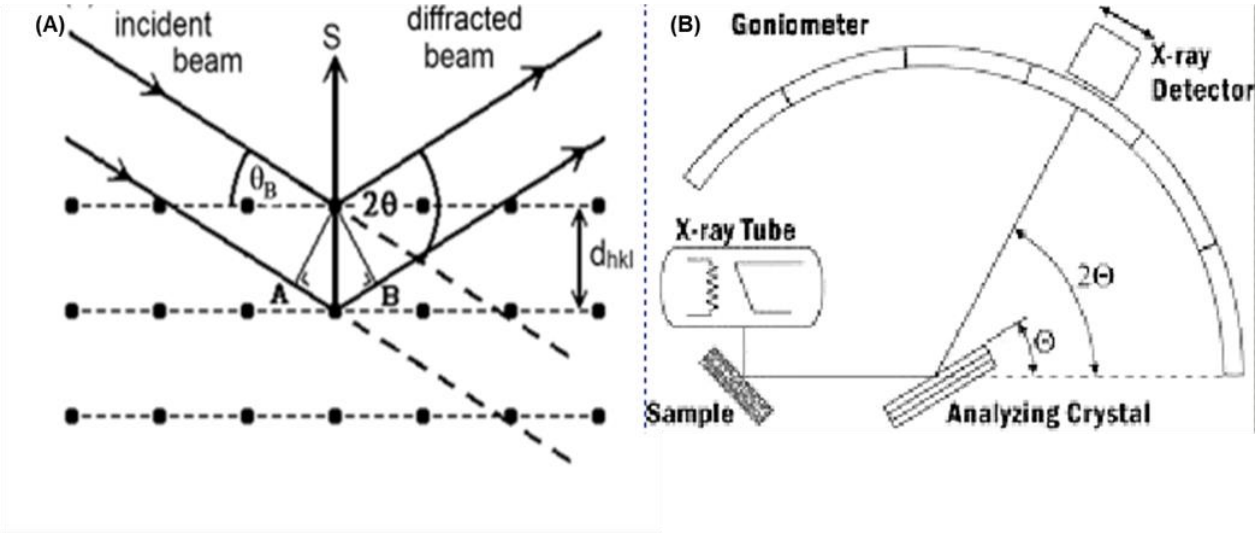

Figure 3.1: (A) Bragg's law[1], **(B)** Diffractometer System[2]

3.3.1.2. Powder XRD diffraction (PXRD)

In this technique, the diffraction pattern is usually gotten from the powder of the material instead of the individual crystal. This makes this technique much convenient and easier than single crystal diffraction since no individual crystals need to be made. Scherrer formula is then used in the determination of the particle size i.e.

$D_{hkl} = K\lambda/(B_{hkl}\cos\theta)$……3.2

where k= Scherrer constant assigned 0.9, D_{hkl}= Size of Crystals, λ= 0.15406 nm (incident x-ray wavelength), B_{hkl}= FWHM and (θ)= Position of Peak (radians)

PXRD patterns were recorded on Bruker D2 Phaser powder X-ray diffractometer with a copper (Cu) Kα (λ = 0.154060 nm) radiation X-ray source, operating at 30 kV and 10 mA. The samples were ground into a fine powder using an agate mortar and pestle, mounted onto the sample holder and flattened with a glass plate. The patterns were collected between 2θ values of 5° and 90°.

3.3.2. X-ray photoelectron spectroscopy (XPS)

This analytical technique is surface sensitive which makes it a powerful technique. It involves bombarding the materials' surface with X-rays and measuring the KE of emitted electrons. Its capabilities in revealing information about the chemical states of the elements present in the sample makes it very unique. It detects all the elements apart from helium and hydrogen and it is used to study the surface of the materials. This understanding and study of surfaces determines properties such as charge transfer, corrosion, adhesion and surface wettability, and catalysis. Photoelectric effect is the basis of XPS which was first discovered by Heinrich Hertz in the year 1887. He made an observation that surfaces emit electrons when irradiated with light while Kai Siegbahn introduced XPS through his work which at the time it was referred to as ESCA. This technique measures both auger electrons and photoelectrons[3].

3.3.2.1. Principle of technique

Soft rays are used to irradiate the sample and the KE of the emitted electrons is analyzed. The complete transfer of X-ray energy to a core level electron results in the emission of electrons which is expressed as: ($hv = BE + KE + \Phi_{spec}$). This states that the X-ray's energy is equal to the summation of binding energy, kinetic energy, and spectrometer work function. This work function is included since binding energy is a result of the samples' Fermi level. The representation of XPS survey spectra is the y-axis (intensity in counts) and x-axis (binding energies in electron volts) with the B.E reducing their values from left to right. For the transition metals, the oxidation state affects the binding energy primarily because when an atom loses electron density it is hard to eject an electron from that atom hence resulting in a higher B.E.

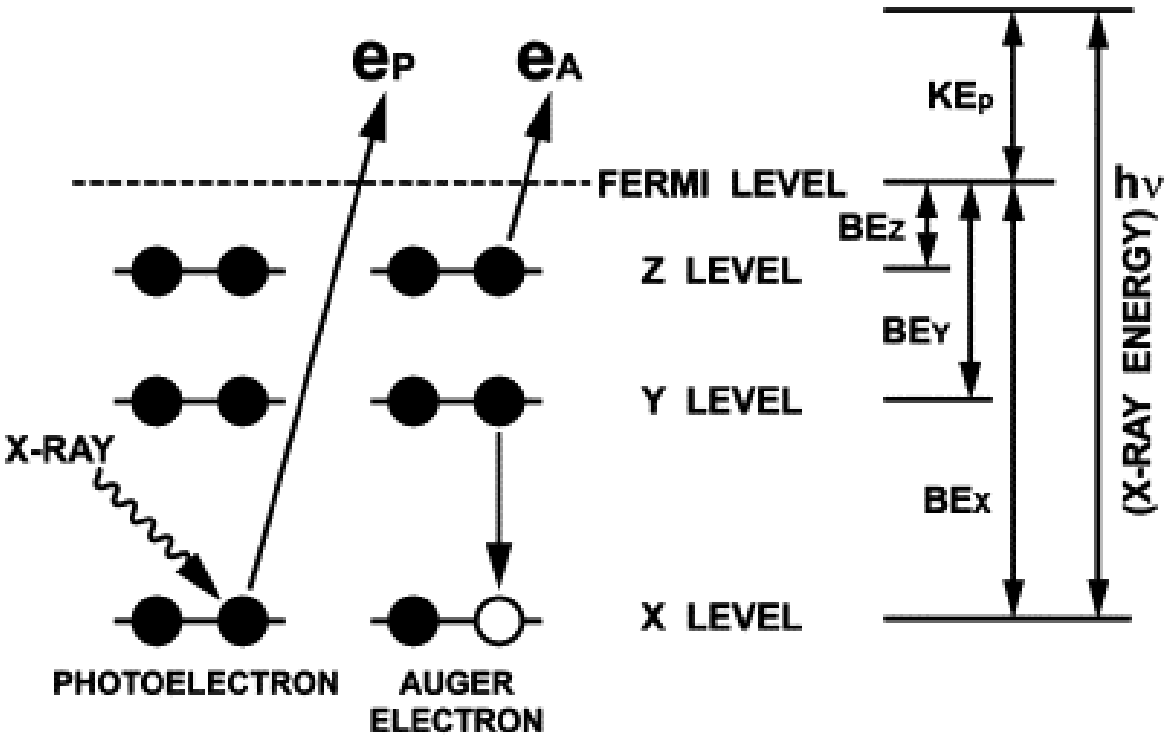

Figure 3.2: Emission processes of photoelectrons and auger electrons [3]

3.3.2.2. Instrumentation and operation

The XPS instrument is made up of a sample stage, extraction lenses, an analyzer, an X-ray source, and a detector. The X-ray source provides a large number of X-rays since this number is proportional to the emitted electrons. The extraction lenses define the acceptance angle for the collection of ejected electrons. They also control the area of the sample within which electrons are collected. Electrons usually travel through the analyzer which is of two types: concentric hemispherical and cylindrical analyzers. Only electrons with specified energies have the ability to travel through the analyzer.

3.3.2.3. Peak identification

Every XPS line with exception of the s orbitals occurs as doublets which is a result of spin-orbit coupling. Additional peaks known as satellite peaks also occur which result when x-rays of more than one energy excite a sample and the result is additional XPS peaks located at the lower BE. There is also the formation of ‘shakeups’ or ‘loss peaks’ which occur due to a de-excitation process whereby outgoing core electrons interact with

valence electrons leading them to being excited to higher energy levels. These peaks occur at a BE than the core level XPS peak. Multiplet splitting of peaks also occurs whereby the unpaired electrons in the valence states result in unexpected peak splitting. This is known to affect the S orbitals of some transition elements such as Mn, Cr, and Fe. Metals also experience asymmetric peak shapes with a tail located at the high B.E which is because metals have a lot of closely spaced unfulfilled states and hence excitation of valence electrons to these states occurs which leads to a tail instead of a peak [4].

X-ray photoelectron spectroscopy (XPS) measurements in this work were studied using ESCAlab 250Xi XPS with a monochromatic Al kα radiation source (1486.7eV). Survey spectra were taken at a pass energy of 100 eV and a high-resolution pass energy of 20 eV.

3.3.3. Raman spectroscopy

Spectroscopy can be defined as the study of electromagnetic radiation with matter and the spectroscopic methods are based on fluorescence, scattering, absorption, and emission. This characterization technique got its name from C.V. Raman who alongside K.S Krishnan wrote a paper based on it [5]. The major advantage of this technique is that it helps to resolve the limitations of other spectroscopic techniques and is useful qualitatively and quantitatively. Frequency and intensity of scattered radiations are measured whereby frequency gives qualitative information while intensity provides quantitative information. In addition, Raman signal quality is hardly affected by water, and hence it is used in plenty of applications where infrared analysis is not dependable.

3.3.3.1. Principle and instrumentation

The interaction of matter with electromagnetic radiation is by absorption, transmittance, and scattering technique. The difference between absorption and scattering technique is that absorption technique involves matching the energy of the incident photons with the energy gap between 2 electronic energy levels while scattering technique does not need adequate energy levels since it occurs through the interaction of a photon with a molecule which induces distortion of the electron cloud and it changes the polarization involving the virtual states. Two types of scattering processes are involved i.e. elastic and inelastic

scattering. The scattering is elastic when the scattered photon's energy matches the incoming photon's energy and the electrons involved return to a state with equal energy as the initial one (Rayleigh scattering). Inelastic scattering /Raman scattering is formed by the reverse process, whereby the gain or loss of photon energy is equal to the difference in energy between the final and initial energy/electronic levels. In addition, if the outgoing photons' energy is lower than the incoming one, Stokes scattering is achieved, while if it has higher energy it is referred to as anti-Stokes[6], while the difference in energy between the outgoing and incoming photon is termed as 'Raman shift'. Measuring of the scattered radiation is done at right angles to the incident radiation. The scattering usually relies on the wavelength of the incident radiation. Presentation of Raman spectra is by intensity vs shift of wavelength [7]. Dispersive and non-dispersive Raman spectrophotometers exist; whereby the dispersive spectrophotometers make use of prisms while non-dispersive employ interferometers.

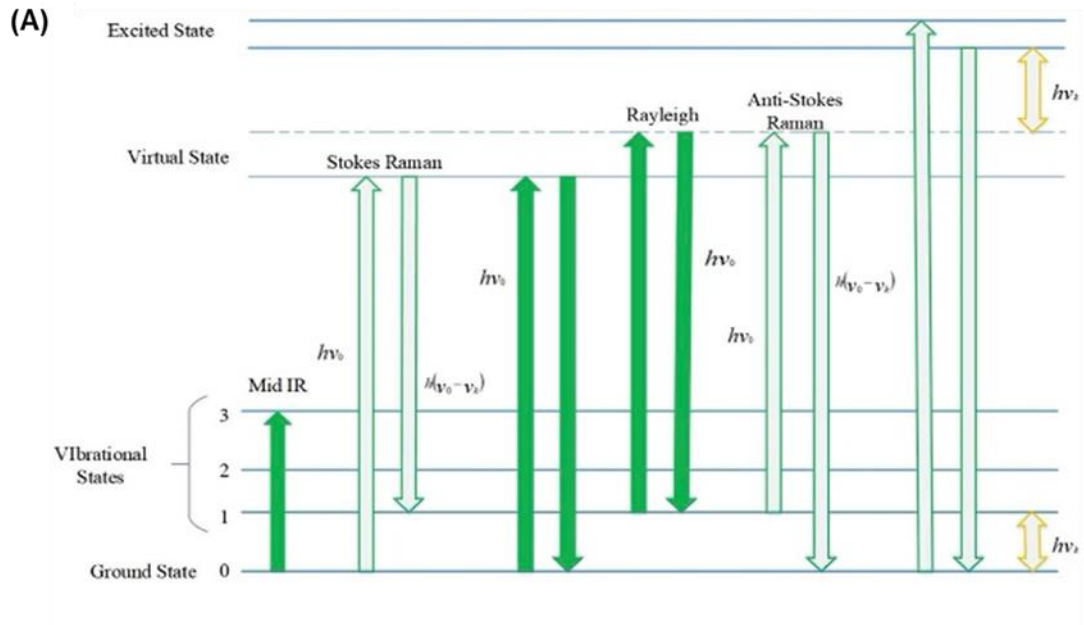

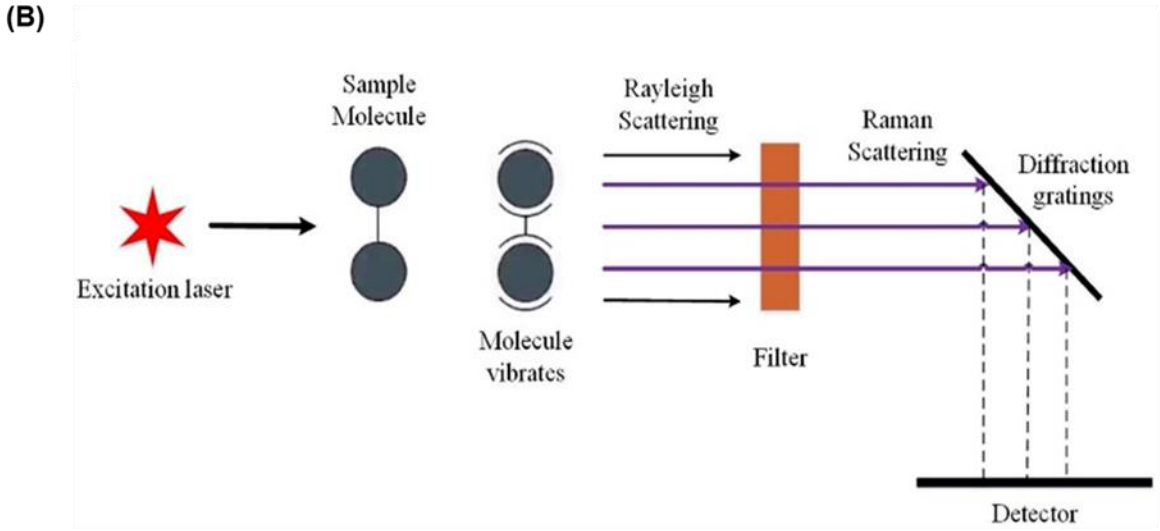

Figure 3.3: Raman Spectroscopy **(A)** Energy level diagram, **(B)** Schematic diagram [8].

The Raman spectra were acquired from the Horiba LabRAM HR Raman spectrometer equipped with an Olympus BX41 microscope. A 514.5 nm line of a Lexel Model 95 SHG argon ion laser was used and data was captured using LabSpec v5 software.

3.3.4. Scanning transmission spectroscopy (SEM)

SEM is a used magnification tool whereby it uses focused beams of electrons to gather the information. High-resolution 3D images are produced by this method. These images give morphological, topographical, and compositional information which brings about their value in industry and science. SEM was presented by McMullan in the years 1988 and 2006, however, the idea dates back to 1933 when the first electron microscope was constructed by the works of two physics scientists Max Knoll and Ruska. Manfred Von Ardenne also contributed by inventing a true microscope with a high magnification and also went further to discuss the possibilities, detection modes, and theories of SEM [9]. SEM utilizes the same principles as light microscopes but utilizes beams of electrons instead of photons in the magnification.

3.3.4.1. Instrumentation and working system

It is made up of the following components:

- A source (used to generate electrons hence the term electron gun).

- Column (passage for electrons)
- Scan coils (used as a deflection system)
- Detector (used to detect backscattered and secondary electrons).

The analysis is done by applying a beam of electrons down the column and into the electromagnetic lenses that compresses the spot size and directs the electron into the specimen. This is because the produced spot size is too large to produce a sharp image. The movement of the scan coils determines the image of the specimen that is formed. They make the beam to deflect a small cross area in case a high magnification of images is required [10]. This beam is usually focused on the stage where the specimen sample is placed. Detectors are used to attract different types of signals(emitted) electrons from the specimen samples, whereby it detects x-ray, backscattered, and secondary electrons whereby the backscattered electrons are incidental electrons that are reflected backward. Both backscattered and secondary electrons can be detected when a positive voltage is applied while only backscattered electrons are applied when negative voltages are applied. Samples usually need some preparation before being put into the vacuum chamber which includes sputter coating which is mostly done for non-conductive samples and dehydration for biological samples. EDS usually works alongside SEM in providing both qualitative and semi-quantitative information.

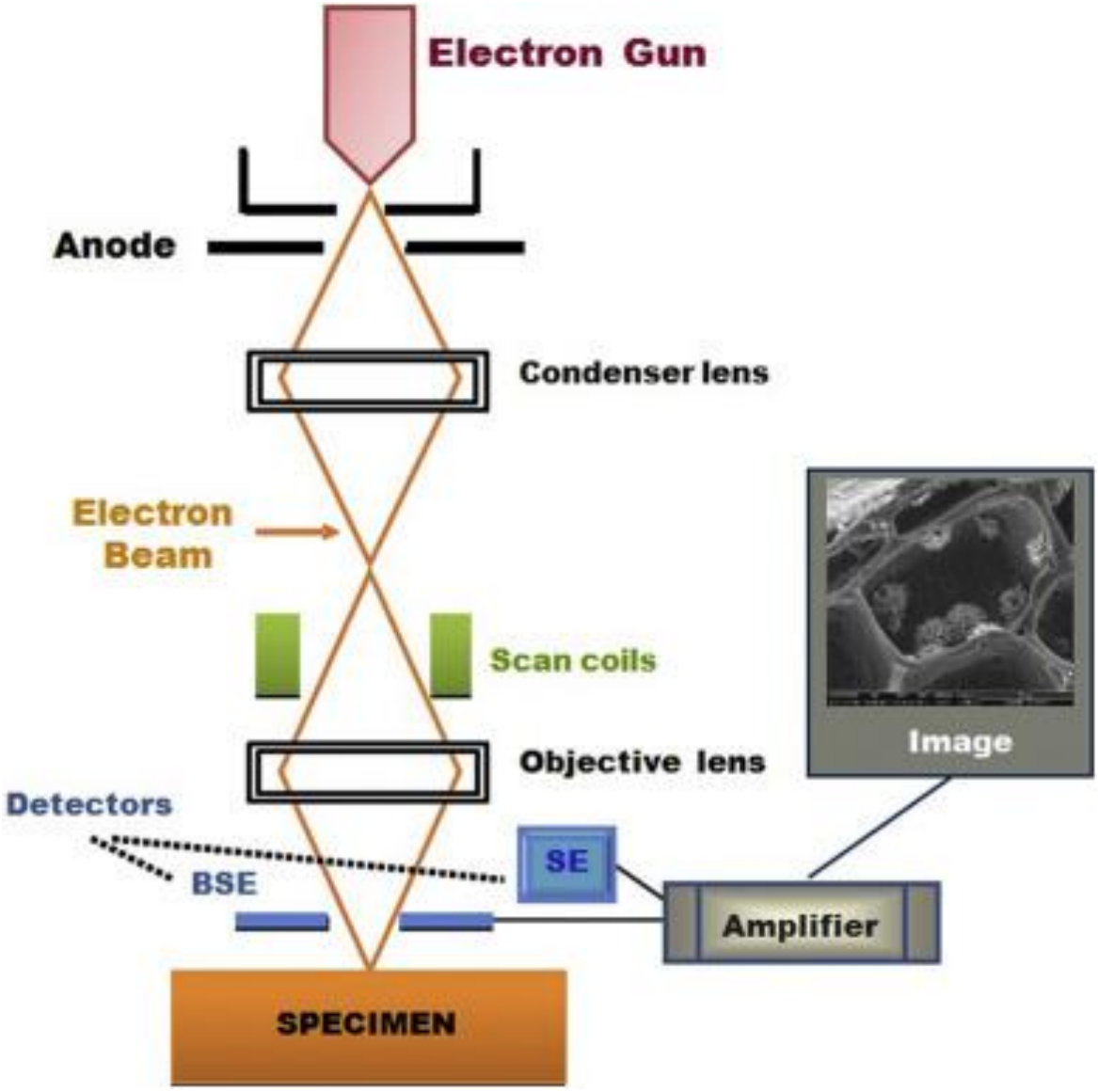

Figure 3.4: SEM instrument

For this work, samples were stuck onto stubs using double sided carbon tape, since it is conductive. The samples were then coated with carbon, using the Epitech carbon coater. Once coated they were placed on a stage and inserted into a Zeiss Auriga Field Emissions Scanning Electron Microscope (SEM). SmartSEM software was used to collect the images.

Energy dispersive X-ray spectroscopy (EDS)

The development of EDS solved different number of challenges in the Electron Probe field. The detector in the EDS functions to separate the X-ray characteristics of various elements within the sample into an energy spectrum. Analysis of the spectrum by the EDS detectors then follows which functions to identify the amplitude of the specific elements. Then the chemical compositions of the elements are determined both quantitatively and qualitatively. For this work, Oxford X-max with Aztec software was used as a detector.

3.3.5. Transmission electron spectroscopy (TEM)

This technique involves transmitting electron beams through ultra-thin specimens. A team of researchers that included Ernst Ruska and Max Knoll invented the first electron microscope. It utilizes electrons to provide compositional, morphological, and crystallographic information of the sample specimens. It produces high-resolution 2D images hence receiving a lot of applications in industry and science.

3.3.5.1. Components and imaging

It comprises of a lanthanum hexaboride or tungsten filament emission source. This is then connected to a source of high voltage and given sufficient current, and electrons are emitted either by field electron emission or thermionic into the vacuum. The Wehnelt cylinder assists in the extraction of electrons. The manipulation of the electron beam in TEM is through two physical effects. Electrons interact with the magnetic field causing them to move with respect to the right hand rule. This allows the manipulation of the electron beam by electromagnets. Electrons are deflected through a constant angle by the use of electrostatic fields. Beam convergence is done by the lenses whereby the angle of convergence varies and hence it is capable of changing magnification by modifying the flow of current. Different types of lensing exist in TEM: projector, objective, and condenser lenses. Condenser lenses are responsible for primary beam formation; objective lenses focus the beam coming through the sample while projector lenses expand the beam onto the imaging devices. The image's magnification is according to the ratio of the distance between the specimen and the objective lens. TEM consists of

imaging systems that consist of a phosphor screen that is made up of fine particulate zinc sulfide. The evacuation of TEM to low pressures is done in order to increase the mean free path of electron gas interaction [11]. This decreases the collision frequency between the gas atoms and electrons to negligible levels and allows a voltage difference between the ground and cathode without any generation of an arc. Some of the components such as the cartridges and specimen holders are replaced or inserted routinely hence they require a system capable of re-evacuating on a regular basis. The interaction occurring between the electrons and samples leads to the production of a high-resolution black-and-white image. There are lighter and darker areas of the image whereby the light areas represent the areas in which a huge number of electrons passed through the sample while the dark areas are the dense areas of the object [12]. These contrasts provide information of the samples' shape, structure, size, structure, and texture. For the analysis, thin slicing of the sample specimen is done in order for the passage of electrons. This is the electron transparency property. The samples also need special preparation in order to withstand the vacuum chamber.

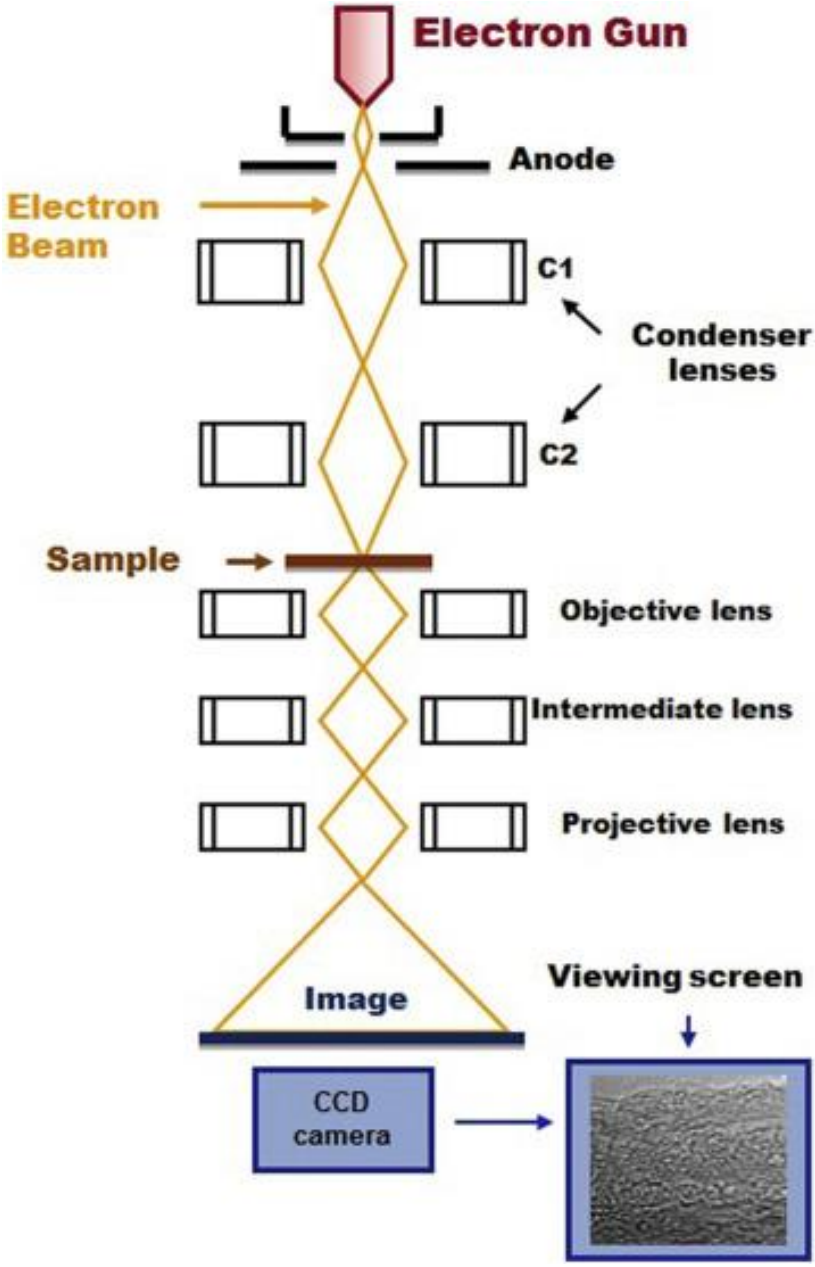

Figure 3.5: TEM Instrument

The instrument used was JEOL JEM 2100 at 200Kv. Samples were dissolved in ethanol and sonicated for ± 20mins and dispersed on a carbon coated copper grid for analysis.

3.4. Electrochemical characterization techniques

3.4.1. Fabrication of coin cells for ZIBs

Preparation of the cathode was done by mixing 70 wt.% of either α-MnO_2, β-MnO_2 or $CoCuMnFeNi)_3O_4$, 20 wt.% of carbon (OLC, Ketjen black, carbon black) and 10 wt.% PVDF binder in NMP to form a slurry. To achieve homogeneity, the slurry was stirred overnight. This was followed by pasting on the carbon current collector and drying at 80°C overnight. The dried laminate was punched into 10mm discs for coin cell assembly. The assembly of cells was done in an ambient environment. A zinc plate was used as the anode, Whatmann filter paper as the separator, and 3M $ZnSO_4.7H_2O$ as the electrolyte. The coin cells were used for electrochemical measurements using the Biologic System for CV, GCD, and EIS. BT-Lab and EC-Lab were used for data analysis.

3.4.2. Fabrication of coin cells for LSBs

The preparation of cathodes was done by mixing 80 wt.% of ($HESO_x$/OLC/S and OLC/S), 10 wt.% of carbon (OLC) and 10 wt.% PVDF in NMP to form a slurry. To achieve uniformity, the slurry was stirred on a magnetic stirrer overnight. Using a doctor blade, the slurry was spread into an aluminium current collector and dried in a vacuum oven at 60°C overnight. The dried electrode film was then cut into 12mm discs and used for coin cell assembly in an argon-filled glove box. Lithium foil, Celgard, and 1 M-(LiTFSI) in 1,3-(DOL) and 1,2-(DME) (volume ratio 1:1) with 1 wt.% $LiNO_3$ was used as the anode, separator, and electrolyte respectively. Electrochemical measurements such as CV, GCD, and EIS were then carried out using a Biologic System.

3.5. Electrochemical characterization techniques

3.5.1. Cyclic voltammetry

In order to begin CV measurements, determination of the terminal voltage (E_1 and E_2) and the scan rate is required. When the electrode reaction occurs at the selected electrochemical window and the current almost ends to zero at the ending points, then the terminal voltage and scan rate are appropriate. Current response in batteries is used to identify the peak current (i_p) and peak voltage (E_p). From the difference between peak voltage in cathodic and anodic ΔE_p, and the ratios of the peak currents, segments can be

used to determine whether a reaction is reversible or irreversible. Two modes of current response have been identified: faradaic and non-faradaic. It is defined as a non-faradaic current response when chemical reactions do not occur. Faradaic current is usually separated by the reactions that occur at the bulk and reactions at the surface because their response modes based on the scan rates are different. These separate modes are due to the charge carriers' differences in diffusion. The current that is contributed by the bulk part redox processes is linearly proportional to the square root of the scan rate whereby this relationship (i_p vs $v^{1/2}$) is used in the calculation of the diffusion coefficients. The laboratory-fabricated batteries are not ideal Nernst systems, whereby in the ideal systems the peak voltage is independent of the scan rates. In the fabricated batteries, a shift occurs when the scan rate changes. The assumption is that the shift is due to an increase in the polarization hence the plots of (i_p vs $v^{1/2}$) are collected at different voltages unlike the Nernst system which is done at the same voltage [13].

3.5.1.1. Reaction kinetics in cyclic voltammetry

The use of nanomaterials as electrodes mainly enhances the rate performance since high surface area (SA) usually leads to rapid diffusion-controlled processes and high pseudo-capacitive performance. Pseudo-capacitive behavior can be quantified based on: ($i=av^b$), where the constants are a and b where b is the slope of the graph (i_p versus $v^{1/2}$). The boundary values of b values are 1.0 and 0.5 which correspond to diffusion-controlled and pseudo-capacitive processes. In order to quantify the contributions to pseudo-capacitance and diffusion-controlled based on the Dunn method of differentiation, i vs V curves are plotted based on the equation: $i/v^{1/2} = k_1v^{1/2} + k_2$. This is an equation of a straight line y= mx +c, therefore k_1 and k_2 represent the slope and y-intercept respectively.

3.5.2. Galvanostatic charge-discharge (GCD)

This technique is used to assess a variety of electrochemical properties i.e. reversibility, stability, CE and rate performance. Firstly, the terminal voltage is determined which in most cases is the same as that used in the CV analysis. Charge and discharge plateaus are obtained which represent the anodic and cathodic peaks from the CV. This correlation is brought about by the electrode materials' thermodynamics. The GCD current is normalized to the area of electrodes (areal capacity) and mass of active materials

(gravimetric capacity). The gravimetric capacity (units: $mAhg^{-1}$) is mostly used. The current is standardized to the specific current (units: Ag^{-1}) or the C-rate current where 1C is the current needed in one hour for the battery to reach full capacity.

3.5.2.1. Coulombic efficiency (CE)

It assesses the battery materials' lifespan with respect to the charge sustainability and therefore its calculation is very essential and depends on the electrode materials. For cathode electrode materials (charge carrier donors), CE is the ratio of the quantity of charge carriers that are reinserted to those extracted (i.e. discharge-charge capacity ratio). For the anode materials (charge carrier acceptors), CE is the ratio of charge carriers that are re-extracted to those inserted (i.e. charge-discharge capacity ratio) [13].

3.5.2.2. Cycling analysis

By charging and discharging repeatedly, the cycle life is obtained. The lifespan is one of the most important parameters in batteries hence it is crucial to perform these tests. Long-term cycling analysis is usually performed at high-rate currents. This is because low-current cycling is very time-consuming.

3.5.2.3. Rate capability

It is determined by the adjustment of current in a suitable range. As the current rate rises, there is a reduction in capacity. This is as a result of an increase in polarization.

3.5.3. Electrochemical impedance spectroscopy (EIS)

It is a fast, non-invasive, and highly effective technique, that is widely used for the analysis of conductive materials. Impedance is the amount of opposition to the flow of current under an applied voltage influence. It assists in the efficiency, magnitude, and impact evaluation of different circuit elements. This technique enables the evaluation of mass transport behavior, kinetics, evaluating the diffusion coefficients and rate constants. The measurements usually differentiate between capacitance and resistance due to the fact that resistance of a system is independent to the frequency of the AC while capacitance inversely depends on it. Typical AC circuit elements represent the physical processes involved in the electrochemical reactions. The presence and magnitude of each of the elements provides particular information about the physicochemical behavior within the circuit. The circuit elements that are most common are capacitors and resistors whereby

they can be multiple of them in a circuit. The four most prevalent types of resistance include: R_{elec} (electronic resistance), R_s (solution resistance/ohmic resistance), R_{ion} (ionic resistance), and R_{CT} (charge transfer resistance). R_s represents the resistance between the reference and working electrode, while R_{ion} and R_{elec} are the opposition to the ionic and electronic movement respectively within the electrode's structure. Double layer capacitance is mostly represented by C_{dl} which gives the specific capacitance at the electrode-electrolyte interface.

3.5.3.1. Nyquist plots

It is one of the graphical representations of the EIS data. It is also referred to as an Argand diagram or complex plane plot and is mostly used due to its visibility and simplicity. It is represented by having the real part of impedance (Z_{Re} or Z') on the x-axis and the negative value of the imaginary impedance (Z_{Im} or Z'') on the y-axis. The negative value significance is to maintain the graph in the 1st quadrant of the Cartesian plane. The beginning of the plot is an area where diffusion is limited which is because the frequencies that are applied are high hence only charge-transfer processes remain. The R_s magnitude is given by the x-intercept. This is followed by a semicircle region which is a result of current passing through the C_{dl} and R_{CT} regions. The final part is the Warburg which has a 45° angle beyond the arc from the semi-circular region. However, deviations from the ideal case (45°) exist due to the non-ideal behavior of most systems.

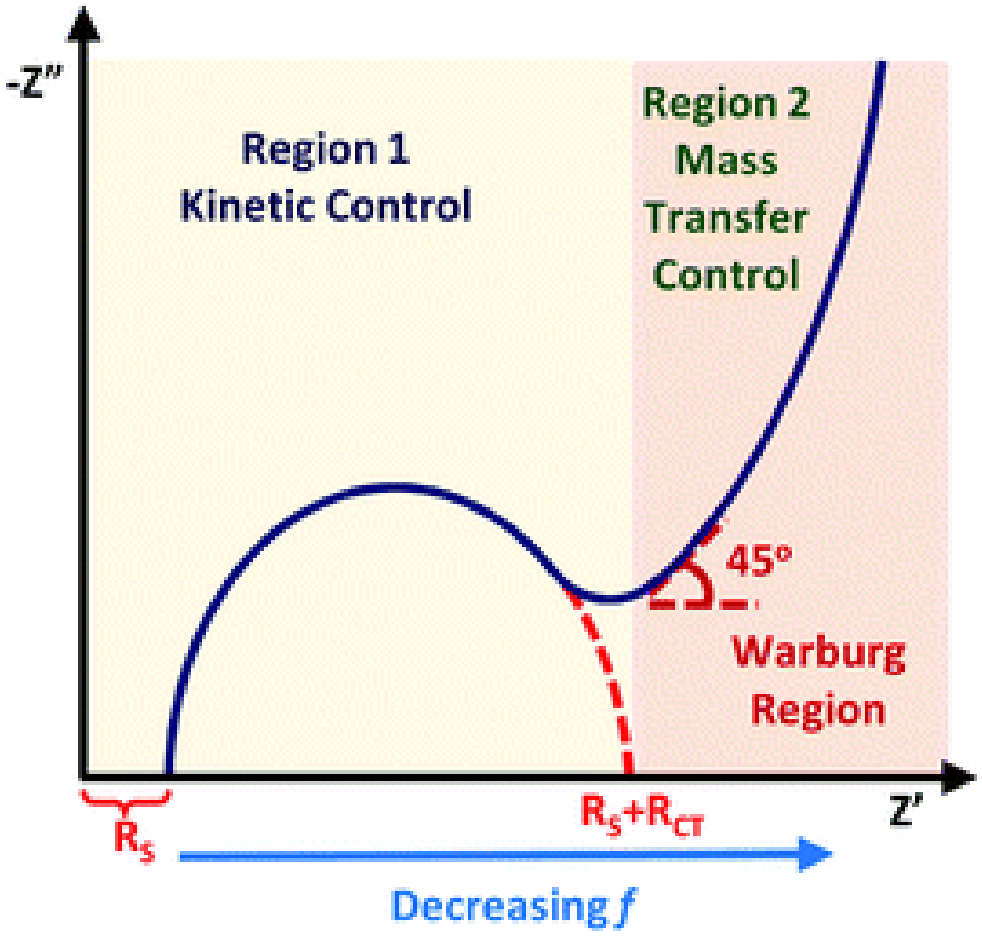

Figure 3.6: Characteristics of a Nyquist plot [14]

3.5.3.2. Randles plot

This plot is composed of Z' vs $\omega^{-1/2}$ where ω is the frequency and Z' represents the real impedance. The slope of the linear section of the low-frequency region represents the Warburg coefficient (σ). This is useful in the calculation of the diffusion coefficient.

3.5.3.3. Bode plot

It can be plotted in two forms whereby in both forms log frequency is plotted on the x-axis. Phase angle or log of the real Impedance are plotted on the y-axis which results in the Bode phase angle plot and Bode phase magnitude plot respectively [15]. Bode plots are used to study the properties of capacitors whereby (-90°) is the angle of an ideal capacitor. This angle represents the maximum shift that would occur between the current and the voltage. A phase angle of near -45° represents pseudo capacitance behavior.

The Bode phase magnitude plots that contain slopes near 0 and -1 represent resistive and capacitive materials respectively.

3.6. References

1. Pandey, A., et al., Structural characterization of polycrystalline thin films by X-ray diffraction techniques. Journal of Materials Science: Materials in Electronics, 2021. **32**: p. 1341-1368.
2. Bunaciu, A.A., E.G. UdriŞTioiu, and H.Y. Aboul-Enein, X-ray diffraction: instrumentation and applications. Critical reviews in analytical chemistry, 2015. **45**(4): p. 289-299.
3. Seyama, H., M. Soma, and B.K.G. Theng, Chapter 12.4 X-ray Photoelectron Spectroscopy, in Developments in Clay Science, F. Bergaya, B.K.G. Theng, and G. Lagaly, Editors. 2006, Elsevier. p. 865-878.
4. Fred A .Stevie, C.L.D., Introduction to X-ray photoelectron spectroscopy. Journal of Vacuum Science and Technology A, 2020. **A.38**.
5. Gurvinder Singh Bumbrah, R.M.S., Raman Spectroscopy-Basic principle, instrumentation and selected applications for the characterization of drugs of abuse. Egyptian Journal of Forensic Sciences, 2015.
6. Paul Rostron, S.G., Dina Gaber, Raman Spectroscopy, Review. International Journal of Engineering and Technical Research, 2016. **6**(1).
7. Andrea Orlando, F.F., A Comprehensive Review on Raman Spectroscopy Applications. Chemosensors, 2021.
8. Wang, L., et al., Applications of Raman Spectroscopy in Bacterial Infections: Principles, Advantages, and Shortcomings. Frontiers in Microbiology, 2021. **12**.
9. O.P Choudhary, P.C., Scanning Electron Microscope: Advantages and Disadvantages in Imaging Components. International Journal of Current Microbiology and Applied Sciences, 2017.
10. Azad Mohammed, A.A., Scanning Electron Microscopy: A review. Proceedings of 2018 International Conference of Hydraulics and Pneumatics, 2018.
11. Babita, R.T.a.A., Transmission Electron Microsopy- an Overview. International Research Journal for Inventions in Pharmaceutical Sciences, 2013.
12. Priyanka, O.P.C., Uses of Transmission Electron Microscope in Microscopy and its Advantages and Disadvantages. International Journal of Current Microbiology and Applied Sciences, 2018. **7**: p. 743-747.

13. Yang, X. and A.L. Rogach, Electrochemical Techniques in Battery Research: A Tutorial for Nonelectrochemists. Advanced Energy Materials, 2019. **9**(25): p. 1900747.
14. Laschuk, N.O., E.B. Easton, and O.V. Zenkina, Reducing the resistance for the use of electrochemical impedance spectroscopy analysis in materials chemistry. RSC advances, 2021. **11**(45): p. 27925-27936.
15. Nadia O. Laschuk, E.B.E., Olena V. Zenkina, Reducing the resistance for the use of electrochemical impedance spectroscopy analysis in materials chemistry. RSC Advances, 2021: p. 27925-27936.

Chapter 4

Investigating and comparing the performance of α-MnO_2 and β-MnO_2 in aqueous zinc-ion batteries

4.1. Introduction

Non-renewable energy consumption is responsible for multiple challenges whereby issues such as energy depletion and climate change are intense on a daily basis which is a serious threat to the survival of the human race and its development. Developing clean and sustainable energy sources is a necessity [1] [2]. Rechargeable batteries have become attractive because of their good stability, affordable nature, and because they are environmentally friendly. Among the various battery studies over the years, LIBs have been occupying the market niche because of their high energy density, good durability, and favorable power density [3]. However, it does have some challenges that limit its large-scale distribution such as its high assembly cost, hazardous organic electrolyte that is employed, and the limited resource distribution. This has led to a focus on aqueous rechargeable battery systems to solve some of the challenges.

Over the years, there has been increased development on rechargeable secondary batteries that include SIBs, MIBs, KIBs, AIBs, and ZIBs. KIBs and SIBs commercialization is hindered due to the employment of toxic and flammable electrolytes [4], whereas for MIBs, the magnesium ions are unable to intercalate/de-intercalate because of their high polarization effect [5]. For AIBs, they are corroded easily during the process of charging and discharging and an oxide film is formed on the surface that affects their performance. ZIBs are unique due to the high specific capacity of zinc (819 mAh/g), low electrochemical potential (-0.763 V relative to SHE), low cost and toxicity, and abundant metal resources. Among the components of ZIBs, the cathode material significantly affects their overall electrochemical performance. Hence the cathode material design has become a major topic with the majority of interest focused on manganese-based compounds with most attention towards manganese dioxide.

The usage of MnO_2 in plenty of applications for centuries is due to its attractive properties such as its high capacity and safety, affordability, and it is environmentally friendly. In the 19th century, it was used in the Daniel and Leclanche cells [6] and afterward, it was used in LIBs due to the ease in the intercalation and de-intercalation of Li^+ into the MnO_2 [7] [8]. There was improved electrochemical performance in the LIBs, such as (longer cycle life and high CE), and the cathode material is now being extensively applied in ZIBs. These batteries comprise of zinc as the anode and a cathode that allows intercalation and deintercalation of Zn^{2+} easily. During the insertion of Zn^{2+}, the spinel type $ZnMn_2O_4$ is formed. However, MnO_2 has a high reversibility hence MnO_2 phase is retained after complete charging.

α-MnO2 has gained a lot of attention due to its large tunnel structure (2x2) along its c-axis which is composed of four edge-sharing MnO_6 octahedral units. Nanostructures improve the zinc diffusion kinetics by shortening the diffusion pathway for transport of electrons and ions which is attributed to their high SA [9]. They also possess high electrode-electrolyte contact areas which is beneficial in the Zn^{2+} insertion and extraction. Controlling the morphology and the structure of materials at the nano size has attracted considerable attention. One-dimensional morphology such as nanowires and nanorods are studied in this research work because of their unique properties from the bulk state such as surface reactivity that is region-dependent, and anisotropic/isotropic behavior [10].

4.2. Results and discussion

Several synthetic routes have been reported to obtain the nanostructured MnO_2. These include facile controlled synthesis [11], homogeneous catalytic route [12], hydrothermal route [13], microwave-assisted synthesis [14], and solid-state reactions route [15]. In this study, hydrothermal and microwave methods are used to provide tunnel α-MnO_2 and layered β-MnO_2 electrodes with the main aim of developing fast, affordable, and simple ZIBs. The synthesis of α-MnO_2 and β-MnO_2 in 1D dimensions has been done so that there is ease and efficient transport of electrons since they are the smallest dimensions and hence may provide the opportunity to detect the theoretical operating limits of the AZIBs. Most 1D structures have been geared to LIBs as a result of the small ionic size of Li^+ hence it is of great interest to discover if they can be used for the insertion/de-insertion of

Zn^{2+}. The most exciting thing about the 1D nanostructures is their ability to address the space-confined transport phenomena and their related applications. In the prepared 1D nanostructures, the focus is mainly on the assembly of atoms or building blocks into structures with nm sizes but with larger lengths. In most reported literature, catalysts or templates have been used in growing nanostructures, whereby the purpose of the template has been confining the growth of wires while the catalysts function as favorable sites for the adsorption of reactant moleculars [16] [17] [18] [19] [20]. This introduction of catalysts or templates is a complicated process that involves an additional step of catalysts' preparation and the templates' selection can lead to an increase in the concentration of impurities in the final step. Studies have recently shown that it is possible to prepare 1D nanostructures even without the use of templates or catalysts under properly controlled conditions hence the process is thermodynamically preferable under certain conditions [21] [22] [23] [24]. In this study, a low-temperature method has been used. It involves the oxidation of Mn^{2+} by $[S_2O_8]^{2-}$.

The chemical reaction that occurs is:

$$MnSO_4+(NH_4)_2S_2O_8+2H_2O\rightarrow MnO_2+(NH_4)_2SO_4+2H_2SO_4 \quad \text{.....4.1}$$

This is a process that is brought about by two half-reactions;

$$Mn^{2+}+2H_2O\rightarrow MnO_2+4H^{+}+2e\ (E°=1.23\ V) \quad \text{.....4.2}$$

$$S_2O_8^{2-}+2e\rightarrow 2SO_4^{2-}(E°=2.01\ V) \quad \text{.....4.3}$$

$[NH_4]^+$ and $[SO_4]^{2-}$ play significant roles whereby $[NH_4]^+$ stabilizes the ions for the tunnel structures while an increase in the $[SO_4]^{2-}$ concentration decreases the Mn^{4+} formation rate. It can be concluded that since the entire process involves the growth of crystals, the concentration of reactants has multiple effects on the preparation of 1D crystal structures.

4.2.1. PXRD analysis

The crystal phases of α-MnO_2 and β-MnO_2 samples were determined as shown below. Figure 4.1 (A), shows that α-MnO_2 diffraction patterns portray tetragonal symmetry with (*I*4/*m*) space group and JCPDS No. 44-0141 [25]. The sample is of high purity since there is no evidence of other phases. The characteristic peaks located at 12.49°, 18.11°, 28.67°, 37.59°, 42.76°, 49.79°, 56.59°, 60.11° correspond to (110), (200), (310), (211, (301), (411), (600) and (521) α-MnO_2 crystal planes. In Figure 4.1 (B), β-MnO_2 shows main peaks at 28.6°, 37.3°, 42.7°,56.5°,59.2°,65.1°,67.4° which correspond to the (110),

(101), (111), (211), (220), (002) and (310) crystal planes with P4_2/mnm space group and JCPDS No. 24-0735 [26]. α-MnO_2 contains (2x2) tunnels that are useful in accommodating foreign cations. The ionic radius of Li^+ is (68pm), while that of Zn^{2+} is (74 pm) which makes them comparable hence since MnO_2 has successfully been used in LIBs, it is anticipated that it will be successful in intercalating Zn^{2+}.

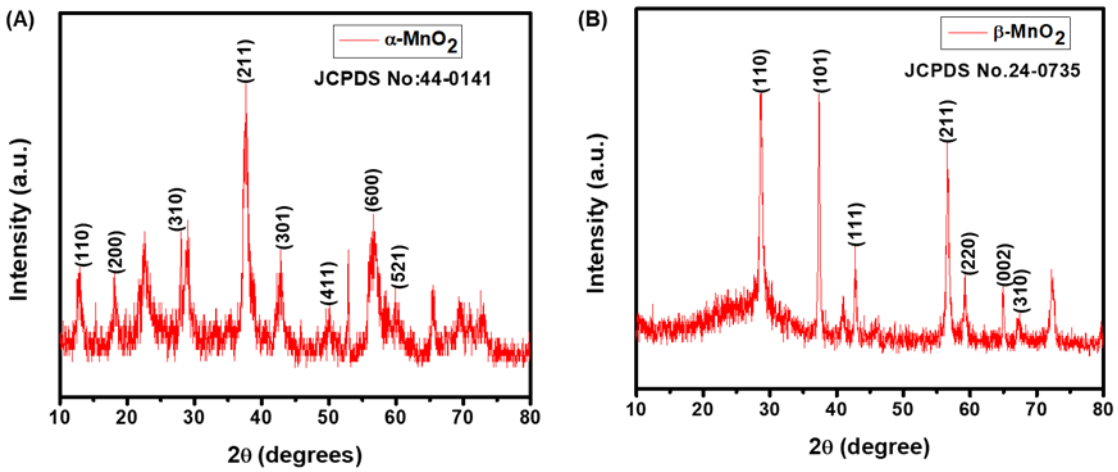

Figure 4.1: XRD pattern for **(A)** α-MnO_2 and **(B)** β-MnO_2

4.2.2. SEM analysis

SEM analysis determined the size distribution and morphology of both α-MnO_2 and β-MnO_2. Figure 4.2 (A) shows α-MnO_2 nanowires morphology while (B) shows β-MnO_2 nanorod morphology. The calculation of the average diameters was done using ImageJ software.

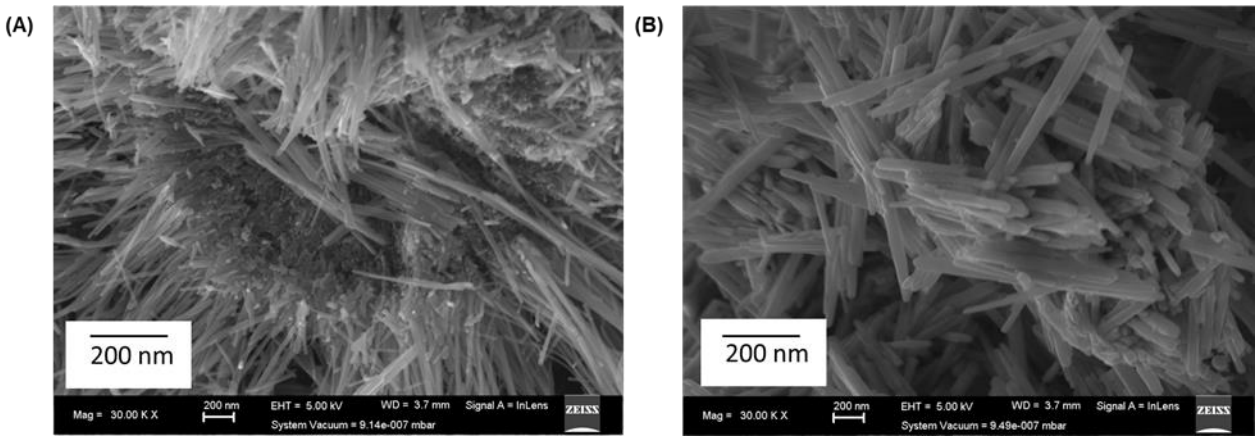

Figure 4.2: SEM plot of **(A)** α-MnO_2 and **(B)** β-MnO_2

Figure 4.3 shows the average diameters that were calculated from the SEM plots. The average diameter of α-MnO_2 was 34.487 nm while β-MnO_2 was 82.413 nm.

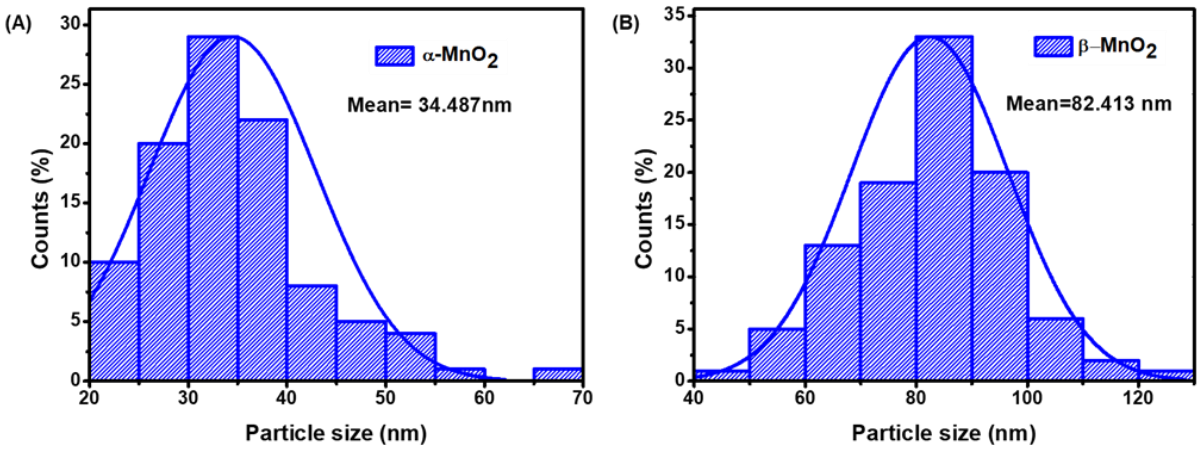

Figure 4.3: Particle size distribution of **(A)** α-MnO_2 and **(B)** β-MnO_2

4.2.3. EDS mapping

Elemental mapping by EDS in Figure 4.4 confirms the presence of manganese and oxygen elements. The elemental analysis confirmed that for β-MnO_2 the product MnO_2 is around 97.2% by mass with a small amount of sulfur (2.8%). The presence of a small amount of sulfur could be anticipated from $MnSO_4$ and $(NH_4)_2S_2O_8$ used in the synthesis.

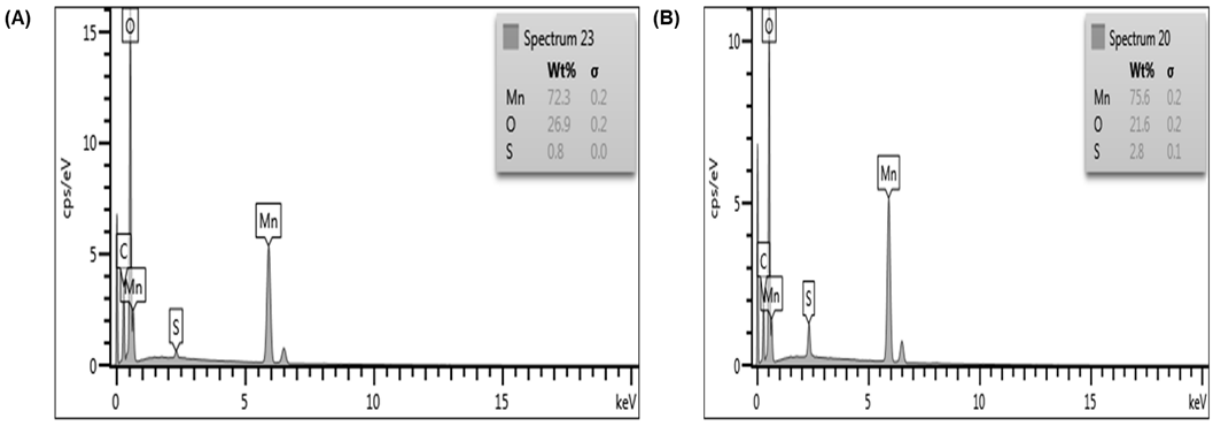

Figure 4.4: EDS mapping of **(A)** α-MnO_2 and **(B)** β-MnO_2

4.2.4. TGA analysis

TGA analysis was done to determine the weight losses that were a result of the deoxidization of MnO_2 in the presence of nitrogen gas. Figure 4.5 shows the results that were obtained. The transformations that occur when MnO_2 is heated in nitrogen are:

$MnO_2 \rightarrow Mn_2O_3 \rightarrow Mn_3O_4 \rightarrow MnO$ [27],[28].

Three main weight losses were observed during the calcination across the temperature range 35-900°C: Stage 1: 30°C -300°C, with a corresponding mass loss of 4.27% for α-MnO_2 and 1.59% for β-MnO_2. This is as a result of the loss of chemically and physically adsorbed water molecules. The amount of water lost by β-MnO_2 is lower because it has less water absorbability [29] due to its lower tunnel structure (1 × 1). Stage 2: 300°C-600°C is a result of MnO_2-Mn_2O_3 transformation. Stage 3: above 600°C is due to Mn_2O_3-Mn_3O_4 transformation. In Stages 2 and 3, the mass loss is as a result of gaseous oxygen that is released when MnO_2 goes through thermal decomposition [30].

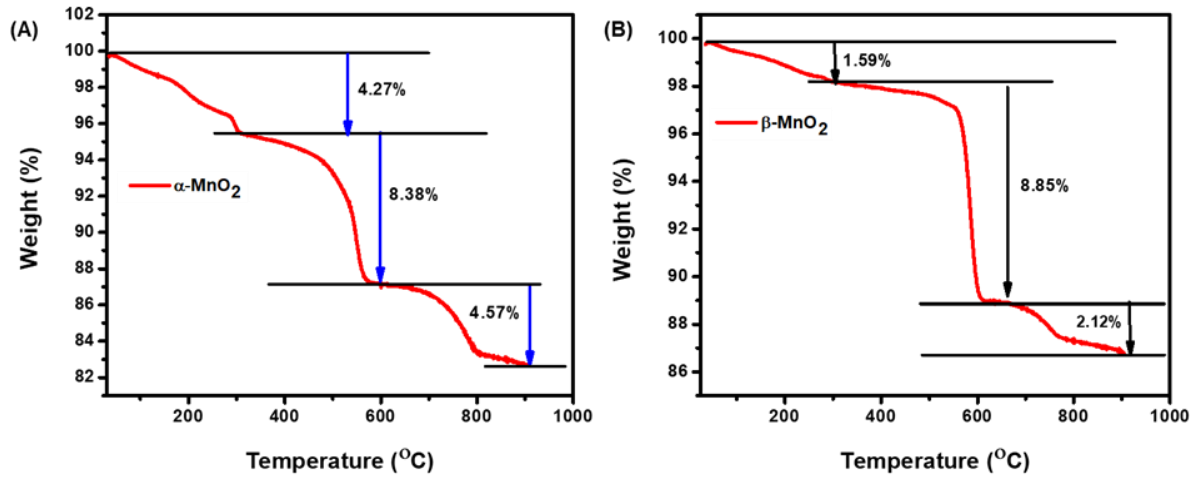

Figure 4.5: TGA analysis of **(A)** α-MnO_2 and **(B)** β-MnO_2

Figure 4.5 (A) shows that only 83% of α-MnO_2 while Figure 4.5 (B) shows that 87% of β-MnO_2 remained in the system. This confirms that β-MnO_2 had a better thermal resistance than α-MnO_2. Figure 4.6 shows the DTA curves of α-MnO_2 and β-MnO_2. Figure 4.6 (A) portrays that the decomposition of α-MnO_2 occurred at 548°C while Figure 4.6 (B) shows that the decomposition of β-MnO_2 occurred at 586°C. This shows that β-MnO_2 had a better thermal resistance than α-MnO_2. The 3 stages of weight loss described in the TGA results are also indicated the DTA graph.

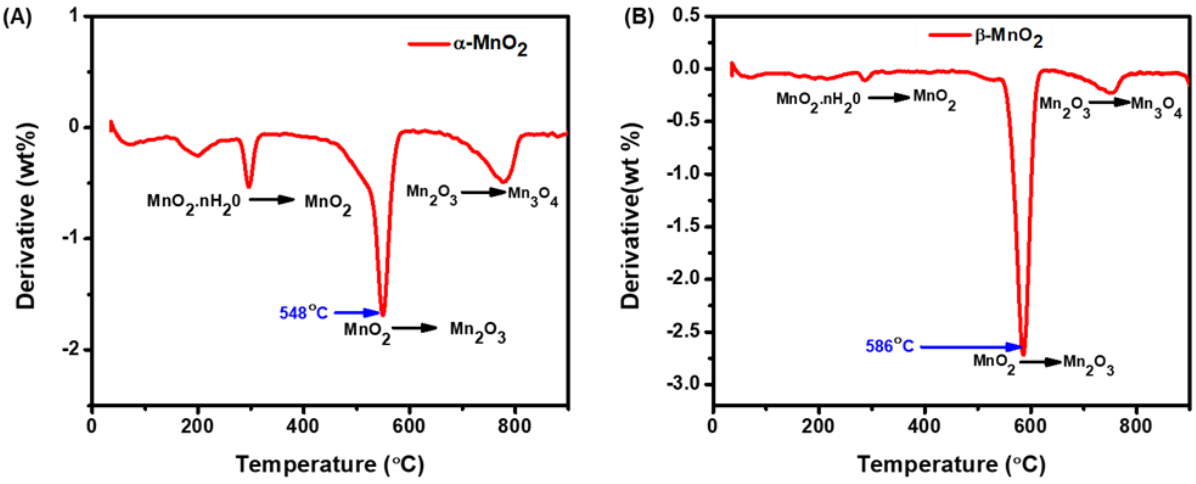

Figure 4.6: DTA curves of (**A**) α-MnO_2 and **(B)** β-MnO_2

4.3. Electrochemical measurements

4.3.1. CV analysis

CV analysis was performed at a sweep rate of 0.1 mVs^{-1} within the potential/voltage range of 1.0-1.8 (V vs Zn^{2+}/Zn) and the obtained comparison graph is shown in Figure 4.8. For both α-MnO_2 and β-MnO_2, there exists a reduction peak at 1.2 V that indicates stable Zn^{2+} insertion into the host structures. This corresponds to Mn^{4+} to Mn^{3+} reduction due to the insertion of Zn^{2+}. A higher potential range of around 1.59 V corresponds to Zn^{2+} extraction from both α-MnO_2 and β-MnO_2. According to the literature, the peak around 1.4 V and 1.6 V corresponds to the insertion/extraction of H^+ [31] which in this case corresponds to (1.39 V and 1.63 V) for β-MnO_2 and (1.40 V and 1.61 V) for α-MnO_2. β-MnO_2 showed a higher peak current response demonstrating a higher reaction activity than α-MnO_2.

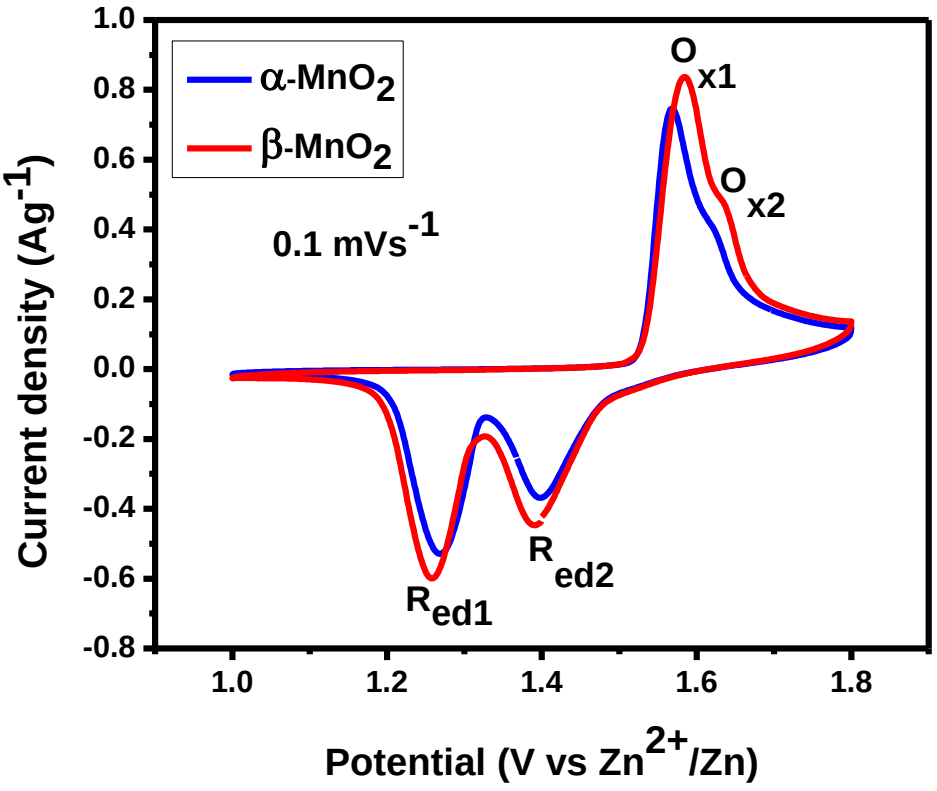

Figure 4.7: CV comparison plot of α-MnO_2 and β-MnO_2

Cyclic voltammetry curve shape (peak height and symmetry) is used to determine the reversibility of a reaction in a battery system. This is achieved by comparing the I_{pa}/ I_{pc} ratio, whereby if this value is unity, then the electrode materials are perfectly reversible [32]. Table 4.1 shows that the I_{pa}/ I_{pc} ratios are (1.73, 1.42) and (1.63, 1.50) for α-MnO_2 and β-MnO_2 respectively which shows the reversible intercalation/deintercalation of Zn^{2+}.

The extent of electron kinetics is described by the peak-to-peak separation potential (ΔE_p, V). The smaller the ΔE_p, the faster the reaction kinetics and vice versa. Table 4.1 shows that ΔE_p of α-MnO_2 (0.30 and 0.22) are much lower than that of β-MnO_2 (0.33 and 0.24), indicating that α-MnO_2 has higher diffusion kinetics corroborating Figure 4.7.

Table 4.1: CV parameters of α-MnO_2 and β-MnO_2

	α-MnO_2		**β-MnO_2**	
CV parameter	**O_{x1}, R_{ed1}**	**O_{x2}, R_{ed2}**	**O_{x1}, R_{ed1}**	**O_{x2} R_{ed2}**
E_{pa}, V	1.57	1.62	1.59	1.63
E_{pc}, V	1.27	1.40	1.26	1.39
$E^{1/2}$, V	1.42	1.51	1.43	1.51
ΔE_p, V	0.30	0.22	0.33	0.24
***I_{pa}*, mA**	0.71	0.37	0.80	0.45
***I_{pc}*, mA**	0.41	0.26	0.49	0.30
I_{pa}//I_{pc}	1.73	1.42	1.63	1.50

4.3.2. Storage kinetics of α-MnO_2 and β-MnO_2

The reaction kinetics and storage mechanism of CV are discussed in order to gain insight of the root of the electrochemical performance for both α-MnO_2 and β-MnO_2. Figure 4.8 displays the CV curves of α-MnO_2 and β-MnO_2 at different scan rates (0.1 mV/s to 1.0

mV/s). The CV curves maintain a similar shape with an increase in scan rates. This indicates that both α-MnO_2 and β-MnO_2 have excellent reversibility.

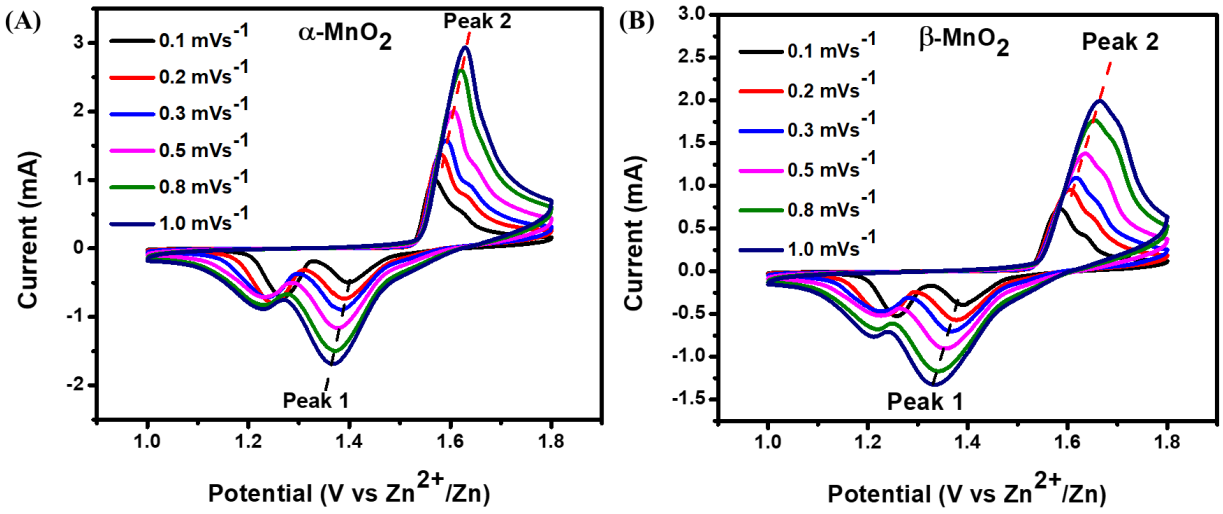

Figure 4.8: CV plot of **(A)** α-MnO_2 and **(B)** β-MnO_2

The Zn^{2+} diffusion behavior in the α-MnO_2 and β-MnO_2 is analyzed by the equation:

$$i=av^b \quad \text{.....(4.4)}$$

where i represents the current and v represents the scan rate, a and b are adjustable parameters. This equation can be rearranged to the form of equations in a straight line i.e.

$$\log i = b \log v + \log a \quad \text{.....(4.5)}$$

The b values of Peak 1 and 2 are (0.531, 0.463) and (0.523,0.435) for α-MnO_2 and β-MnO_2 respectively. When the value of b approaches 0.5, it indicates an ionic diffusion process while if it approaches 1, it represents a capacitive process [33]. The b values obtained from both α-MnO_2 and β-MnO_2 shows that the charge/discharge processes are controlled by both diffusion and capacitance contributions, with diffusion-controlled

processes being higher than the capacitance contributions.

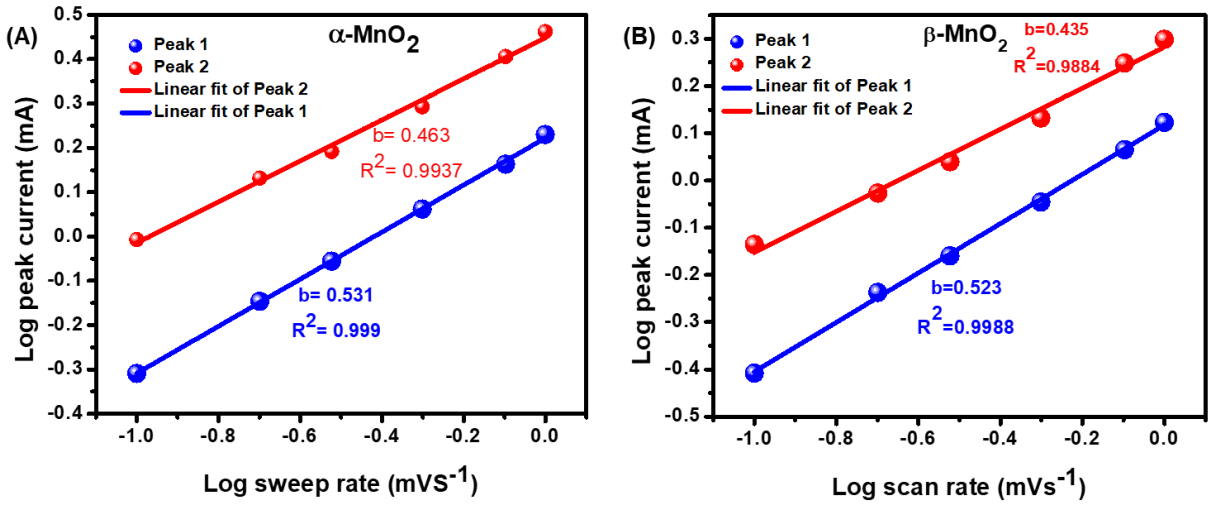

Figure 4.9: Log peak current vs log scan rate for **(A)** α-MnO_2 and **(B)** β-MnO_2

The current (i) is divided into capacitance (k_1V) and diffusion ($k_2V^{1/2}$) reactions according to the equation: $i=k_1v+ k_2v^{1/2}$ [31, 33, 34]. Dunn method of differentiation was done to determine the capacitive and diffusion process of β-MnO_2 since it had a higher current response in the CV analysis as shown in Figure 4.7. The calculated capacitive contribution for β-MnO_2 was 35.74% at 0.1 mV/s scan rate and is represented by the blue shaded area in Figure 4.10.

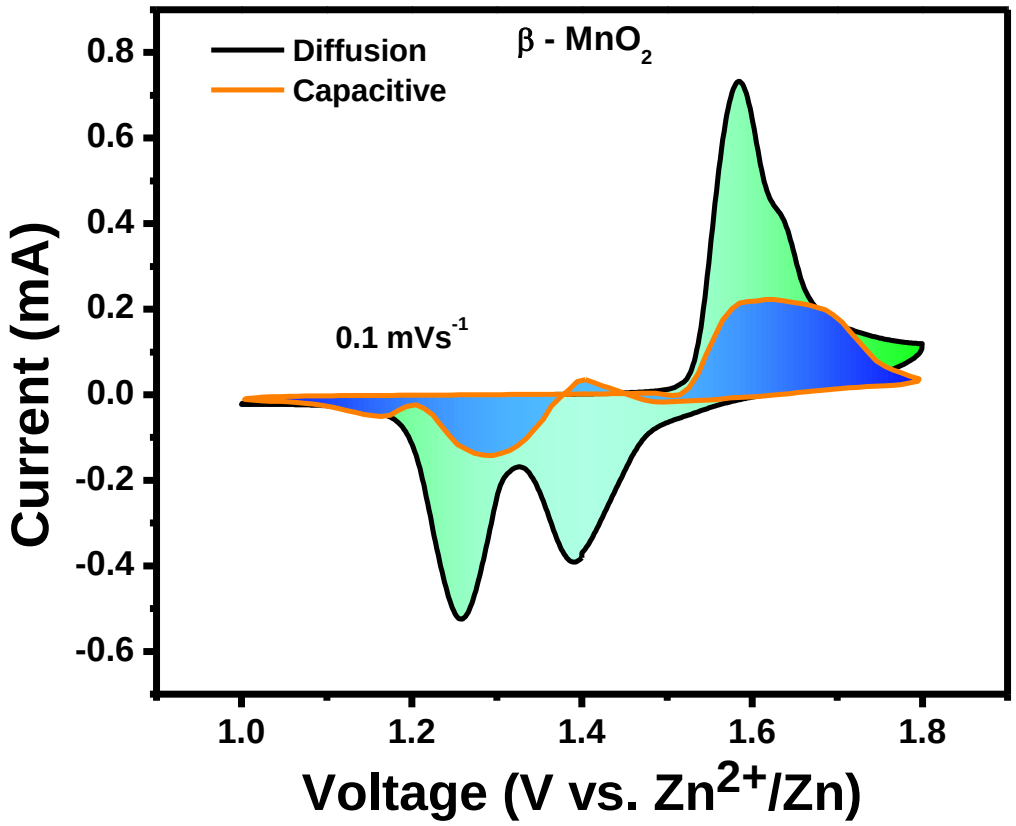

Figure 4.10: Diffusion and capacitive contribution of β-MnO_2

Due to the higher CV response of β-MnO_2 shown in Figure 4.7, we calculated the capacitive contributions. Figure 4.11 shows that these contributions were 35.74%, 48.63%, 59.90%, 75.40%, 90.08% and 97.91% at scan rates of 0.1-1.0 mVs^{-1}. This indicates that the capacitance contribution ratio increases when the scan rate increases, while diffusion-controlled process occupies the dominant role at low scan rates. This is because at higher san rates, the electrolyte only penetrates the surface of the material due to limited time, whereas at lower scan rates, the electrolyte is able to penetrate the bulk of the material.

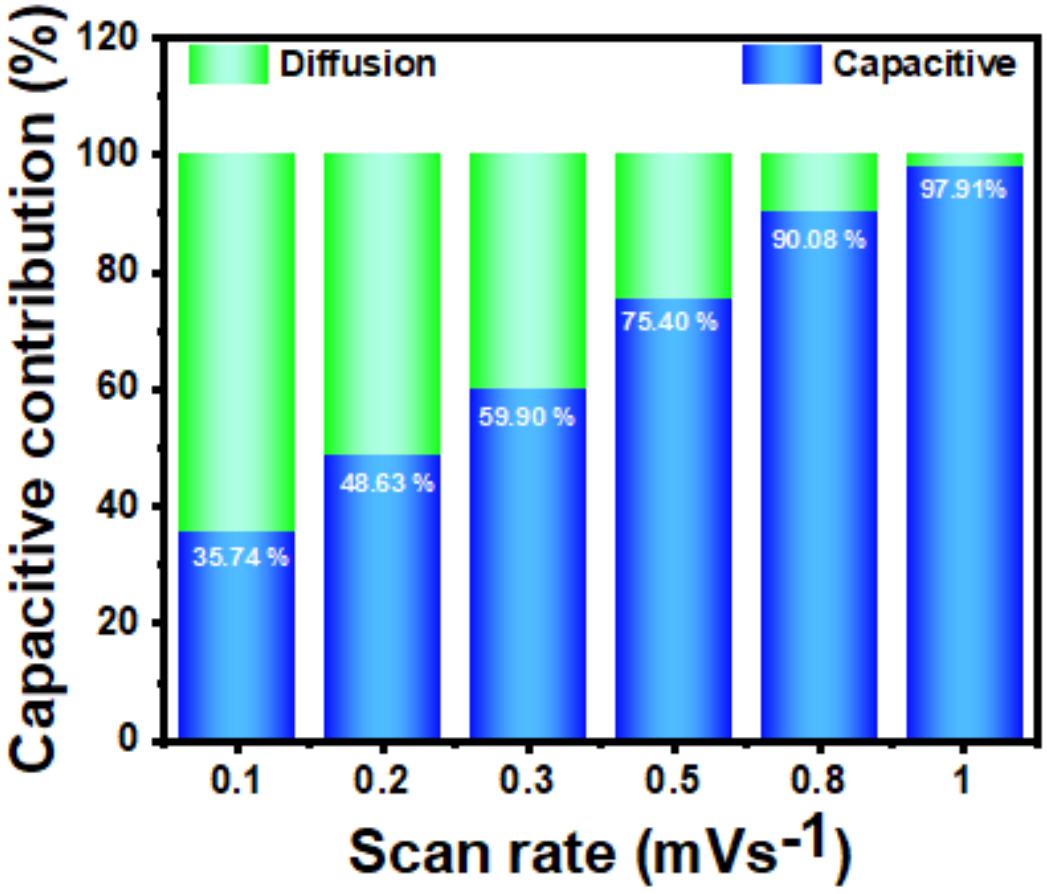

Figure 4.11: β-MnO_2 diffusion and capacitance contributions

Cyclic voltammetry curve shape (peak height and symmetry) is used to determine the reversibility of a reaction in a battery system. The reaction mechanism including redox processes and kinetic parameters are achieved from information on the cyclic voltammetry plots. The redox currents increase with the increase in scan rate. Randles Sevcik is used to calculate the ion diffusion coefficient based on the relationship between peak current and scan rate:

$$i_p = 2.69\times10^5 n^{3/2} A D_{Zn}^{1/2} C_{Zn} V^{1/2} \quad \text{.....(4.6)}$$

where i_p=represents peak current (A), A is the contact area between electrode and electrolyte (0.5 cm^2), C_{zn} is the concentration of zinc ions (3M), n is the number of transferred electrons per molecule (2), V is the scanning/sweep rate (Vs^{-1}), and D is the

ion diffusion. The ion diffusion cannot be calculated unless i_p and V are in a linear relationship which is represented in Figure 4.12.

This simplifies the equation further to:

$$ip/V^{1/2}\,(\text{slope}) = 2.69 \times 10^5 n^{3/2} A D_{Zn}^{1/2} C_{Zn} \quad \ldots\ldots(4.7)$$

This allows us to proceed in the determination of the ion diffusion coefficients. The diffusion coefficients for peak 1, 2 and 3 are ($2.3053e^{-12}$ cm^2s^{-1} and $2.7393e^{-12}$ cm^2s^{-1}) for α-MnO_2 and ($1.3999e^{-12}$ cm^2s^{-1} and $2.6118e^{-12}$ cm^2s^{-1}) for β-MnO_2. This proves that the diffusion kinetics for α-MnO_2 are higher than for β-MnO_2.

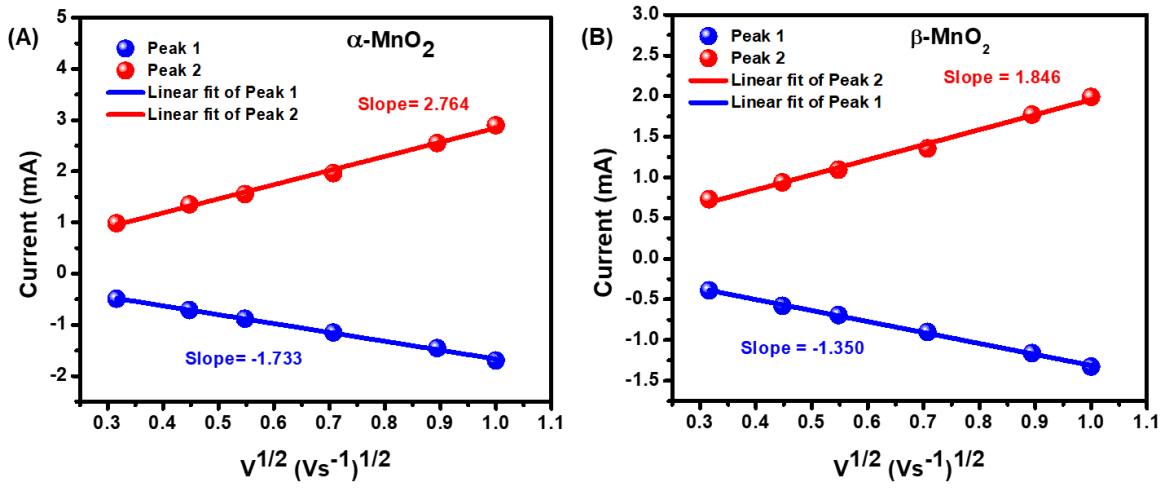

Figure 4.12: Peak current vs $V^{1/2}$ for **(A)** α-MnO_2 and **(B)** β-MnO_2

4.3.2. GCD analysis

Figure 4.13 compares the discharge and charge curves of both α-MnO_2 and β-MnO_2 in order to determine the insertion process of both MnO_2 electrodes at 0.1 Ag^{-1} current density. A turning point exists between the 1st and 2nd discharge plateaus that show that there is a change in the charge storage mechanism [25]. β-MnO_2 possesses a specific capacity of 297 $mAhg^{-1}$ with a capacity of the first plateau possessing 157.6 $mAhg^{-1}$ making up to 53.1 % of the total capacity while α-MnO_2 possess a specific capacity of 262 $mAhg^{-1}$ with a capacity of the first plateau possessing 137.6 $mAhg^{-1}$ which accounts for 52.5% of the overall capacity. The second plateaus show a capacity of 139.4 $mAhg^{-1}$

and 124.4 $mAhg^{-1}$ for β-MnO_2 and α-MnO_2 respectively which concludes that for both α-MnO_2 and β-MnO_2, the larger capacity originates from the first plateau. These results agree with CV data (Figure 4.7). H^+ inserts first into the MnO_2 structure which corresponds to the 1st plateau while Zn^{2+} ions insert later forming the 2nd plateau.

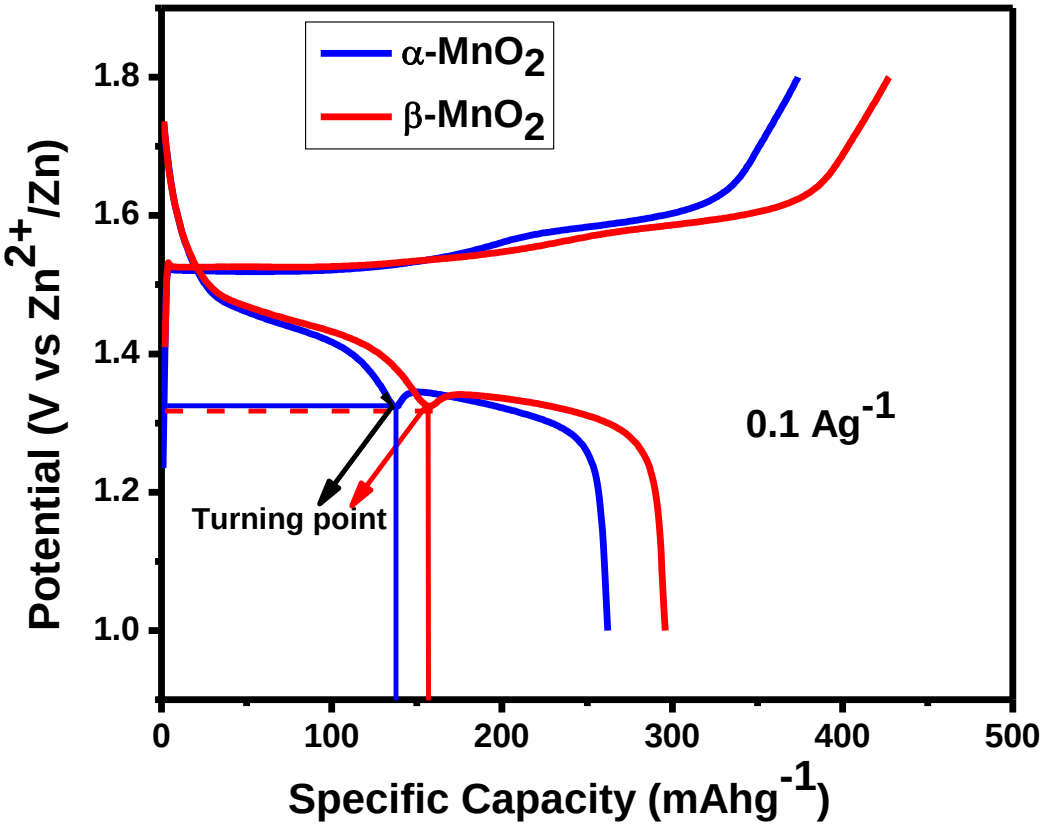

Figure 4.13: GCD Comparison plots

4.3.3. Cycling performance

In aqueous systems, cycling performance is affected by the deposition of dendrites on zinc plate, the irreversible surface passivation of zinc anode, and the dissolution and phase transformation of the MnO_2 cathode. These factors contribute to the capacity degradation [35]. Efforts have been made to avoid the formation of passivation layers and other irreversible reactions whereby in this study, we achieved this with the help of mild

acidic electrolyte. In this work, the capacity retention after 100 cycles is ~56% for β-MnO_2 and ~72% for α-MnO_2 which is quite a big difference. The stability in both cases is affected by corrosion and HER which are unavoidable especially because of the presence of aqueous electrolyte. The poor capacity retention, is a result of low intrinsic electronic conductivity and Jahn Teller distortion in the cathode which is caused by formation of unstable Mn^{3+} states during the insertion of Zn^{2+} [36].

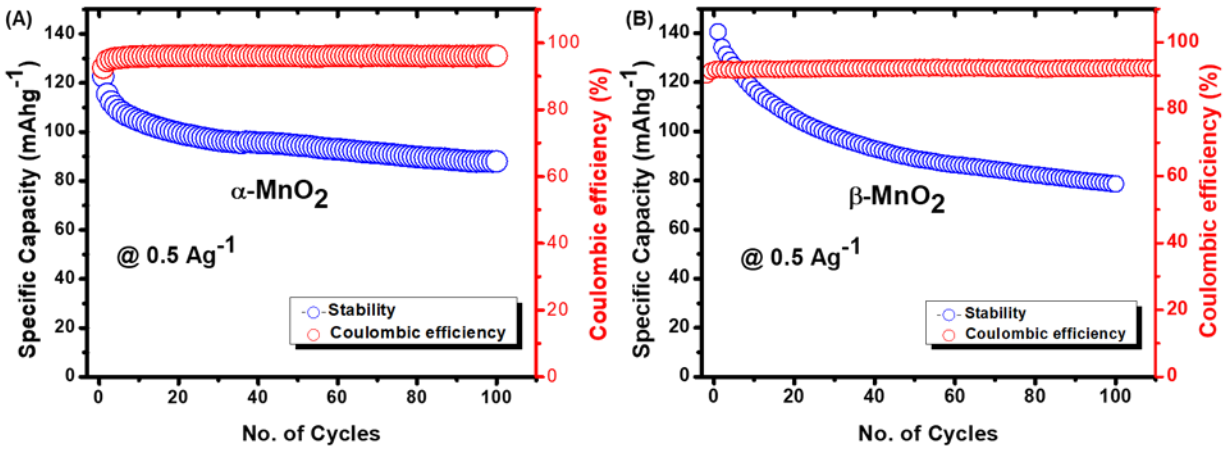

Figure 4.14: Cycling performance of **(A)** α-MnO_2 and **(B)** β-MnO_2

4.3.4. Rate capability studies

The rate performance of α-MnO_2 and β-MnO_2 was determined under different current densities as shown in Figure 4.15. The obtained discharge capacities were:

262.08mAhg^{-1}, 212.42mAhg^{-1}, 174.28mAhg^{-1}, 133.36mAhg^{-1}, 97.25mAhg^{-1}, 72.85mAhg^{-1} and 174.59mAhg^{-1} for α-MnO_2 and 295.81mAhg^{-1}, 229.37mAhg^{-1}, 182.10 mAhg^{-1}, 136.04mAhg^{-1}, 100.67mAhg^{-1}, 72.26mAhg^{-1}, and 190.38mAhg^{-1} for β-MnO_2 under different current densities as shown below. This shows a capacity retention of 66.62% of α-MnO_2 and 64.36% of β-MnO_2 which are quite comparable.

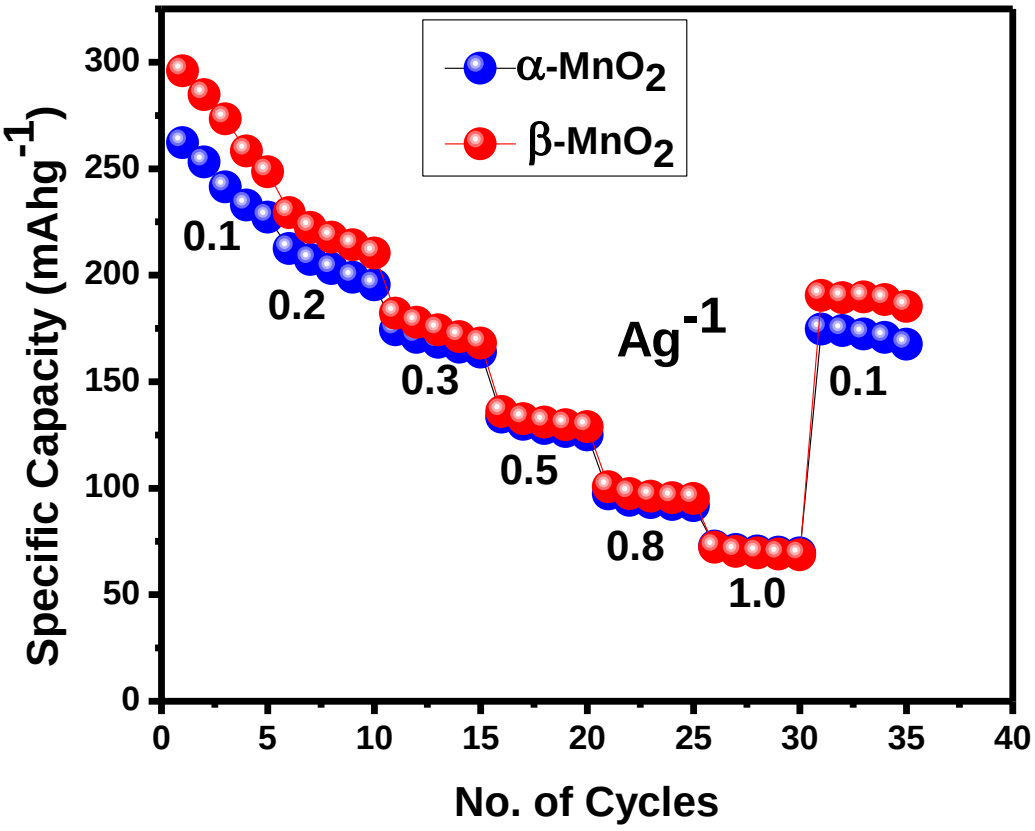

Figure 4.15: Rate capability comparison between α-MnO_2 and β-MnO_2

4.4.5. Electron impedance spectroscopy

EIS spectra was done in order to determine the diffusion kinetics of α-MnO_2 and β-MnO_2. The semi-circle in the high-mid frequency region was due to faradaic reactions and charge transfer resistance [37] whereby the small diameters of the semi-circles resulted in reduced charge transfer resistance. R_{CT} usually shows significant changes that are attributed to the Zn^{2+} insertion and extraction, whereby very large R_{CT} values indicate that the charge transferring process at that particular stage is quite difficult due to a large amount of zinc ions intercalated in the Zn-MnO_2 (there is full insertion of zinc ions). In relation, large diffusion resistance also implies full insertion of Zn^{2+} [38].

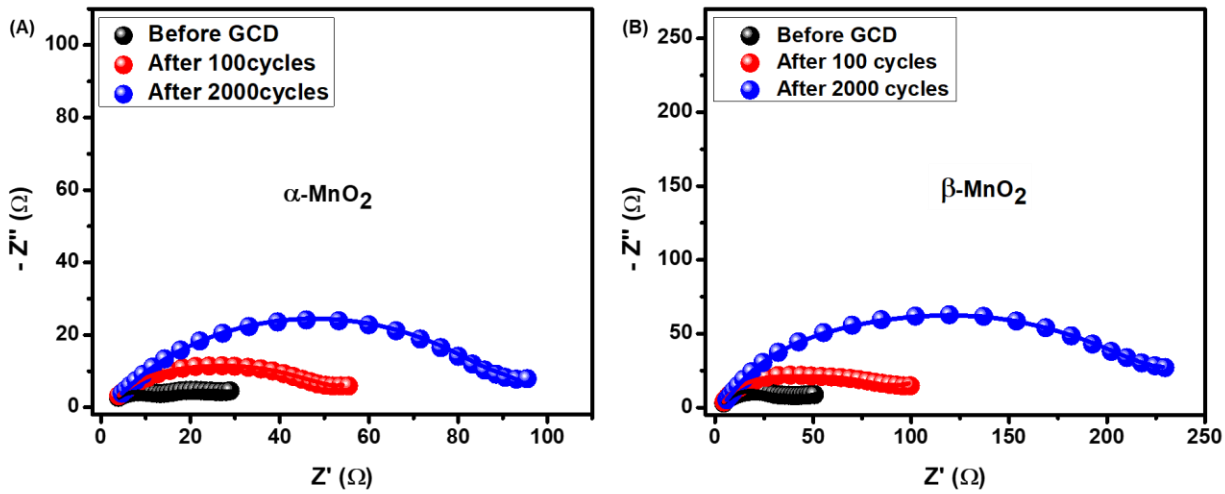

Figure 4.16: Nyquist plot before Galvanostatic charge-discharge (GCD), after 100 cycles and 2000 cycles for **(A)** α-MnO_2 and **(B)** β-MnO_2

Equivalent circuit that was used was:

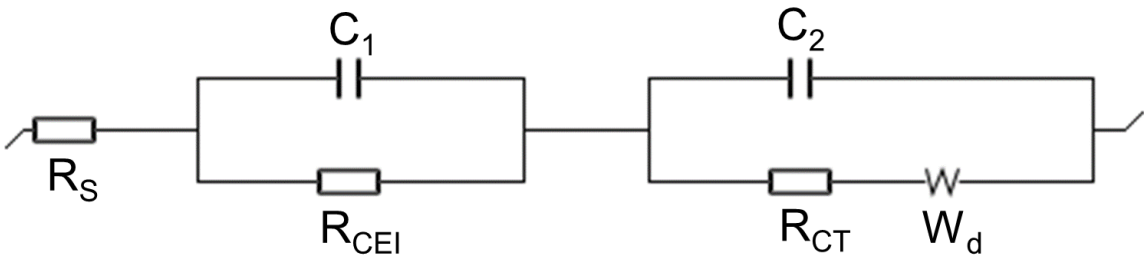

Figure 4.17: Circuit used in EIS fittings

Table 4.2: EIS fittings for α-MnO_2

Circuit Elements	Before GCD	After 100 cycles	After 2000 cycles
R_s (Ω)	3.36 ± 1.33	3.70 ± 0.93	4.57 ± 0.79
C_1 (μF)	(6.74 ± 3.10)	(7.13 ± 1.04)	(6.83 ± 0.03)
R_{CEI} (Ω)	8.76 ± 2.32	13.50 ± 4.90	16.39 ± 5.06
C_2 (mF)	(0.20 ± 0.17)	(0.054 ± 0.027)	(0.029 ± 0.0070)
R_{CT} (Ω)	8.89 ± 1.27	24.37 ± 4.29	53.48 ± 4.49
W_d ($\Omega s^{-1/2}$)	18.01 ±3.16	28.88 ± 2.74	42.75 ± 2.91

Table 4.3: EIS fittings of β-MnO_2

Circuit Elements	Before GCD	After 100 cycles	After 2000 cycles
R_s (Ω)	4.11 ± 0.96	4.46 ± 0.54	6.22 ± 0.33
C_1 (μF)	(7.43 ± 1.60)	(6.18 ± 0.46)	(5.55 ± 0.42)
R_{CEI} (Ω)	13.63 ± 7.87	24.89 ± 6.90	34.15 ± 5.63
C_2 (μF)	(46.10 ± 41.78)	(37.03 ± 14.19)	(17.00 ± 1.87)
R_{CT} (Ω)	18.5 ± 7.08	42.18 ± 6.07	132.40 ± 4.56
W_d ($\Omega s^{-1/2}$)	35.7 ± 2.48	64.32 ± 3.56	128.20 ± 3.69

R_s represents the solution resistance (identified by where the semi-circle begins) and originates from the electrolyte solution, CPE represents the constant phase element and is as a result of the inhomogeneous morphology of electrode surfaces, R_{CEI} represents the cathode electrolyte resistance (high-frequency resistance), and R_{CT} represents the charge transfer resistance and encompasses the contact resistance of current collector and active materials. R_{CT} is identified by where the semi-circle ends. α-MnO_2 portrays lower values of R_s (3.36, 3.70, 4.57) than β-MnO_2 (4.11, 4.46, 6.22) before GCD, 100 cycles, and 2000 cycles respectively.

The R_s mostly keeps the same level regardless of the states, hence this difference could be due to the deviation when fitting the EIS data. The values for R_{CT} for α-MnO_2 (8.89, 24.37, 53.48) are also lower than those of β-MnO_2 (18.50, 42.18,132.40) before GCD, 100 cycles, and 2000 cycles respectively. Even though α-MnO_2 has a large band gap, it has the least R_{CT} because its tunnel-shaped nanostructure is well organized [39]. In addition, the R_{CEI} values of α-MnO_2 (8.76, 13.50,16.39) are quite lower than those of β-MnO_2 (13.63, 24.89, 34.15) before GCD, 100 cycles, and 2000 cycles.

The bode plots in Figure 4.18, further prove the characteristics of constant phase elements since the values of the slopes are less than 1 while the R^2 is close to 1 which is a characteristic of batteries and not capacitors.

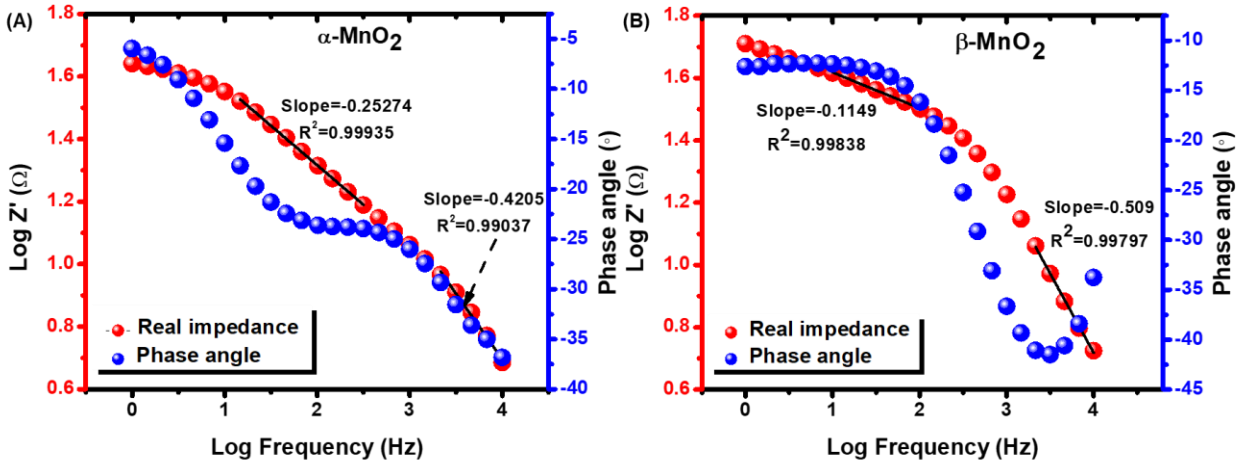

Figure 4.18: Bode plot for **(A)** α-MnO_2 and **(B)** β-MnO_2

Figure 4.19 shows the Randles plot that is used in the calculation of diffusion coefficient. This coefficient also referred to as the mass transfer parameter, is the amount of molar flux to pass through a surface. It follows Fick's second law of diffusion where the high values of diffusion coefficient indicate faster ion movement [40]. The formula used to calculate the diffusion coefficient is as follows:

$$D = R^2T^2/2A^2n^4F^4C^2\sigma^2 \quad \text{(4.8)}$$

where D is the diffusion coefficient, R is the gas constant (8.3145 Jmol/K), T is the absolute temperature (298 K), n is the number of electrons per molecule during oxidation, F is the Faraday's constant (96485 C/mol), A is the area of the cathode/electrolyte interface ($0.5cm^2$), C is the concentration of zinc ions (3M) while σ is the Warburg factor which has the relationship:

$$Z' = R_s+R_{CT}+\sigma\omega^{-1/2} \quad \text{(4.9)}$$

whereby σ was determined from the slope of the graph [41-43]. The calculated ion diffusion coefficients were $4.7493e^{-18}$ cm^2s^{-1} for α-MnO_2 and $5.3697e^{-18}$ cm^2s^{-1} for β-MnO_2 respectively in BoL.

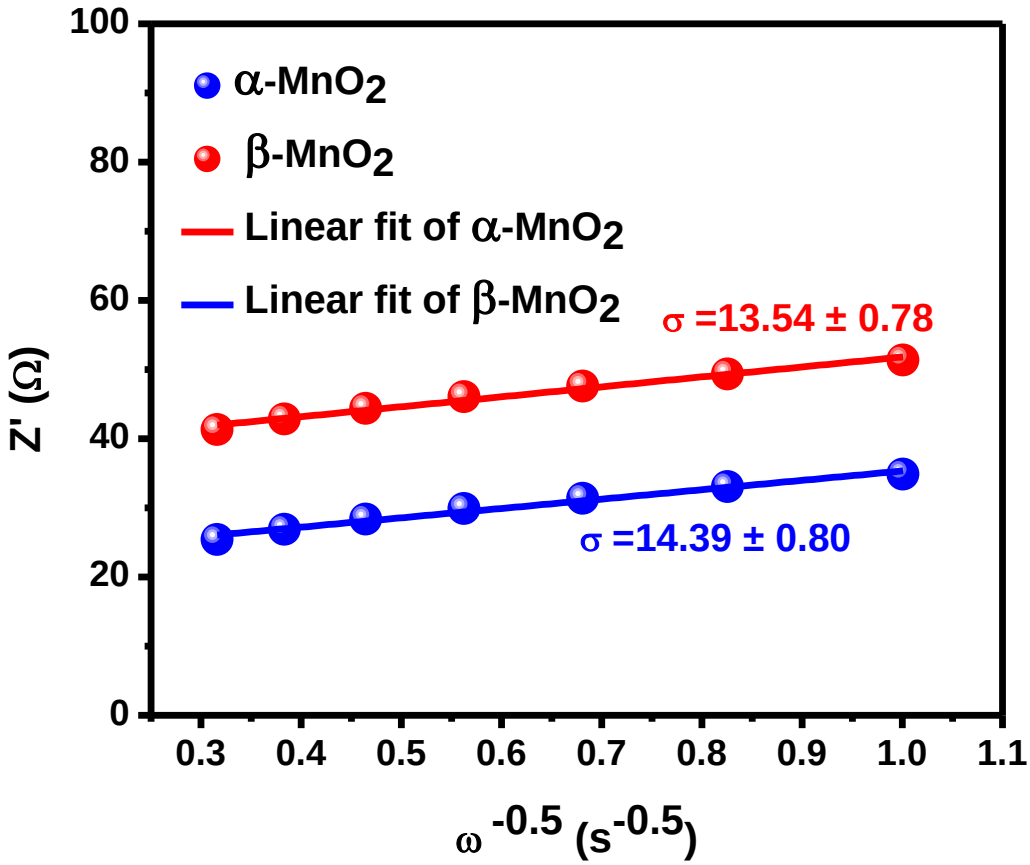

Figure 4.19: Randles plot comparison at the BoL

However, after 100 cycles the diffusion coefficients were $5.6868e^{-19}$ cm^2s^{-1} for α-MnO_2 and $3.1744e^{-19}$ cm^2s^{-1} for β-MnO_2, which further reduced to $3.0639e^{-19}$ cm^2s^{-1} and $4.3450e^{-20}$ cm^2s^{-1} for α-MnO_2 and β-MnO_2 respectively after 2000 cycles. This increase in diffusion coefficient upon cycling can be attributed to the activation process. α-MnO_2 portrays a larger diffusion coefficient than β-MnO_2 because of its larger tunnel size (4.6x4.6) allowing the ease in the diffusion of zinc ion [44]. However, even with a lower tunnel size of (2.3x2.3) β-MnO_2 still portrays a high capacity which can be based on the mode of preparation. The microwave synthesis in β-MnO_2 has been known to reduce Jan Teller distortion hence improving the overall performance of β-MnO_2.

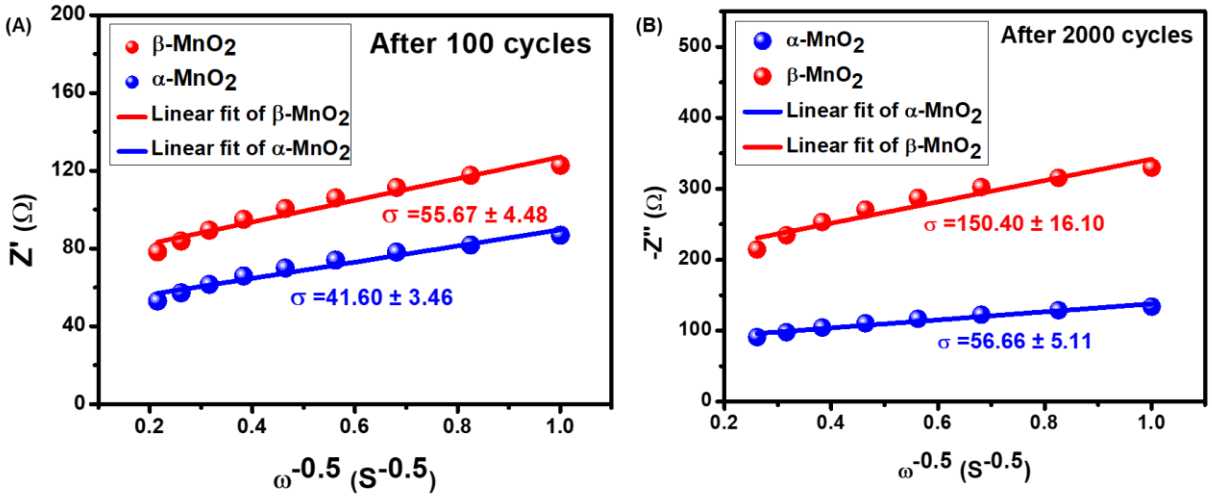

Figure 4.20: Randles plot comparison plot after **(A)** 100 cycles and **(B)** 2000 cycles

According to literature sources, the addition of additives has the benefits of: enabling uniform and fast charge transfer, facilitating the desolvation of zinc ions, reducing the chemical activity of the free water molecules and suppressing the parasitic reactions that are induced by them, enabling uniform zinc plating and stripping without the formation of dendrites, broadening the stability electrochemical window, and improving the stability of electrolytes at low and high temperatures [45] [46] [47] [48] [49]. For this research work we added the Mn^{2+} cation in the electrolyte in order to investigate any improved performance in α-MnO_2. Figure 4.22 shows that the addition of Mn^{2+} additive to α-MnO_2 improves the charge transfer kinetics (consistent with previous observation of CV and EIS data above). This is because Mn^{2+} augments the type and number of the ions that are conductive [46].

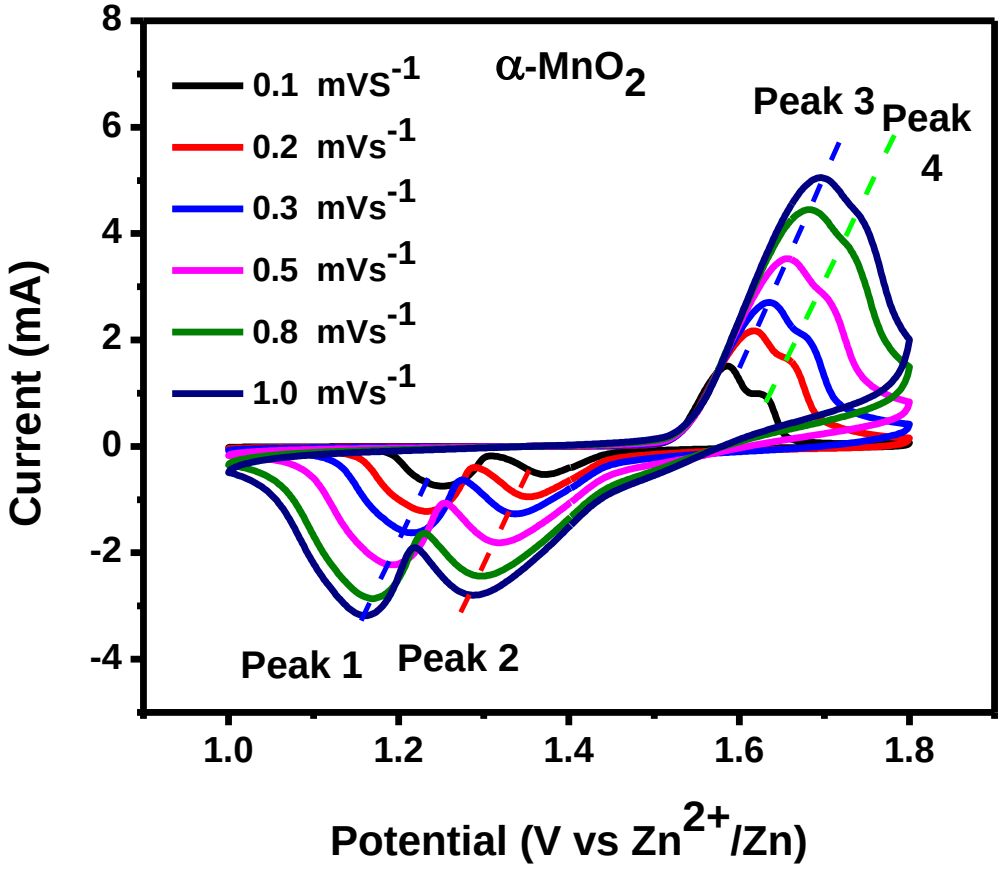

Figure 4.21: CV curve of α-MnO_2 after addition of additive

Rate capability was done under different current densities. The discharge capacities were 402.04 $mAhg^{-1}$, 403.63 $mAhg^{-1}$, 367.04 $mAhg^{-1}$, 327.77 $mAhg^{-1}$, and 381.10 $mAhg^{-1}$ at different current densities as shown in Figure 4.22. The capacity retention was 95% which represents excellent performance brought about by the addition of Mn^{2+} in the electrolyte.

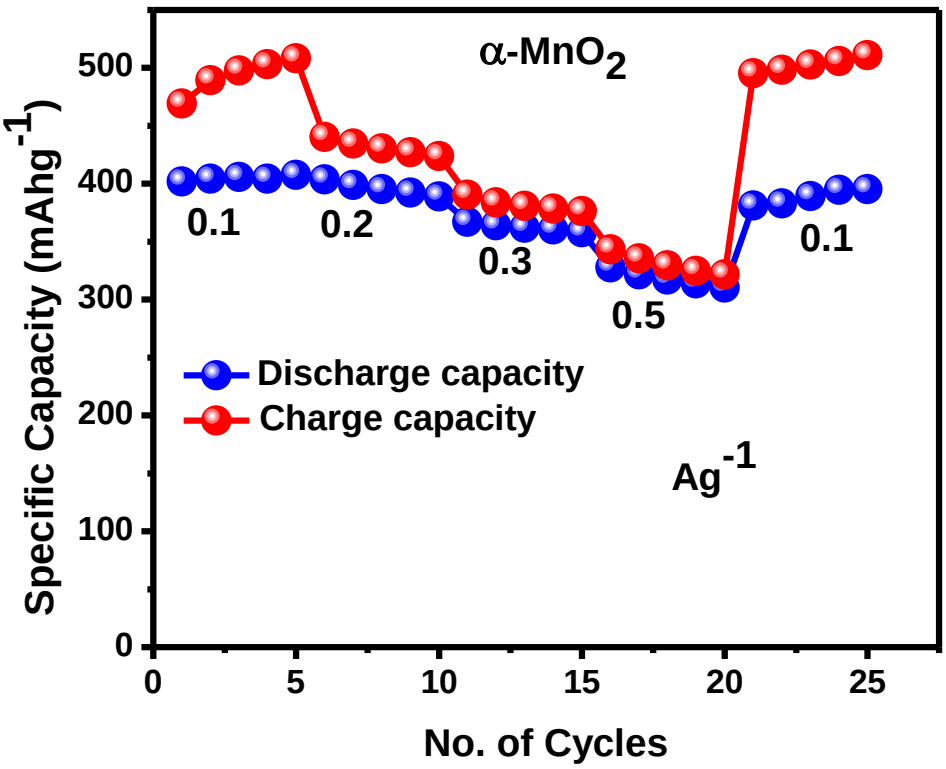

Figure 4.22: Rate capability of α-MnO_2 with additive

In Figure 4.23, the difference of region (1.6-1.8 V) of α-MnO_2 with and without additive is clearly shown. From this figure, the slope region of α-MnO_2 with additive is larger than of α-MnO_2 without additive and this difference is the reason behind its high capacity and improved electrochemical performance [50].

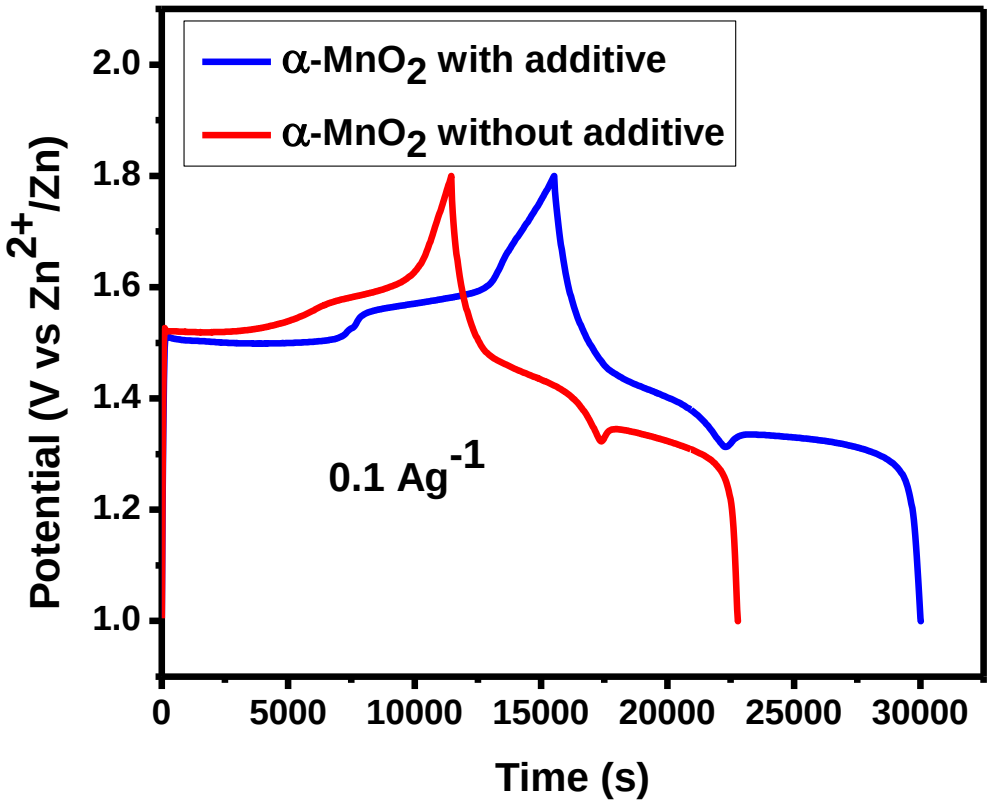

Figure 4.23: Charge-discharge graph comparison

4.4. Summary

In conclusion, XRD results showed successful synthesis of α-MnO_2 and β-MnO_2 which both portrayed tetragonal symmetry corresponding to JCPDS No. 44-0141 for α-MnO_2 and JCPDS No. 24-0735 for β-MnO_2. SEM analysis showed α-MnO_2 had thinner longer nanowires while β-MnO_2 had shorter and bigger nanorod morphology. Electrochemistry results show that α-MnO_2 is kinetically more favoured but energetically (thermodynamically) less favoured while the reverse applies for β-MnO_2. α-MnO_2 also shows a higher capacity retention of ~72% than β-MnO_2 which showed ~56% capacity retention.

4.5. References

1. Amin, M., et al., Hydrogen production through renewable and non-renewable energy processes and their impact on climate change. International Journal of Hydrogen Energy, 2022. **47**(77): p. 33112-33134.
2. Owusu, P.A. and S. Asumadu-Sarkodie, A review of renewable energy sources, sustainability issues and climate change mitigation. Cogent Engineering, 2016. **3**(1): p. 1167990.
3. Diouf, B. and R. Pode, Potential of lithium-ion batteries in renewable energy. Renewable Energy, 2015. **76**: p. 375-380.
4. Vignarooban, K., et al., Current trends and future challenges of electrolytes for sodium-ion batteries. International Journal of Hydrogen Energy, 2016. **41**(4): p. 2829-2846.
5. Medina, A., C. Pérez-Vicente, and R. Alcántara, Advancing towards a Practical Magnesium Ion Battery. Materials, 2021. **14**(23): p. 7488.
6. Ghosh, S. and J.P. Brenet, Study of the mechanism of cathodic reduction of gamma manganese dioxide in the leclanche cell system. Electrochimica Acta, 1962. **7**(4): p. 449-455.
7. Chen, J., et al., Electrochemical properties of MnO2 nanorods as anode materials for lithium ion batteries. Electrochimica Acta, 2014. **142**: p. 152-156.
8. Thackeray, M., et al., The versatility of MnO2 for lithium battery applications. Journal of power sources, 1993. **43**(1-3): p. 289-300.
9. Ling, W., et al., Nanostructure design strategies for aqueous zinc-ion batteries. ChemElectroChem, 2020. **7**(14): p. 2957-2978.
10. Wang, X. and Y. Li, Synthesis and formation mechanism of manganese dioxide nanowires/nanorods. Chemistry–A European Journal, 2003. **9**(1): p. 300-306.
11. Cheng, F., et al., Facile controlled synthesis of MnO2 nanostructures of novel shapes and their application in batteries. Inorganic chemistry, 2006. **45**(5): p. 2038-2044.

12. Li, Z., et al., Rational growth of various α-MnO2 hierarchical structures and β-MnO2 nanorods via a homogeneous catalytic route. Crystal growth & design, 2005. **5**(5): p. 1953-1958.
13. Pang, S.C., S.F. Chin, and C.Y. Ling, Controlled synthesis of manganese dioxide nanostructures via a facile hydrothermal route. Journal of Nanomaterials, 2012. **2012**: p. 2-2.
14. Davoglio, R.A., et al., Synthesis and characterization of α-MnO2 nanoneedles for electrochemical supercapacitors. Electrochimica Acta, 2018. **261**: p. 428-435.
15. Qingwen, L., W. Yiming, and L. Guoan, pH-response of nanosized MnO2 prepared with solid state reaction route at room temperature. Sensors and Actuators B: Chemical, 1999. **59**(1): p. 42-47.
16. Fan, Z. and H. Zhang, Template synthesis of noble metal nanocrystals with unusual crystal structures and their catalytic applications. Accounts of chemical research, 2016. **49**(12): p. 2841-2850.
17. Huang, Y., et al., Growth of au nanoparticles on 2D metalloporphyrinic metal-organic framework nanosheets used as biomimetic catalysts for cascade reactions. Advanced Materials, 2017. **29**(32): p. 1700102.
18. Sierra-Sastre, Y., et al., Vertical growth of Ge nanowires from biotemplated Au nanoparticle catalysts. Journal of the American Chemical Society, 2008. **130**(32): p. 10488-10489.
19. Ding, J.H. and D.L. Gin, Catalytic Pd nanoparticles synthesized using a lyotropic liquid crystal polymer template. Chemistry of materials, 2000. **12**(1): p. 22-24.
20. Bigall, N.C., et al., Fungal templates for noble-metal nanoparticles and their application in catalysis. Angew. Chem. Int. Ed, 2008. **47**(41): p. 7876-9.
21. Wang, X. and Y. Li, Selected-Control Hydrothermal Synthesis of α- and β-MnO2 Single Crystal Nanowires. Journal of the American Chemical Society, 2002. **124**(12): p. 2880-2881.
22. Li, Y.D., et al., Artificial Lamellar Mesostructures to WS2 Nanotubes. Journal of the American Chemical Society, 2002. **124**(7): p. 1411-1416.
23. Li, Y., et al., Bismuth Nanotubes: A Rational Low-Temperature Synthetic Route. Journal of the American Chemical Society, 2001. **123**(40): p. 9904-9905.

24. Li, Y., et al., From Surfactant–Inorganic Mesostructures to Tungsten Nanowires. Angewandte Chemie International Edition, 2002. **41**(2): p. 333-335.
25. Gao, X., et al., H+-Insertion Boosted α-MnO2 for an Aqueous Zn-Ion Battery. Small, 2020. **16**(5): p. 1905842.
26. Han, M., et al., Oxygen defects in β-MnO2 enabling high-performance rechargeable aqueous zinc/manganese dioxide battery. Iscience, 2020. **23**(1).
27. Zhao, B., et al., Phase structures, morphologies, and NO catalytic oxidation activities of single-phase MnO2 catalysts. Applied Catalysis A: General, 2016. **514**: p. 24-34.
28. Stobbe, E.R., B.A. de Boer, and J.W. Geus, The reduction and oxidation behaviour of manganese oxides. Catalysis Today, 1999. **47**(1): p. 161-167.
29. Cetinkaya, T., et al., A parametric study on the rapid synthesis of one dimensional (1D) α-MnO2 nanowires. Microelectronic Engineering, 2014. **126**: p. 54-59.
30. Song, J., et al., Thermal decomposition behavior and computational analysis of alpha and beta manganese dioxide nanorods. Journal of Alloys and Compounds, 2023. **962**: p. 171208.
31. Jing, F., et al., High-performance reversible aqueous Zinc-Ion battery based on Zn2+ pre-intercalation alpha-manganese dioxide nanowires/carbon nanotubes. Journal of Colloid and Interface Science, 2022. **609**: p. 557-565.
32. Ehirim, T.J., et al., Onion-like Carbons Provide a Favorable Electrocatalytic Platform for the Sensitive Detection of Tramadol Drug. ACS Omega, 2022. **7**(51): p. 47892-47905.
33. Bi, S., et al., Free-standing three-dimensional carbon nanotubes/amorphous MnO2 cathodes for aqueous zinc-ion batteries with superior rate performance. Materials Today Energy, 2020. **18**: p. 100548.
34. Zhao, Y., et al., Uncovering sulfur doping effect in MnO2 nanosheets as an efficient cathode for aqueous zinc ion battery. Energy Storage Materials, 2022. **47**: p. 424-433.
35. Corpuz, R.D., et al., Binder-Free α-MnO2 Nanowires on Carbon Cloth as Cathode Material for Zinc-Ion Batteries. International Journal of Molecular Sciences, 2020. **21**(9): p. 3113.

36. Alfaruqi, M.H., et al., A high surface area tunnel-type α-MnO2 nanorod cathode by a simple solvent-free synthesis for rechargeable aqueous zinc-ion batteries. Chemical Physics Letters, 2016. **650**: p. 64-68.
37. Xin, S., et al., β-MnO2/three-dimensional graphene-carbon nanotube hybrids as cathode for aqueous zinc-ion battery. Journal of Alloys and Compounds, 2023. **968**: p. 172115.
38. Zhang, Y., et al., Aqueous Zn-MnO2 battery: Approaching the energy storage limit with deep Zn2+ pre-intercalation and revealing the ions insertion/extraction mechanisms. Journal of Energy Chemistry, 2022. **67**: p. 225-232.
39. Devi, R., et al., Electrochemical Analysis of MnO2 (α, β, and γ)-Based Electrode for High-Performance Supercapacitor Application. Applied Sciences, 2023. **13**(13): p. 7907.
40. Laschuk, N.O., E.B. Easton, and O.V. Zenkina, Reducing the resistance for the use of electrochemical impedance spectroscopy analysis in materials chemistry. RSC Advances, 2021. **11**(45): p. 27925-27936.
41. Tan, Y., et al., Reaction kinetics in rechargeable zinc-ion batteries. Journal of Power Sources, 2021. **492**: p. 229655.
42. Rui, X.H., et al., Determination of the chemical diffusion coefficient of Li+ in intercalation-type Li3V2(PO4)3 anode material. Solid State Ionics, 2011. **187**(1): p. 58-63.
43. Khamsanga, S., et al., δ-MnO2 nanoflower/graphite cathode for rechargeable aqueous zinc ion batteries. Scientific Reports, 2019. **9**(1): p. 8441.
44. Guo, C., et al., A case study of β- and δ-MnO2 with different crystallographic forms on ion-storage in rechargeable aqueous zinc ion battery. Electrochimica Acta, 2019. **324**: p. 134867.
45. Zheng, Z., et al., Electrolyte additives toward practical aqueous zinc-ion batteries: recent advances and future challenges. Next Energy, 2023. **1**(4): p. 100073.
46. Guo, S., et al., Fundamentals and perspectives of electrolyte additives for aqueous zinc-ion batteries. Energy Storage Materials, 2021. **34**: p. 545-562.
47. Du, Y., et al., Electrolyte salts and additives regulation enables high performance aqueous zinc ion batteries: a mini review. Small, 2022. **18**(43): p. 2104640.

48. Ji, H., et al., Stabilizing zinc anode for high-performance aqueous zinc ion batteries via employing a novel inositol additive. Journal of Alloys and Compounds, 2022. **914**: p. 165231.
49. Liu, Z., et al., A dual-functional organic electrolyte additive with regulating suitable overpotential for building highly reversible aqueous zinc ion batteries. Advanced Functional Materials, 2024. **34**(5): p. 2214538.
50. Chen, H., et al., Successive electrochemical conversion reaction to understand the performance of aqueous Zn/MnO2 batteries with Mn2+ additive. Materials Today Energy, 2021. **20**: p. 100646.

Chapter 5

Pechini-assisted Synthesis of High-Entropy Spinel Nanoparticles for Rechargeable Aqueous Zinc-ion batteries

Abstract

Here, a novel material composed of a high-entropy spinel oxide $(CoCuMnFeNi)_3O_4$ is proposed as a cathode material for aqueous rechargeable zinc-ion batteries (ZIBs). This cathode material portrays an excellent charge/discharge capacity with an initial capacity of 143.7A/g and a coulombic efficiency of 84.14% which is higher than some of the reported cathode materials. This superior electrochemical performance can be ascribed to the synergistic effects of the five metal elements in the spinel, the entropy stabilization effect, and the presence of oxygen vacancies. The synergistic contribution produces multivalence redox transition activity (Ni^{3+}/Ni^{2+}, Fe^{3+}/Fe^{2+}, Mn^{3+}/Mn^{2+}, Co^{3+}/Co^{2+}, Cu^{2+}/Cu^{+}) that enable the insertion and migration of zinc ions. This research work introduces the application of high-entropy spinel oxides($HESO_x$) in ZIBs and concludes that they are competitive cathode materials for these batteries.

5.1. Introduction

ZIBs have gained much attention in academia and industry due to their high volumetric capacity (5851 $mAhcm^{-3}$), gravimetric capacity (820 $mAhg^{-1}$), decreased cost, and the use of aqueous electrolytes. In recent years, transition metal elements have been employed as anode materials in sodium and lithium-ion batteries on account of their high theoretical specific capacities and high safety [1]. Nevertheless, they experience non-ideal cycling stability resulting from severe volume expansion. They are prone to low electronic transfer efficiency, and slow kinetic properties of the multi-electron transfer processes which are caused by a delay in the local charge compensation process of the monometallic and bimetallic reactions of the cathode oxides [2]. In addition, Zn^{2+} ions have a high charge density (112 Cmm^{-3}) which produces high electrostatic repulsion in the lattices that lead to inferior long-term stability and structure collapse. The transition metal oxides that have mostly been applied in aqueous zinc ion batteries (AZIBs) are (V_2O_5 and MnO_2) whereby V_2O_5 experiences high theoretical specific capacities but they experience inferior electron transfer efficiencies. MnO_2 (also referred to as 'holy grail') experiences severe phase transitions which are attributed to lattice distortions which are a result of the high charge density of Zn^{2+}. Doping, defect engineering, addition of electrolyte additives, and carbon coating methods have been used to improve MnO_2 performance [3-9]. However, even after applying the modification strategies, the rate capabilities, and cyclic stability still need major improvement.

Hence to improve MnO_2 performance, high-entropy systems have been developed due to the inherent 'entropy stabilization effect'. The high-entropy oxides concept was introduced in 2015 [10]. This can be explained by thermodynamics using the Gibbs equation ($\Delta G = \Delta H - T\Delta S$). From this equation, a large increase in temperature leads to high-entropy and less Gibbs energy which leads to stabilization of the crystal structure and in turn stabilizes the electrode materials. This high entropy stabilization has been known to delay the phase transitions in lithium-ion batteries, hence it would be of interest to investigate if this effect can be applied to multivalent ion systems. There exists an intense lattice strain which is generated by the different atomic sizes that contribute to their outstanding mechanical properties.

The major merit of the spinel structures compared to other structures such as rock salt structures is that they contain 2 Wyckoff sites (A and B) which allow the presence of high valent ions and assist in extending the voltage range over which ions undergo redox reactions and have the ability to increase the specific capacities of electrode materials. Therefore, it is worthwhile to study high-entropy spinel oxides ($HESO_x$) for RZIBs.

Herein, we introduce $(CoCuMnNiFe)_3O_4$ $HESO_x$ as a model cathode material for AZIBs. Mixing of the polymetallic elements plays an important role whereby it broadens the d band centers (ε_d) value ranges of the monometallic density hence reducing their degeneracy. The cocktail effect plays a crucial role in the local charge compensation process due to increased electron/ion diffusion which functions to enhance the rate capability. The lattice distortion functions to relieve the structural collapse that is a result of high electrostatic force between Zn^{2+} and a fixed lattice structure hence ensuring robust long-term stability.

Nickel, cobalt, and manganese (NMC) cathodes have been used as substitutes for $LiCoO_2$ used in LIBs and have shown to have good performance due to the synergistic properties of the metals. The addition of nickel causes an increase in the cycle capacity due to the multivalent state conversion [11]. Doping with manganese ions makes the electrostatic repulsion of Ni^{2+} to cations better by the principle of electron neutrality due to the electrochemically inert properties of Mn^{4+} [12]. This leads to a stabilization of the electrode structure and improvement in the ion transport capacity. Cobalt ions (Co^{2+}, Co^{3+}) have been shown to inhibit Jan Teller effects and also promote ion diffusion [12].

Oxygen vacancies defects associated $HESO_x$ have a significant impact in LIBs and SIBs. Thus, it is duty-bound work to introduce $HESO_x$ as cathode materials for ZIBs, determine the significance of oxygen vacancies and entropy stabilization effects, and open up new ideas for the development of advanced cathode materials for ZIBs.

5.2. Results and discussion

$(CoCuMnFeNi)_3O_4$ $HESO_x$ was prepared *via* Pechini-assisted synthesis. This led to the formation of a pure, highly dispersed, and homogenous spinel oxide since the particle

morphology and stoichiometry properties was controlled by the use of low temperature for precursor treatment (500°C).

5.2.1. PXRD analysis

PXRD was performed to determine the unique crystal structure of $HESO_x$ using a copper radiation source. Figure 5.1 shows nine major diffraction peaks that were indexed to (111), (220), (311), (222), (400), (331), (422), (511), and (440) planes of the spinel structure [13]. It corresponds to an inverse spinel due to the dominant (311) crystal plane. It shows a secondary phase which was identified as tenorite (CuO). The spectrum was compared using the CIF of magnetite (Fe_3O_4) and that of MEET research group ($HESO_x$. Ozoemena CIF) whereby the peaks from $HESO_x$ shifted to higher 2θ angles which was attributed to lattice contraction.

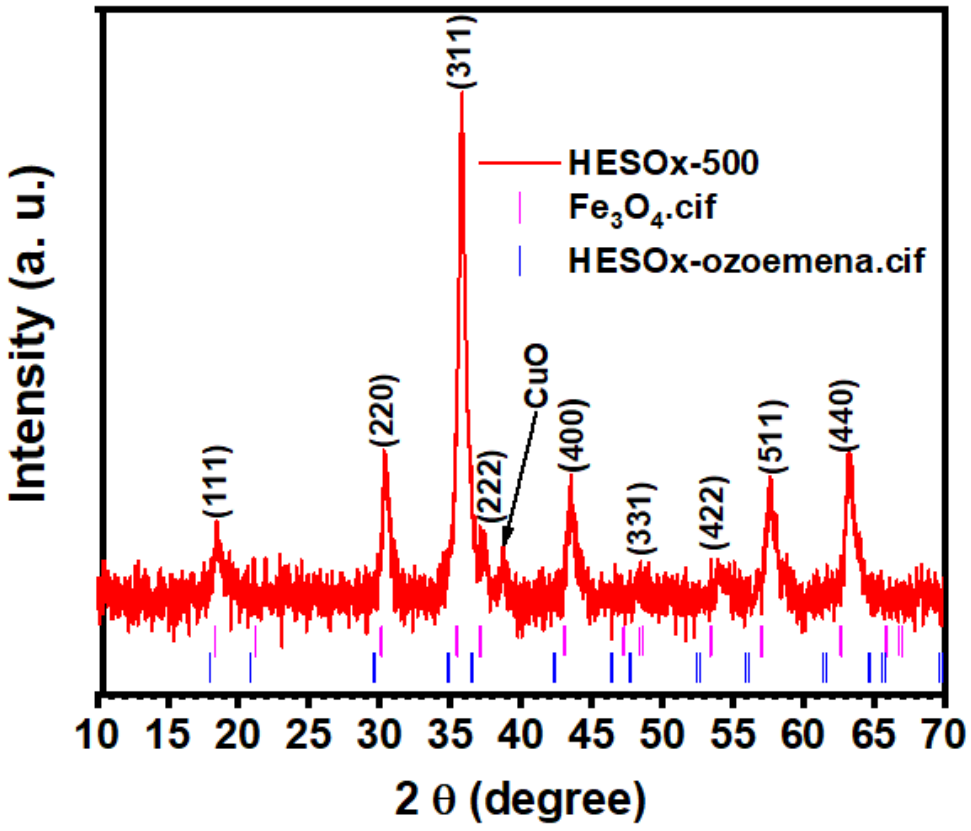

Figure 5.1: $HESO_x$ XRD spectrum

5.2.2. XPS analysis

XPS analysis was also useful in determining the surface properties of $HESO_x$. The survey spectrum shows the presence of copper, cobalt, manganese, iron, nickel, carbon, and oxygen in the sample.

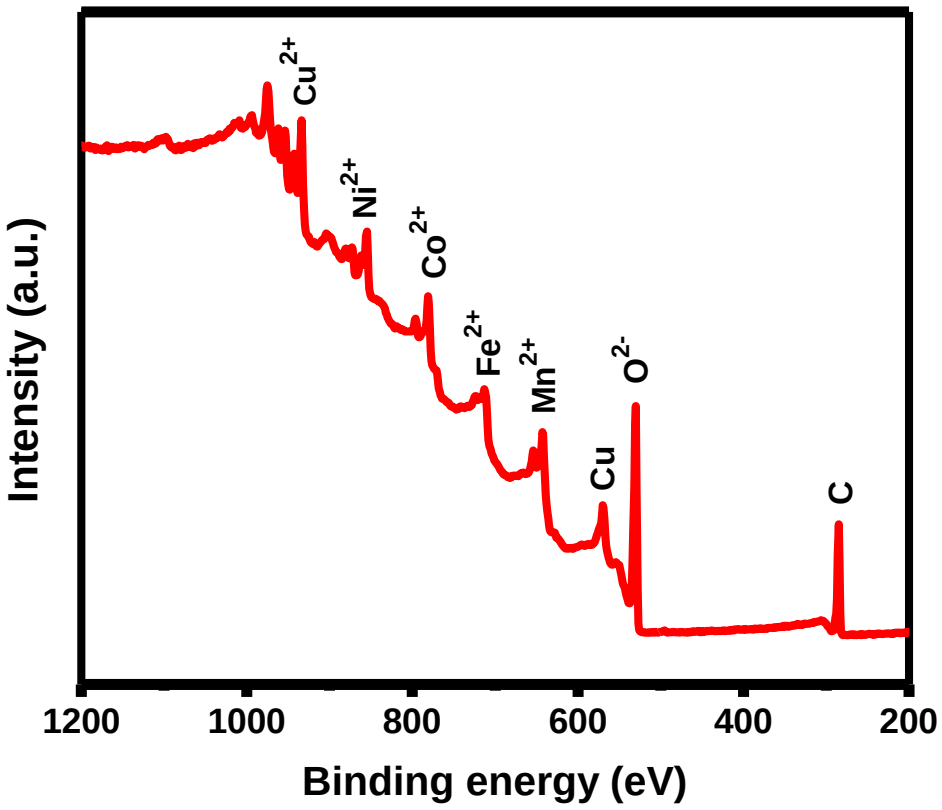

Figure 5. 2: $HESO_x$ XPS spectrum

Figure 5.3 (A) gives the fine scan Cu-2p XPS spectra in which Cu $2p_{1/2}$ is located around 953.6 eV while Cu $2p_{3/2}$ is located at 933.9 eV. There exist some satellite peaks around 962.1 eV, 943.3 eV and 941.3 eV [14]. Figure 5.3 (B) represents the Co-2p XPS spectra that exhibited two main spin-orbit lines at 795.4 eV and 780.1 eV which are attributed to Co $2p_{1/2}$ and Co $2p_{3/2}$ respectively [15, 16]. The binding energy at around 780.1 eV is attributed to Co^{2+} while that at about 781.9 eV is majorly attributed to Co^{3+}.

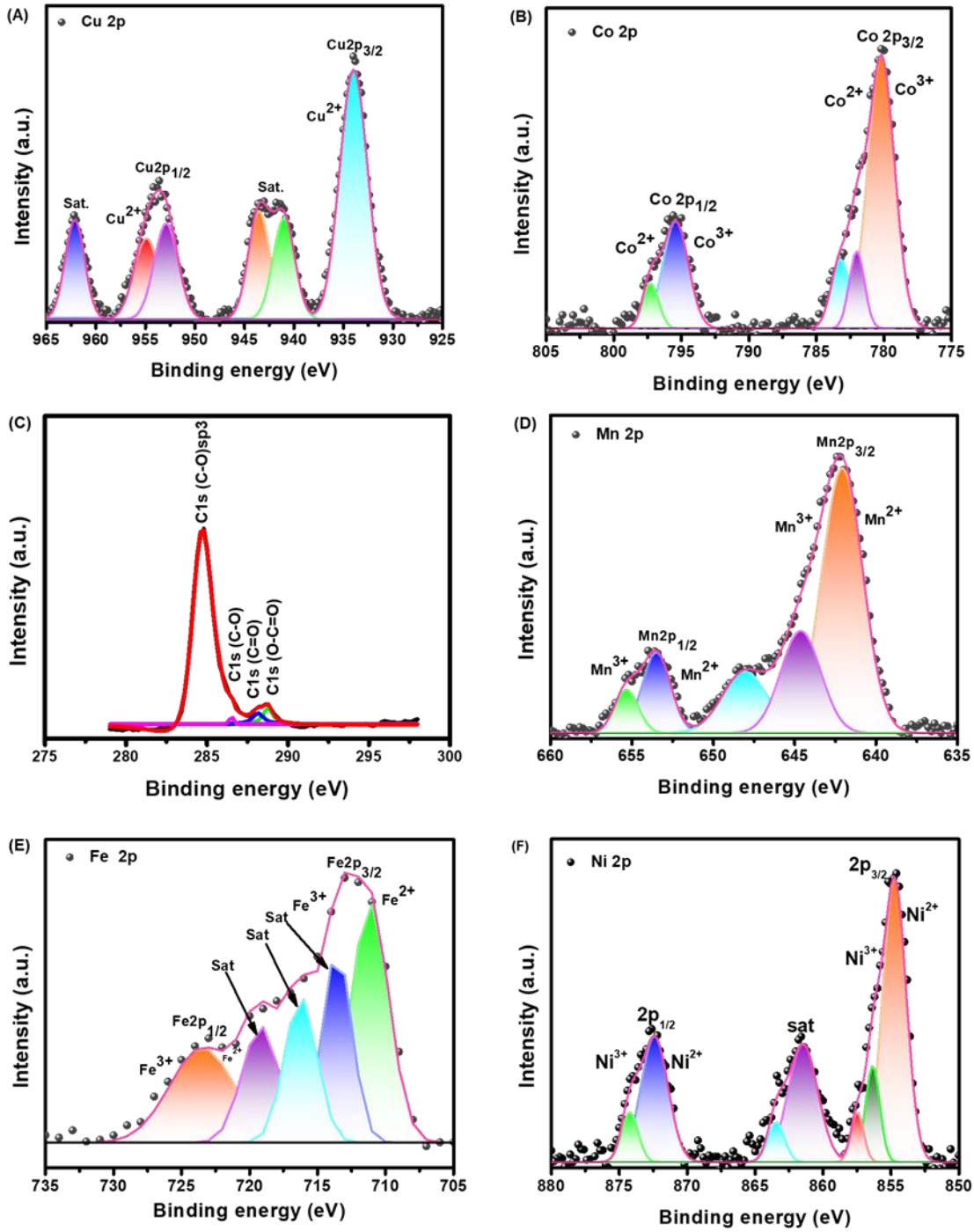

Figure 5. 3: XPS spectrum of **(A)** Cu 2p, **(B)** Co 2p **(C)** Carbon, **(D)** Mn 2p, **(E)** Fe 2p and **(F)** Ni 2p

According to Figure 5.3 (D) Mn-2p XPS exhibited two main peaks at 642.2 eV attributed to Mn-$2p_{3/2}$ and 653.6 eV as a result of Mn-$2p_{1/2}$ [17]. The main peak at 642 eV is strongly due to Mn^{3+}. Figure 5.3 (E) represents the Fe-2p XPS spectra, whereby the binding energy at 712.9 eV and 719.0 eV is largely attributed to Fe^{3+} while the peak at binding energy of 723.7 eV and 716.0 eV is mainly due to Fe^{2+} [18, 19]. Figure 5.3 (F) represents the Ni XPS spectra. Ni $2p_{3/2}$ is located at 854.8 eV while Ni $2p_{1/2}$ is located at 872.4 eV [20]. There exist peaks of Ni^{3+} at 856.4 eV and 874.1 eV. A shakeup peak is located at 861.5 eV which is an indicator of the mixed valence states that exist in nickel metal [21]. Figure 5.3 (C) represents the carbon XPS spectra.

Figure 5.4 represents the XPS oxygen spectra, the oxygen peak at 529.58 eV represents the lattice oxygen, the peak at 531.4 eV represents the oxygen vacancies and the peak at 533.14 eV represents the surface adsorbed molecules. Oxygen vacancies are as a result of O^- and O_2^{2-} dangling bonds [22]. Table 5.1 shows that the percentages were: lattice oxygen was 65.6%, oxygen vacancies 28.8%, and surface adsorbed molecules 5.6%. These percentages were calculated from the areas under the peaks.

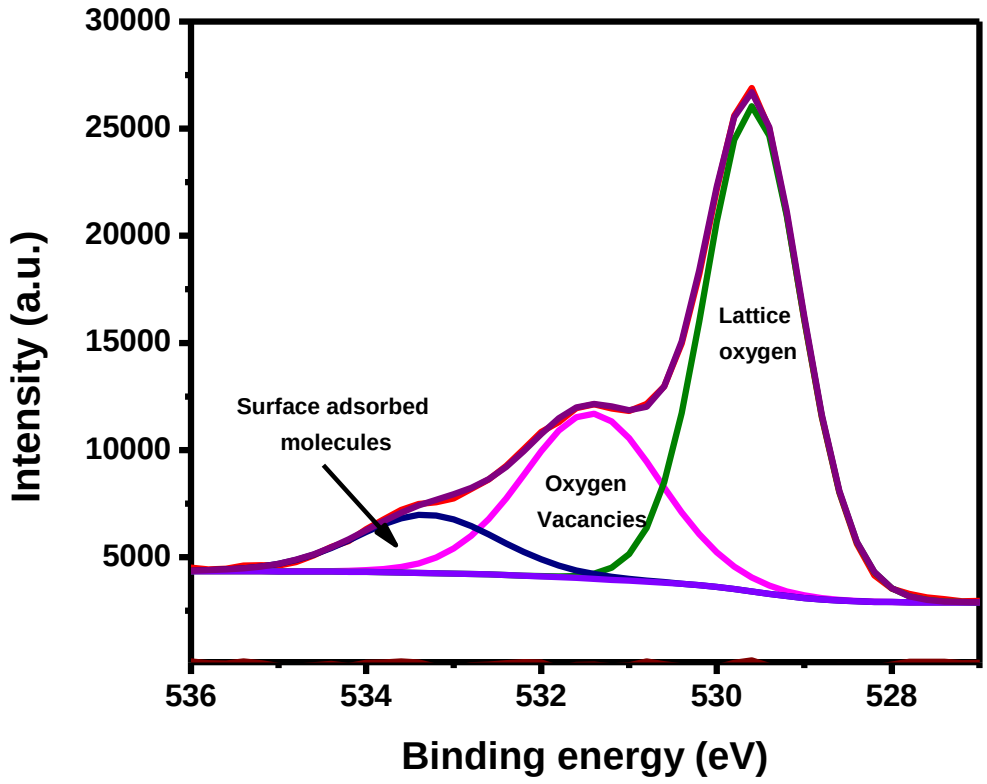

Figure 5.4: Oxygen XPS spectrum

Table 5.1: Area and % concentrations of O survey spectrum

Peak position	Area	% Concentration
529.58	33192.4	65.6
531.4	14567.4	28.8
533.14	2846.9	5.6
	Total area (50606.7)	

5.2.3. SEM and EDS analysis

SEM and EDS analysis were used to determine the morphology, and chemical compositions of the powders calcined at 500°C. From the SEM image in Figure 5.5 (A) the samples are composed of spherical granular powders and are porous. The crystals are also agglomerated. Figure 5.5 (B) shows the EDS spectra shows the homogenous distribution of the metals and oxygen in $HESO_x$ without any specific element segregation.

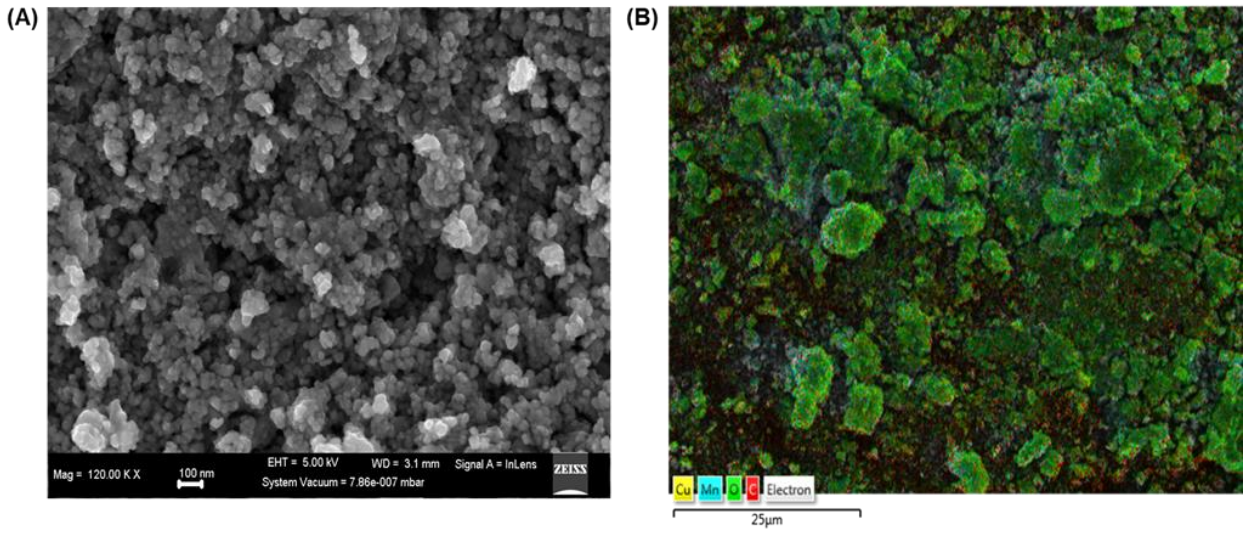

Figure 5.5: **(A)** SEM plot of $HESO_x$ **(B)** EDS spectra of $HESO_x$

Figure 5.6 shows the individual EDS spectra of the metals and oxygen.

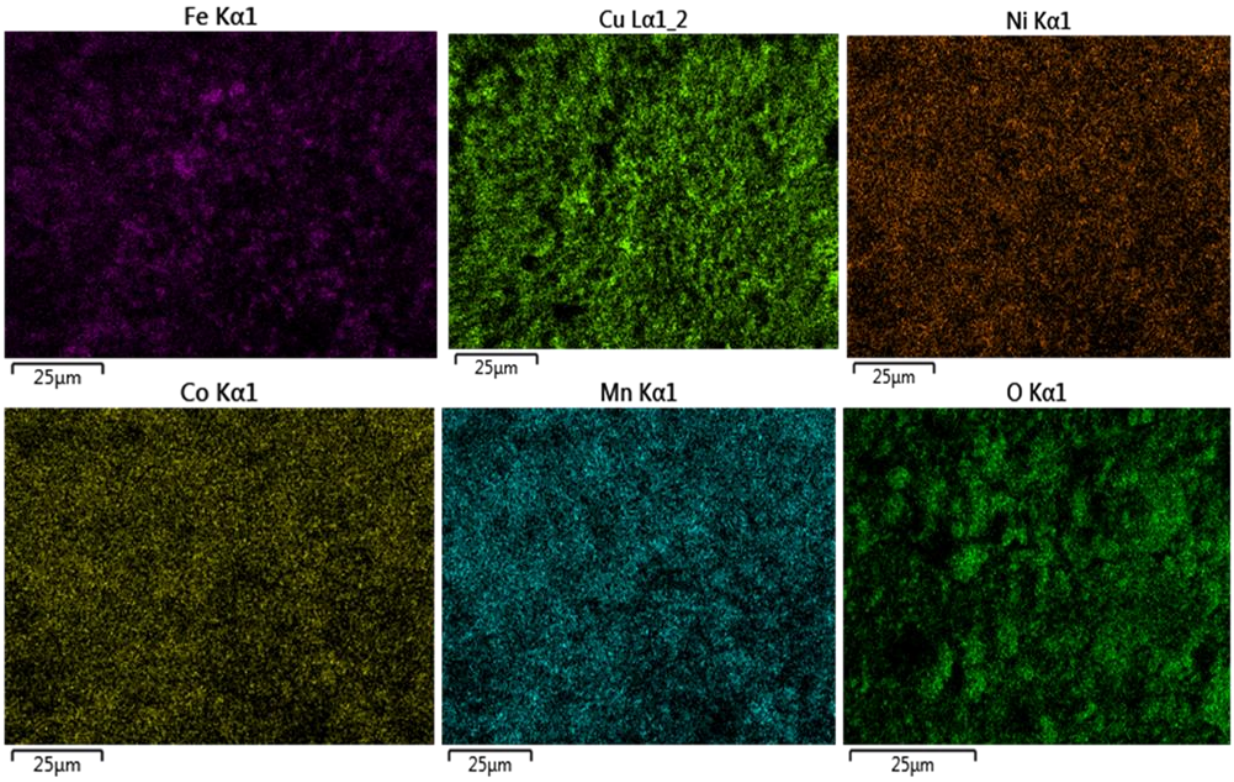

Figure 5.6: EDS Spectra of the metals and oxygen

Table 5.2 shows the ratios of Co, Cu, Mn, Fe, Ni, and O that were obtained from EDS analysis. As seen in the table, the proportions are closer to each other. This verifies that the metals in $HESO_x$ had near-equimolar proportions.

Table 5.2: Atomic and weight % of the $HESO_x$ from EDS

Element	Co	Cu	Mn	Fe	Ni	O
Weight %	12.68	18.70	11.72	12.05	13.91	30.94
Atomic %	6.92	9.47	6.87	6.95	7.62	62.18

5.3. Electrochemical measurements

5.3.1. Cyclic voltammetry

To investigate the zinc storage mechanisms of $(CoCuMnFeNi)_3O_4$ the cyclic voltammetry curves were measured on $HESO_x$ under a voltage window of 0.6V - 2.0V with different scan rates and using carbon black (Super C-45) as a conductive agent.

Figure 5.7 shows cathodic peaks at 0.85V, 1.0V, and 1.3V which are due to the stepwise reduction of transition metal oxides that contain M^{4+}/M^{3+} to M^{2+} and a further reduction of M^{2+} to M^0. The redox peaks at 1.2V/1.3V can be attributed to the reversible conversion of Mn^{4+}/Mn^{3+} since these potentials are similar to those reported for the system of $ZnNi_{1/2}Mn_{1/2}CoO_4$ [23]. This work also portrayed the occurrence of Co^{4+}/Co^{3+} at a voltage of 1.75V which is quite similar to the redox peak at 1.7V. Correspondingly, during the anodic reaction process, the peaks at 1.0V,1.2V, and 1.7V were attributed to the reversible oxidation of copper, manganese, iron, nickel, and cobalt.

Cyclic voltammetry was also performed using Ketjen black carbon, and carbon black (Super C45).

The results show a big similarity in the location of the redox peaks with the only difference being that some of the peaks are not as pronounced as those with the carbon black. This proves that the reduction of the metal oxides and the oxidation of the metals into metal oxides occurs at the specified voltages.

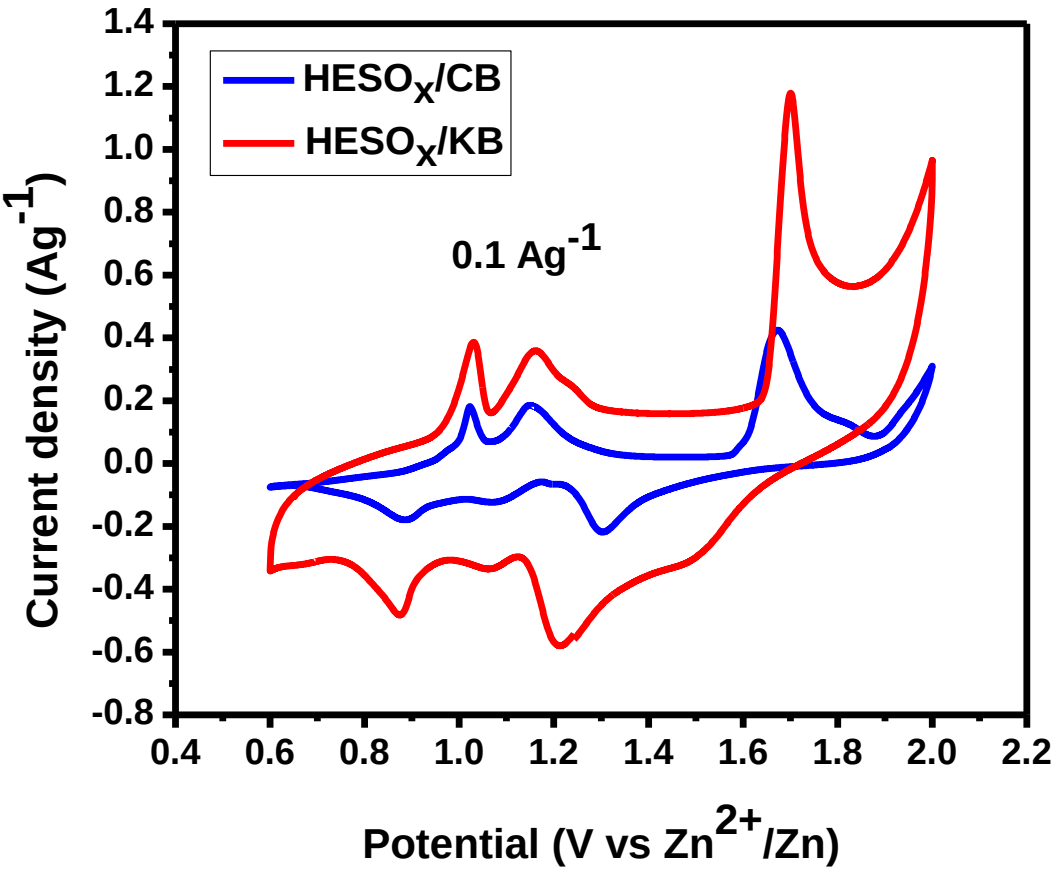

Figure 5.7: CV comparison plots between HESO$_X$/CB and HESO$_X$/KB

5.3.2. Charge-discharge analysis

Figure 5.8 shows that after activation, discharge plateaus could be seen at 1.1V, 0.9V 1.2V, and 1.7V depending on the constituents of the cathode material. Specific capacities of 143.03mAhg^{-1} and 24.35mAhg^{-1} which corresponded to HESO$_X$/KB and HESO$_X$/CB respectively were achieved. HESO$_X$/KB gave a higher performance and we postulated that this performance was due to its higher surface area that enabled Zn^{2+} intercalation.

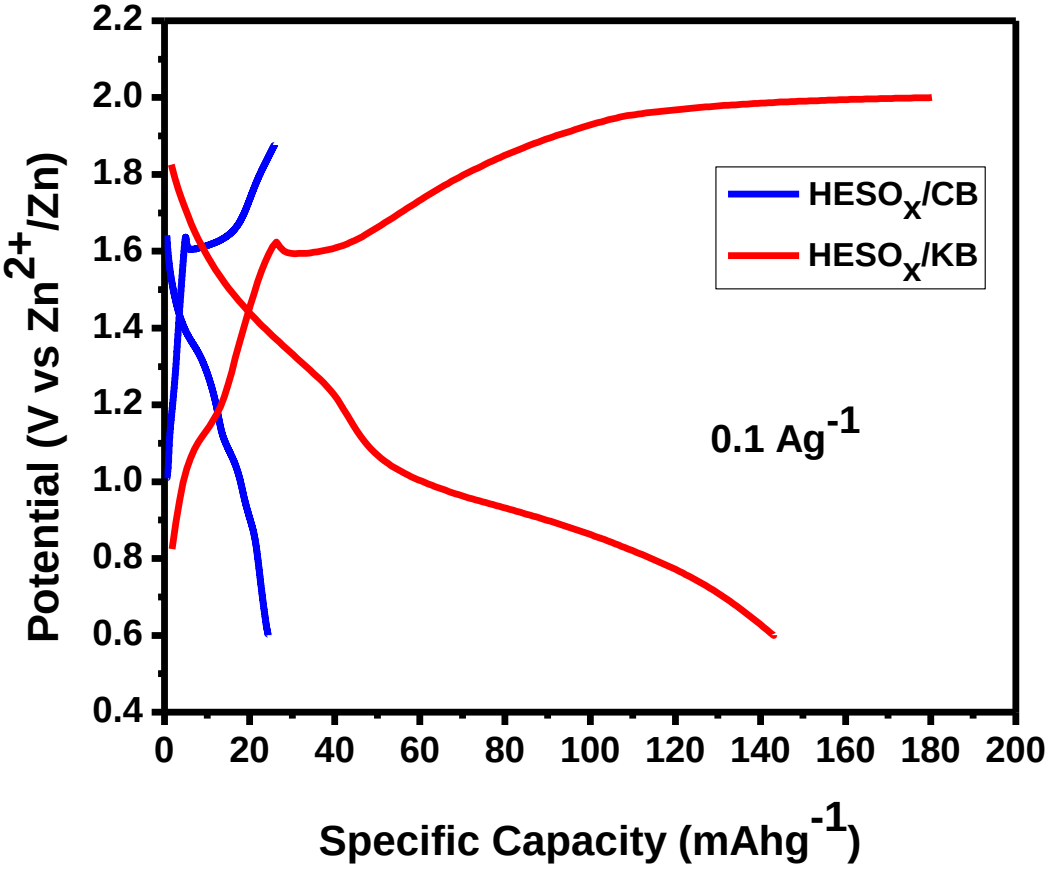

Figure 5.8: Comparison of GCD analysis

5.3.3. Rate capability studies

Figure 5.9 shows the rate capabilities of $HESO_x$ under different current densities. The results show that $HESO_x$ suffers from capacity decay when the current densities are increased from $0.1Ag^{-1}$ to $1.0Ag^{-1}$. $HESO_x$ containing Ketjen black portrays a higher discharge capacity of $143.03Ag^{-1}$ compared to carbon black whose discharge capacity was $24.35Ag^{-1}$. This is due to the high surface area of Ketjen black. However, when the current gets back to $0.1Ag^{-1}$ a capacity of $119.61Ag^{-1}$ and $23.56Ag^{-1}$ can be recovered from $HESO_x$ containing Ketjen black and carbon black respectively. This indicates that $HESO_x$ containing carbon black demonstrates higher reversibility and structural stability [16]. In addition, the attractive rate capability in both of them is also a result of oxygen

vacancies as seen in the XPS spectrum, which leads to enhanced charge transfer mechanisms.

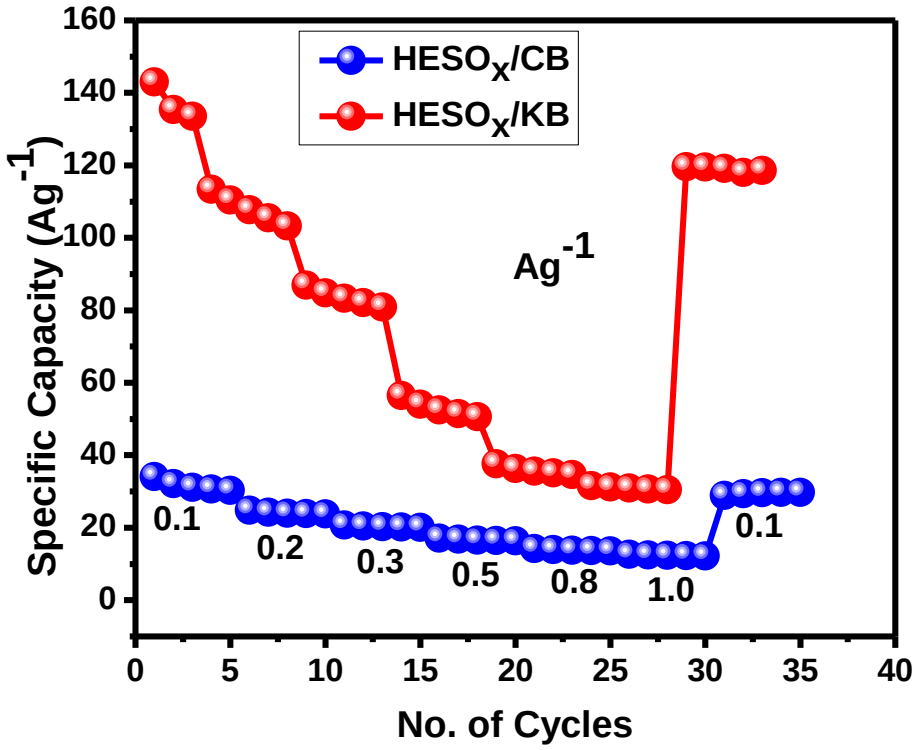

Figure 5.9: Rate capability

5.3.4. Cycling performance and stability studies

Figure 5.10 shows the cycle performance and stability of $HESO_x$. $HESO_x$ containing Ketjen black has a capacity retention of 84.4% while that of carbon black has a retention of 97%.

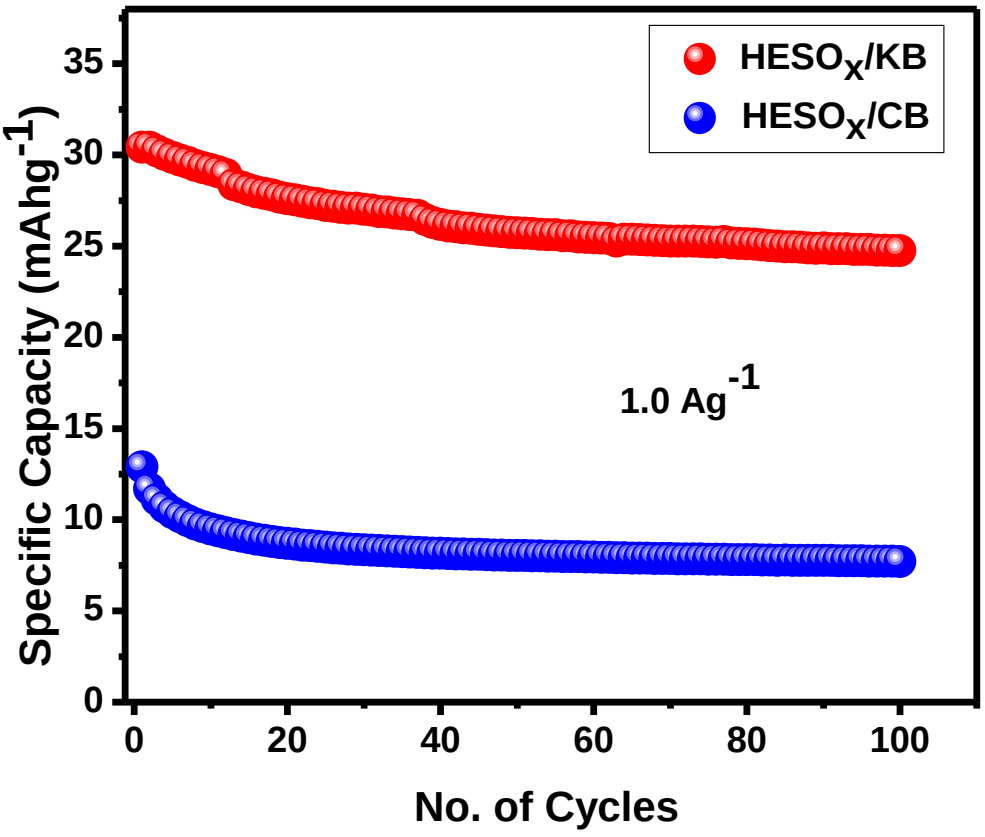

Figure 5.10: Cycling stability comparison

5.3.5. EIS analysis

Figure 5.11 shows the circuit that was employed.

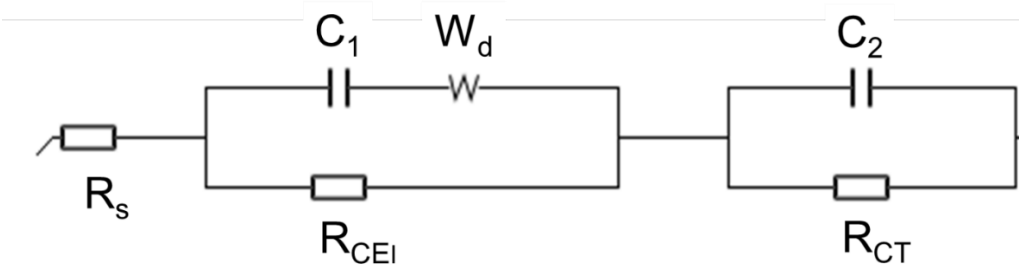

Figure 5.11: Equivalent EIS circuit

Figure 5.12 shows the fitted EIS plot comparison between HESO$_x$/KB and HESO$_x$/CB at the BoL. The circuit elements values from Table 5.3 and 5.4 below shows the difference in the impedance of these two materials.

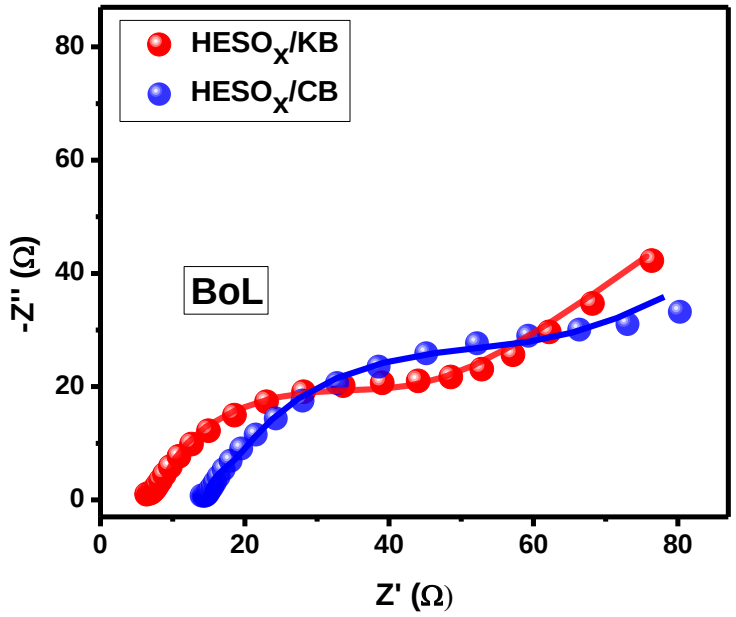

Figure 5.12: EIS Spectra Comparison BoL

Figure 5.13 (A) represents the EoL EIS for HESO$_x$/CB while Figure 5.13 (B) shows the EoL EIS for HESO$_x$/KB. HESOx/KB has a higher impedance than HESOx/CB as proved by the values from Tables 5.3 and 5.4.

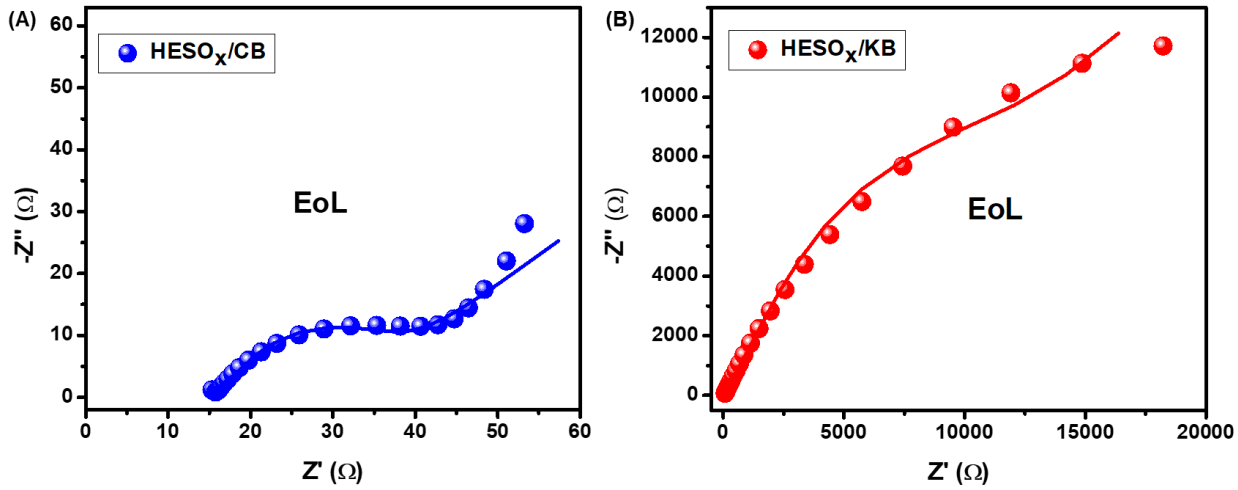

Figure 5.13: EIS spectra comparison EoL

Table 5.3 and 5.4 shows the fitted values of R_S, R_{CEI}, C_1, C_2, R_{CT} and W_d. According to the R_{CT} values, $HESO_x$/KB showed R_{CT} values of 85.61 Ω and 21409 Ω in the beginning of life (BoL) and end of life (EoL) respectively while $HESO_x$/CB R_{CT} values were 59.54 Ω and 95.35 Ω in the BoL and EoL respectively.

Table 5.3: EIS fittings of $HESO_x$/KB

Circuit elements	BoL	EoL
R_s (Ω)	5.88 ± 0.61	6.74 ± 0.59
C (mF)	0.17 ± 0.04	0.0021 ± 0.00001
W_d ($\Omega s^{-1/2}$)	161.50 ± 61.38	15836 ± 53.23
R_{CEI} (Ω)	47.32 ± 3.01	6303 ± 6.12
C_2 (mF)	2.69 ± 0.71	0.0057 ± 0.00001
R_{CT} (Ω)	85.61 ± 17.33	21409 ± 11.35

Table 5.4: EIS fittings of $HESO_x$/CB

Circuit elements	BoL	EoL
R_s (Ω)	13.74 ± 0.57	14.73 ± 0.66
C (mF)	0.45 ± 0.15	0.00024 ± 0.00009
W_d ($\Omega s^{-1/2}$)	98.79 ± 39.66	169.00 ± 71.96
R_{CEI} (Ω)	51.23 ± 18.74	31.28 ± 3.29
C_2 (mF)	3.89 ± 3.21	5.12 ± 1.55
R_{CT} (Ω)	59.54 ± 13.27	95.35 ± 59.54

Figure 5.14 shows the Bode plots which further prove the characteristics of constant phase elements since the values of the slopes are less than 1 while the R^2 is close to 1 which is a characteristic of batteries and not capacitors.

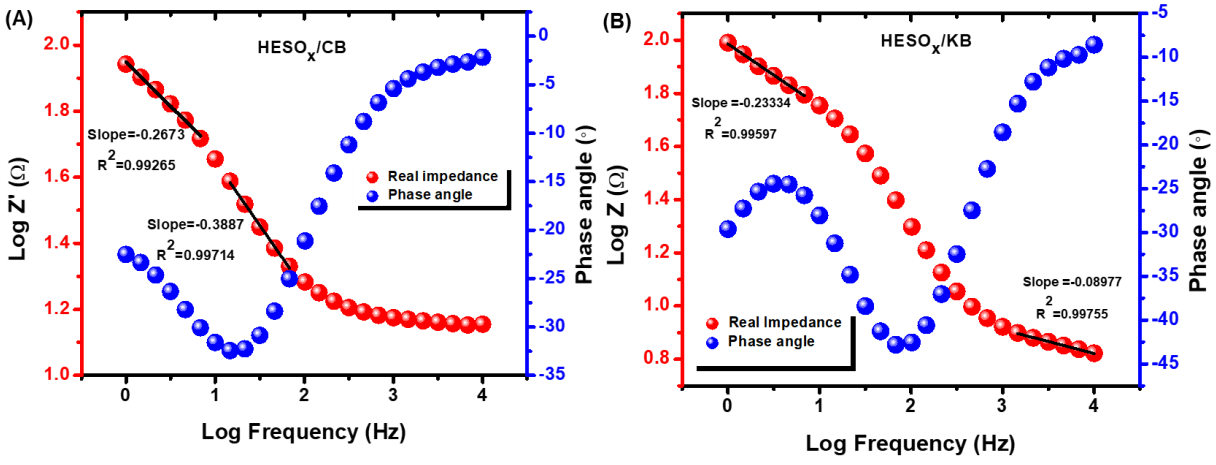

Figure 5.14: Bode plots of **(A)** $HESO_x$/CB and **(B)** $HESO_x$/KB

The diffusion coefficients of the BoL were calculated from the Randles plot in Figure 5.15. The values obtained were $3.0174e^{-19}$ cm^2s^{-1} and $3.1023e^{-19}$ cm^2s^{-1} for $HESO_x$/KB and $HESO_x$/CB respectively.

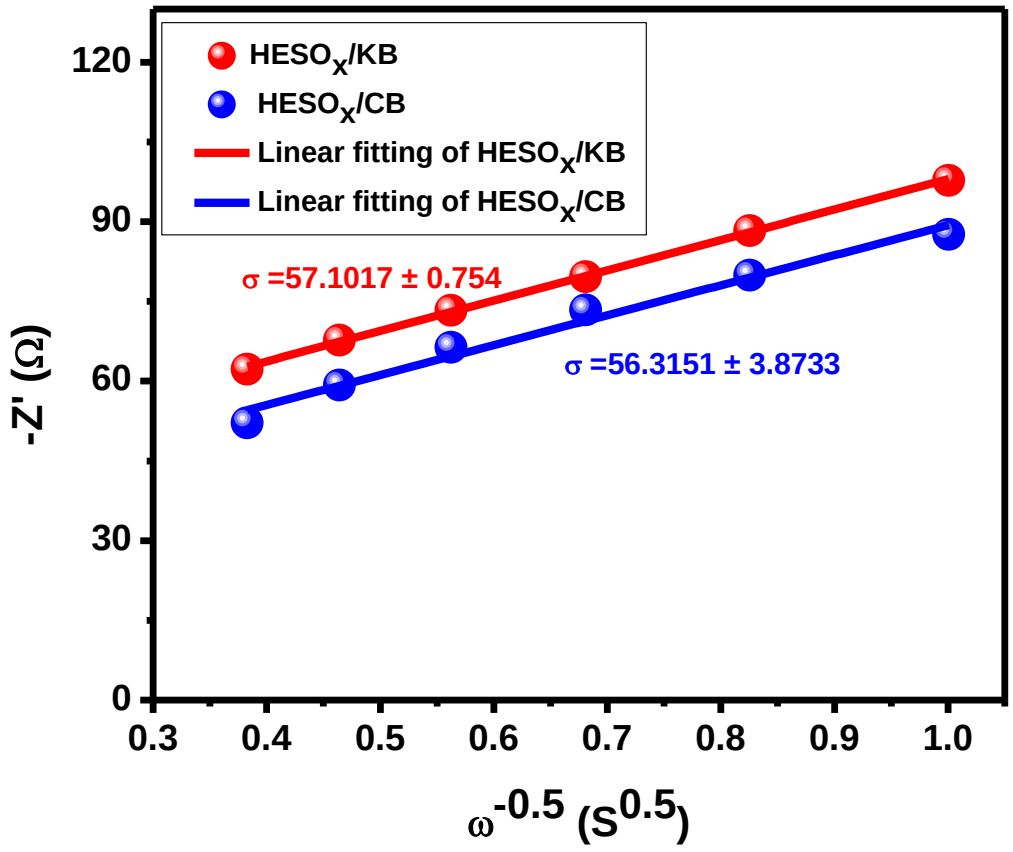

Figure 5.15: Randles plot Comparison plot

5.4. Summary

In summary, XRD spectrum showed the successful synthesis of HESOx reverse spinel corresponding to the Cif of Fe_2O_3 and the Cif from our research group (Kenneth Ozoemena Cif). SEM analysis showed the presence of spherical agglomerates while EDS analysis showed the homogenous distribution of all metal constituents (Co, Cu, Ni, Mn, Fe) and oxygen. XPS spectra then proved the existence the metal cations in divalent and trivalent states and their location in tetrahedral and octahedral crystal sites. Two types of

carbon (Ketjen black and carbon black) were added to the HESOx and according to the electrochemistry results $HESO_x$ containing Ketjen showed better energy storage properties which we postulate are from its higher surface area.

5.5. References

1. Bian, W., et al., Entropy stabilization effect and oxygen vacancy in spinel high-entropy oxide promoting sodium ion storage. Electrochimica Acta, 2023. **447**: p. 142157.
2. Du, K., et al., High Entropy Oxides Modulate Atomic-Level Interactions for High-Performance Aqueous Zinc-Ion Batteries. Advanced Materials, 2023. **35**(51): p. 2301538.
3. Zhang, Y., et al., MnO2 cathode materials with the improved stability via nitrogen doping for aqueous zinc-ion batteries. Journal of Energy Chemistry, 2022. **64**: p. 23-32.
4. Zhao, Y., et al., Uncovering sulfur doping effect in MnO2 nanosheets as an efficient cathode for aqueous zinc ion battery. Energy Storage Materials, 2022. **47**: p. 424-433.
5. Ni, Z., et al., Tin doping manganese dioxide cathode materials with the improved stability for aqueous zinc-ion batteries. Materials Chemistry and Physics, 2022. **287**: p. 126238.
6. Du, M., et al., Strategies of structural and defect engineering for high-performance rechargeable aqueous zinc-ion batteries. Journal of Materials Chemistry A, 2021. **9**(35): p. 19245-19281.
7. Huang, J., et al., Improving the capacity of zinc-ion batteries through composite defect engineering. RSC advances, 2021. **11**(54): p. 34079-34085.
8. Islam, S., et al., Carbon-coated manganese dioxide nanoparticles and their enhanced electrochemical properties for zinc-ion battery applications. Journal of energy chemistry, 2017. **26**(4): p. 815-819.
9. Wan, J., et al., A double-functional additive containing nucleophilic groups for high-performance Zn-ion batteries. ACS nano, 2023. **17**(2): p. 1610-1621.
10. Rost, C.M., et al., Entropy-stabilized oxides. Nature Communications, 2015. **6**(1): p. 8485.

11. Xing, F., et al., A carbon-coated spinel zinc cobaltate doped with manganese and nickel as a cathode material for aqueous zinc-ion batteries. Dalton Transactions, 2021. **50**(17): p. 5795-5806.
12. Ji, J., et al., Co2+/3+/4+-Regulated Electron State of Mn-O for Superb Aqueous Zinc-Manganese Oxide Batteries. Advanced Energy Materials, 2021. **11**(6): p. 2003203.
13. Tian, L., et al., High-entropy spinel oxide nanofibers as catalytic sulfur hosts promise the high gravimetric and volumetric capacities for lithium–sulfur batteries. Energy & Environmental Materials, 2022. **5**(2): p. 645-654.
14. Lin, Y., et al., Impact of reducing conditions on the stabilization of Mg0.2Co0.2Ni0.2Cu0.2Zn0.2O high-entropy oxide. Ceramics International, 2022. **48**(20): p. 30184-30190.
15. Raza, H., et al., High-entropy stabilized oxides derived via a low-temperature template route for high-performance lithium-sulfur batteries. EcoMat, 2023. **5**(4): p. e12324.
16. Wang, D., et al., Spinel-structured high entropy oxide (FeCoNiCrMn)3O4 as anode towards superior lithium storage performance. Journal of Alloys and Compounds, 2020. **844**: p. 156158.
17. Chung, S.-H., et al., High Entropy Oxide (CrMnFeNiMg)3O4 with Large Compositional Space Shows Long-Term Stability as Cathode in Lithium-Sulfur Batteries. ChemSusChem, 2023. **16**(8): p. e202300135.
18. Nguyen, T.X., et al., High entropy spinel oxide nanoparticles for superior lithiation–delithiation performance. Journal of Materials Chemistry A, 2020. **8**(36): p. 18963-18973.
19. Wang, B., et al., Spinel-type high-entropy (Co0.2Mn0.2Fe0.2Zn0.2Ti0.2)3O4 oxides constructed from disordered cations and oxygen vacancies. Journal of Alloys and Compounds, 2022. **897**: p. 163188.
20. Zhu, H., et al., Structure and magnetic properties of a class of spinel high-entropy oxides. Journal of Magnetism and Magnetic Materials, 2021. **535**: p. 168063.
21. Xiao, B., et al., High-entropy oxides as advanced anode materials for long-life lithium-ion Batteries. Nano Energy, 2022. **95**: p. 106962.

22. Merino, N.A., et al., La1− xCaxCoO3 perovskite-type oxides: Identification of the surface oxygen species by XPS. Applied Surface Science, 2006. **253**(3): p. 1489-1493.
23. Pan, C., et al., ZnNixMnxCo2–2xO4 Spinel as a High-Voltage and High-Capacity Cathode Material for Nonaqueous Zn-Ion Batteries. Advanced Energy Materials, 2018. **8**(22): p. 1800589.

Chapter 6

High-entropy spinel oxide $(CoCuMnFeNi)_3O_4$/OLC as an electrocatalyst for high-performance lithium-sulfur batteries

6.1. Introduction

Lithium-sulfur batteries (LSBs) attract a lot of recognition from researchers due to their high theoretical capacity (1672 $mAhg^{-1}$) which is a result of the sulfur-based cathodic reactions whereby sulfur undergoes heterogeneous chemical conversion from S_8 to (Li_2S_8/Li_2S_6, Li_2S_4) intermediates and eventually to (Li_2S/Li_2S_2) [1], their appealing gravimetric and volumetric energy densities (2500 $Whkg^{-1}$), (2780 WhL^{-1}) respectively [2], abundant sulfur resources and low cost [3]. Lithium-ion battery (LIB) is widely used in the current energy systems but has a limitation of a lower energy density of 240 WhL^{-1} hence there is a need to develop more battery systems to meet the stringent energy demand. LSBs however face a limitation whereby they experience the formation of lithium polysulfides (LiPSs) intermediates that dissolve in the liquid ether electrolyte which exacerbates the shuttle effect leading to rapid loss of material, low coulombic efficiency, and capacity fading, which severely undermines applications of LSBs [4].

To conquer these challenges, tremendous hosts of sulfur have been proposed to hinder the dissolution of LiPSs either by physisorption or chemisorption and to enhance the performance of LSBs. Carbon materials that include carbon nanotubes, graphene, mesoporous carbon, carbon fibers, and carbon spheres have been widely used as host materials of sulfur due to their outstanding conductivity and porous structure. They however have limited confinement to LiPSs due to their weak confinement due to their weak interaction of physical adsorption through van der Waals forces, volume expansion during discharge, and decrease in volumetric energy densities because carbon is a lightweight material. Alternatively, metal oxides are employed due to their strong chemical adsorption for the LiPSs i.e. the formation of metal-sulfur and lithium-oxygen bonds [2]. In particular, much attention has been focused on transition metal oxides due to their

intrinsic polar surfaces and the formation of metal-sulfur bonds. They offer a robust chemical confinement weakening the S-S bonds in the LiPSs intermediate hence accelerating the LiPSs-Li_2S_2, Li_2S conversion kinetics that is responsible for most of the theoretical capacity. The metal cations that are present $HESO_x$ are significant for chemisorption and electrocatalysis due to the strong metal-sulfur bonds and they display a unique electrocatalytic ability for the conversion of LiPSs.

Unary metal oxides have been employed such as titanium oxide which shown to immobilize LiPSs effectively through the formation of Li-O and Ti-S bonds [5]. RuO_2 has also been used and it trapped the LiPS through the formation of Ru-S bonds [6] while Nb_2O_5 gave a better adsorption capability due to the defects formation [7]. MnO_2 has also been employed. It however demonstrates a different reaction mechanism whereby the conversion of soluble LiPSs to Li_2S_2/ Li_2S is through the formation of polythionate ($O_3S_2{-}S_{x-2}{-}S_2O_3$) and thiosulfate ($S_2O_3^{2-}$) giving it very unique behavior which is the main reason for the further exploration of the oxide. Consequently, multicomponent metal oxides display preferable properties due to synergistic effect between metal cations, good chemical stability and electronic conductivity. Mixed metal oxides such as $ZnCo_2O_4$@N-RGO have been prepared to mitigate the shuttle effect by chemical confinement while $Ba_{0.5}Sr_{0.5}Co_{0.8}Fe_{0.2}O_{3-\delta}$ were used as a promoter to anchor the LiPSs intermediates. Due to the vast attributes of multicomponent oxides, high-entropy oxides(HEOs) have been explored for LSBs. They comprise of 5 or more metals to form a single phase oxide structure. They are very advantageous because of the reasons that follow. First and foremost, they have a high dispersion of metal species which leads to exposure of active sites that confine the LiPSs during charge-discharge process. They also possess chemical and thermodynamic stability and provide good uniformity without any agglomerated metal species. In addition, they entrap the LiPSs via a strong chemical bond between the HEOs and Li_2S_6 (a high order LiPS intermediate).

Herein, we present a high-entropy spinel oxide ($HESO_x$) and onion-like carbon (OLC): $(CoCuMnNiFe)_3O_4$ /OLC as a host material and electrocatalyst for LSBs. It comprises of cobalt, copper, manganese, nickel, iron metals that have each proven to improve the LSBs performance in single oxide or mixed oxides forms [2]. The incorporation of OLC

was to improve the conductivity. With the combination of these metals and OLC we demonstrate that $HESO_x$/OLC shows improved stability and capacity retention of 98%.

6.2. Results and discussion

6.2.1. PXRD analysis

The synthesized $HESO_x$ was analyzed by X-ray diffraction shown in Figure 6.1. The diffraction peaks at 18.37°, 30.39°, 35.62°, 37.31°, 43.39°, 53.85°, 57.38°, 63.03° correspond to (111), (220), (311), (222), (400), (422), (511) and (440) planes of the spinel which are attributed to magnetite spinel (Fe_3O_4).

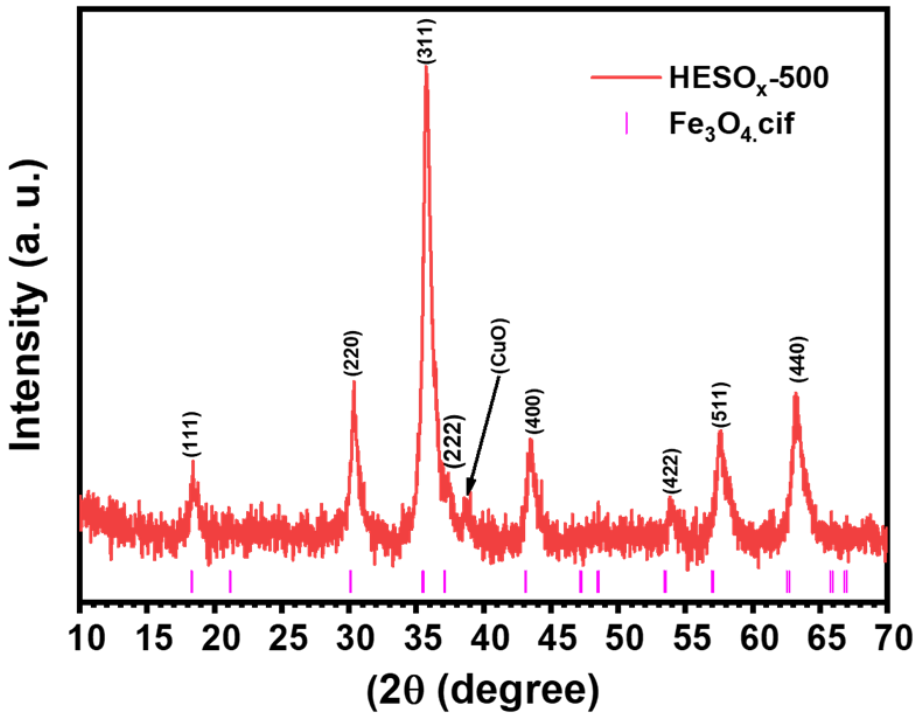

Figure 6.1: $HESO_x$ XRD spectrum

Table 6.1 represents the interplanar spacing and lattice parameter calculated from Bragg's law as described in detail in Appendix B and Table S3. The crystallite size was calculated from Scherrer formula shown in Appendix B and the calculated values are represented in Table S4.

Table 6.1: Interplanar spacing and lattice parameter of $HESO_x$

Sample	Interplanar spacing (d_{hlk}) (Å)	Lattice Parameter (Å)	Crystallite size (nm)
$HESO_x$	2.5185	8.386	6.1526

6.2.2. Raman spectroscopy

Raman spectrum of $HESO_x$ was compared to that of ferrite systems whereby the vibrational modes were given as:

$\Gamma = A_{1g} + E_g + F_{1g} + 3F_{2g} + 2A_{2u} + 2E_u + 4F_{1u} + 2F_{2u}$ [8, 9] where A, E, and F notations represent 1D, 2D and 3D respectively and g is the symmetry with reverse to the center of inversion. The Raman active modes are A_{1g}, $3F_{2g}$, and E_g (5 optical modes). The inactive modes are $2A_{2u} + 2E_u + 2F_{2u}$ while $4F_{1u}$ are infra-red active modes [10]. The Raman bands occurred at $314cm^{-1}$ (E_g), $248cm^{-1}$(F_{2g} 1), $408cm^{-1}$(F_{2g} 2), $502cm^{-1}$(F_{2g} 3) and $610cm^{-1}$(A_{1g}) as shown in Figure 6.2.

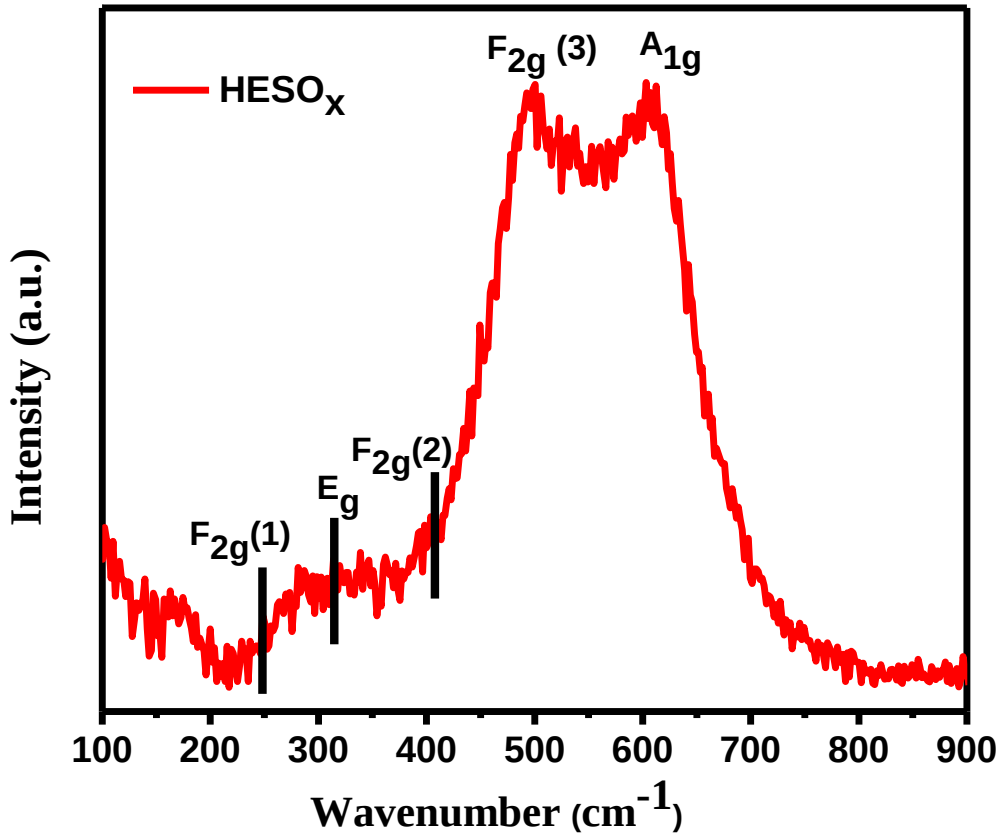

Figure 6.2: Raman spectrum of $HESO_x$

6.3. Electrochemical characterizations

6.3.1. CV analysis

Figure 6.3 shows the comparison of carbon and aluminium current collectors for LSBs. Aluminium foil shows two anodic peaks that symbolizes the complete oxidation of Li_2S_n-S_8. The current density is also higher on aluminum foil hence we proceeded with aluminium foil current collector in the subsequent analysis.

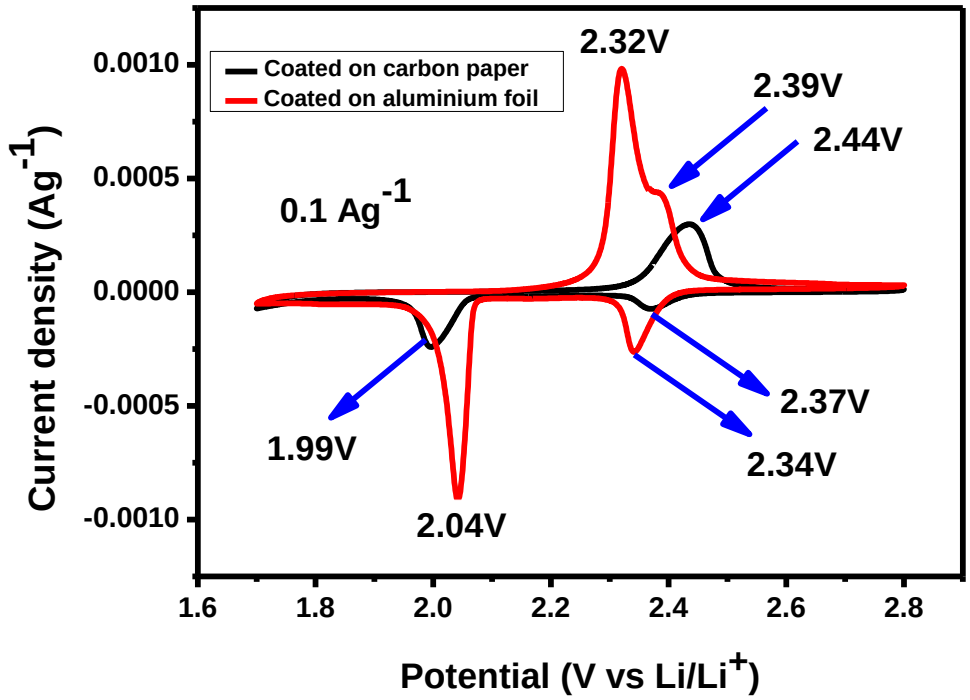

Figure 6.3: CV comparison plot

CV purposes to highlight the electrochemical behavior of the $HESO_x$/OLC/S and OLC/S cathodes in the LSBs. The potential window used was 1.7 V-2.8V which is within range in the working voltages of LSBs. In Figure 6.4 (using 50% sulfur loading) two cathodic peaks were observed which corresponded to the reduction of sulfur to long chain/high order polysulfides (Li_2S_n) ($4 \leq n \leq 8$) which are soluble and the subsequent conversion of these species to insoluble short chain/low order polysulfides Li_2S_2 and Li_2S respectively. There is a formation of one anodic peak which shows the reverse process. The sharp anodic peak represents an improvement of the reaction kinetics and a higher conversion of soluble polysulfides to insoluble polysulfides [11].

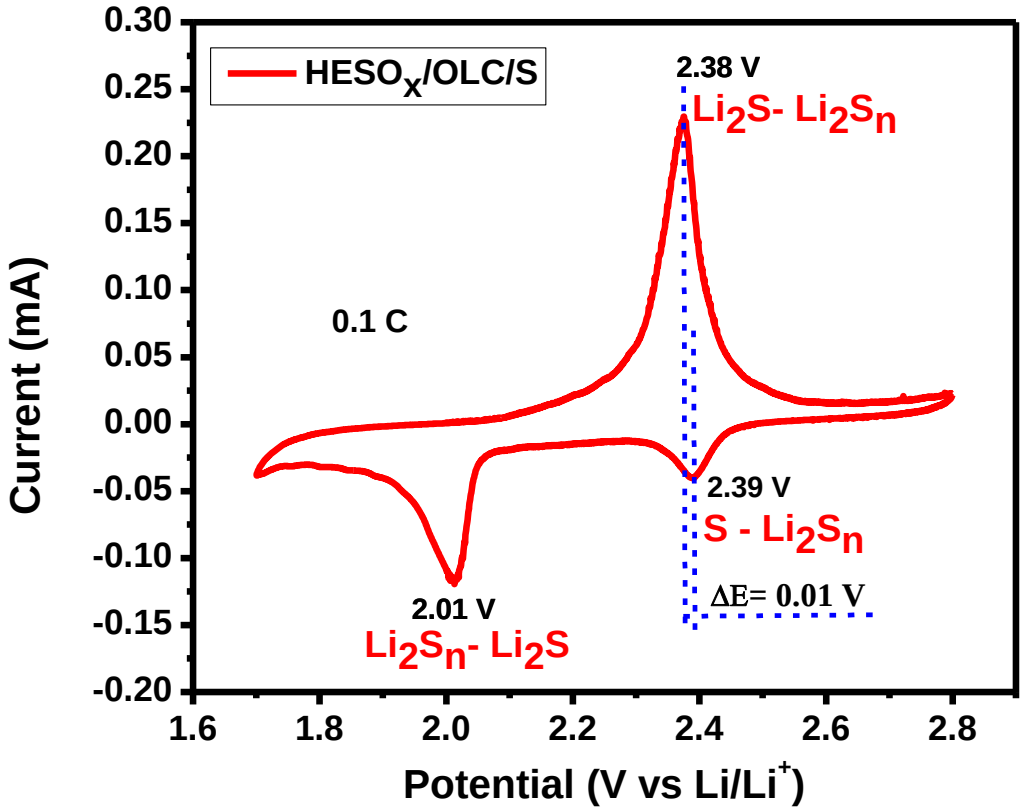

Figure 6.4: CV plot of $HESO_x$/OLC/S (50%)

Upon repeated performance using 75% of sulfur in the loading, the CV in the same voltage range, there was a significant change in the anodic peaks whereby instead of one peak, two peaks were formed signifying the corresponding reverse cathodic reactions, shown in Figure 6.5. Hence we proceeded with the 75% sulfur loading in the subsequent electrochemical measurements. OLC/S was used as a control and it showed a higher current density compared to $HESO_x$/OLC/S.

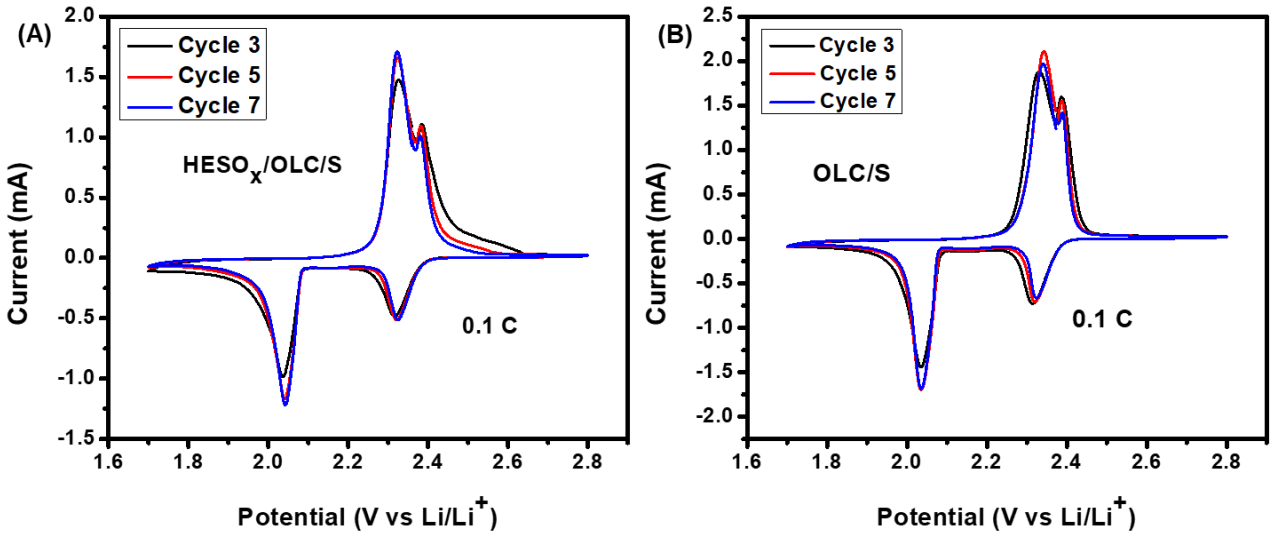

Figure 6.5: CV plot of **(A)** $HESO_x$/OLC/S (75%) and **(B)** OLC/S (75%)

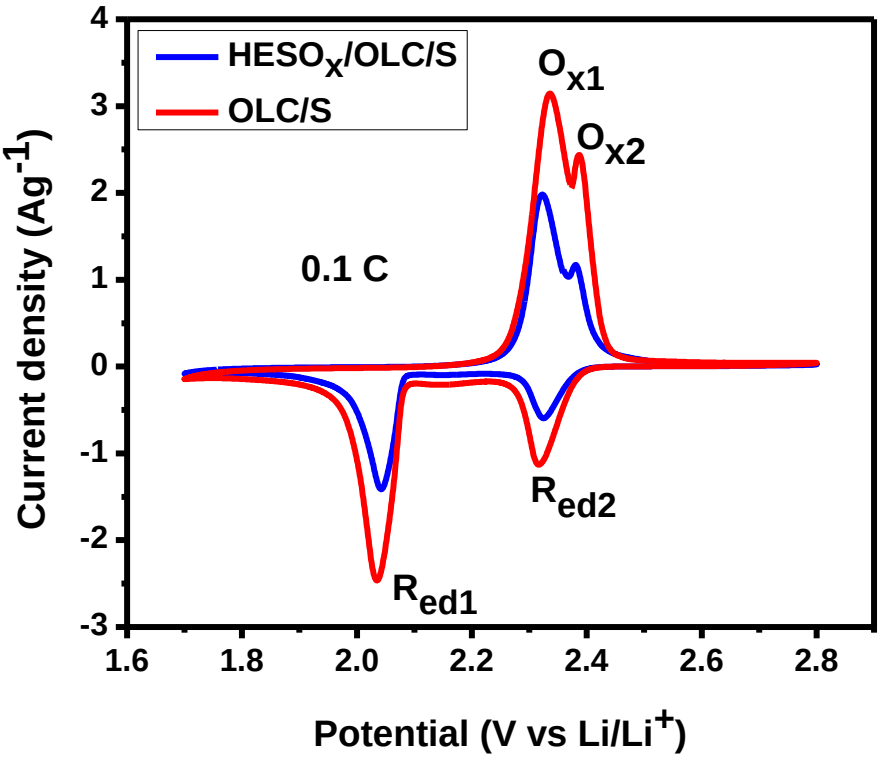

Figure 6.6: Comparison CV plots of $HESO_x$/OLC/S and OLC/S

Figure 6.6 shows CV comparison plots between HESOx/OLC/S and OLC/S whereby O_X and R_d represent oxidation and reduction respectively. The reversibility of cathode materials was determined from Figure 6.6 and the resulting results were summarized in Table 6.2. From this table the I_{pa}/ I_{pc} ratios were greater than 1, which indicated reversible processes. ΔE_p values of $HESO_x$/OLC/S were lower for both of the oxidation and reduction peaks shown in Figure 6.6. This proved that $HESO_x$/OLC/S had higher diffusion kinetics than OLC/S.

Table 6.2: CV parameters of HESOx/OLC/S and OLC/S

	$HESO_X$/OLC/S		**OLC/S**	
CV parameter	**O_{x1}, R_{ed1}**	**O_{x2}, R_{ed2}**	**O_{x1}, R_{ed1}**	**O_{x2} R_{ed2}**
E_{pa}, V	2.32	2.38	2.34	2.39
E_{pc}, V	2.04	2.32	2.04	2.32
$E^{1/2}$, V	2.18	2.35	2.19	2.36
ΔE_p, V	0.28	0.06	0.30	0.07
***I_{pa}*, mA**	1.74	0.86	2.64	1.78
***I_{pc}*, mA**	1.27	0.54	2.27	1.02
I_{pa}//I_{pc}	1.37	1.59	1.16	1.75

6.3.2. GCD analysis

Figure 6.7 compares the GCD curves of $HESO_x$/OLC/S and OLC/S for the 1st and 5th cycles. Any changes in the discharge plateaus reflect the electrochemical activity of the cathodes [12]. One charge plateau at ~2.4 V and two discharge plateaus at ~2.03 V and ~2.0 V are evident in the profiles which are consistent with the CV redox peaks. These discharge plateaus are more prolonged for OLC/S than for $HESO_x$/OLC/S whereby for OLC/S the initial discharge capacities are 509.37 $mAhg^{-1}$ and 473.52 $mAhg^{-1}$ for the 1st

and 5th cycle respectively while for $HESO_x$/OLC/S they are 302.53 $mAhg^{-1}$ (1st cycle) and 294.27 $mAhg^{-1}$ (5th cycle). The stability of $HESO_x$/OLC/S highlights its function in enhancing the retention of polysulfides and conversion whereby it portrays a retention of 99% while OLC/S retains 93%.

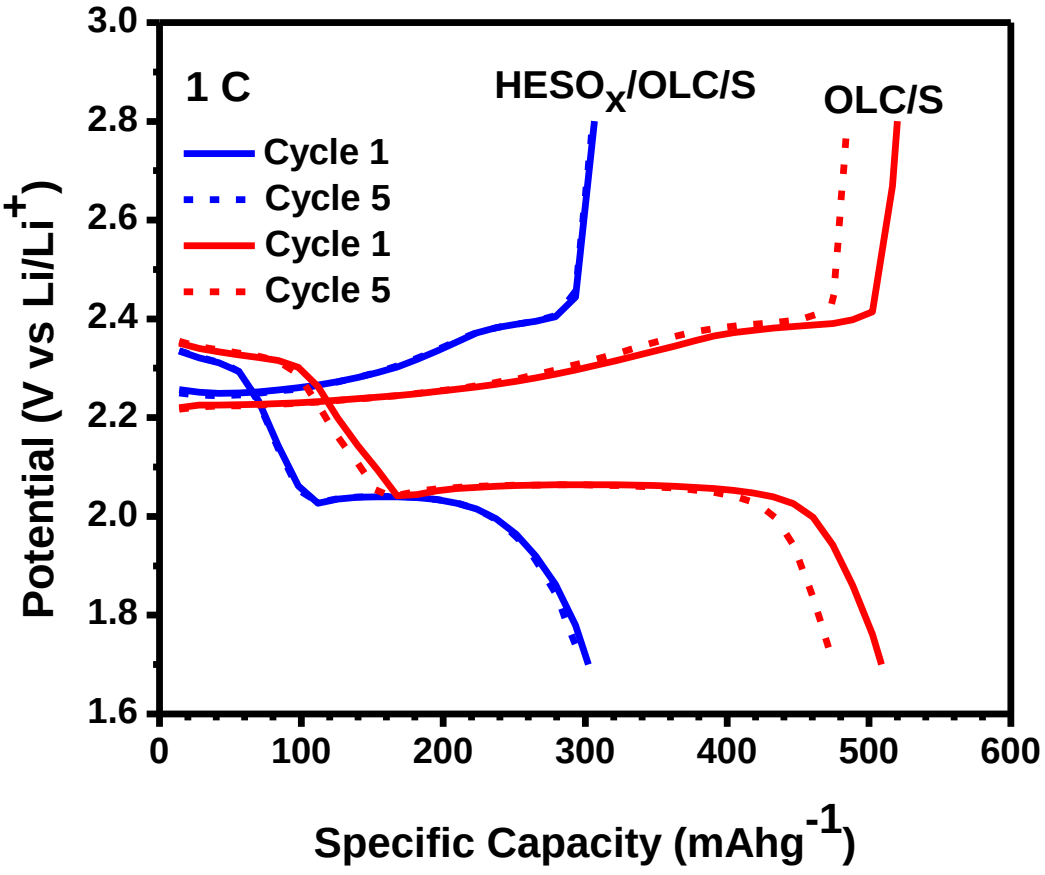

Figure 6. 7: GCD profile comparison plot

6.3.3. Rate capability analysis

Figure 6.8 (A and B) shows the rate performance of $HESO_x$/OLC/S and OLC/S cathodes at 0.1 C, 0.2 C, 0.3 C, 0.5 C, 2.0 C. The discharge capacities for OLC/S were 523.10$mAhg^{-1}$, 329.02$mAhg^{-1}$, 275.21$mAhg^{-1}$, 263.22$mAhg^{-1}$, 237.89$mAhg^{-1}$, with 45% capacity recovery while $HESO_x$/OLC/S discharge capacities were 220.33$mAhg^{-1}$, 196.20$mAhg^{-1}$, 192.35$mAhg^{-1}$,180.87$mAhg^{-1}$,163.89$mAhg^{-1}$ with 74% capacity recovery. This proves that OLC/S experiences a very high capacity decay and this proves the need

of $HESO_x$ as an electrocatalyst. This performance of $HESO_x$ can be attributed to the random metal action species that capture the polysulfides more efficiently by means of chemisorption.

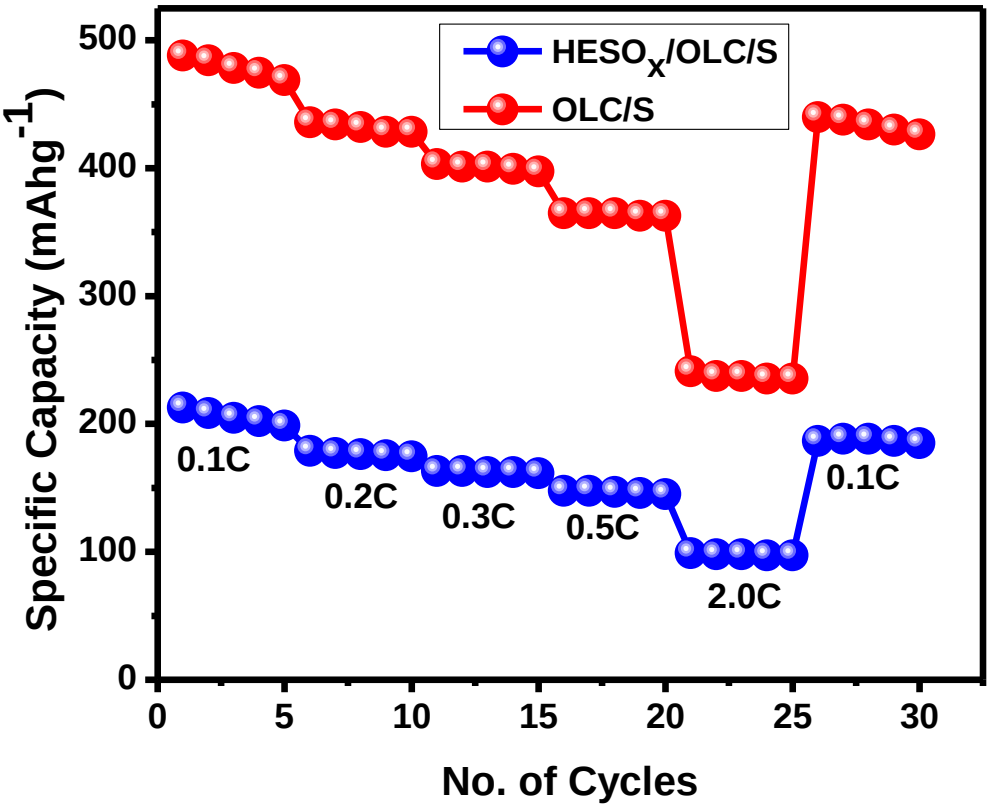

Figure 6.8: Rate capability of **(A)** $HESO_x$/OLC/S and **(B)** OLC/S

6.3.4. Cycling stability

Figure 6.9 compares the cycling performance between $HESO_x$/OLC/S and OLC/S for 100 cycles at a current density of 1 C. The calculated capacity retention is 98% for $HESO_x$/OLC/S and 63% for OLC/S. This indicate the major function of $HESO_x$ in improving the stability of the cathode.

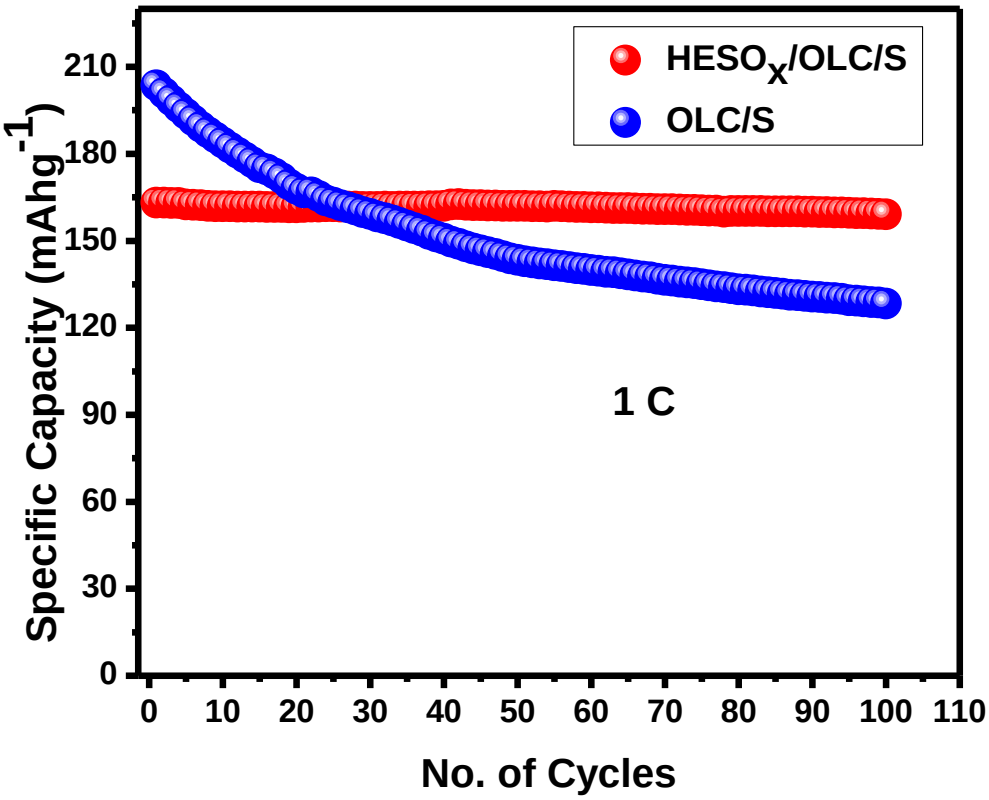

Figure 6.9: Cycling stability comparison

6.3.5. Electron impedance spectroscopy analysis (EIS)

EIS spectra for $HESO_x$/OLC/S and OLC/S in the BoL and EoL were compared as shown in Figure 6.10.

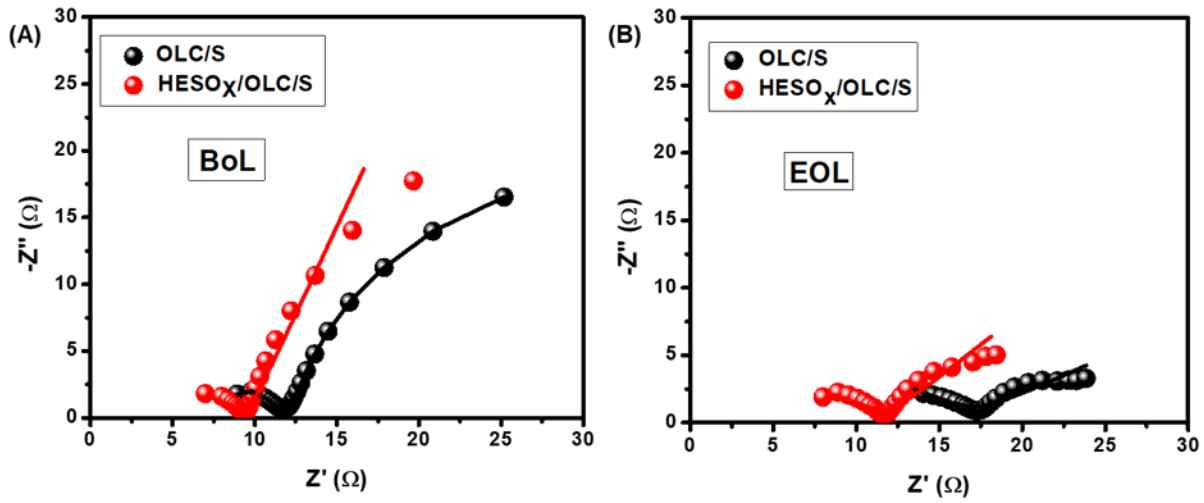

Figure 6.10: (A) Nyquist plot comparison between $HESO_x$/OLC/S and OLC/S

Equivalent Circuit

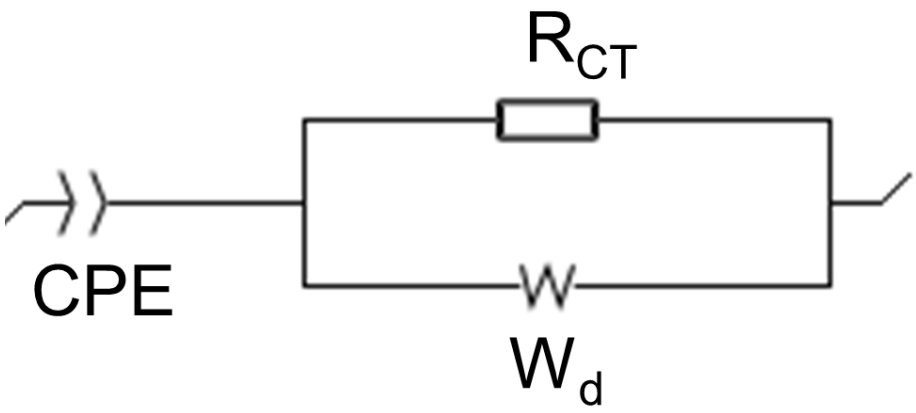

Figure 6.11: Equivalent EIS Circuit

Tables 6.3 and 6.4, indicate the values obtained from fitting the circuits. The R_{CT} values of OLC/ S are (11.92 and 16.30) while those of $HESO_x$/OLC/S are (9.61 and 11.65) in the BoL and EoL respectively. This shows that the charge transfer impedance is almost

comparable for both composites at the EoL. OLC/S shows W_d values of (6338 and 9963) while $HESO_x$/OLC/S shows W_d values of (4994 and 4642) in the BoL and EoL respectively. The low diffusion impedance $HESO_x$/OLC/S contributes to fast kinetics of LIPS conversion [13].

Table 6.3: EIS fittings BoL

Circuit elements	$HESO_x$/OLC/S	OLC/S
R_{CT} (Ω)	9.61 ± 0.60	11.92 ± 0.67
W_d ($\Omega s^{-1/2}$)	4994 ± 1407	6338 ± 1508
CPE (Fsa^{-1})	$(12.22 \pm 2.20)\times10^{-3}$	$(13.7 \pm 2.38)\times10^{-3}$
a	0.78	0.70

Table 6.4: EIS fittings EoL

Circuit elements	$HESO_x$/OLC/S	OLC/S
R_{CT} (Ω)	11.65 ± 1.097	16.3 ± 2.09
W_d ($\Omega s^{-1/2}$)	4642 ± 1123	9963 ± 1579
CPE (Fsa^{-1})	0.045 ± 0.015	0.064 ± 0.015
a	0.49	0.32

The Li^+ diffusion coefficients were calculated for the Randles plot in figure 6.12. $HESO_x$/OLC/S shows diffusion coefficients of $2.6172e^{-17}$ cm^2s^{-1} and $3.4535e^{-17}$ cm^2s^{-1} in the BoL and EoL respectively while OLC/S portrays Li^+ diffusion coefficients of $1.6591e^{-17}$ cm^2s^{-1} and $4.8146e^{-17}$ cm^2s^{-1} respectively. The high Li^+ diffusion coefficient from the EoL of OLC/S explains its high performance compared to $HESO_x$/OLC/S.

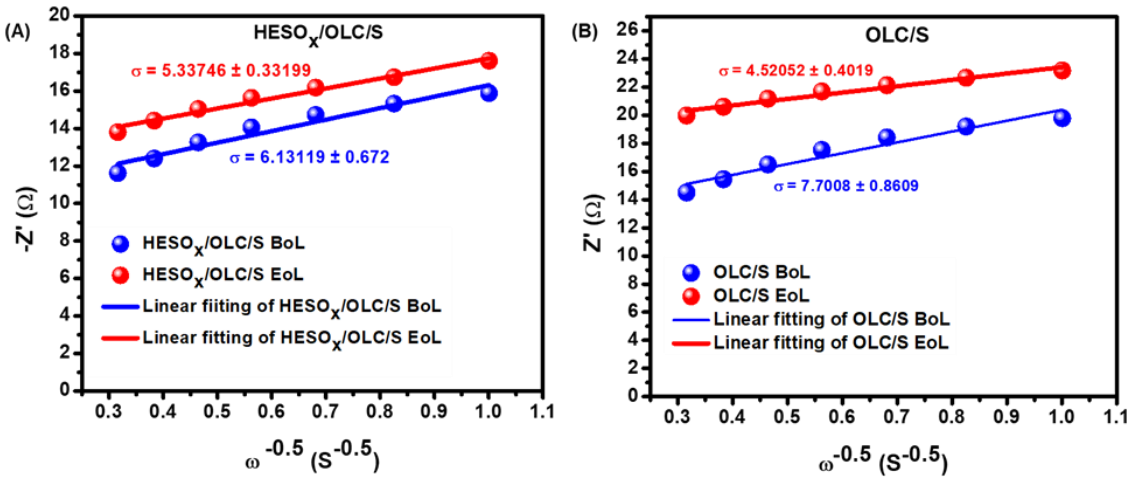

Figure 6.12: Randles plot of **(A)** $HESO_x$/OLC/S and **(B)** OLC/S

6.4. Summary

In conclusion, XRD showed the successful synthesis of $HESO_x$ inverse spinel. Raman spectra gave five Raman active bands (E_g), (F_{2g} 1), (F_{2g} 2), (F_{2g} 3), and (A_{1g}) which corresponded to ferrite systems. $HESO_x$ was then mixed with OLC/S by melt diffusion and used in electrochemistry. Similarly, OLC/S was prepared by the same synthesis route and used as a control. HESOx/OLC/S composite showed higher diffusion kinetics based on results from CV and EIS spectra. From the CV, HESOx/OLC/S showed a smaller ΔE_p while from the EIS it had lower R_{CT} values. OLC/S showed better energy storage properties which was evident in the GCD analysis.

6.5. References

1. Wang, Y.-Q., et al., High-Entropy Oxide Nanofibers as Catalytic Host Promising High Volumetric Capacity of Sulfur-Based Composites for Lithium–Sulfur Batteries. ACS Applied Energy Materials, 2023. **6**(16): p. 8377-8387.
2. Chung, S.-H., et al., High Entropy Oxide (CrMnFeNiMg)3O4 with Large Compositional Space Shows Long-Term Stability as Cathode in Lithium-Sulfur Batteries. ChemSusChem, 2023. **16**(8): p. e202300135.
3. Zheng, Y., et al., A high-entropy metal oxide as chemical anchor of polysulfide for lithium-sulfur batteries. Energy Storage Materials, 2019. **23**: p. 678-683.
4. Zhao, M., et al., A Perspective toward Practical Lithium–Sulfur Batteries. ACS Central Science, 2020. **6**(7): p. 1095-1104.
5. Wang, Y., et al., Enhancing Catalytic Activity of Titanium Oxide in Lithium–Sulfur Batteries by Band Engineering. Advanced Energy Materials, 2019. **9**(24): p. 1900953.
6. Wang, Z.-Y., et al., Conductive RuO2 stacking microspheres as an effective sulfur immobilizer for lithium–sulfur battery. Electrochimica Acta, 2020. **337**: p. 135772.
7. Wang, J., et al., Engineering the Conductive Network of Metal Oxide-Based Sulfur Cathode toward Efficient and Longevous Lithium–Sulfur Batteries. Advanced Energy Materials, 2020. **10**(41): p. 2002076.
8. Ubaldini, A., et al., Preparation and Characterization of Isostructural Na2MoO4 and Na2WO4 and a Study of the Composition of Their Mixed System. Molecules, 2023. **28**(18): p. 6602.
9. Galinetto, P., et al., Raman spectroscopy in zinc ferrites nanoparticles. Raman spectroscopy, 2018(InTech): p. 223.
10. Modi, K.B., et al., Raman and Mossbauer Spectroscopy and X-ray Diffractometry Studies on Quenched Copper–Ferri–Aluminates. Inorganic Chemistry, 2015. **54**(4): p. 1543-1555.
11. Fan, H., et al., Grapevine-like high entropy oxide composites boost high-performance lithium sulfur batteries as bifunctional interlayers. Green Energy & Environment, 2022.

12. Raza, H., et al., High-entropy stabilized oxides derived via a low-temperature template route for high-performance lithium-sulfur batteries. EcoMat, 2023. **5**(4): p. e12324.
13. Chatterjee, A., et al., Rare-Earth Doped Configurational Entropy Stabilized High Entropy Spinel Oxide as an Efficient Anchoring/Catalyst Functional Interlayer for High-Performance Lithium-Sulfur Battery. Batteries & Supercaps, 2023. **6**(7): p. e202300082.

Chapter 7

Conclusion and recommendation for future work

7.1. Conclusion

Material development is the backbone of the evolution of societies and sustainability. The development of manganese-based oxides which are generally referred to as 'holy grail' has been of great interest in energy application systems. They however succumb to multiple challenges hence this research work has been based on multiple modification strategies. First and foremost, we fabricated alpha MnO_2 and β-MnO_2 with hydrothermal and microwave irradiation respectively, and compared their performance. Microwave irradiation of β-MnO_2 was employed to reduce the Jan-Teller distortion that mostly occurs in manganese oxides. The success of this method was indicated by the high electrochemical performance of β-MnO_2 in relation to high specific capacity and current response. We then modified the alpha MnO_2 by adding Mn^{2+} additive to the electrolyte. This greatly improved its specific capacity because it reduced the Mn dissolution by achieving a proper balance between the electrode and electrolyte.

Secondly, we synthesized a manganese-based high-entropy spinel oxide $(CoCuMnFeNi)_3O_4$ for zinc-ion batteries. We chose Co, Cu, Ni, and Fe metals due to their comparable ionic radius and because they exist in the same period as manganese (Period 3). The high-entropy spinel oxide had a merit of 'cock-tail' effect which is the synergistic contribution of each of the metals. Cu ions were mostly useful in increasing the operating voltage of the battery, Co ions were used as structural support to enhance the stability during the cycling process while Ni^{2+} ions were employed due to their good electrochemical activity. The main goal of using high-entropy spinel oxides was the availability of 2 Wyckoff sites (A and B) which represent tetrahedral and octahedral positions respectively, for the accommodation of ions.

Lastly, we employed the manganese-based high-entropy spinel oxide $(CoCuMnFeNi)_3O_4$ to lithium-sulfur batteries. This work provided full evidence of entropy stabilization effect

whereby lattice distortion which is a major core effect, stabilized the battery with the spinel oxide $(CoCuMnFeNi)_3O_4$/OLC/S.

7.2. Recommendation for future work

- Studies using operando and in-situ methods are necessary in order to acquire instantaneous information about the reaction mechanisms, intermediates, and structure reactivity relationships. It will be of significance in defining the catalytic reactions.
- Optimizing the geometric configuration and composition of the $HESO_x$ catalyst through comprehensive investigation using density functional theory (DFT) simulations.
- Incorporation of the $HESO_x$ catalysts in separators.
- Use of gel electrolytes for ZIBs.
- Studying in-depth the E/S ratio in lithium-sulfur batteries.
- Use of Mn^{2+} additive in manganese-based high-entropy for zinc-ion battery.
- Post-mortem XRD, XPS, and Raman for the electrode material.

Appendix A

Supporting information for Chapter 4

Galvanostatic intermittent titration technique (GITT)

It was first proposed by R.A. Huggins and W. Weppnerand in 1977 as a test method that combined steady-state and transient measurements[1]. This characterization technique is mainly for electrochemical devices with large ions such as Zn^{2+}, NH^{4+}, Na^{+}, and K^{+} as charge carriers. It determines the diffusion kinetics in the electrochemical processes. This is due to the difficulties encountered in the insertion and extraction of ions which has made scientists to study more on the reaction kinetics [2].

This analysis was performed using Neware Software BTSClient80 in South East University (China). This was done by applying a constant current pulse to the system to raise the potential of the coin cell. This was followed by interrupting the current to enter into a relaxation phase. The above process was then repeated 5 times and the results were recorded.

Figure S1 shows the GITT curves for both β-MnO_2 and α-MnO_2. These results portrayed a voltage drop immediately after applying current which was as a result of R_{CT} and uncompensated resistance. During relaxation time, the voltage also changed gradually, which was a result of the diffusion properties of ions [3, 4].

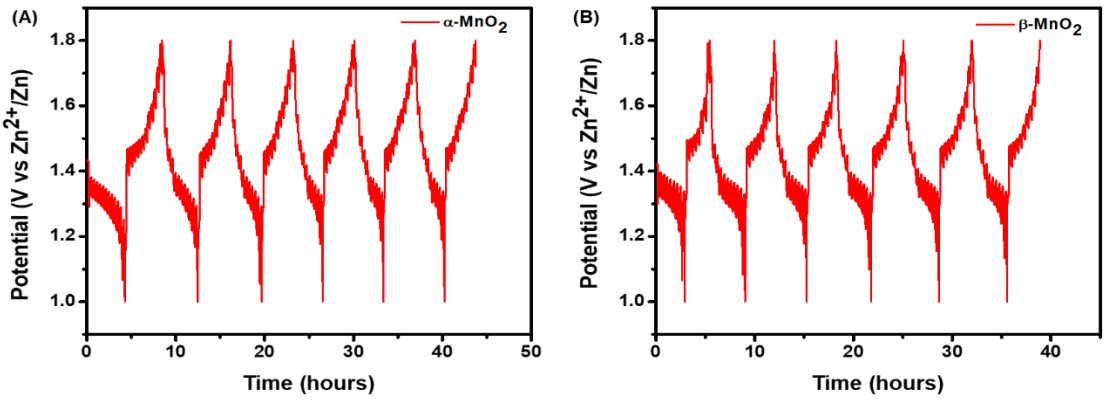

Figure S.1: GITT results of **(A)** α-MnO_2 and **(B)** β-MnO_2

Table S.1: Comparison table for α-MnO_2

Material	Reversible Capacity (mAh/g)		Capacity retention (%)	Electrolyte	Ref/ Year	Current density
	Before Aging	After Aging				
α-MnO_2	194	147 after 30 cycles	76	1.0M $ZnSO_4$	[5] 2014	C/20
α-MnO_2	240	140 after 300 cycles	58	2M $ZnSO_4$ +0.2M $MnSO_4$	[6] 2020	0.1 Ag^{-1}
α-MnO_2	60	50 after 2000 cycles	83	0.1M $Zn(OTf)_2$ DMSO	[7] 2020	0.1 Ag^{-1}
α-MnO_2	200	104	46	1.0M $ZnSO_4$	[8] 2016	83 $mAhg^{-1}$
α-MnO_2, $Ag_{0.4}Mn_8O_{16}$	135, 220	81 , 110 after 800 cycles	60, 50	2.0 M $ZnSO_4$ +0.2 M $MnSO_4$	[9] 2022	1 Ag^{-1}
Fe/α-MnO_2@PPy	200	198 after 100 cycles	98.9	2 M $ZnSO_4$ +0.1 M $MnSO_4$	[10] 2021	100 $mAhg^{-1}$

α-MnO_2	91.5	73 after 100 cycles	80	1.0 M $ZnSO_4$/ 0.1M $MnSO_4$/gelatin gel	[11] 2020	333 mAg^{-1}
α-MnO_2/graphene scrolls (MGS)	382.2	362.6 after 100 cycles	95	2M $ZnSO_4$	[12] 2018	0.1 Ag^{-1}
α-MnO_2@2-MI, α-MnO_2	58	41 ,10 After 2000 cycles	70	2 M $ZnSO_4$ and 0.2 M $MnSO_4$	[13] 2021	1000 mAg^{-1}
α-MnO_2/rGO-PPy,α-MnO_2/rGO, α-MnO_2	213.8, 158.1, 86.4	183.7 after 100 cycles	85.9	$Zn(CF_3SO_3)_2$	[14] 2021	0.5 Ag^{-1}
α-MnO_2/Super P	180	84.6 after 1000 cycles	47	2M $ZnSO_4$	[15] 2021	1.0 Ag^{-1}
α-MnO_2	233	147 after 50 cycles	63	1M $ZnSO_4$	[16] 2015	83 mAg^{-1}
α-MnO_2/CNTs	302	116 after 2000 cycles	78.4	0.1 M $MnSO_4$ and 2.0 M $ZnSO_4$	[17] 2022	100 mAg^{-1}

α-MnO_2 This work	140.60	78.60 after 100 cycles	55.9	3M $MnSO_4$	**This work**	0.5 Ag^{-1}
α-MnO_2 This work	374.71	217.93 after 100 cycles	58.2	2M $ZnSO_4$ +0.2M $MnSO_4$	**This work**	0.1 Ag^{-1}

Table S.2: Comparison table of β-MnO_2

Material	**Reversible Capacity (mAh/g)**		**Capacity retention (%)**	**Electrolyte**	**Ref/ Year**	**Current density**
	Before Aging	**After Aging**				
β-MnO_2	218	199	91.4 after 200 cycles	3M $ZnSO_4$ +0.2M $MnSO_4$	[18] 2019	0.5C
	161	134	83.2 after 1000 cycles			4C
β-MnO_2 @ graphene oxide	278.6	236.6	After 200cycles	3M $ZnSO_4$ +0.2M $MnSO_4$	[19] 2021	1C
	166.9	129.6	After 2000 cycles			
β-MnO_2		110	After 1000 cycles	2M $ZnSO_4$ +0.5M $MnSO_4$	[20] 2021	0.2 Ag^{-1}

β-MnO_2	100	99	99% after 100 cycles	1M $ZnSO_4$ +0.1M $MnSO_4$	[21] 2019	100 mAg^{-1}
MnO_2@CC		90-100	For 700 cycles	3M $ZnSO_4$ +0.1M $MnSO_4$	[22] 2019	2000 mAg^{-1}
β-MnO_2	500		94% after 300 cycles	$ZnSO_4$	[23] 2019	50 mAg^{-1}
β-MnO_2/PPy	291.3(50^{th} cycle)	361.8 (100^{th} cycle)		2M $ZnSO_4$ +0.1M $MnSO_4$	[24] 2021	0.2 Ag^{-1}
β-MnO_2	104.7(50^{th} cycle)	85.3 (100^{th} cycle)				
β-MnO_2/GPE-CNT			50.02% after 500 cycles	3M $ZnSO_4$	[25] 2023	
β-MnO_2		224.7	After 250 cycles		[26] 2023	0.3 Ag^{-1}
β-MnO_2@C		100	300 cycles	$Zn(CF_3SO_3)_2$ +0.1M ZnSO4	[27] 2020	300 mAg^{-1}
β-MnO_2		100 75	After 1500 cycles After 2000 cycles	2M $ZnSO_4$	[28] 2022	1.0 Ag^{-1}

β-MnO_2			88% after 1000 cycles	1.8M $ZnSO_4$ + 0.2M $MnSO_4$	[29] 2022	1.0 Ag^{-1}
β-MnO_2	135	Decays rapidly		2M $ZnSO_4$ + 0.1M $MnSO_4$	[30] 2023	0.5 Ag^{-1}
β-MnO_2 without vacancies	106		65% after 1000 cycles	2M $ZnSO_4$ +0.2M $MnSO_4$	[31] 2022	2.0 Ag^{-1}
β-MnO_2		163	94% after 1000 cycles	1M $ZnSO_4$ +0.1M $MnSO_4$ + 0.1M Na_2SO_4	[32] 2021	3.0 Ag^{-1}
β-MnO_2 This work	123	88	72% after 100 cycles	3M $ZnSO_4$	**This work**	0.5 Ag^{-1}

Appendix B

Supporting Document for Chapter 6.

Powder X-Ray diffraction

The table below shows the interplanar spacing and lattice parameters that were calculated by the equations below:

Bragg's equation: $n\lambda=2d \sin(\theta)$

where λ is the wavelength of incident X-rays which is assigned 1.5406, (θ) is the peak position (radians), n is the order of diffraction which is assigned 1, and d is the interplanar spacing or d-spacing.

The equation was simplified to: $d= n \lambda / (2 \text{ Sin } \theta)$

There is a relationship between the interplanar spacing and the lattice parameter.

$1/d= h^2/a^2 + k^2/b^2 + l^2/c^2$ since in a cubic structure the dimensions of the cube a=b=c then the equation can be simplified to:

Lattice parameter = d* (square root $(h^2+k^2+l^2)$) which was used in the calculations.

Table S.3: Interplanar spacing and lattice parameter

2theta	Theta	Miller indices			Interplanar Spacing	Lattice Parameter	Average
		h	k	l			
18.37	9.185	1	1	1	4.8257532	**8.358449735**	**8.385887**
30.39	15.195	2	2	0	2.93889894	**8.312461467**	
35.62	17.81	3	1	1	2.51846033	**8.35278797**	
37.31	18.655	2	2	2	2.40817369	**8.342158362**	
43.39	21.695	4	0	0	2.08377476	**8.335099033**	
53.85	26.925	4	2	2	1.70110322	**8.333669767**	
57.38	28.69	5	1	1	1.60455633	**8.337519284**	
63.03	31.515	4	4	0	1.47363291	**8.714949657**	

The crystallite size was calculated based on the Scherrer formula:

$D_{hkl} = K\lambda/(B_{hkl}\cos\theta)$,

where k is the Scherrer constant assigned 0.9, D_{hkl} is the size of crystals, λ (0.15406 nm) is the wavelength of the incident X-ray, B_{hkl} is the full-width half maximum (FWHM) and (θ) is the peak position in radians.

Table S.4: Calculation of crystallite size

Peak position	**FWHM**	**Crystallite Size D (nm)**	**Average**
18.42432	0.94798	**8.48972635**	9.152584
30.36885	0.7698	**10.69326511**	
35.7684	0.90849	**9.188494102**	
43.51612	0.91797	**9.318033177**	
57.62871	1.03852	**8.730595845**	
63.26919	1.09833	**8.495388406**	

References

1. Kim, J., et al., Principles and applications of galvanostatic intermittent titration technique for lithium-ion batteries. Journal of Electrochemical Science and Technology, 2022. **13**(1): p. 19-31.
2. Jia, M., et al., Re-understanding the galvanostatic intermittent titration technique: Pitfalls in evaluation of diffusion coefficients and rational suggestions. Journal of Power Sources, 2022. **543**: p. 231843.
3. Sun, W., et al., Zn/MnO2 battery chemistry with H+ and Zn2+ coinsertion. Journal of the American Chemical Society, 2017. **139**(29): p. 9775-9778.
4. Wang, G., et al., Hierarchical K-Birnessite-MnO2 Carbon Framework for High-Energy-Density and Durable Aqueous Zinc-Ion Battery. Small, 2021. **17**(45): p. 2104557.
5. Lee, B., et al., Electrochemically-induced reversible transition from the tunneled to layered polymorphs of manganese dioxide. Scientific Reports, 2014. **4**(1): p. 6066.
6. Gao, X., et al., H+-Insertion Boosted α-MnO2 for an Aqueous Zn-Ion Battery. Small, 2020. **16**(5): p. 1905842.
7. Corpuz, R.D., et al., Binder-Free α-MnO2 Nanowires on Carbon Cloth as Cathode Material for Zinc-Ion Batteries. International Journal of Molecular Sciences, 2020. **21**(9): p. 3113.
8. Alfaruqi, M.H., et al., A high surface area tunnel-type α-MnO2 nanorod cathode by a simple solvent-free synthesis for rechargeable aqueous zinc-ion batteries. Chemical Physics Letters, 2016. **650**: p. 64-68.
9. Fenta, F.W., et al., Structural engineering of α-MnO2 cathode by Ag+ incorporation for high capacity aqueous zinc-ion batteries. Journal of Power Sources, 2022. **548**: p. 232010.
10. Xu, J.-W., et al., High-performance reversible aqueous zinc-ion battery based on iron-doped alpha-manganese dioxide coated by polypyrrole. Journal of Colloid and Interface Science, 2021. **598**: p. 419-429.
11. Putro, D.Y., et al., Quasi-solid-state zinc-ion battery based on α-MnO2 cathode with husk-like morphology. Electrochimica Acta, 2020. **345**: p. 136189.

12. Wu, B., et al., Graphene Scroll-Coated α-MnO2 Nanowires as High-Performance Cathode Materials for Aqueous Zn-Ion Battery. Small, 2018. **14**(13): p. 1703850.
13. Cao, X.-W., et al., In-situ Co-precipitated α-MnO2@2-methylimidazole cathode material for high performance zinc ion batteries. Journal of Alloys and Compounds, 2022. **896**: p. 162785.
14. Niu, T., et al., Preparation and electrochemical properties of α-MnO2/rGO-PPy composite as cathode material for zinc-ion battery. Journal of Materials Science, 2021. **56**(29): p. 16582-16590.
15. Yang, C., et al., α-MnO2/super-P with conductive carbon network for rechargeable aqueous Zinc ion batteries. Materials Letters, 2021. **302**: p. 130419.
16. Alfaruqi, M.H., et al., Enhanced reversible divalent zinc storage in a structurally stable α-MnO2 nanorod electrode. Journal of Power Sources, 2015. **288**: p. 320-327.
17. Xie, J., et al., α-MnO2/CNTs with cross-linked reticular structure: Towards ultralong life zinc-ion batteries. Diamond and Related Materials, 2022. **125**: p. 109024.
18. Liu, M., et al., Tuning phase evolution of β-MnO2 during microwave hydrothermal synthesis for high-performance aqueous Zn ion battery. Nano Energy, 2019. **64**: p. 103942.
19. Ding, S., et al., Oxygen-deficient β-MnO2@ graphene oxide cathode for high-rate and long-life aqueous zinc ion batteries. Nano-Micro Letters, 2021. **13**(1): p. 173.
20. Liu, W., et al., β-MnO2 with proton conversion mechanism in rechargeable zinc ion battery. Journal of Energy Chemistry, 2021. **56**: p. 365-373.
21. Guo, C., et al., A case study of β- and δ-MnO2 with different crystallographic forms on ion-storage in rechargeable aqueous zinc ion battery. Electrochimica Acta, 2019. **324**: p. 134867.
22. Deng, Z., et al., β-MnO2 nanolayer coated on carbon cloth as a high-activity aqueous zinc-ion battery cathode with high-capacity and long-cycle-life. Materials Letters, 2019. **248**: p. 207-210.
23. Han, M., et al., Oxygen defects in β-MnO2 enabling high-performance rechargeable aqueous zinc/manganese dioxide battery. Iscience, 2020. **23**(1).

24. Liao, X., et al., Synthesis of three-dimensional β-MnO2/PPy composite for high-performance cathode in zinc-ion batteries. Journal of Alloys and Compounds, 2021. **888**: p. 161619.
25. Xin, S., et al., β-MnO2/three-dimensional graphene-carbon nanotube hybrids as cathode for aqueous zinc-ion battery. Journal of Alloys and Compounds, 2023. **968**: p. 172115.
26. Xu, S., et al., Exploring the Mechanism of Single-Crystal MnO2 as Cathodes for Zinc Ion Batteries. ChemPlusChem, 2023. **88**(8): p. e202300341.
27. Jiang, W., et al., Facile plasma treated β-MnO2@C hybrids for durable cycling cathodes in aqueous Zn-ion batteries. Journal of Alloys and Compounds, 2020. **827**: p. 154273.
28. Li, H., et al., Interface regulated MnO2/Mn2+ redox chemistry in aqueous Zn ion batteries. Chemical Engineering Journal, 2022. **446**: p. 137205.
29. Huang, J., et al., Amphiphilic-molecular templated porous β-MnO2 for high-performance rechargeable aqueous Zn-MnO2 batteries. Electrochimica Acta, 2022. **424**: p. 140646.
30. Wang, K., et al., Structural Transformation by Crystal Engineering Endows Aqueous Zinc-Ion Batteries with Ultra-long Cyclability. Small, 2023. **19**(29): p. 2300585.
31. Wang, Z., et al., Manipulating Oxygen Vacancies by K+ Doping and Controlling Mn2+ Deposition to Boost Energy Storage in β-MnO2. ACS Applied Materials & Interfaces, 2022. **14**(42): p. 47725-47736.
32. Cai, X., et al., Hydrothermal synthesis of β-MnO2 nanorods for highly efficient zinc-ion storage. Ionics, 2021. **27**(9): p. 3943-3950.